Development and Characterisation of Functionally Coated Steel as a Bipolar Plate Material for Polymer Electrolyte Membrane Fuel Cells

---

By

Tanveerkhan Shabbirahmedkhan Pathan

A thesis submitted to University College London for the degree of Doctor of Philosophy

Electrochemical Innovation Lab

Department of Chemical Engineering,

Torrington Place, WC1E 7JE

May 2017

Declaration

I, Tanveerkhan Shabbirahmedkhan Pathan, confirm that the work presented in this thesis is my own. Where information has been derived from other sources, I confirm that this has been indicated in the thesis.

T.S.Pathan

May 2017

Dedicated to the five men whose lives have influenced and shaped mine:

Rasulkhan Rahimkhan Pathan

Mohammedkhan Rahimkhan Pathan

Dr Habibkhan Rahimkhan Pathan

Ahmed Abdul Razak Shaikh

Bashir Malam

Acknowledgement

First of all, I would like to thank the Almighty Allah for His Mercy and for everything that He has blessed me with and for making me capable of undertaking this PhD.

There are probably not enough words for me to thank Dr Paul R. Shearing, my PhD supervisor. He has shown immense patience and has always showed faith in me and motivated me to pursue the goal. He has trusted me when the performance was not at its best. I would like to extend my gratitude to him for accepting to work with me and providing me with continuous guidance, ideas and supervision during the period of my research. I am grateful that he went out of his way to apply for the Dean's award to cover the international tuition fees for this PhD project. Beyond the PhD project, his character, his humility and his moral values have influenced me deeply and he has motivated me to improve myself as a researcher and more importantly as a human being.

I would like to thank Prof Daniel J.L. Brett who considered my application for a PhD at the Electrochemical Innovation Lab and first introduced me to Dr Shearing. His expertise on corrosion electrochemistry has been immensely useful in this thesis. I would like to thank Prof Brett for having his door open for quick unplanned chats that were extremely useful.

I would also like to thank Dr Patrick L. Cullen for his expertise on graphene deposition and the facilities at the Department of Physics and Astronomy at UCL. The electrophoretic deposition of graphene would not have been possible without his insight on obtaining graphene solutions.

I am deeply thankful to my industrial supervisor, Dr Christopher Mills without whom this project would not have had the industrial insight that was needed. I would also like to thank Dr Sivasambu Bohm at Tata Steel UK for helping me acquire the industrial funding for this project and materialising the collaboration between UCL and Tata Steel Europe. I would like to thank Dr John Collingham, who despite being senior manager and being so busy,

took interest in my project and helped every time an external publication approval was needed. The same gratitude goes towards my line manager Dr Sohail Hajatdoost for his time and discussions on this project and to Dr Samson Patole for his expert opinions during the monthly review meetings. I would also like to extend my thanks to Dr Maurice Jansen (Tata Steel NL) who has big input in the samples that are studied in this PhD. His fuel cell bipolar plate knowledge has helped me a lot in this project. I would also like to thank Dr Debbie Hammond and Dr Sreedhara Sarma for the support they have rendered.

I would like to thank my colleagues and friends at the EIL for creating a wonderful social atmosphere to work in. I would like to thank Tobias Neville for his in-depth discussions on corrosion and for the never ending support that was promptly available whenever I asked for. I would like to thank the post-doctoral researchers; Dr Quentin, Dr Ana, Dr Leon, Dr Francesco and the colleagues Josh and Alvin for their help and support during the analysis of my samples. I would like to thank my friends Vidal, Eric, Simon, Dami and Fabiola for their advice and the moral support in difficult times. Special thanks to Dr Jason Millichamp and Dr Tom Mason, for all the help and insight you have given me with my project. I am grateful to Mike and Simon and the admin team at the department for their help throughout my research. I would like to thank again, all my friends and colleagues at EIL for their help and support.

Finally, I would like to thank my parents for their continuous support and love that has made me what I am today. And as for my wife's contributions are concerned, I don't think any words are worthy enough to justify her sacrifices. A living example of selflessness, passion and love, and without her support; both moral and financial, the completion of this thesis may have been a lot more difficult. Thank you very much Farheen!

Abstract

Polymer Electrolyte Membrane Fuel Cells (PEMFCs) produce electricity with minimum environmental impact. The major hurdles in commercialisation of PEMFCs are the high commissioning and operation costs and the durability of the cell. A bipolar plate (BPP) is a key weight and cost determining component in PEMFC that undertakes significant performance-determining functions in the cell. Currently, stainless steel is used as a BPP in large number of commercial PEMFCs; however, corrosion within the harsh fuel cell operating environment remains a major concern. Further, the formation of passivation layers reduces the electrical conductivity and the overall performance.

The aim of the study is to develop and characterise functional coatings for different grades of steel, including mild steel for BPP applications. Compared to stainless steel, mild steel is low cost, but has poor corrosion properties, thereby requiring a coating. Mild steel with a proprietary coating was analysed with improved contact resistance and corrosion resistance under simulated fuel cell environment. Potentiodynamic, potentiostatic and accelerated corrosion tests have been used to analyse the coated mild steel and the results are compared with commercial SS 316L. *In situ* fuel cell results are reported using SS 316L and compared with graphite to demonstrate the significance of passive layer.

Graphene was deposited on different grades of steel owing to its excellent chemical and mechanical properties, high durability, excellent corrosion resistance and high electrical conductivity. This was achieved using chemical vapor deposition; with improved contact resistance and electrophoretic deposition; with improved corrosion resistance.

Finally, a novel method of corrosion analysis is presented using 3D x-ray computed tomography in an attempt to understand the sub-surface propagation of corrosion in coated samples.

Abstract

This study results in better understanding of the corrosion phenomena in PEMFC environment and also provides coating options for reducing the cost of PEMFC operation whilst improving overall output.

Table of Contents

List of Figures

List of Tables

Nomenclature

Symbols and Variables

Symbol	Description
Δg_f	Gibbs free energy $(kj.mol^{-1})$
n	Avogadro's number (6.023×10^{23})
e	Charge of electron $(1.602 \times 10^{-19} coulomb)$
F	Faraday constant $(96485\ C)$
E	Energy or cell voltage (V)
$E^o(E_{rev})$	Nernst voltage or Standard-state reversible cell voltage (V)
R	Universal gas constant $(8.314\ J.mol^{-1}.K^{-1})$
T	Absolute temperature (K)
a	Activity of the concerned species
E_{irrev}	Irreversible voltage loss (V)
η_{act}	Activation overpotential (V)
η_{ohmic}	Ohmic overpotential (V)
η_{conc}	Concentration overpotential (V)
α	Charge transfer coefficient (for most reactions, α ranges from $0.2\ to\ 0.5$ and for symmetrical reactions, α is 0.5)
j	Current density $(A.cm^{-2})$
j_o	Exchange current density for the reaction $(A.cm^{-2})$
ASR	Area specific resistance $(\Omega.cm^2)$
j_L	Limiting current density $(A.cm^{-2})$
I_D	Raman intensity of D (disorder) peak for graphene
I_G	Raman intensity of G (graphitic) peak for graphene
$\emptyset$	Inner potential or Galvani potential
$\Delta\emptyset$	Galvani potential difference

J	Flux of reacting species $(mol.cm^{-2}.s^{-1})$
$V(t)$	Instantaneous voltage (V) at time t
V_m	Maximum or peak value of voltage (V)
ω	Angular frequency $(radians)$
$j(t)$	Instantaneous current (A) at time t
j_m	Maximum or peak value of current (A)
θ	Phase difference
C	Capacitance
L	Inductance
$Z\ (j\omega)$ or $Z\ (\omega)$	Impedance
r	Rate of corrosion (usually $mm.year^{-1}$)
M	Molecular weight of the corroding metal $(g.mol^{-1})$
ρ	Density of metal $(g.cm^{-3})$
i_{corr}	Corrosion current density $(A.cm^{-2})$
j_a	Anodic partial current density $(A.cm^{-2})$
j_c	Cathodic partial current density $(A.cm^{-2})$
η_a	Anodic overpotential
η_c	Cathodic overpotential
$b_a = \left\{\frac{2.303RT}{(1-\alpha)nF}\right\}$	Anodic Tafel slope $(Volt\ per\ decade)$
$b_c = -\left\{\frac{2.303RT}{\alpha nF}\right\}$	Cathodic Tafel slope $(Volt\ per\ decade)$
R_p	Polarisation resistance (Ω)
E_p	Energy of photon $(joules)$
h	Planck's constant $(6.6256 \times 10^{-34} joule.sec)$
v_p	Frequency of photon (Hz)
c	Velocity of light $(2.998 \times 10^{-10} cm.sec^{-1})$
$\bar{v}$	wavenumber (cm^{-1})
ΔE_m	Change in energy of molecule $(joules)$
v_m	Frequency of molecule (Hz)
v_i	Frequency of incident photon (Hz)
v_s	Frequency of scattered photon (Hz)

Abbreviations

2D	Two dimensional
3D	Three dimensional
AC	Alternating current
AES	Auger Electron Spectroscopy
AFC	Alkaline Fuel Cell
AFM	Atomic force microscope
AISI	American Iron and Steel Institute
ASTM	American Society for Testing and Materials
BPP	Bipolar plate
BSE	Backscattered electron
CPE	Constant phase element
CT	Computed tomography
CVD	Chemical vapor deposition
DC	Direct current
DLC	Diamond like carbon
DMF	Dimethylformamide
DMFC	Direct Methanol Fuel Cell
DOE	United States Department of Energy
EDM	Electrical discharge mechanism
EDS	X-ray energy dispersive spectrometry
EIS	Electrochemical impedance spectroscopy
EMF	Electromotive Force
EPD	Electrophoretic deposition
E-T	Everhart-Thornley electron detector
FLG	Few layer graphene
GDL	Gas diffusion layer
GIC	Graphite intercalation compound
GO	Graphene oxide
GO-EPD	Graphene oxide electrophoretic deposition
HOPG	Highly oriented pyrolytic graphite
ICP/AAS	Inductively coupled plasma / atomic absorption spectroscopy
ICP/OES	Inductively coupled plasma / optical emission spectrometry
ICP-MS	Inductively coupled plasma-mass spectrometry
ICR	Interfacial Contact Resistance

ITO	Indium tin oxide
LPR	Linear polarisation resistance
LSV	Linear sweep voltammetry
MCFC	Molten Carbonate Fuel Cell
MEA	Membrane electrode assembly
NMP	N −methyl-pyrrolidone
OCV or OCP	Open Circuit Voltage or Open Circuit Potential
PAFC	Phosphoric Acid Fuel Cell
PEMFC	Polymer Electrolyte Membrane Fuel Cell
PGM	Platinum group metal
PTCVD	Photo-Thermal Chemical Vapor Deposition
PVD	Physical vapor deposition
RF	Radio frequency
RHE	Reversible hydrogen electrode
SCE	Saturated calomel electrode
SE	Secondary electron
SEM	Scanning electron microscopy
SOFC	Solid Oxide Fuel Cell
SPM	Scanning probe microscope
SS	Stainless Steel
STM	Scanning tunnelling microscope
TEM	Transition electron microscopy
VSSA	Volume specific surface area
XPS	X-ray photoelectron spectroscopy
XRD	X-ray diffraction

1. Introduction

A fuel cell is a type of an engine that electrochemically converts hydrogen fuel into electricity. Hydrogen presents a clean fuel option that can be produced abundantly and safely; in theory, an engine that burns pure hydrogen as a fuel produces almost no pollution. A brief history of the development of fuel cells is discussed, along with the types of fuel cells available. The Polymer Electrolyte Membrane Fuel Cell (PEMFC) is a type of fuel cell that has an ion-permeable polymer membrane as an electrolyte. Further, fuel cell electrochemistry and the working of PEMFC are discussed, as well as operating requirements for a range of applications. Finally, the aim and structure of the PhD thesis are discussed with the focus on a particular component of PEMFC; the bipolar plate.

1.1. Overview

The impetus behind the success of the modern civilisation and the development of humanity is energy. Energy can be defined as the ability of a physical system to undertake work, may it be useful or otherwise and the efficiency of any system is then termed as the fraction of useful work out of the total work. Energy is available in a number of forms, such as kinetic energy, potential energy, heat, nuclear power, etc. The very existence of modern human society is predicated on operations such as agriculture, transportation, communication, and industrial production which are all based on the utilisation of different forms of energy. Traditionally, physical labour was the main source of energy, either from humans or animals, and then came the utilisation of fire, wind and water energies. The invention of steam engines then fuelled the industrial revolution. As the use of wood for fire could not keep up with the demand for energy, it led to the dawn of the use of fossil fuels and coal mining in the nineteenth century. The discovery of oil changed the way in which humans consumed fossil fuels for various energy requirements. For decades now, the major source of energy has been fossil fuels such as coal, natural gas or crude oil and today the majority of energy is still derived from these fossil fuels[1].

The extensive use of these natural resources and the ignorance towards the consequences of their use, has led to a negative impact on the environment; including environmental pollution and extensive mining of natural resources. Energy demand and supply is the primary source of release of greenhouse gases[2], and in particular, CO_2. Global fossil fuel CO_2 emissions have increased at a rapid rate in the last century and there is almost a tenfold increase in the last fifty years; this is evident from Figure 1.1 that was published by the United States Department of Energy in 2010[3].

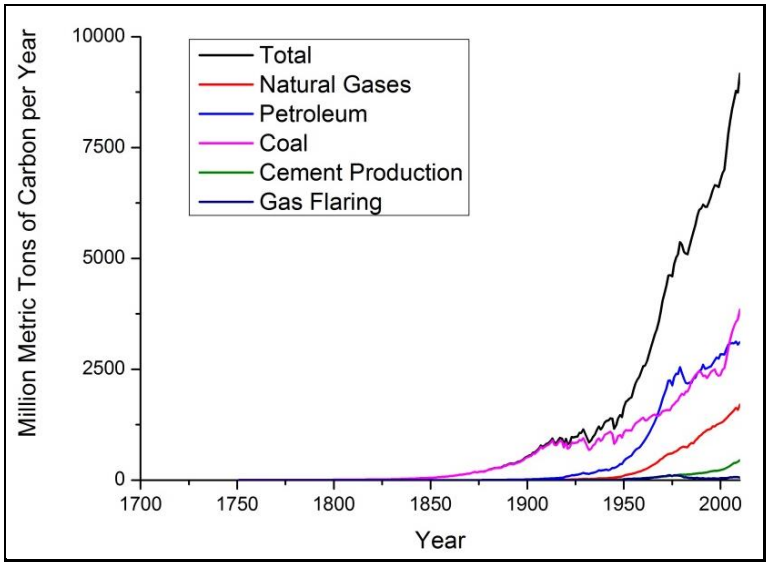

Figure 1.1: CO_2 emissions from different sources from 1750 to 2010 (adapted from[3])

As a consequence, it is obvious that greenhouse gas emission, and the resultant effects of global warming, will directly impact on future energy production. Furthermore, most of the sources of energy that are used today are non-renewable; their extensive usage has led to the depletion in the amounts of fossil fuel that are available. The depletion of fossil fuels also poses a challenge for energy sustainability in future[2]. As a result of the depletion of fossil fuels and the emission of greenhouse gases from utilisation of these fuels, a need has arisen for a cleaner, greener and safer source of energy. In the last few decades, alternative and renewable sources of energy such as solar energy, wind energy, tidal energy, hydro energy, bio-fuels, geo-thermal energy, etc. have been explored or rediscovered. However, conventional energy sources, such as the petroleum-based products, have not been replaced completely because of

the fact that these alternative sources of energy are either not directly applicable for transportation purposes or there are hindrances in their applications including the power available from these sources, energy storage, infrastructure, costs, etc.

1.2. Fuel Cell

Fuel cells are a promising alternative to combustion engines for application in the transportation sector[4]. A fuel cell can be defined as an electrochemical device that converts the chemical energy of the fuel directly into electrical energy[5]. In contrast to an internal combustion heat engine, which tend to have high energy loss due to the heat production and the mechanical work involved in the process, fuel cells produce electric current directly using oxygen and fuel. Fuel cells generate power with high efficiency as they are not limited by the conventional thermodynamic limitations of heat engines such as Carnot efficiency. In addition to this, as there is no thermal combustion involved, fuel cells produce power with minimum pollution and very low environmental impact. The remarkable difference, as compared to the internal combustion engine, is that electrical energy is produced instead of heat.

1.2.1. A Brief History of Fuel Cells

The working of a fuel cell is similar to that of primary battery. However, the striking difference between the two can be explained in terms of the consumption of the fuel. In case of a battery, all the available chemical energy is stored within the battery and it can be described as an energy storage device. The battery stops producing electrical power when the reactants are consumed. However, a fuel cell is an energy conversion device that produces electrical power as long as the reactants (the fuel and the oxidant) are provided. In principle, fuel cells produce power continuously as long as the fuel is supplied[6]. The basic operation of a fuel cell can be depicted in Figure 1.2.

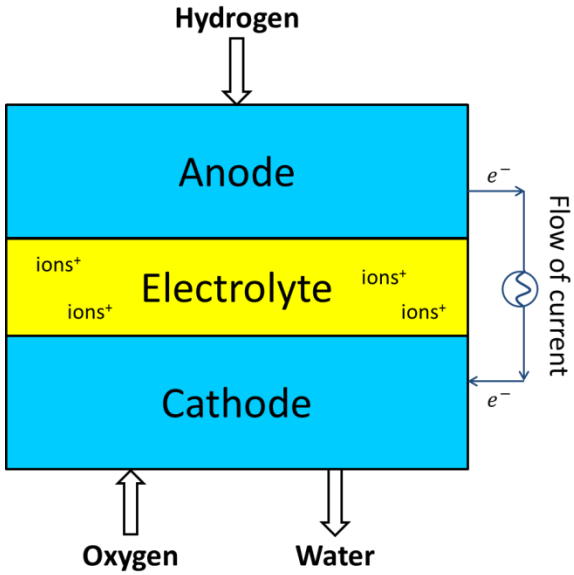

Figure 1.2: General concept of a hydrogen-oxygen fuel cell (adapted from[7])

The discovery of the fuel cell operating principle is attributed to a Welsh lawyer-turned scientist, Sir William Robert Grove, in 1839[8]. However, no real practical use was found for the technology for another century[4,9], the first practical application of the fuel cell was in the United States space programme. The General Electric Company began developing fuel cells in the 1950s and was awarded the contract for the Gemini space mission in 1962. In the 1960s, improvements were made by incorporating Teflon in the catalyst layer directly adjacent to the electrolyte. Significant improvements were made in the technological developments in the early 1970s and onwards, including the application of a fully fluorinated Nafion® membrane as the membrane electrolyte. In 1993, Ballard Power Systems demonstrated fuel cell-powered buses. Significant research in the catalyst area was carried out by the Los Alamos National Laboratory and others[9]. By the end of the twentieth century, almost all car companies had demonstrated a fuel cell-powered vehicle with the efforts fuelled by the United States Department of Energy (DOE). Towards the onset of the twenty first century a new industry was born. The developments lead to the increase in the utilisation of active catalyst and at the same time reduced the amount of precious platinum metal needed. A number of fundamental technical breakthroughs have been achieved during the last two decades; however, there are still many challenges, such as cost reduction and improvement in durability whilst maintaining performance, which remain as

a barrier to the commercialisation of PEMFCs. Table 1.1 summarises the important breakthroughs achieved in the development of a fuel cell.

Table 1.1: A brief history of fuel cells (adapted from[10,11])

1800	W.Nicholson & A.Carlisle describe the process of using electricity to "break" water
1839	Sir William Grove demonstrates fuel cell
1889	Separate teams: L.Mond & C.Langer / C.Wright & C.Thompson / L.Cailleteton & L.Colardeau performed various fuel cell experiments
1893	F.Ostwald describes the role of fuel cell components
1896	W.Jacques constructed a carbon battery
Early 1900s	E.Baur and students conducted experiments on high temperature devices
1959	Bacon demonstrates a practical $5\ kW$ fuel cell system
	Harry Karl Ihrig fitted a modified $15\ kW$ Bacon cell to an Allis-Chalmers agricultural tractor
	Allis-Chalmers went on to develop fuel cell powered forklift trucks, golf cart and submersible vessels in partnership with the US Air Force
1960s	Willard Thomas Grubb & Leonard Niedrach invented PEMFC technology at GE
	The Grubb-Niedrach fuel cell was developed in cooperation with NASA and used in the Gemini space programme
	International Fuel Cells (later UTC Power) developed a $1.5\ kW$ AFC for use in Apollo Space Missions, subsequently developed a $12\ kW$ AFC to provide on board power on all space shuttle flights
1970s	The oil crisis prompts development of alternative energy technologies
	General Motors experimented with the hydrogen fuel cell powered Electrovan and although limited to demonstrations, it marked on of the earliest fuel cell electric vehicles
	Shell involves in developing alcohol fuel cells
	German, Japanese and US vehicle manufacturers began

	experimenting with FCEVs
	Significant progress in the development of PAFC, including a $1\ MW$ unit developed by IFC
1980s	US Navy uses fuel cells in submarines
	Ambitious conceptual designs for municipal utility power plant applications of up to $100\ MW$ output were published
	1983 saw the beginning of fuel cell research by the Canadian company, Ballard
1990s	Large stationary fuel cells are developed for commercial and industrial locations with focus on PEMFC and SOFC
	Early applications of PEMFC and DMFC including portable soldier-borne power, power for devices such as laptops and mobile phones
	Advances in MCFC technology, particularly for large stationary applications sold by Fuel Cell Energy and MTU
	Multiple fuel cell companies are listed on stock exchanges in the late 1990s
2000s	European Union, Canada, Japan, South Korea and the US are engaged in high profile fuel cell demonstration projects, particularly for stationary and transport fuel cells
	Fuel cell buses are deployed in Europe, China and Australia
2007	Fuel cells begin to be sold commercially as stationary backup power units
2008	Honda launches the $100\ kW$ FCX Clarity fuel cell electric car
2009	Residential fuel cell micro-combined heat and power (micro CHP) units become commercially available in Japan
	A number of portable fuel cell battery chargers sold
	Toshiba launches Dynario fuel cell battery charger
2011	Suzuki launches $2.5\ kW$ scooter in Europe
2013	IKEA opens the first hydrogen station for fuel cell forklift trucks in France
	Toyota develops hydrogen fuel cell forklift prototype (Toyota Forklift)
2015	Sintropher project undertaken in the north west Europe for Hydrail (hydrogen rail) and trams

2016	Toyota launches the $114\ kW$ Mirai
Present date	Continuous research in a number of aspects of fuel cells to promote commercialisation for transportation and other niche applications

1.2.2. Types of Fuel Cells

Fuel cells can be classified into different types on the basis of the electrolyte they use[4,12] as shown in Figure 1.3.

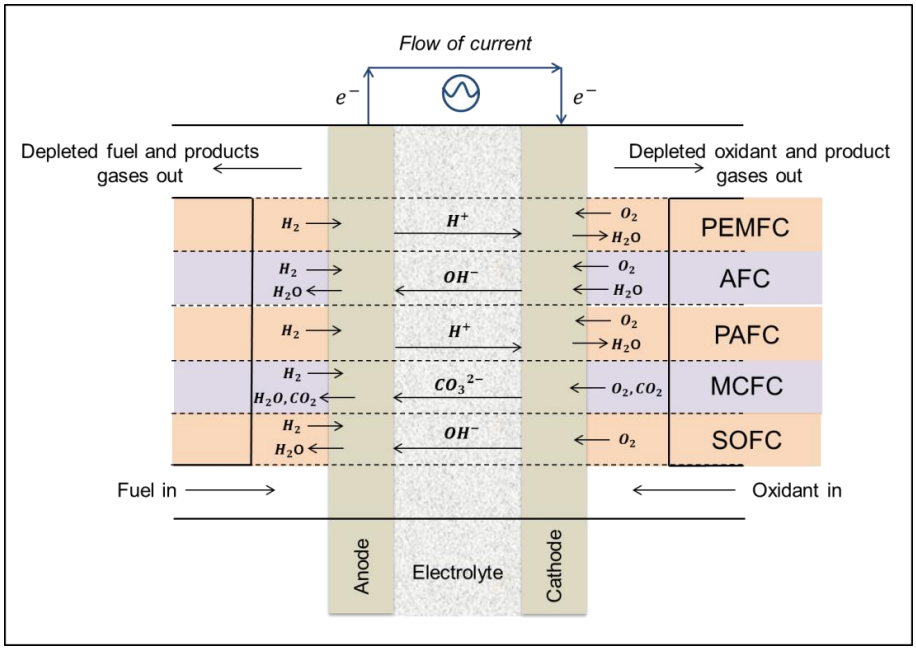

Figure 1.3: Types of fuel cells and their reaction ions (adapted from[4])

- PEMFC use a very thin proton conductive membrane (e.g. perfluorosulphonated acid polymer), ideally less than 50 μm thick as the electrolyte. A typical catalyst for PEMFC is platinum supported on carbon with a loading of about[4] 0.3 $mg.cm^{-2}$. The operating temperatures are in the range of 60 – 80 °C. PEMFC are a promising candidate for transportation applications, along with stationary power generation and portable power applications.
- Alkaline Fuel Cell (AFC) use $85\ wt\%$ concentrated KOH as an electrolyte for high temperature applications (250 °C) and $35 – 50\ wt\%$ for lower temperatures (<120 °C). $Ni, Ag,$ metal oxides and noble metals are amongst the wide range of electrocatalysts that can be employed in AFC. However, the AFC is intolerant towards

carbon dioxide in either the fuel or the oxidant. These cells have been used in the Apollo space program and the Space Shuttles since the 1960s.

- Phosphoric Acid Fuel Cell (PAFC) use phosphoric acid as the electrolyte. To retain the acid, usually, a SiC matrix is used and, as with PEMFC, platinum is the electrocatalysts in both the anode and cathode. Operating temperatures range between 150 and 200 °C. These are semi-commercially available in packages of $200\ kW$ for stationary electrical generation. Hundreds of units have been installed around the world.
- Molten Carbonate Fuel Cell (MCFC) incorporate an electrolyte composed of a combination of alkali metal carbonates, retained in a ceramic matrix of $LiAlO_2$. Operating temperatures lie between 600 to 700 °C, whereby the carbonates form a highly conductive molten salt. The carbonate ions provide the ion conduction. An advantage of using MCFC is that the high operating temperatures do not require a platinum group metal (PGM) catalyst. These are useful for stationary power generation.
- Solid Oxide Fuel Cell (SOFC) use a solid, non-porous, metal oxide as the electrolyte which is usually a Y_2O_3 – stabilised O_2 (YSZ). These fuel cells operate at a high temperature, ranging from 600 to 1000 °C, where the oxygen ions provide the ionic conductivity. Similar to MCFC, these do not require a PGM catalyst and are pre-commercially used for stationary power generation. However, smaller units are being developed for portable and auxiliary power in automobiles.

Direct Methanol (Alcohol) Fuel Cell (DMFC) is also sometimes referred to as a type of fuel cell which uses alcohol directly without reforming as a fuel. However, according to the classification using the type of electrolyte they use, DMFCs are essentially a type of polymer membrane fuel cell that uses methanol instead of hydrogen.

Due to the low operating temperatures, PEMFC have the advantage of quick start-up and, as the electrolyte is a solid membrane, offers resistance to gas crossover. PEMFCs have shown to be the most promising fuel cells to be developed for automobile applications and are used primarily for

transportation applications and some stationary applications. Due to their fast start-up time and favourable power-to-weight ratio, PEMFCs are particularly suitable for use in passenger vehicles, such as cars and buses. For example, the 2008 Honda FCX Clarity and the 2016 Toyota Mirai are based on a hydrogen fuel cell. Some of the crucial properties of fuel cells that make them a beneficial source of energy are listed below[4]:

- They promise a higher efficiency as compared to internal combustion heat engines.
- They promise a low emission or even zero emission of greenhouse gases when operated on pure hydrogen.
- The simplicity of operation is advantageous when it comes to commercialisation or mass production.
- As there are no moving parts in the fuel cells, they offer a long life and resistance to wear and tear during long term operation.
- Fuel cells operate quietly which makes them an attractive energy source for portable power supply, backup power and military applications.
- Depending on the requirements, fuel cells can be made in a variety of sizes and weights, with power output ranging from microwatts to megawatts.

1.2.3. Polymer Electrolyte Membrane Fuel Cell (PEMFC)

PEM fuel cells operate at relatively low temperatures, around 80°C. Low-temperature operation allows them to start quickly and results in less wear on system components, resulting in better durability. However, it requires that a noble-metal catalyst (typically platinum) be used to separate the hydrogen's electrons and protons, adding to system cost. The platinum catalyst is also extremely sensitive to carbon monoxide poisoning, making it necessary to employ an additional reactor to reduce carbon monoxide in the fuel gas if the hydrogen is derived from a hydrocarbon fuel adding to the cost.

The overall basic reaction for the hydrogen/oxygen fuel cell can be written as:

$$\mathbf{2H_2 + O_2 \rightarrow 2H_2O} \qquad \textit{Equation 1.1}$$

In order to understand the energy production, the two separate reactions can be explained as the anodic and the cathodic reactions. At the anode of an acidic PEMFC, hydrogen oxidises to produce protons (H^+) ions and electrons (e^-).

$$\mathbf{2H_2 \rightarrow 4H^+ + 4e^-} \qquad \textit{Equation 1.2}$$

At the cathode, oxygen reduces by reacting with the electrons to complete the other half reaction and produce oxygen anions (O^{2-}).

$$\mathbf{O_2 + 4e^- \rightarrow 2O^{2-}} \qquad \textit{Equation 1.3}$$

At the cathode, the protons and the anions combine to produce water.

$$\mathbf{4H^+ + 2O^{2-} \rightarrow 2H_2O} \qquad \textit{Equation 1.4}$$

The electrons produced at the anode flow through an external circuit to the cathode and the protons flow through the electrolyte. The electrolyte must allow only the protons to pass through and not the electrons, hence they must then pass through the external circuit generating electricity. Figure 1.4 summarises these reactions and depicts the working principle of a single cell fuel cell.

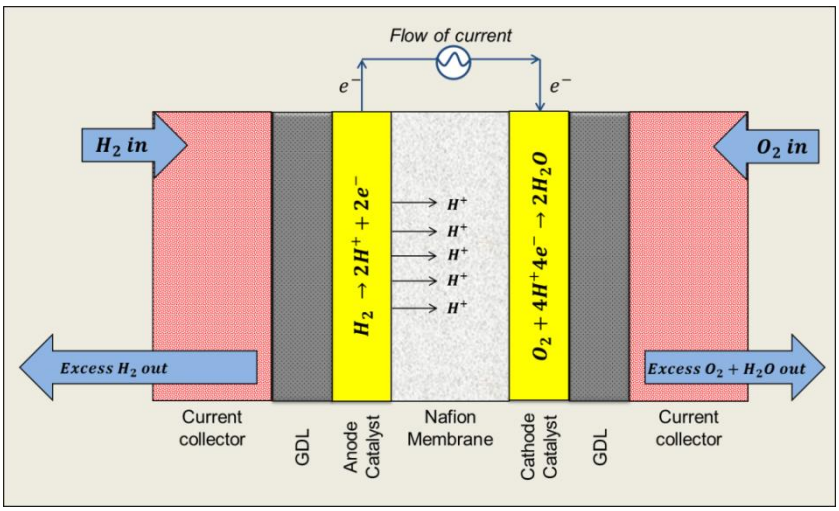

Figure 1.4: Schematic of a PEMFC (adapted from[12])

1.3. Fuel Cell Electrochemistry

As discussed, the overall reaction for PEMFC operation is written as:

$$\boldsymbol{H_2 + \frac{1}{2}O_2 \rightarrow H_2O} \qquad \textit{Equation 1.5}$$

1.3.1. Gibbs Free Energy

In the reaction in Equation 1.5, the product is one mole of H_2O and the reactants are one mole of H_2 and half a mole of O_2. By definition[13], the Gibbs free energy of formation is given by:

$$\Delta \boldsymbol{g_f = \Delta g_f\ of\ products - \Delta g_f\ of\ reactants}$$

$$\Delta \boldsymbol{g_f = (\Delta g_f)_{H_2O} - (\Delta g_f)_{H_2} - \frac{1}{2}(\Delta g_f)_{O_2}} \qquad \textit{Equation 1.6}$$

The Gibbs free energy of formation is not constant and changes with the temperature and the phase of the reaction. The Δg_f for the formation of one mole of water[6] at 25 ^{o}C in liquid phase is $-237.2\ kJ.mol^{-1}$. Theoretically, if there are no other losses in the fuel cell, then all the Gibbs free energy can be converted into electrical energy. This can then be used to calculate the reversible voltage of a fuel cell.

In order to produce one molecule of water, two electrons are transferred to complete the reaction. Hence, for each mole of Hydrogen used, $2n$ electrons go through the circuit. If $-e$ is the charge of each electron, the charge that flow through the circuit is given by:

$$\boldsymbol{-2ne = -2F\ coulombs} \qquad \textit{Equation 1.7}$$

Where n = Avogadro's number (6.023×10^{23}), e = charge of electron $(1.602 \times 10^{-19})\ coulomb$, F = Faraday constant $(6.023 \times 10^{23}) \times (1.602 \times 10^{-19}) = 96485\ C$.

If E can be defined as the voltage of the fuel cell, the electrical work done can be defined as:

$$\boldsymbol{Electrical\ work\ done = charge \times voltage} \\ \boldsymbol{= -2FE\ joules} \qquad \textit{Equation 1.8}$$

Therefore, as explained earlier, given that there is no energy lost; this electrical work done would be equal to the Gibbs free energy released.

$$\Delta \boldsymbol{g_f = -2FE} \qquad \textit{Equation 1.9}$$

Thus,

$$\boldsymbol{E = \frac{-\Delta g_f}{2F}} \qquad \textit{Equation 1.10}$$

Consequently, this fundamental equation gives the electromotive force (EMF), i.e. the reversible open circuit voltage (OCV) or open circuit potential (OCPof the hydrogen fuel cell. For example, for a fuel cell operating under standard conditions with $\Delta g_f = -237.2\ kj.mol^{-1}$

$$\boldsymbol{E = \frac{237200}{2 \times 96485} = 1.229\ V} \qquad \textit{Equation 1.11}$$

1.3.2. Effect of Concentration and Temperature on Reversible Voltage: Nernst Equation

Taking into consideration the effect of temperature and the concentrations of the reactants, the resulting voltage (Nernst Voltage) is given by the Nernst equation:

$$\boldsymbol{E = E^o - \frac{RT}{nF} ln \frac{a_{H_2O}}{a_{H_2}.a_{O_2}^{0.5}}} \qquad \textit{Equation 1.12}$$

Where $E =$ Actual cell voltage (V), $E^o =$ Standard-state reversible cell voltage (V), $R =$ Universal gas constant $(8.314\ J.mol^{-1}.K^{-1})$, $T =$ Absolute temperature (K), $n =$ Number of electrons, and $a =$ Activity of the concerned species.

Taking into consideration the effects of temperature and the concentrations of the reactants, the resulting Nernst voltage under standard conditions can be calculated using the Nernst Equation 1.12 as follows:

$$E = 1.229 - \frac{8.314 \times 298}{2 \times 96485} ln \frac{1}{1 \times 0.21^{0.5}} = 1.219\,V$$ *Equation 1.13*

Theoretically, the fuel cell is more efficient at lower temperatures as demonstrated in Figure 1.5. However, in practice, this does not hold true due to kinetic limitations.

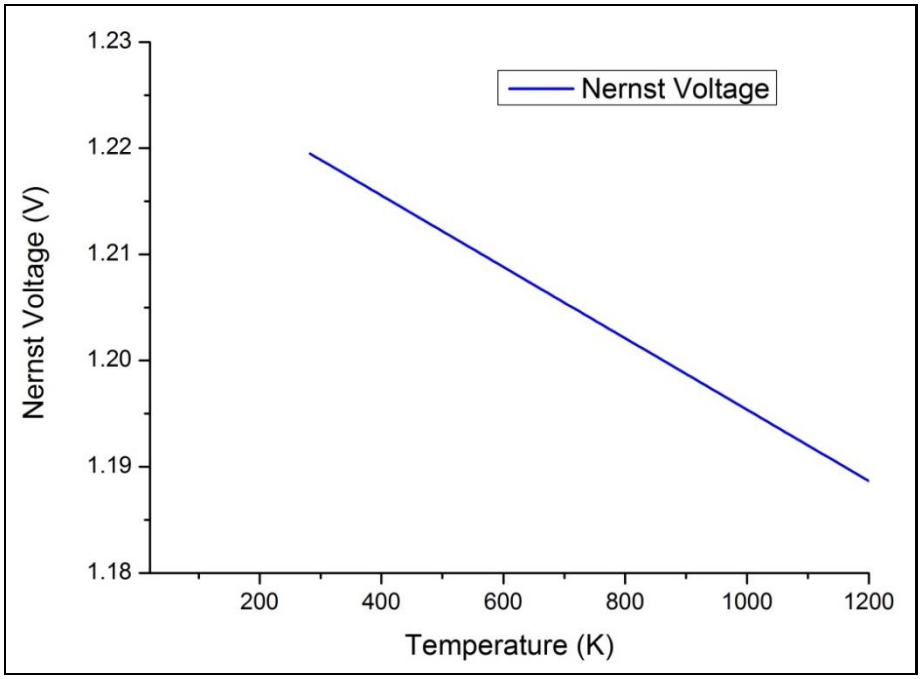

Figure 1.5: Nernst voltage as a function of temperature

1.3.3. Fuel Cell Irreversibility & Voltage Loss

The actual open circuit voltage of a fuel cell is lower than the derived theoretical estimate. The voltage losses that occur as the irreversible cell voltage or the overpotential can be attributed to three main causes: (i) Activation losses, (ii) Ohmic losses and (iii) Mass transport losses. The operating cell voltage can be represented as a sum of losses deducted from the theoretical reversible fuel cell voltage as defined by the Nernst equation.

$$E = E_{rev} - E_{irrev} = E^o - \eta_{act} - \eta_{ohmic} - \eta_{conc}$$ *Equation 1.14*

Where E_{irrev} = Irreversible voltage loss (V), η_{act} = Activation overpotential (V), η_{ohmic} = Ohmic overpotential (V) and η_{conc} = Concentration overpotential (V).

1.3.3.1. Activation Losses

Activation overvoltage is the most important cause of voltage drop in low temperature fuel cell operations. These losses are caused by the reactions that occur at the electrode surfaces, a fraction of the voltage that is generated is lost in driving the chemical reaction that transfers the electrons from and to the electrodes. The effect of the exchange current density on the activation loss can be explained using Figure 1.6. The activation losses are inversely proportional to the exchange current densities.

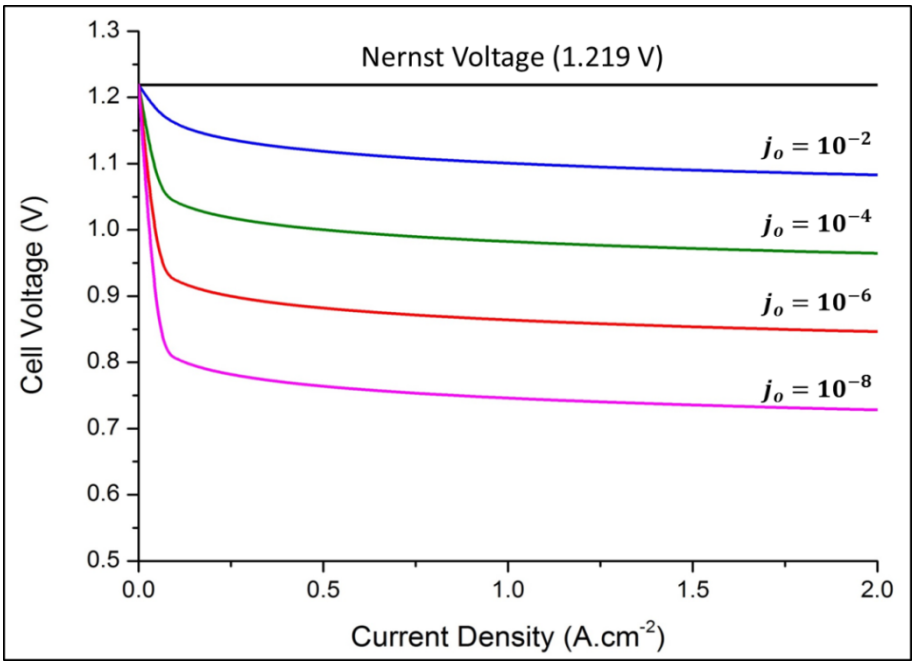

Figure 1.6: Effect of exchange current density on the activation losses (Curves calculated for various values of j_o with $\alpha = 0.5, n = 2, and\ T = 295\ K$ (adapted from[7])

The amount of voltage drop is related to the current densities by the following equation.

$$\eta_{act} = \frac{RT}{\alpha nF}(\ln j - \ln j_o) \qquad \textit{Equation 1.15}$$

Where: $\alpha =$ Charge transfer coefficient (for most reactions, α ranges from $0.2\ to\ 0.5$ and for symmetrical reactions, α is 0.5), $j =$ Current density $(A.cm^{-2})$ and $j_o =$ Exchange current density for the reaction.$(A.cm^{-2})$.

1.3.3.2. Ohmic Losses

The Ohmic losses can be seen through the full current range and are observed as a result of electrical resistance between the electrode-electrolyte and the resistance to the flow of electrons or ions in the electrolyte. The extent of the voltage loss is directly proportional to the current and is given by the equation:

$$\boldsymbol{\eta_{ohmic} = j.(ASR_{ohmic})} \qquad \textit{Equation 1.16}$$

Where: $ASR =$ Area specific resistance $(\Omega.cm^2)$.

The effect of Ohmic loss on the overall cell potential can be seen in Figure 1.7.

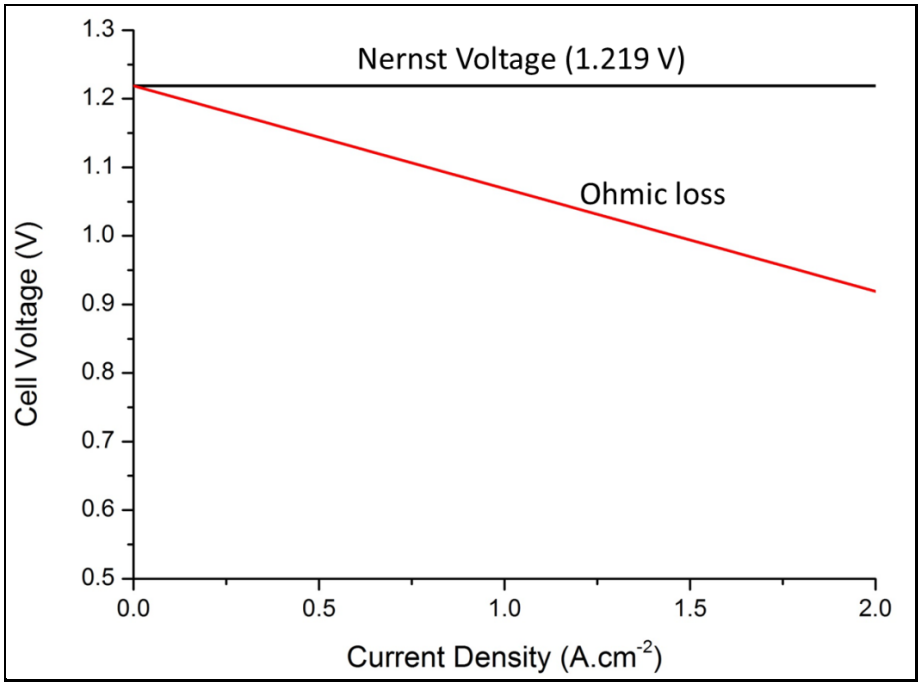

Figure 1.7: Resistive (Ohmic) losses in a fuel cell $(ASR = 0.15\ \Omega.cm^2)$ *(adapted from[4])*

1.3.3.3. Concentration Losses

The concentration (or mass transport) losses result from the change in the concentration of the reactants at the surface of the electrodes as the reactants are consumed. These are limited by the ability of the fresh reactants to reach to the surface of the electrodes. Thus, the concentration of the reactants affects the voltage output of the fuel cell. As the reduction in concentration is a result of a failure to transport sufficient fresh reactants to the electrode surface, this type of loss is often referred to as mass transport loss.

The concentration losses are given by:

$$\eta_{conc} = \frac{RT}{nF}\{ln(j_L) - ln(j_L - j)\} \qquad \textit{Equation 1.17}$$

Where: j_L = Limiting current density $(A.cm^{-2})$.

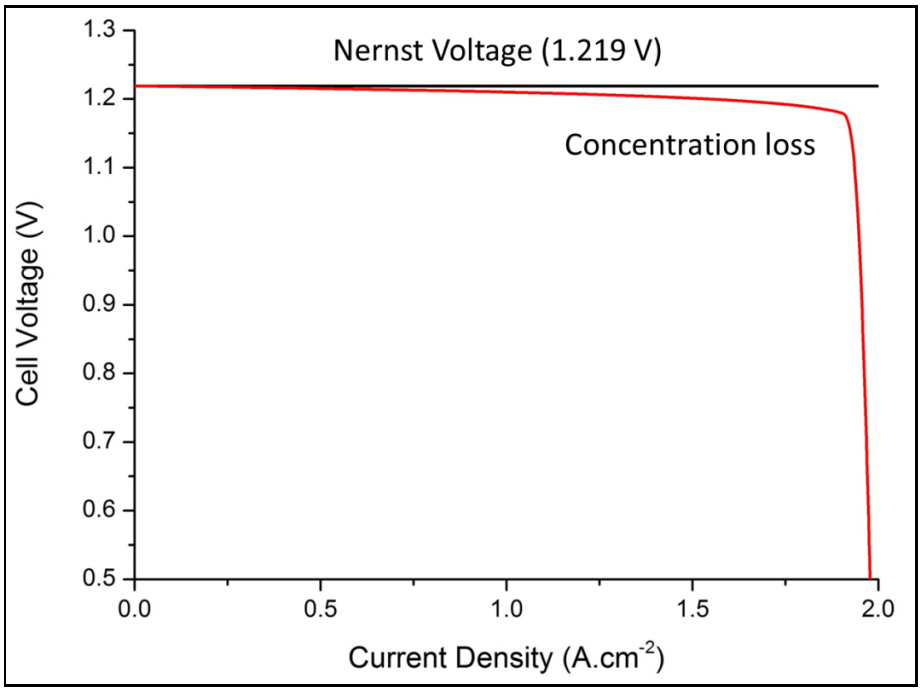

Figure 1.8: Concentration (mass transport) losses in a fuel cell (adapted from[4])

According to Equation 1.17 and as shown in Figure 1.8, there would be a sharp drop in the cell voltage once the limiting current is approached. This is, however, not the case in a real fuel cell because of the non-uniform conditions over the whole area of the porous electrodes. In practice, the

limiting current is never experienced by a fuel cell. Some areas may reach the limiting current density sooner than the others. In addition to this, the exchange current density depicted in Figure 1.6 is also a function of concentration of reactants at the catalyst surface. As the current density approaches the limiting current density, the surface concentration and consequently, the exchange current density approaches zero, which in turn, adds to the overall voltage loss.

Figure 1.9 represents the overall polarisation curve for a fuel cell. As explained, the overall voltage loss is a result of the added effect of the activation, Ohmic and concentration losses. At any given current density, the activation losses contribute the largest share of the overall voltage loss for the fuel cell. The large initial voltage loss is also attributed to the activation polarisation.

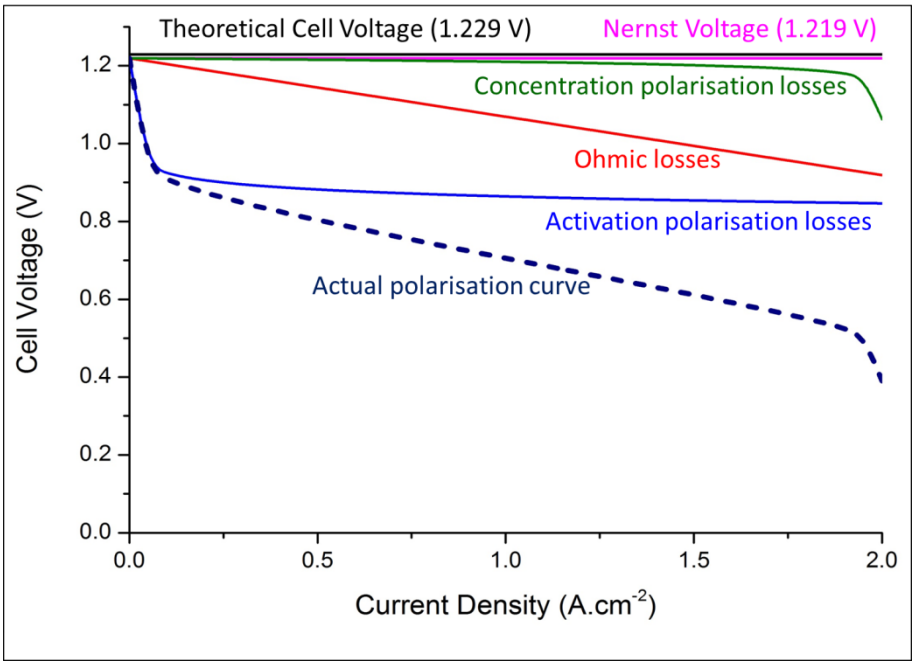

Figure 1.9: Overall voltage losses in a fuel cell and the resulting polarisation curve (adapted from[4])

1.4. Aims and Objectives

The research work in this PhD project is focused on the current collector plates for PEMFC. The operational voltage of a single fuel cell is as low as $0.7\ V$ and as a result of this, in order to produce a useful voltage, a number

of cells are required to be connected in series[6]. These connected cells are collectively known as a 'stack'. In a fuel cell stack, the anode of one cell is connected to the cathode of the next cell, and so on through the stack. To simplify the complexities of the anode and cathode arrangement, a bipolar plate is used to interconnect the cells. This acts as an anode for one cell and as a cathode for the next cell, which results in the name bipolar plate (BPP).

The two half reactions, i.e., the oxidation and the reduction reactions are kept separate[14] in the fuel cell. A single cell is comprised of two BPPs, two seals and a membrane electrode assembly (MEA). The MEA consists of two catalyst layers and two gas diffusion layers (GDL) on each side. The membrane acts as an electrolyte in each single cell and separates the two half reactions. It allows the protons to pass through it which completes the reaction. The electrons are forced to flow through an external circuit where they produce current. In a fuel cell stack, a BPP supports two adjacent cells and is a vital component that carries out a number of operational functions, such as, separating the cells in a stack, transporting current to the external circuit, providing uniform compression of membranes and providing channels for reactant delivery. BPPs also manage the heat and water produced in the fuel cell. Figure 1.10 depicts the cells connected in a series to maximise the output voltage.

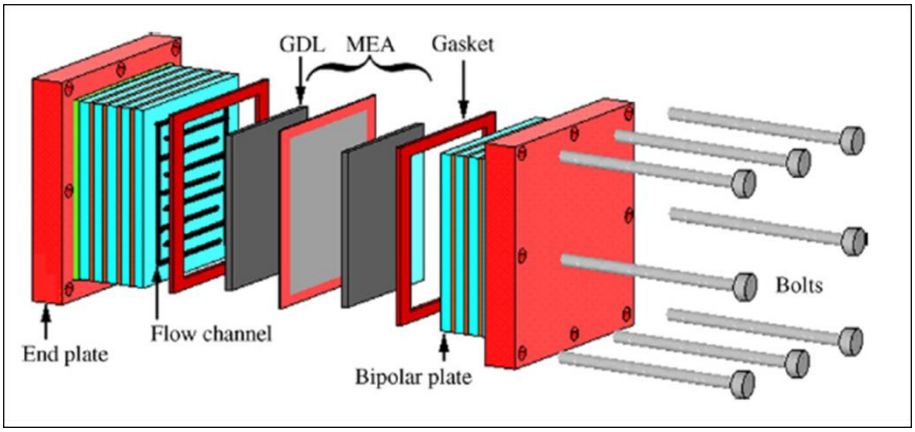

Figure 1.10: Schematic of a PEM fuel cell stack connected in series (reprinted from[15])

Historically, BPPs were made from graphite because of its low surface contact resistance and high corrosion resistance[16,17], however because of

the cost and problems related to high volume manufacturability, brittleness and permeability to gases, there is increasing interest in other materials. Composite BPPs are an alternative to pure graphite BPPs[18], being made of a mixture of polymers and graphite particles, however, these present the challenge in terms of reduced conductivity due to the presence of polymers. Alternatively, metals have been studied extensively for BPP production, given the advantages of high mechanical strength, improved durability to shocks and vibrations, zero gas permeation and far superior manufacturability and cost effectiveness as compared to carbon based materials[17]. However, the biggest drawback of any metal is the tendency to corrode. In addition to the qualities of metals mentioned here, Stainless Steel (SS) also have a range of alloying options suitable for mass production. These characteristics make SS a popular option for use as BPPs. Indeed, ferritic and austenitic are probably the only materials that can be employed as a BPP without any coating[19]. The major concern that still remains is that of corrosion and formation of passivation layer that reduce the electrical conductivity.

This PhD project is undertaken in collaboration with Tata Steel Europe Ltd. and a key part of the project is to develop a more cost effective alternative to stainless steel bipolar plates by using functionally coated mild steel. The work has been undertaken to develop and characterise a novel coating solution for mild steel bipolar plates to be applied in PEMFCs and the contact resistance and corrosion performances are compared to the benchmark results obtained using commercial SS 316L. A Tata proprietary coated mild steel material is analysed with an improved contact resistance and improved corrosion resistance compared to bare mild steel. Graphene is presented as a viable coating option for BPP applications. Two different routes of graphene deposition have been employed and have resulted in improved contact resistance performance via one route and improved corrosion performance via the other. Finally, a novel method to study sub-surface corrosion is presented using 3-dimenisonal X-ray microtomography. The details of the thesis structure and the chapters are discussed below:

- Chapter 2 presents a literature review for materials used as bipolar plates. The current benchmark material; SS 316L is reviewed in

detail along with coated SS 316L options. Coated mild steel material is also reviewed as a viable option for BPPs. The second half of the chapter presents an overview of carbon based coatings for BPP applications and different methods of graphene deposition. This chapter also reviews the electrochemical methods used for corrosion analysis of different materials, thereby laying the foundation for the work undertaken in this thesis.

- Chapter 3 gives an insight to the fundamentals of corrosion and the electrochemistry and mechanism of corrosion. This also refers to the fundamental theory of the electrochemical techniques used to analyse the corrosion performance of different materials tested as a part of this project.
- Chapter 4 provides a review of the testing methodologies and surface analysis techniques used throughout the project to study the performance of candidate samples in terms of their contact resistance and corrosion resistance. This chapter also presents the methodology for *in situ* PEMFC operation using graphite and SS 316L as BPPs.
- Chapter 5 presents the benchmark results for *ex situ* contact resistance and corrosion performance obtained using a commercial SS 316L material in comparison to the published literature. A Tata proprietary coated mild steel material is also analysed for its contact resistance and corrosion performance in comparison to SS 316L. Potentiodynamic, potentiostatic and accelerated corrosion tests using electrochemical impedance spectroscopy are used to analyse the corrosion performances of different samples. The chapter also include *in situ* fuel cell results using graphite and SS 316L BPP.
- Chapter 6 presents graphene as a viable coating option for anti-corrosion performance. Two different routes for graphene deposition are discussed; chemical vapor deposition and electrophoretic deposition. Chemical vapor deposition of graphene is achieved using two different routes; firstly via using a nickel catalyst layer before the graphene growth and second direct graphene growth on different grades of steel without a catalyst layer. An improved contact resistance performance is reported however, more work is needed to improve the corrosion resistance. Few-layers of

graphene are successfully deposited on SS 316L using electrophoretic deposition. An improved corrosion performance is reported for the graphene coated SS 316L using electrophoretic deposition.

- Chapter 7 presents a novel method of studying sub-surface corrosion using 3-dimensional computed tomography. An SS 316L wire is studied before and after corrosion tests to study the surface changes as a result of corrosion. A graphene coated SS 316L wire via chemical vapor deposition route is also analysed for coating performance using 3-dimensional computed tomography.
- Chapter 8 provides the conclusions derived from this project and suggestions for future investigations.

2. Literature Review: Metallic Bipolar Plates

This chapter presents an overview of the materials that have been applied as BPP in PEMFCs. The impetus behind the evolution of the BPP materials has been to reduce the volume and weight of the fuel cell and eventually the overall cost. As a BPP is a key part of a fuel cell stack, it contributes significantly towards the total weight and cost of a of a fuel cell stack[20]. The most important performance indicating parameters for a BPP are the interfacial contact resistance and the corrosion resistance. Over the period of time, different materials have been used; from graphite to composite polymers and currently, metals are used as BPPs. In addition to the evolution of the base material, a number of coatings have also been developed to enhance the performance of the BPPs; improving conductivity and corrosion resistance.

Graphene possesses excellent chemical and mechanical strength; it is highly durable with excellent corrosion resistance and high electrical conductivity. This chapter presents an introduction to graphene and presents a review of different methods of graphene deposition. Two routes of graphene deposition are discussed in particular, chemical vapor deposition and electrophoretic deposition of graphene. Graphene coated steel is also reviewed as a BPP candidate for PEMFCs.

In summary, the chapter provides the review on the literature published on different base materials and coatings used as BPPs. It also provides a foundation for the work undertaken in this thesis to develop a novel coating solution for mild steel to be applied as a BPP in PEMFCs.

2.1. Materials Used for Bipolar Plates

The DOE has set-up targets that provide a guideline for the candidate materials to be used as BPPs in PEMFCs. The cost of the fuel cell stack is one of the key reasons hindering the commercialisation of fuel cells, and a

BPP being a volume and cost determining component of the fuel cell, the ideal scenario would be to reduce the weight, volume and hence, the cost of the BPP. Table 2.1 summarise the requirement criteria for the BPP materials published in the DOE report[21] in 2012 and it depicts the 2011 status of the best BPP materials and the targets for 2017 and subsequently, 2020.

Table 2.1: DOE technical targets for BPPs (adapted from[21])

Characteristic	**Unit**	**2011 Status**	**2017 Targets**	**2020 Targets**
Cost	$\$ / kW$	5-10	3	3
Plate H_2 permeation coefficient	$Std\ cm^3 (sec.cm^2.Pa)$ @ $80^{\circ}C, 3\ atm,$ $100\%\ Relative\ Humidity$	N/A	<1.3 x 10^{-14}	<1.3 x 10^{-14}
Corrosion (anode)	$\mu A / cm^2$	<1	<1	<1
Corrosion (cathode)	$\mu A / cm^2$	<1	<1	<1
Electrical conductivity	S / cm	>100	>100	>100
Area specific resistance	$Ohm.cm^2$	0.03	0.02	0.01
Flexural strength	Mpa	>34 (Carbon plate)	>25	>25
Forming elongation	%	20-40	40	40

In general, the key functions for a BPP material in a PEMFC are to separate the cells in a stack, transport current to the external circuit, provide uniform compression of membranes, provide channels for reactant delivery and manage heat and water produced in the fuel cell. The key requirements for the BPPs have been grouped into four major categories; the design criteria related to the stack performance, system performance,

manufacturing and the environmental impact. Table 2.2 describes the design requirements for BPPs as summarised by Cooper[22] . In addition to the design requirement criteria reported by Cooper[22], Brett and Brandon[16] have also reported the characteristics of an ideal BPP.

Table 2.2: Summary of PEM fuel cell BPP design requirements (adapted from[14,16,22,23])

Category	Requirements
Stack performance related design criteria	Minimum electrical and thermal resistance
	Allow distribution of fuel, oxidant, residual gases and water without leaks
	Withstand mechanical load during operation
	Minimum difference between the coefficient of thermal expansion of the base metal plate and any coating
System performance related design criteria	Minimum mass and volume per kW (plate should be light weight and slim) with maximum design life
	Stacks must operate in freezing and cold conditions
Manufacturing related design criteria	The stack should be inexpensive to manufacture
	Plate design should have manufacturing processes with high yields relative to mass production
	Length/width should be system defined (flexible cross section)
	The plate surface finish requirements should be minimised and high tolerance to increase manufacturing options
Environmental impact related design criteria	Plate material should recyclable following a vehicle accident or when vehicle retires and plate should be made from recyclable materials

Brett and Brandon[16] suggested that an ideal BPP material should be thermally stable, should have a low permeability to gases, should be

corrosion resistance and should be resistant to ion leaching, in addition to the characteristics reported by Cooper[22].

A variety of materials have been suggested in the literature on the basis of their chemical properties, resistance to corrosion, cost, density, electronic conductivity, gas impermeability, manufacturability, stack volume per kW, thermal conductivity etc.[14].

Traditionally, BPPs have been made up of graphite because of its low surface contact resistance and high corrosion resistance[16,17]. Since it is brittle and porous, the BPPs must be made thicker which reduces the specific volumetric and gravimetric power density of the fuel cell stack. Since the durability and the cost are the two major challenges that hinder the proliferation of fuel cell technology, a significant amount of attention is given to exploring different materials that could meet the criteria for the manufacturing of BPPs.

Composite[18] BPPs are a mixture of polymers and graphite particles. These materials enjoy the feasibility of mass production at reasonable costs using injection molding. Examples of polymer materials used for these composite BPPs include; polypropylene, phenolic bonded graphite, polyphenylene sulfide, polyether sulfone[24,25]. The polymer matrix makes BPPs more flexible and hence the mechanical strength is improved. The chemical stability remains as it is; however, due to the incorporation of insulating polymers, the electrical conductivity is negatively affected. This makes the formulation of composite graphite plates very complex to achieve without sacrificing the conductivity. Even with these benefits, the mechanical strength of graphite and graphite composites remain a challenge.

Amongst the other materials explored, metals have been studied extensively: metals have the positives of high mechanical strength, better durability to shocks and vibrations, no gas permeation and far superior manufacturability and cost effectiveness as compared to carbon based materials[17] and the biggest drawback of any metal is the tendency to corrode. Metals operating in the highly acidic environment of the fuel cell at temperatures around 80 $^{\circ}$C lead to dissolution. The ions leached a result of this may poison the MEA and decrease the output of the fuel cell[26]. In addition, the passivation layer formed will increase the contact resistance of

the BPP. Combination of these factors results in negative effects on the overall power of the fuel cell. These problems can be minimised to an extent by using different coatings on top of the metal surfaces.

Gold-coated titanium and niobium were the materials used by General Electric[27] back in the 1960s which were then replaced by graphite composites in the early 1970s to reduce the cost and weight of the fuel cell. In the recent years, due to the above mentioned drawbacks of graphite, a considerable amount of research has been done to find alternative materials. Variety of metals and metal alloys have been tested and evaluated to develop BPPs that can combine the advantages of both graphite and metals.

Hermann *et al.*[28] have broadly categorised the materials that are used as BPPs for PEM fuel cell as described in Figure 2.1.

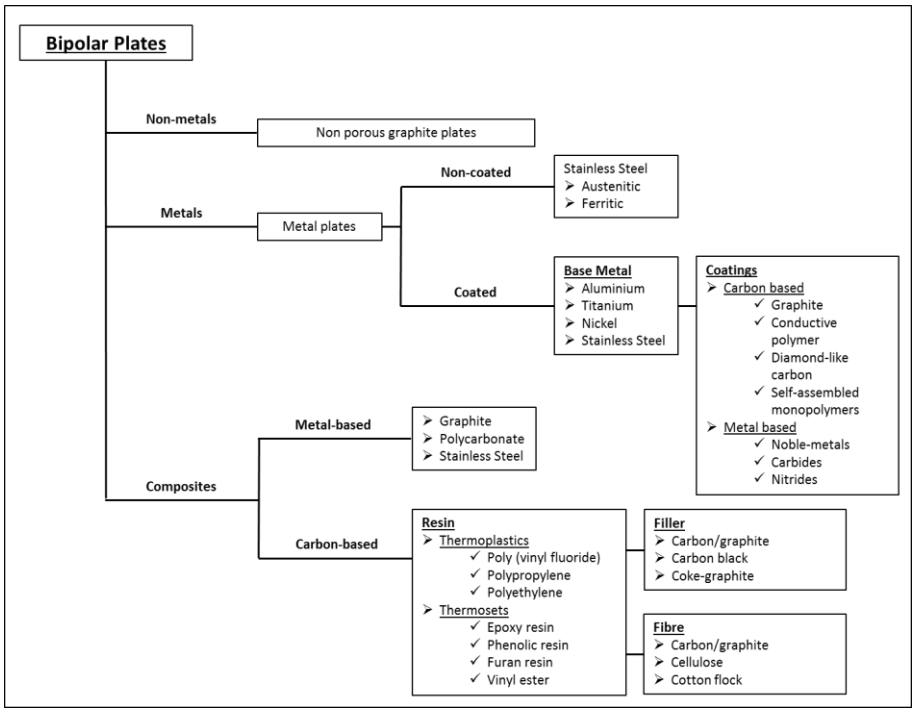

Figure 2.1: Classification of materials for BPPs used in PEM fuel cell (adapted from[28])

Brett and Brandon[16,29] have listed the advantages and disadvantages of the different materials that have been used as BPPs which are summarised in Figure 2.2.

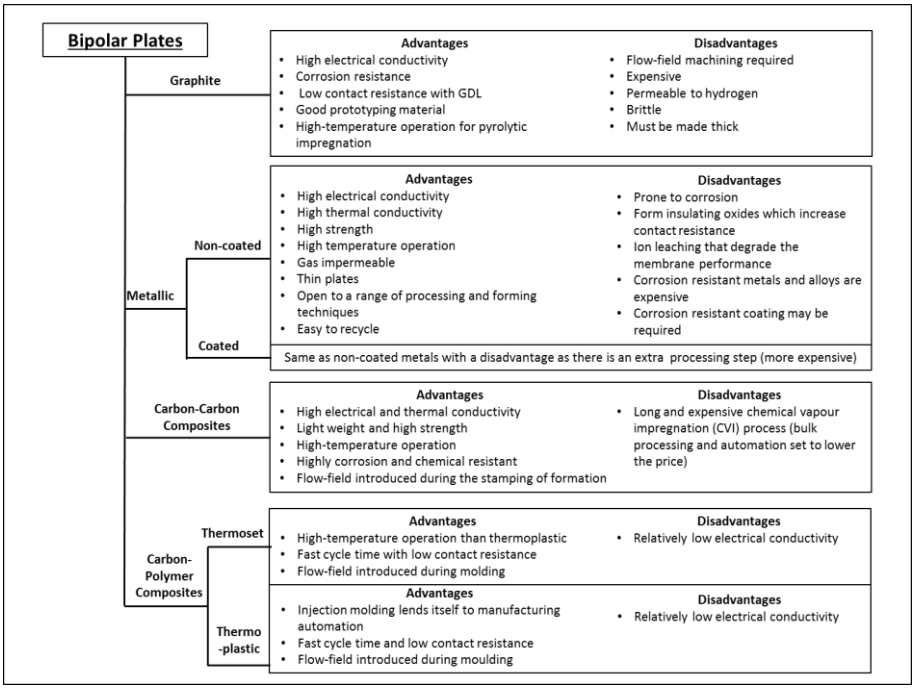

Figure 2.2: Advantages and disadvantages of different BPP materials (adapted from[16,29])

2.1.1. Stainless Steel

SS demonstrate relatively high mechanical strength, high chemical stability, low gas permeability and have a range of alloying options and it is reliable for mass production. These characteristics make SS a popular option to be used as BPPs without any coating. Indeed, SS is probably the only material that can be employed as a BPP without any coating[19]. These may include austenitic, ferritic, martensitic and other grades of stainless steels. The major concern that still remains is that of corrosion and the formation of passivation layer that reduces the electrical conductivity.

Davies *et al.*[30,31] concluded that the performance of the BPP is extensively dependent upon the thickness of the passive layer and the interfacial contact resistance (ICR). The analysis of the passive film revealed that increased performance was related to the decreased film thickness and decreased surface contact resistance. On analysis of different grades of SS, they indicated that under the compaction force imposed for the fuel cell experiments at $220\ N.cm^{-2}$, the relative ICR decreased in the order of 321 > 304 > 347 > 316 > Ti > 310 > 904 > Incoloy 800 > Inconel 601 > Poco® graphite. The authors carried out the depth profiling of the samples with

Auger Electron Spectroscopy (AES) which revealed that the oxygen levels varied significantly. In case of the high alloying samples, the oxygen was not as prominent as other samples of SS which, in turn, suggested that the passive film was thinner in these samples. They deduced that the thickness of the passive film decreased in the order of 321 > 304 > 316 > 347 > 310 > 904 > Incoloy 800 > Inconel 601. This trend was found to be in agreement with the surface resistance series discussed above. During the long-term fuel cell operation ($1300\,h$) of the four selected materials, Poco® graphite produced the best results. Increased polarisation was observed in the metal plates in the order of Poco® graphite < 310 < Ti < 316. Despite the concerns of the corrosion of SS in the fuel cell environment, there was very little change noticed in the performance of Poco® graphite, 310 and 316. Post fuel cell analysis of the membrane revealed that no SS corrosion products had leached into the membrane. However, with titanium much decreased performance was observed that was in correlation with the surface resistance measurements carried out after the fuel cell testing. Thus, the performance of the BPP is related to the thickness of the passive layer and the ICR. The authors[31] analysed 910, 310 and 316 SS for over $3000\,h$ endurance testing and revealed that ICR in the SS samples decreased with increasing chromium and nickel content. No evidence of corrosion products was found in the membrane post fuel cell testing.

Wang *et al.*[26] tested different SS samples in simulated fuel cell environment and carried out ICR measurements. The authors found out that the ICR between the carbon paper and SS increased due to the formation of a passive layer. Nevertheless, as soon as a stable passive film is formed the ICR is stabilised. The SS samples studied were 316L ($16.2 - 16.8\,\%\,Cr$), 317L ($18.1 - 18.6\,\%\,Cr$), 904L ($20.5\,\%Cr$) and 349™ ($23\,\%\,Cr$).The electrochemical testing of the samples were carried out in $1\,M\,H_2SO_4 + 2\,ppm\,F^-$ solution at 70 °C in order to simulate the fuel cell environment. Sulphuric acid was selected as the membranes are pre-treated in the acid and the water analysis of running fuel cell system revealed the fluoride ion concentration at that level[19]. The electrolyte was purged with hydrogen to simulate the anodic fuel cell environment and with air to simulate the cathodic environment. The authors concluded that the peak current density for passivation decreases with the increase in the Cr content of the alloy as it is the primary passivating element in stainless steels. The authors

reported that both the critical current and the passivation current were found to be lower in the case of cathodic simulation as compared to the anodic simulation indicating the positive effects of air in the formation and maintenance of passive film. Furthermore, for all four alloys, the passivation current was found to be more or less similar ($\sim 10\ \mu A.cm^{-2}$) indicating the similar nature of the passive films for all the alloys, irrespective of the Cr content. The performance order for both anode and cathode environments was found in the order of 349™> 904L > 317L > 316L. The ICR for all four alloys were found to be similar indicating the similarities in the passive films formed in the air. In general, the contact resistance decreased with the increase in the Cr content of the alloy. Figure 2.3 depicts the values for the interfacial contact resistance in relation to the compaction force. At a compaction force of $140\ N.cm^{-2}$, the ICR was found to be in the range of $100 - 160\ m\Omega.cm^2$, decreasing with the increasing Cr content. The ICR between the carbon paper and the samples was in the order of 349™< 904L < 317L < 316L. These results were found to be in concurrence with those published by Davies *et al.*[30].

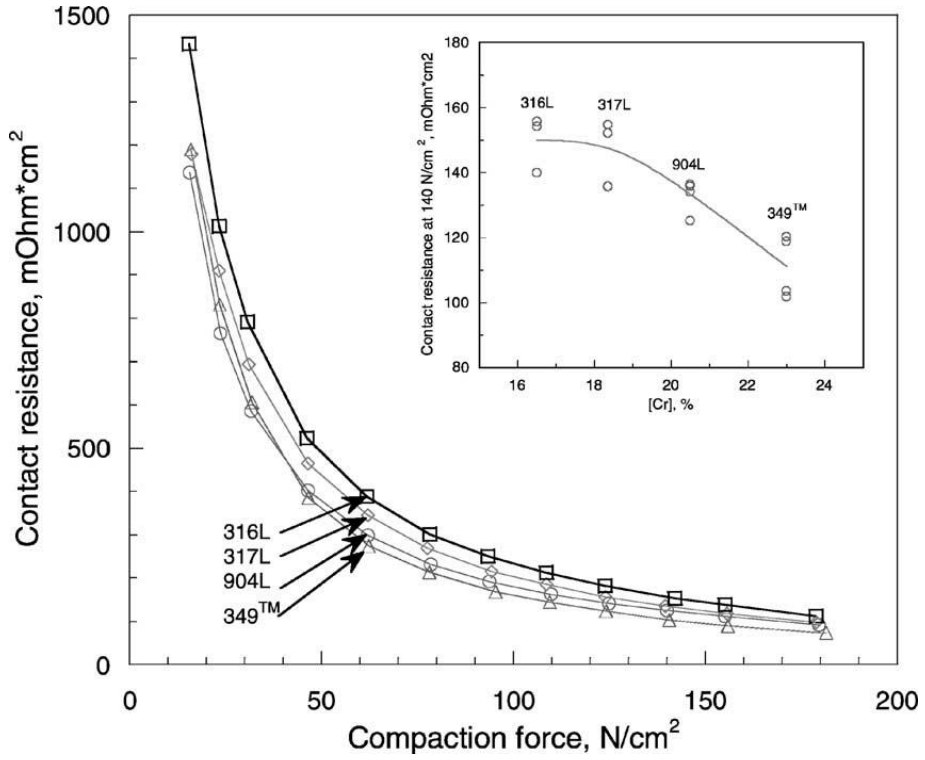

Figure 2.3: ICR values for different stainless steels and carbon paper at different compaction forces. The inset shows the ICR for different steels at a compaction force of $140\ N.cm^{-2}$ *(reprinted from[26])*

Wang *et al.*[32] performed similar experiments as discussed before using ferritic SS instead of austenitic SS. The SS samples of AISI434, AISI436, AISI441, AISI444 andAISI446 were studied and the authors concluded that AISI446 could be considered as a candidate material for BPP. They verified that in both anodic and cathodic fuel cell environments, AISI446 underwent passivation and the resultant passivation layer was found to be very stable. In terms of the polarisation results, in the simulated anodic PEMFC environment, the SS materials performance was found to be in the order of AISI446 > AISI444 > AISI436 > AISI434 > AISI441. The performance for the cathodic environment was AISI446 > AISI444 > AISI436 ≥ AISI441 > AISI434. Nevertheless, both the series suggested that AISI446 was the best candidate for BPP applications; however, the formation of a thick non-conductive, surface passive layer of Cr_2O_3 will increase the resistance. The authors concluded that as the Cr content increases, the corrosion resistance is improved which agrees with the conclusion of Davies *et al.*[31]. The ICR results reveal the performance of the alloys was in the order of AISI444 > AISI436 > AISI441 > AISI434 > AISI446. This correlates with the series order of the electrochemical performance with the exception of AISI446. This high ICR values could be attributed to the formation of non-conductive Cr_2O_3 layer. Even so, AISI446 remained an excellent candidate for BPPs as the differences in ICR values were very small. X-ray photoelectron spectroscopy (XPS) depth profiling revealed that AISI446 had a thicker oxide layer as compared to the austenitic 349™. AISI446 had higher ICR values to those of 349™, indicating that the higher values were due to the thicker film[26,32]. The authors noted that neither iron oxides nor chromium oxides dominated the composition of air-formed film on AISI446. This is in agreement with the previous investigations of 349™, indicating that the air-formed surface oxide film on SS are of same composition, regardless of the bulk structure. In addition to this, the authors noted that the passive films are also formed of chromium oxide and iron oxide. However, in this case, chromium oxide dominates the passive film composition. The sample treated with cathode environment had a thicker passive than that of the anode environment. The thickness of the passive film on AISI446 was estimated to be $2.6\ nm$ for the film formed in the anode environment and $3.0\ nm$ for the film formed at the cathode environment.

Silva *et al.*[33] compared the ICR values of various SS samples with that of graphite samples. They found that the ICR values decreased in the order of 304 > 316L > 310S > 904 > BMA5 > XM 9612. These results agreed the trend observed by Davies *et al.*[31] and Wang *et al.*[26]. The authors pointed out the strong relationship between the oxide film composition and the electrical conductivity of SS passive layer. They noted that the SS samples have high ICR values and undergo corrosion in both anodic and cathodic environments. They also studied the suitability of four different Ni-based alloys to be operated in the fuel cell environment.

Makkus *et al.*[34,35] tested several SS samples for their applicability as a BPP material. The fuel cell experiments were performed under three different sets of conditions, viz., high compaction pressure, low compaction pressure and long term stability tests. All the experiments were conducted using Nafion 117 as the electrolytic membrane and Nafion impregnated E-tek Elat with platinum loading of $0.35\ mg.cm^{-2}$ was used for both the anode and the cathode. MEAs were prepared by hot-pressing the Nafion 117 and the Nafion impregnated E-tek electrodes together at a temperature of 308 °C and a pressure of $35\ bar$ for 1.5 min. In the SS test samples, a single serpentine channel, $1\ mm$ in depth and width, was machined. Following machining, the samples were cleaned and pickled and all MEAs were post-test analysed for contaminants. The authors observed that on the cathode side, the oxide layer formed on the surface protected the underlying bulk SS material from dissolving into the water produced and the membrane. However, at the anode side, as no protective layer was formed, a large amount of metal ions were found in the membrane. The dissolution of metal ions from 316L SS in the membrane was studied using inductively coupled plasma / atomic absorption spectroscopy (ICP/AAS); the level of metal ions reported were $200\ ppm\ Fe$, $60\ ppm\ Cr$ and $35\ ppm\ Ni$. Further, the authors noted that the direct contact of the SS and the membrane enhanced the contaminant levels and suggested the use of an appropriate pre-treatment and a coating to prevent direct contact between SS and the membrane.

Wang and Northwood[36] studied the effect of oxygen and hydrogen environments on the corrosion of 316L in simulated fuel cell environment. The authors noted that corrosion happened at both the anode and the cathode. The potentiodynamic tests, as shown in Figure 2.4, depicts that

less corrosion took place in the simulated cathode environments as compared to the anode. This has been attributed to the cathodic protection capabilities of oxygen-containing environments as it was easier to passivate in the oxygen atmosphere. This was in agreement with the trend as observed by Makkus *et al.*[34,35]. The curves also demonstrate the three particular regions for SS materials; the active, passive and trans-passive regions.

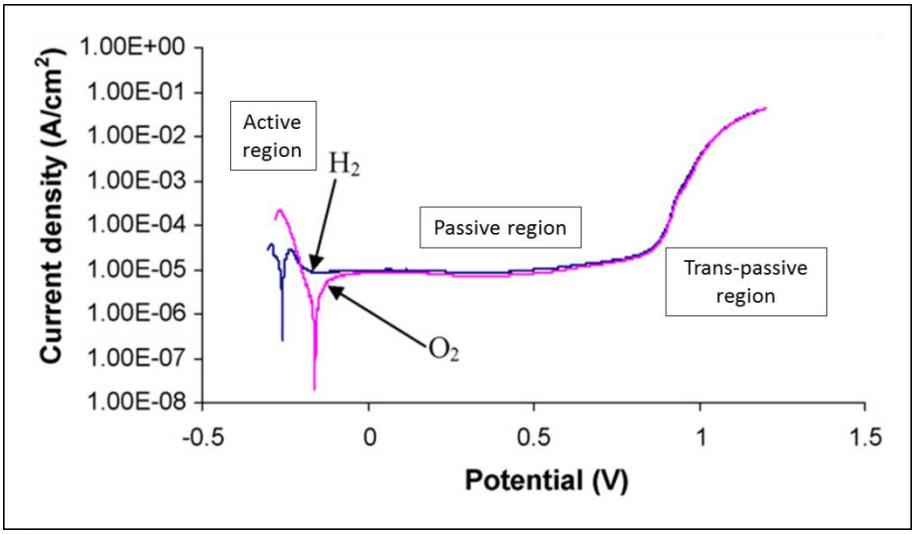

Figure 2.4: Potentiodynamic curves for SS 316L at 70 °C in $0.5M\ H_2SO_4$ *bubbled with* H_2 *or* O_2 *(adapted from*[36]*)*

However, the inductively coupled plasma / optical emission spectrometry (ICP/OES) tests that were conducted on the electrolytes after the potentiodynamic and potentiostatic tests responded with metal ion concentrations of about 25 and $42\ ppm$ at the anode and the cathode respectively. The authors concluded that such levels of ion concentrations can negatively affect the membrane and the overall performance of the fuel cell and hence SS BPP must be coated with protective coatings in order to reduce the corrosion.

In summary, a variety of different grades of SSs have been used as BPPs in PEMFCs. These include the two most common grades of SS; austenitic and ferritic. In case of austenitic, 316, 317 and 904 have been used more commonly and for ferritic, 434, 436, 441 and 441 have been used. These grades have been applied as BPPs without any coatings. These grades have in general offered excellent corrosion resistance, especially SS 316L.

Table 2.3 summarises different SS materials analysed for their feasibility as a BPP material in PEMFC and the various analysis tests conducted on the same.

Table 2.3: A review of various SS samples used for BPP applications and the analysis tests conducted

Material	**Type of test conducted and surface analyses used**	**Reference**
SS 304, 310, 316, 321, 347, 904, Ti, graphite	ICR $(0 - 300\ N.cm^{-2})$, Fuel cell operation for up to $3000\ h$ ($0.3\ mg.cm^{-2}\ Pt$, 50 °C, $2220\ N.cm^{-2}, 0.7\ A.cm^{-2}$)	Davies *et al.*[30,31]
SS 316L, 317L, 904L, 349™	ICR $(0 - 180\ N.cm^{-2})$, Corrosion tests ($1\ M\ H_2SO_4\ + 2\ ppm\ F^-$ solution at 70 °C, purged with air or H_2, potentiostatic and potentiodynamic tests)	Wang *et al.*[26]
Ferritic SS: AISI 434, 436, 441, 444, 446	ICR $(0 - 180\ N.cm^{-2})$, Corrosion tests ($1\ M\ H_2SO_4\ + 2\ ppm\ F^-$ solution at 70 °C, purged with air or H_2, potentiostatic and potentiodynamic tests), XPS depth profile	Wang *et al.*[32]
SS 304, 316L, 310S, 904	ICR $(0 - 220\ N.cm^{-2})$, Corrosion tests ($10^{-3}\ M\ H_2SO_4\ + 1.5 \times 10^{-4}\ M\ HCl + 15\ ppm\ HF$, 25–70 °C, purged with air or H_2, potentiostatic and potentiodynamic tests), SEM imaging	Silva *et al.*[33]
Various grades of SS	ICR $(0 - 140\ N.cm^{-2})$, Fuel cell operation up to $7000\ h$ under various conditions, SEM and EDX analysis	Makkus *et al.*[34,35]
SS 316 L	Corrosion tests ($0.5\ M\ H_2SO_4$ at 70 °C bubbled with O_2 or H_2 potentiostatic and potentiodynamic tests), SEM imaging	Wang and Northwood[36]

The question still remains that of high interfacial contact resistance as a result of the oxide layer. Indeed, these have been used without any coatings successfully and have not degraded even in long-term fuel cell tests, but the high resistance demands for a conductive coating to be

applied on top of the SS material to enhance the ICR peroperties in addition to the corrosion resistance properties that these SSs possess. The next section will focus on the literature on the coated SSs and a number of coating options that have been applied on SS substrates are discussed.

2.1.2. Coated Stainless Steel

SSs provide good corrosion protection, however, as a consequence, they do suffer from poor contact resistance due to the formation of the passive oxide layer. Coatings on SS surface have been used in order to improve the corrosion resistance and the contact resistance properties. The key requirements for the coatings are the same as the requirements for bare metal substrate to be used as a BPP. Coatings must be conductive, should have good adhesion to the SS substrate and should have a compatible thermal expansion coefficient with that of the substrate to avoid cracking and damage to the coating. Coatings are mainly divided into two types: carbon-based and metal-based[14,28,37]. Hermann *et al.*[28] gave a broad description of the different coating options available for BPP applications that was described in Figure 2.1. Among those, the carbon-based coatings include graphite, conductive polymers, graphene, diamond-like carbon and organic self-assembled monopolymers which will be discussed in a separate section. Metal-based coatings include noble metals, metal nitrides and metal carbides. Different metal based coatings used for application in BPPs are discussed in the next sections.

2.1.2.1. Noble Metal Coatings

Ihonen *et al.*[38] compared the contact resistance performance of platinum coated 316 SS samples. The authors noted that the contact resistance of SS was reduced by platinum plating via simple plating procedure. The contact resistance of Pt-coated SS surface was found to be much lower and much more stable as compared to that of the bare SS surface. However, corrosion was evident on the anode side of the BPP in long term tests. The authors noted if the content of the plating metal is too low, it could lead to localised corrosion and the critical content of the coating (Pt or Cr) is dependent on temperature and gas composition of the environment. The MEAs were prepared using the thin film preparation technique. Nafion® membranes were used with a varying thickness and

equivalent weight. The catalyst loading was in the range of 0.15 and $0.3\ mg\ Pt.cm^{-2}$. The loading was controlled by measuring the weight of the membranes before and after the painting procedure. The gas diffusion backing material used was commercial double-sided ELAT® backing. In the in-house cell, the flow rates for the gases were $60\ cm^3.s^{-1}$ for both O_2 and H_2.

In order to avoid the formation of an oxide layer that increases the ICR and to avoid the dissolution of nickel, Wind *et al.*[39] coated SS 316L samples with a thin layer of gold. The authors reported that there was no difference in the performance of Au-coated SS 316L and graphite BPP. After $1000\ h$ of standard fuel cell operation, almost no deterioration of voltage was observed which suggested that the oxide formed was very thin to affect the cell ICR. The chemical analysis of the MEA after the fuel cell operation showed that the amount of Ni was reduced considerably in case of Au-coated samples as compared to the bare SS samples suggesting that gold coating was a good diffusion barrier for Ni under standard operating conditions. Similar results on gold coated 316L SS samples were reported by Hentall *et al.*[40]. Eventually, Au-coated SS BPPs are far from a feasible option for metallic BPPs. Due to the high costs of gold, other relatively inexpensive corrosion resistant coatings are developed. Further, the coating techniques and the surface preparations must be optimised for maximum bonding strength between gold and the substrate BPP material[17]. Taking into consideration, the cost-effectiveness of gold coated SS as BPP material, Wind *et al.*[39] have studied a number of low cost coatings to be applied on SS 316L. Chemical analysis of the MEA was carried out after $100\ h$ of cell operation. These cell tests were carried out in single cells of $49\ cm^2$ active area. The MEA was made up of Nafion 113.5 membranes and Toray paper TGP90 with a catalyst loading of $4\ mg.cm^{-2}$ on each electrode. The flow field chosen for comparison was a serpentine flow field with two parallel channels. The operation temperature was 75 °C, operation pressure was $2.6\ bar$ on both sides. The authors reported the performance five proprietary coatings in comparison to bare SS plate and Au-coated BPP.

Yoon *et al.*[41] evaluated a number of protective coatings deposited via electroplating and physical vapor deposition (PVD) on three types of SS

samples namely 304, 310 and 316. The coatings that were investigated include; $2\ nm\ Au$, $10\ nm\ Au$ and $1\ \mu m\ Au$, $Ti, Zr, ZrN, ZrNb$ and $ZrNAu$. The coating was deposited on as-fabricated substrates without any surface grinding or polishing or any other surface preparation. In order to deposit the coatings, high speed acid gold plating and two methods of PVD were employed. In case of pure gold coatings, the electroplating process was used. The coatings were tested using polarisation tests for corrosion resistance and contact resistance tests were performed on selected samples. A three-electrode system was used for polarisation tests with graphite rod as the counter electrode and a saturated calomel reference electrode. The metal specimen was the working electrode. For the polarisation tests, the voltage was swept from a $-1\ V$ to $1\ V$ with a scan rate of $1\ mV.s^{-1}$. The electrolyte used was a sulphuric acid solution with pH 2 and the temperature was maintained at 80 °C. A Solartron 1287 potentiostat was used for controlling the potential. In order to measure the ICR, an Agilent 4338B milliohm-meter with a resolution of $10\ m\Omega$ was used. The meter supplied an alternating current ($1\ kHz$) ranging from $1\ \mu A$ to $10\ mA$ according to the magnitude of the target resistance. The set-up used in contact resistance tests is shown in Figure 2.5. All of the samples were degreased and rinsed with de-ionised water before conducting the measurements. All measurements were made at a room temperature. The authors reported Zr-coated SS samples to be the best amongst the samples studied. The $10\ nm\ Au$-coated SS samples provided adequate corrosion resistance for the anode side but the coating was not thick enough to protect SS from corrosion at the cathode side.

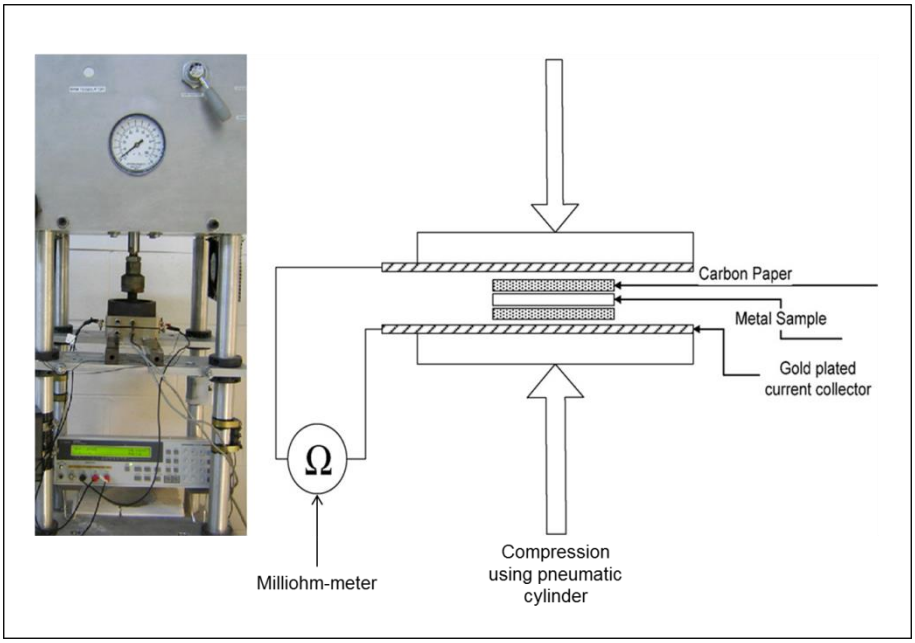

Figure 2.5: A picture (left) and the schematic of the interfacial contact resistance measurement setup (adapted from[41])

Pozio *et al.*[42] studied Niobium-clad SS 430 samples with respect to their ICR and corrosion resistance performance. The samples were compared to Ni-based alloys, PVD-coated $SS304/CrN$. The authors reported that $SS430/Nb$ demonstrated a low ICR value and very good corrosion resistance as compared to the commercial SS, Ni-based alloys and PVD-coated $SS304/CrN$. The scanning electron microscopy (SEM) image in Figure 2.6 displays the cross section of $Nb/SS430/Nb$ layers. The $SS430/Nb$ samples were reported to be suitable for BPP applications as a result of the presence of a conductive oxide layer that led to a reduced ICR values. Further, the results were comparable to those of graphite. These results were found to be in agreement with those reported by Weil *et al.*[43] who studied the corrosion, polarisation and contact resistance properties of Nb-clad BPP materials. The authors reported the results from exposure testing in $1\ M\ H_2SO_4\ +\ 2\ ppm\ HF$ at 80 °C. The ICR properties were found to be exceptional under these conditions and no weight loss was directly measured. The inductively coupled plasma-mass spectrometry (ICP-MS) analysis of the test effluents demonstrated less than 0.02% weight loss over a $2000\ h$ test period.

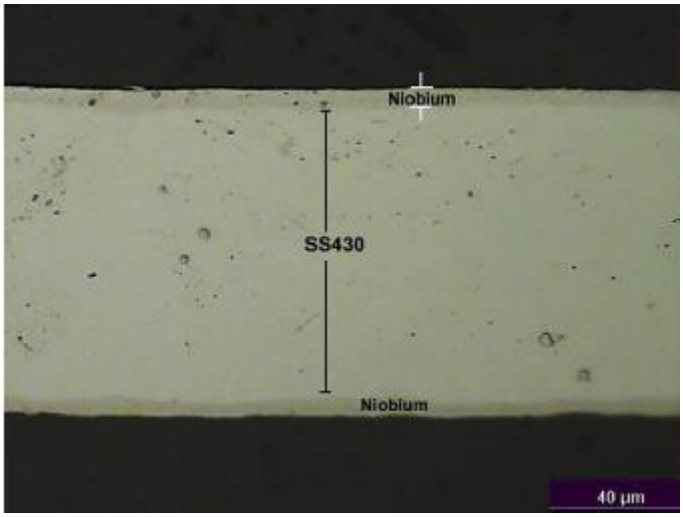

Figure 2.6: SEM micrograph showing a cross section of $Nb/SS430/Nb$ layers (reprinted from[42])

Feng *et al.*[44] studied 316L SS with nickel implanted for 1, 2, 3, 4 and 5 x 10^{17} ions. The potentiodynamic, potentiostatic and the ICR results were found to be in agreement with each other. The corrosion resistance was improved by the formation of a Ni-rich layer in both anode and cathode conditions. SS 316L of $6\,mm$ thickness was used as the substrate and $15\,mm \times 15\,mm$ specimens were cut from the steel plates. Before carrying out ion implantation, the specimens were polished with Al_2O_3 waterproof abrasive paper, degreased with acetone in an ultrasonic cleaner and then dried afterwards. Kratos AXIS Ultra XPS was employed to analyse the elements Fe, Ni, Cr and O in the implanted layer with an accuracy within 1%. The specimens were sputtered at $4.5\,nm.min^{-1}$ with $Al\,K\alpha$ source. The surface topography of nickel implanted samples was measured with an atomic force microscope (AFM).

2.1.2.2. Titanium Nitride (TiN) Coated BPPs

Titanium-Nitride coatings are considered to amongst the better coating options on SS for PEMFC BPP applications[37]. The characteristics such as high conductivity, excellent stability in a wide range of environments, wide industrial feasibility and cost affectivity make TiN coated SS samples to be an excellent option for BPP applications[45].

Wang and Northwood[46] studied the martensitic stainless steel (SS 410) coated with TiN using PVD technology in order to increase the corrosion

resistance. TiN was successfully coated on SS 410 and smooth, continuous coatings with thickness of about $15\ \mu m$ were achieved. TiN coatings formed on SS 410 improved the corrosion resistance. The polarisation resistance of TiN-coated SS 410 was found to be 50 times higher and the corrosion rate was about two orders of magnitude lower as compared to the uncoated SS 410. Further, the authors reported that the coatings also satisfied the physical and mechanical property requirements of a BPP such as low ICR, light weight, high mechanical strength and manufacturability and these were backed up by X-ray diffraction (XRD), (electrochemical impedance spectroscopy (EIS) and Scanning electron microscopy (SEM) analyses (Figure 2.7).

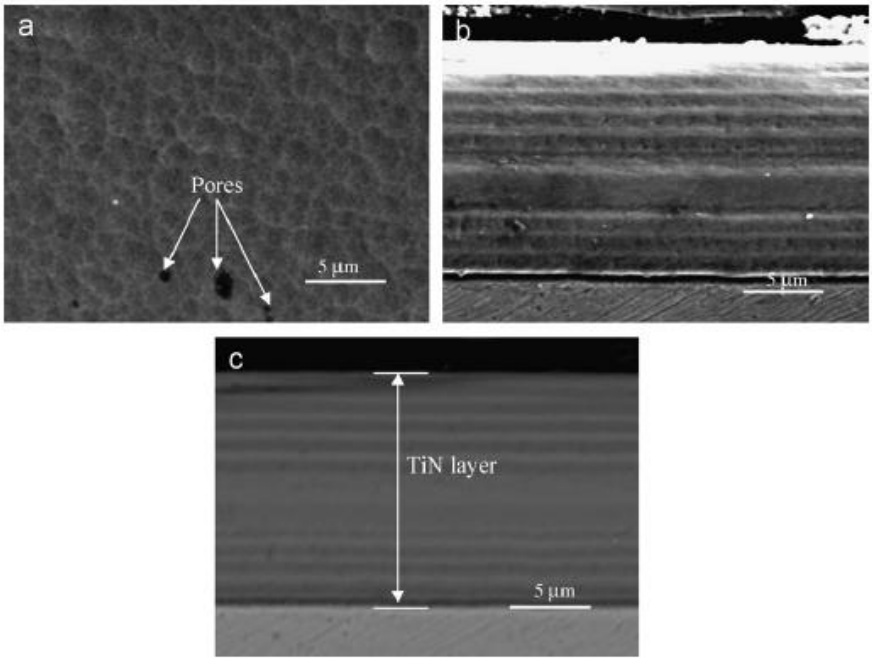

Figure 2.7: TiN coated SS410: (a) TiN coating surface (secondary electron image), (b) cross-sectional view of TiN coating on SS 410 (secondary electron scatter), (c) cross-sectional view of TiN coating on SS 410 (back-scattered electron image) (reprinted from[46])

Li *et al.*[47] investigated the corrosion behaviour and contact resistance of TiN-coated SS 316 in simulated PEMFC environments ($0.01\ M\ HCl$ / $0.01\ M\ Na_2SO_4$) bubbled with pure O_2 and H_2 gases. The TiN-coated SS samples have better corrosion resistance and passivity in both anode and cathode conditions. 316 SS is in passive state in simulated cathode environment, however, it cannot passivate spontaneously in an anode

simulated environment. Under typical load cell conditions of fuel cell for $4\ h$, no significant degradation of the coating in observed. During the immersion tests, small portion of the coating loss occurs in O_2environment for $1000\ h$ and in H_2 environment for $240\ h$ respectively. However, the exposed surface areas passivate in both cases. E_{corr} and EIS data revealed that the coating experienced two corrosion stages during the immersion tests; with the corrosion in the first stage being attributed to the coating defects. When the test solution reached the substrate through the pinholes and microcracks, E_{corr} dropped rapidly as TiN coating is nobler than SS 316; a galvanic corrosion cell was established. E_{corr} gradually increased as the exposed area was passivated slowly under the galvanic effect. In the second stage, E_{corr} does not change significantly as the coating specimen attained a steady corrosion state. The authors emphasised on the need of further efforts to improve the coating quality and the evaluation of the long-term stability of $316\ SS/TiN$ coating system under simulated conditions.

Cho and co-workers[48] studied the corrosion properties of AISI 316 SS coated with TiN in comparison with graphite and bare SS 316 BPPs. 316 SS was coated with TiN layer using hollow cathode discharge ion plating method. The coating process began with chemical etching of $1.5\ mm$ SS 316 plates to form flow channels. The chamber in which the etched plates were coated was vacuumed to $3 \times 10^{-6}\ Torr$ and Argon was purged through the chamber and a Ti target was evaporated at a discharge voltage of $260\ V$. Nitrogen gas was entered at an operating pressure of $6.3 \times 10^{-3}\ Torr$ at a flow rate of 160 standard cubic centimetre that formed the TiN layer. Thickness of the TiN layer was $1\ \mu m$. The authors conducted initial tests in a single cells using graphite, AISI 316, and $TiN/316$ BPPs and the current densities obtained were $996, 796,$ and $896\ mA.cm^{-2}$ respectively at a cell voltage of $0.6\ V$. A $1\ kW$ class short fuel cell stack was manufactured using TiN-coated BPPs and operated for $1028\ h$.

The contact resistance of SS 316 and TiN-coated 316 was almost same and higher than that of graphite at a given compaction pressure. However, the difference was almost negligible at stack assembly conditions. At a compaction pressure of $180\ N.cm^{-2}$, the contact resistance of graphite, SS316 and TiN-coated 316 was measured to be $30.23, 34.19$ and $32.71\ m\Omega.cm^2$ respectively.

Surface energy of BPPs is important in determining the performance of a cell, especially at high current densities. As water is produced as a result of the cathodic reaction, if not removed, it would flood the cathode side of a cell. In order to evaluate this, Cho *et al.*[48] measured the water contact angles of graphite, AISI 316 and $TiN/316$. High contact angle indicates high surface energy or high surface tension and a low surface wetability for the material being examined[48,49]. The authors[48] reported the water contact angle for both graphite and TiN-coated SS was found to be 90° and that of SS 316 was 60°. This implies that SS316 has a lower surface energy and hence would readily flood the cathode. A similar trend has been observed by Taniguchi and Yasuda[50] who reported that the power output of a PEMFC increased when the flow channels showed low wetability.

In the aggressive environment of fuel cell, the corrosion of the coating and that of the substrate would result in a negative effect on the performance of the cell. TiN-coatings provide an excellent coating option due to their low cost and the ease of the coating applicability. Further, as reported by Li *et al.*[47], electrochemical studies indicated that TiN coating specimen were resistant to corrosion under both cathodic and anodic environments but SEM observations detected small parts of coating loss as a result of the defects in the coating process. As the electrolytes reached the substrate through the coating defects, the binding force of TiN coating around the voids or defects would decrease. This would result in the formation and dissolution of passive films on the substrate. Consequently, the coating would be lost and the exposed area of the substrate would be enlarged. Thus, an improvement in the coating process and the coating quality is of great significance.

2.1.2.3. Chromium Nitride (CrN / Cr_2N) Coated BPPs

Brady *et al.*[51] developed preferential thermal nitridation process to form pin-hole free and a defect free CrN/Cr_2N surface on a $Ni-Cr$ alloy. The authors[52] reported excellent corrosion resistance and negligible contact resistance increase over a $4100\ h$ exposure in pH 3 $H_2SO_4 + 2\ ppm\ F^-$ at 80 °C. The ICR increase and the membrane contamination were negligible when the nitrided sample was used as a metallic bipolar plate in a $1000\ h$ fuel cell operation. This similar method was applied to a 349™ austenitic SS

by Wang *et al.*[53]. However, this resulted in a discontinuous mixture of discrete CrN, Cr_2N and $(Cr,Fe)_2N_{1-x}$ $(x = 0-0.5)$ phase surface particles. These particles were overlying on an exposed γ −austenite-based matrix. As a result of the discontinuity in the coating, it resulted in heavy corrosion in simulated PEMFC environments ($1M\ H_2SO_4 + 2\ ppm\ F^-$ at 70 °C), however, the contact resistance of 349™ austenitic SS reduced significantly[53]. On the contrary, the thermal nitridation of a AISI 446 ferritic SS resulted in an adherent, inward growing surface layer[54]. Though the layer was not continuous, it resulted in low ICR and good corrosion resistance under simulated PEMFC cathodic conditions. On the other hand, poor corrosion resistance was reported under the anodic conditions. The nitridation for $2\ h$ at 1100 °C resulted in very little nitrogen uptake. It was reported that a complex heterogeneous modification of the native passive oxide film occurred by nitrogen instead of the required μm level Cr −rich nitride layer.

Lee *et al.*[55] used a low temperature thermal nitridation technique to form a protective and conductive top layer on the 446M SS surface. Surface characterisations revealed that a $130\ nm$ thick continuous, protective and conductive Cr −nitride and Cr −oxide (CrN/Cr_2O_3) film was formed on the surface. This is evident from the transition electron microscopy (TEM) image shown in Figure 2.8. The polarisation data suggested that the corrosion resistance properties of low-temperature nitride 446M SS were found to be much better than that of the high-temperature nitride ones. In addition to this, the low-temperature nitride (CrN/Cr_2O_3) layer was attributed with an excellent stability during the polarisation tests under the anodic and cathodic conditions. As compared to the base metal, the low-temperature nitride 446M SS has a remarkable improvement in the electrical conductivity and there was no increase in the ICR values after the polarisation tests in both PEMFC operating conditions.

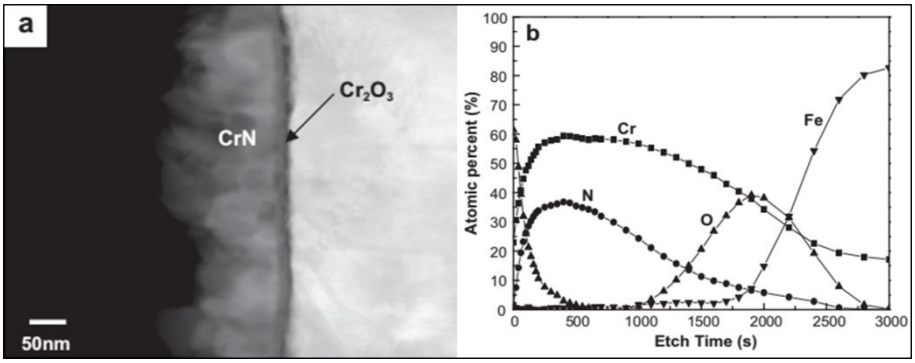

Figure 2.8: (a) Cross-sectional transition electron microscopy (TEM) image and (b) auger electron spectroscopy (AES) depth profile for L-446M stainless steel (adapted from[55])

Hong *et al.*[56] nitrided an austenitic SS sample (AISI 316L) via ICP using a mixture of nitrogen and hydrogen at temperatures between the range of 530 K and 650 K for $30\,min$ at $6.6\,Pa$. The authors noted that after plasma nitriding, a nitrogen-expanded austenite layer S-phase was formed in all samples. The crystal structure of the nitrided samples was characterised using XRD of $CuK\alpha$ radiation. The corrosion properties of the nitrided samples were measured in a $0.1\,N\,H_2SO_4 + 2\,ppm\,HF$ solution at 80 ˚C in order to simulate PEMFC operation conditions. A conventional three-electrode system was used with a carbon rod as the counter electrode and a saturated calomel electrode (SCE) as the reference. The nitrided samples were used as the working electrode. In terms of the ICR performance, at a compaction pressure of $150\,N.cm^{-2}$, the reported value for an untreated sample was $82\,m\Omega.cm^2$, while that of the samples after nitriding at 530, 590 and 650 K were reported to be $40,13$ and $11\,m\Omega.cm^2$, respectively. The increase in the electrical conductivity was attributed to the formation of the dense S-phase. The formation of chromium nitrides on the surface of the treated samples, as well as the suppressed oxide formation due to the nitriding process contributes towards the high electrical conductivity. The authors[56] commented that $Cr-$containing compounds such as CrN or Cr_2N are formed by high-temperature nitridation. As a consequence, $Cr-$depleted regions are created which reduce the corrosion resistance. All nitrided samples had low current densities. The formation of the S-phase without the $Cr-$depleted regions effectively enhanced corrosion resistance. The sample nitrided at 590 K was reported to have the best corrosion properties.

Han *et al.*[57] used Cr −electroplated AISI 316L SS samples and carried out nitridation using ICP. A continuous, thin CrN layer was formed on the surface of the samples after ICP nitriding for $2\,h$ at 400 °C. The authors varied the substrate DC bias voltage from -100 to $-300\,V$ at a constant ICP power of $400\,W$. All the samples exhibited uniform, continuous CrN layers with varying thickness and surface morphologies. The authors concluded that all nitrided samples had excellent corrosion resistance properties in both simulated anode and cathode conditions of the PEMFC.

In conclusion, the metal based-coatings have enhanced the surface properties of different SSs. Carbides and nitrides have offered excellent corrosion resistance as well as excellent contact resistance performances in fuel cell conditions. However, the cost of BPPs still offer a significant challenge in the commercialisation of fuel cells and hence, it is required to develop a cheaper alternative to coated SSs as BPP materials. Mild steel has been studied for its feasibility as a BPP material for PEMFC. The poor corrosion resistance offered by mild steel make it impossible to use as it as a BPP directly; and hence it demands for a corrosion resistant coating. The coated mild steel material is discussed in the next section.

2.1.3. Mild Steel

Stainless Steels (SSs) are promising candidates for BPPs, providing relatively high chemical stability and other qualities discussed earlier. However, the major concern that still remains is that of corrosion and formation of passivation layer that reduces the electrical conductivity. In order to obtain good chemical compatibility, stainless steels need to have high chromium content or surface treatment, which results in high cost of BPPs. As compared to stainless steel, low carbon steel is low at cost, but has poor chemical properties for application as a BPP. Conventional low carbon steel has been used as base metal for BPP and for a good corrosion resistance; coatings or surface treatment methods[58] have been applied on the base low carbon steel. However, the studies of carbons steels as BPP are rare due to the poor corrosion resistance of these materials under the PEMFC atmosphere[59].

Nam *et al.*[58] used a carbon steel (A283-C) sheet with a thickness of $2\,mm$ as the substrate and chromium electroplating was performed to obtain a

thickness of $10\ \mu m$ on the substrate and nitriding was applied for 1 and $2\ h$ at 1373 K in a furnace with $50\ Torr\ N_2$ pressure. They conducted the ICR tests up to a compaction force of $150\ N.cm^{-2}$. The corrosion tests were performed in a $0.1\ N\ H_2SO_4\ +\ 2\ ppm\ F^-$ solution at 80 °C. In case of both cases; depositing chromium and then nitridation, a uniform surface layer without any cracks or defects was observed. The XRD patterns of the chromium nitrided layer for $2\ h$ at 1100 °C in pressure $50\ Torr$ reveals higher Cr_2N diffraction peaks as compared to $1h$ under same conditions. This depicts the formation of more Cr_2N with longer nitriding hold time. In terms of performance, the ICR values were found to be lower for the $1h$ sample as ($15\ m\Omega.cm^2$ at $150\ N.cm^{-2}$) compared to that of the $2\ h$ sample ($45\ m\Omega.cm^2$ at $150\ N.cm^{-2}$). For the corrosion performance tests, the nitride layer of the $2\ h$ sample was thicker than that of the $1\ h$ sample and had resulted in better corrosion resistance.

Bai *et al.*[59] have claimed to be one of the first research groups to have applied a chromized coating on AISI 1045 carbon steel (chemical composition as described in Table 2.4) as a BPP material. The advantages of using AISI 1045 steel are its low cost, high mechanical strength and the ease of forming sheets. The low corrosion resistance and ICR are said to have been improved by pack chromization with an activated pre-treatment of rolling or electrical discharge mechanism (EDM) in order to reduce the operating temperatures and to increase the deposition rates. The pack powder mixture used for chromizing contained master metal chromium, activator ammonium chloride and inert filler aluminium oxide. The pack mixture was heated to 150 °C at the rate of 10 °C per minute and held at this temperature for $1\ h$ before taking the temperature up to 700 °C and then held for $2\ h$ and $4\ h$ for different samples. The process resulted in a coating, containing mostly chromium carbides and some minor chromium nitrides on the substrate.

Table 2.4: Chemical composition of the AISI 1045 steel (adapted from[59])

Ele-ment	Fe	C	Si	Mn	P	S	Cr	Ni	Mo
Wt. %	Bal.	0.47	0.26	0.75	0.01	0.01	0.02	0.01	<0.01

SEM analysis was used to study the morphologies and micro structures of the coatings and the crystalline structures and the constituent phases of the coatings were analysed by the use of XRD using $Cu - K\alpha$ radiation of $\lambda = 0.15405\, nm$ over a scanning range from 30° to 70°. The elemental distribution in the coating was analysed using electron probe X-ray micro analyser. A three electrode system was used to conduct DC-electrochemical tests including potentiodynamic and potentiostatic tests with a SCE as a reference electrode. The potentiodynamic test was carried out in a $0.5\, M\, H_2SO_4$ solution at room temperature without any purging gases. The potential was swept from $-0.5\, V$ to $0.8\, V$ vs SCE and the scan rate used was $0.5\, mV.s^{-1}$. The potentiostatic polarization measurements were executed at simulated anode ($-0.1\, V$ vs SCE) and cathode ($+0.6\, V$ vs SCE) under purged conditions with H_2 and O_2 respectively, at 80 °C for $1\, h$. The coatings prepared by rolling and chromization for $2\, h$ showed excellent corrosion performance. However, their anti-corrosion properties did not further improve by extending the chromization time, i.e., at $4\, h$. However, the corrosion resistance of chromized specimen with the pre-treatment of EDM was improved with increasing the chromization duration from $2\, h$ to $4\, h$. In addition to this, all the chromized specimens have a lower ICR than that of both bare 1045 carbon steel and also SS 304L. AISI 1045-R-Cr(700-2) sample prepared by rolling pre-treatment and chromized at 700 °C for $2\, h$ possess the lowest ICR value of $5.9\, m\Omega.cm^2$. The authors have claimed to enhance this work by using the chromized carbon steels as bipolar plates on the investigation of actual single cell fuel cell.

Leading from the previous work, Bai *et al.*[60] employed rolling pre-treatment along with pack chromization on AISI 1045 steel and used it as a BPP in a single cell fuel cell for $100\, h$ test. As reported before[59], the main constituent phases of the coating were carbides and minor phases were chromium-ferric nitrides and oxides. The modified steel plate (depicted in Figure 2.9) was used as BPPs for fuel cell tests and the performance was compared to conventional graphite BPP.

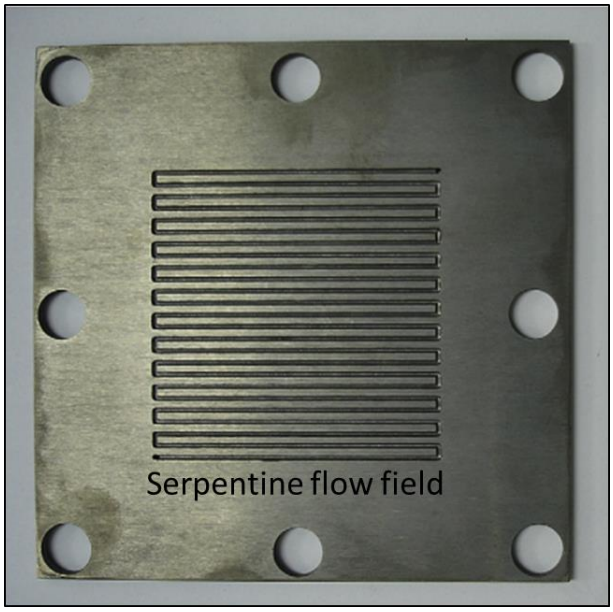

Figure 2.9: The 1045-R-Cr(700-2) (rolling pre-treatment and chromized at 700 °C for $2\ h$) BPP machined with a single serpentine flow field with an active surface area of $25\ cm^2$ (adapted from[60])

Water management is an important factor that affects the cell performance in PEMFC systems. In general, hydrophobic materials possess a contact angle higher than 90° and hence any BPPs would be required to have excellent hydrophobicity and a water contact angle of higher than 90° to avoid flooding and power loss. The authors[60] reported the contact angles of 1045-R-Cr(700-2) and 1045-Cr(700-2) (where: R stands for rolling pre-treatment and both samples are chromized at 700 °C for $2\ h$) to be 98.3° and 94.0°, respectively. These were found to be higher than that of bare 1045 which was reported to be 84.6°. The authors speculated that the dominant factor which affected the contact angles wasn't the surface roughness but the superficial composition of the plates. The bare plate had a lower contact angle as iron oxide has better affinity to water as compared to chromium carbide found on the surface of the chromized samples.

The OCV for all three samples (1045-R-Cr(700-2), 1045-Cr(700-2) and graphite) were found to be $0.948\ V$, $0.945\ V$ and $0.947\ V$ respectively. At $0.6\ V$, the current densities of single cells assembled with graphite and 1045-R-Cr(700-2) were reported to be 671.6 and $679.2\ mA.cm^{-2}$ respectively and the maximum power densities were 0.51 and $0.50\ W.cm^{-2}$, respectively. The performance of rolling pre-treated and

chromized sample was clearly comparable to that of graphite. In order to study the long-term performance of the cell with 1045-R-Cr(700-2) BPPs, it was operated for $100\,h$ at a cell voltage of $0.6\,V$ at 60 °C and the power density of the cell was observed in the range of $0.54 - 0.50\,W.cm^{-2}$. This indicated that the cell did not degrade during the operation.

Similar to work reported by Bai *et al.*[59,60] using AISI 1045 steel, Bai *et al.*[61] have reported the improvements in the surface performance of low-carbon steel AISI 1020 (chemical composition as described in Table 2.5) by reforming pack chromization process at a low temperature of 700 °C for $2\,h$. The steel surface was activated by EDM with different currents before the chromizing procedure. The results have indicated that a dense and homogenous $Cr-$rich layer was formed on the EDM carbon steel by pack chromization. The chromized coatings were pre-treated with electrical discharge currents of $2\,A$ and $10\,A$.

Table 2.5: The chemical composition of the experimental low-carbon steel AISI 1020[61]

Ele-ment	Fe	C	Si	Mn	P	S	Cr	Ni	Mo	V
Wt. %	Bal.	0.23	0.20	0.64	0.02	0.03	0.03	0.03	0.02	<0.01

After the coating process, the coatings were characterised via grazing incident X-ray diffraction using monochromatic $Cu-K\alpha$ radiation with a wavelength of 1.542 Å. The microstructure and chemical composition of the sample was examined by electron probe microanalysis and SEM with X-ray energy dispersive spectrometry (EDS). XPS depth profiles of $C, N, O, Ni, Cr,$ and Fe were also obtained. In terms of the electrochemical performance testing, the corrosion rates were obtained in a $0.5\,M\,H_2SO_4$ solution with a platinum sheet and $Ag/AgCl$ as counter and reference electrodes respectively. Out of the four samples analysed, i.e., 1020-EDM$(10\,A) - Cr$, 1020-EDM$(2\,A) - Cr$, 1020$-Cr$, 1020, the chromized coating pre-treated with electrical discharge currents of $2\,A$ was found to have the lowest corrosion current density of $5.78 \times 10^{-8}\,A.cm^{-2}$ and a corrosion rate of $6.70 \times 10^{-4}\,mm\,per\,year$. The ICR values were obtained using methods

described by Wang *et al.*[26], and 1020-EDM$(2\ A) - Cr$ had the best performance with $11.8\ m\Omega.cm^2$ at $140\ N.cm^{-2}$. The corrosion resistance of all chromized coatings, as one would have expected, were found to be much better than that of the raw material. The corrosion resistance, from best to worse, were found to be in the order of 1020-EDM$(2\ A) - Cr$ > 1020-EDM$(10\ A) - Cr$ > 1020$-Cr$ > AISI 1020.

The previous work[61] was continued and Ni electroplating pre-treatment was employed on the AISI 1020 steel samples along with the EDM before the low temperature pack chromization processes. The samples were analysed for their corrosion performance in a $0.5\ M\ H_2SO_4$ solution at room temperature. The authors reported the corrosion resistance of the samples in the order of (from best to worst) 1020-EDM$-Ni - Cr -$(700-2) > 1020$-Ni - Cr -$(700-2) > 1020$-Cr$(700-2) > 1020. In addition to this, the 1020$-Ni-Cr$(700-2) specimen had the best ICR performance as a result of the less amount of oxides in the superficial coating. The ICR values at $140\ N.cm^{-2}$ for 1020$-Cr$, 1020$-Ni - Cr$ and 1020-EDM$-Ni - Cr$ were reported to be 34.5, 10.5, and $16.2\ m\Omega.cm^2$, respectively.

Coated mild steel material can be looked upon as an alternative to the rather expensive SSs to be applied as BPPs in PEMFCs. In terms of the coating options, metal based coatings and carbon based coating can be explored for mild steel materials. As explained earlier, the coating must have excellent corrosion and contact resistance properties; however, in addition to this, the coating must have good adhesion to the base material to avoid cracks, delamination and consequently, total coating failures. Recently, carbon based coatings have been explored for their excellent corrosion resistance and good conductivity. These are discussed in the next section.

2.2. Carbon-Based Coatings for BPPs: Graphene

Graphite and diamond are the most common allotropes of carbon. In case of diamond, the carbon atoms are bonded together in a three-dimensional tetrahedral lattice arrangement built up of sp^3 hybrid carbons. This

hybridisation state, where all the valence electrons on the carbon are used in bonding, makes the diamond electrically insulating. On the other hand, in graphite the carbon atoms are bonded together in multilayer sheets of a hexagonal sp^2 hybrid carbon lattice. Graphite is highly electrically conductive in the plane of the stacked carbon sheets, and this conductivity is attributed to the delocalised π −electrons spread throughout the entire hexagonal network. Graphene can be defined as a one-atom thick layer of graphite. Ideally, graphene is an infinite 2-dimensional (2D) hexagonal sheet of carbon atoms although in practice, the graphene has finite dimensions. As shown in Figure 2.10, a single layer of graphite, which is graphene, has a lattice constant of $a = \sqrt{3}a_0 = 2.46$ Å where $a_0 = 1.42$ Å is the nearest inter-atomic distance[62]. The inter-planar distance[62] between two adjacent graphene layers is 3.36 Å.

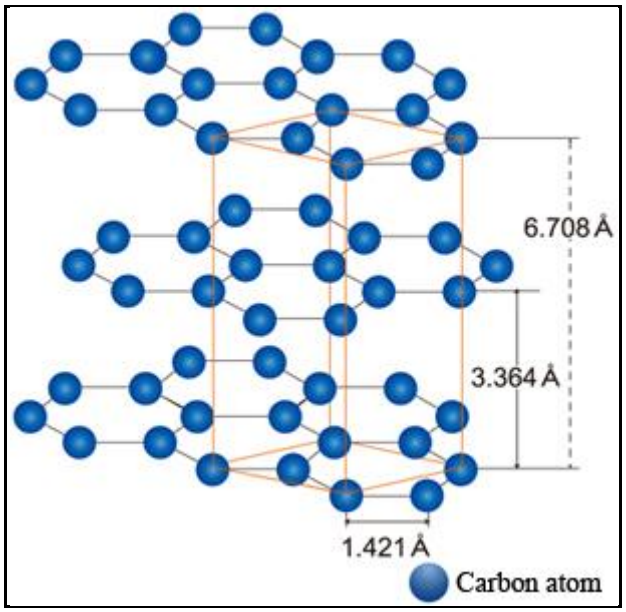

Figure 2.10: Graphite structure with individual graphene sheets stacked in AB fashion. The unit cell of graphite is shown in red lines (adapted from[63])

An understanding of the key properties of elemental carbon is required to understand the atomic structure of graphene. The atomic number of carbon is 6, giving it 2 core and 4 valence electrons. The six electrons occupy the $1s^2$, $2s^2$, $2p_x^1$ and $2p_y^1$ atomic orbitals. Carbon is a tetravalent element and hence the outermost four (valence) electrons take part in covalent bond formation. During bond formation, one of the $2s$ electrons is promoted to the empty $2p_z$ orbital. This results in the formation of hybrid orbitals. In

case of diamond, the $2s$ orbital hybridises with the three $2p$ orbitals to form four energetically equivalent orbitals which form a tetrahedral arrangement and are occupied by one valence electron each. When bonded to neighbouring sp^3 hybrid carbon atoms, the 3-dimensional (3D) carbon structure of diamond is formed. The strength and hardness of diamond comes from the strong binding energies of the $C-C$ bond in the 3D tetrahedral structure.

In case of graphite, only two out of the three p orbitals take part in hybridisation forming three sp^2 hybrid orbitals and resulting in a trigonal planar structure with 120° angles. These sp^2 hybridised carbon atoms form the in-plane covalent "σ bonds" that lead to the hexagonal honeycomb structure of graphite. The remaining $2p$ orbital overlaps with a $2p$ orbital on a neighbouring carbon atom forming a "π bond", which in combination with the σ bond is colloquially referred to as a "double bond", The combination of in-plane σ and π bonds within the graphene layers are twice as strong ($615\ kJ/mol$) as the $C-C$ bonds in the sp^3 hybridised diamond ($345\ kJ/mol$)[64]. However, in graphite the bonding between graphene sheets is not covalent, but rather based on physical van der Waals bonding. This leads to the easy shearing of graphite along the layers.

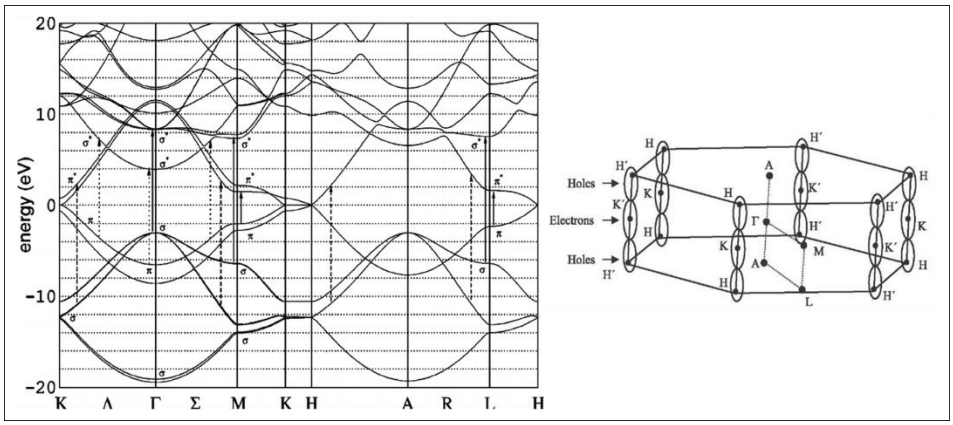

Figure 2.11: The band structure of graphite with its Brillouin zone (adapted from[63])

As shown in Figure 2.11, the quasi 2D character is in the less dispersive energy band feature for both the σ and π bonds in the inter-sheet direction $K \leftrightarrow H$ in the Brillouin zone. The valence π band and the conduction π^* band both split into two sub-bands as a result of the interaction of the two

independent graphene sheets in the unit cell. Both these bands touch each other at the K point resulting in the semi-metallic electronic structure. At the same time, the weakly dispersive π band crosses the Fermi level along the $K \leftrightarrow H$ and the same number of electrons and holes coexist as a result of this. Hence when a single graphene sheet is extracted from graphite, it is free from the inter-sheet interactions and thus a pure 2D electronic structure is formed as shown in Figure 2.12. The features of the electronic structure of graphite are roughly preserved in the graphene[63].

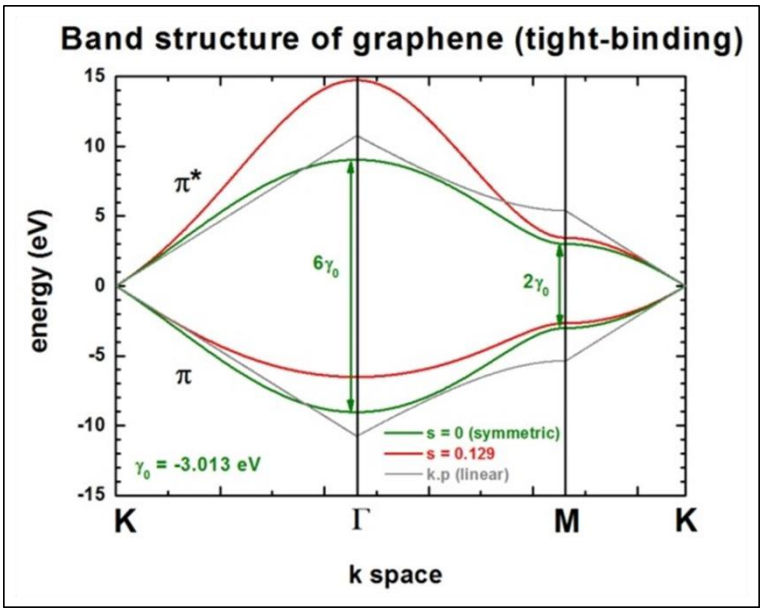

Figure 2.12: $\boldsymbol{\pi}$ bands of graphene derived from the tight binding method (adapted from[63])

The specific lattice structure of graphene, with a monatomic honeycomb lattice and a perfect 2D dimensionality, along with the valence electron configuration of the carbon atoms, results in the peculiar electronic band structure. The quasi-particles (the electrons and the holes) in graphene behave like massless relativistic particles known as Dirac fermions. The electrons and holes are degenerate at the Dirac points[65]. This results in the peculiar physical properties of graphene that are not found in other carbon allotropes.

The characteristic that distinguishes graphene from graphite is the zero band gap semi-conducting feature that is observed at the K point. At this point, the π band (valence band in semiconductor physics) and the π^* band (or conduction band), both possessing linear wave number dependence,

touch each other. The dispersion of these bands in the vicinity of the Fermi level reveals massless electrons at the Fermi level. This unconventional graphene electronic structure was predicted theoretically by Wallace[66] in 1947. After the successful isolation of graphene in 2004[67], theoretical and experimental efforts have unveiled a variety of phenomena in relation to the intriguing features of massless Dirac fermions in graphene. Some of the unique physical phenomena observed are the integer quantum Hall effect, Klein tunnelling, specular Andreev reflection at the graphene-superconductor interface, exceptional thermal conductivity and superior mechanical strength[63,65].

2.2.1. Bilayer, Trilayer and Few Layer Graphene

The electronic properties of graphene depend on the number of graphene layers[64,68]. In general, the graphene community distinguishes between single layer, bilayer and few layer graphene (FLG). By FLG, it is generally understood that the number of layers is less than ten. A structure consisting of more than ten layers of graphene can be labelled as a graphite thin film as it essentially exhibits the electronic properties of graphite[64]. In addition to this, the electronic band structure of graphene is influenced by the manner in which the graphene layers are stacked[64,69]. Three different types of stacking sequences can occur in graphene[70]; simple hexagonal (AAA..., space group), hexagonal (ABAB..., space group) and rhombohedral (ABCABC..., space group). The latter two types of stacking are depicted in Figure 2.13. In case of the AB-Bernal stacking, alternative layers have the same projections on the basal X-Y plane, and the inter-layer spacing is 3.35 Å. The ABC-rhombohedral stacking has the third layer shifted with respect to the first and the second layers. The fourth layer then has the same projection on the basal plane as the first layer and the interlayer separation in this case is 3.37 Å[62,64]. In general, the AB-Bernal stacking is most commonly found in case of graphite and FLG[64].

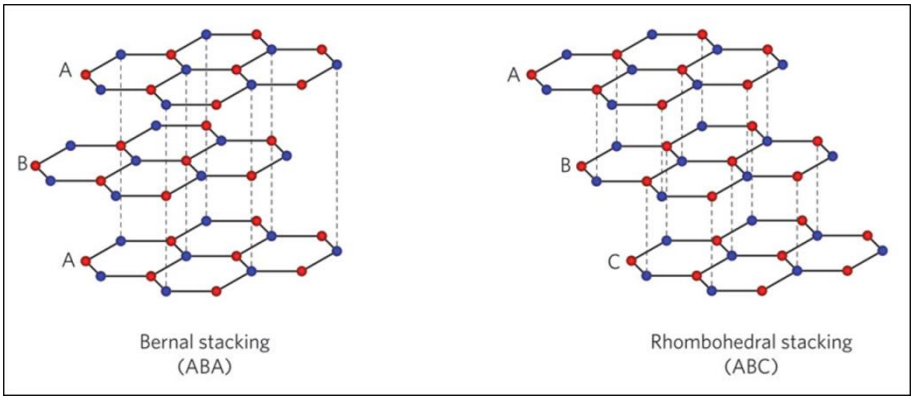

Figure 2.13: AB-Bernal stacking and ABC Rhombohedral stacking in graphene (adapted from[64])

2.2.2. Methods for Obtaining Graphene

2.2.2.1. Mechanical Exfoliation

Mechanical exfoliation can simply be explained as the process where mechanical force is applied to separate graphene layers from bulk graphite. At the lab scale, this process generally involves using an adhesive tape to attach to the surface of graphite and using force to peel off the tape along with the graphene layers attached to the tape. Graphene sheets can also be segregated by rubbing the surface of graphite against another material to slide off graphene layers. The first isolated graphene was obtained by the mechanical exfoliation of graphite in 2004[67] using highly oriented pyrolytic graphite (HOPG) source. A Scotch tape is used to repeatedly stick and peel off graphite crystals into thinner and thinner pieces. These pieces were then transferred on top of an oxidised silicon substrate with $300\,nm$ thick SiO_2. The Si/SiO_2 creates a Fabry-Perrot cavity in the microscope and the graphene layer on top of this adds a tiny optical path to the cavity. At $550\,nm$ wavelength, where the sensitivity of human eye is at the optimal, and under 12% light, the optical contrast between the graphene and the substrate is maximised. Graphene is visible and can be easily identified under an optical microscope. A single layer of graphene deposited on the SiO_2 layer appears light purple with the colour getting darker as the number of graphene layers increases.

Mechanical exfoliation is very simple and so far has resulted in the best graphene samples in terms of structural and electronic properties.

Graphene flakes with sizes up to a few millimetres can be obtained using this method. The ease of production and the low cost make this method the most popular for graphene preparation. However, this approach has very low efficiency and it is impractical for large scale industrial scale up[64,65].

2.2.2.2. Chemical Exfoliation

The van der Waals interactions between the adjacent graphene layers are relatively weak when compared to the stronger in-plane covalent sp^2 hybridised $C-C$ bonds. However, in order to achieve the layer separation, these van der Waals forces that keep the graphene sheets together, need to be overcome. These layers can be separated from bulk by mechanical exfoliation, and also in liquid phase using solution based chemistry. When graphite powder is dispersed in a suitable organic solvent such as N −methyl-pyrrolidone (NMP), the single layers of graphene can be steadily dispersed in the solution in a concentration[71] up to $0.01\ mg/ml$. Once segregated, the polar solvents such as NMP prevent the restacking of graphene sheets and maintain their isolation to form a colloidal like solution[64,65,71]. Larger graphite pieces floating in the solution can be removed using centrifugation and single layer graphene and FLG can be isolated. The process is scalable and the solution is ideal for spray coating, ink-jet printing or electrophoretic deposition of graphene on a substrate.

The earliest reports of direct chemical exfoliation came from the Nobel Prize winners, Novosolev and Geim, in 2008[72]. The authors reported a simple method whereby graphite was placed in dimethylformamide (DMF) and subjected to sonication, resulting in thin graphite pieces and monolayer graphene. The graphite pieces were removed by centrifuging at $13000\ rpm$ for $10\ min$. The DMF solution was then left with monolayer graphene and few layers of graphene sheets. A thin transparent conducting film was produced by spraying this DMF suspension[72]. Separately, Hernandez[71] *et al.* Explored different suspension solutions such as NMP, $N-N$ −dimethylacetamide, γ −butyrolactone and 1,3 dimethyl-2-imidazolidinone. Other organic solvents with a lower boiling point such as 1-2-dicholoroethane can also be used for chemical exfoliation[64].

Sonication is an important step in direct chemical exfoliation of graphene. The final graphene product produced is sensitive to the frequency,

amplitude and power of the sonication system. Hernandez[71] *et al.* used a low power sonic bath for $30\ min$ in their experiments. Excessive sonication may lead to the destruction of graphene[71].

2.2.2.3. Graphene from Graphene Oxide

Graphene that has been oxidised is termed graphene oxide[64] (Figure 2.14). The concept of oxidation of graphite is in existence since the mid-19th century[64,65]. One of the earliest reports, published by Brodie in 1860, describes treating graphite with potassium chlorate $(KClO_3)$ and fuming nitric acid. Since then several oxidation methods have been processed[64,65].

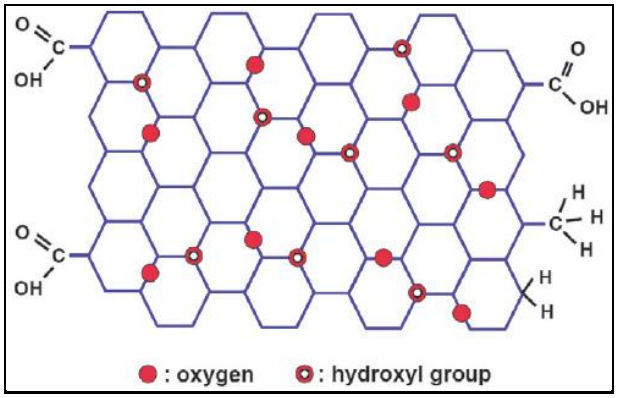

Figure 2.14: Structural model of single layer graphite oxide (adapted from[73])

The electron rich $C = C$ bonds in the graphene sheets react with the oxidising agents to form oxygenous groups that are covalently bonded to the carbon atoms, on both sides and the edges of the graphene sheets. The planar structure of the graphene sheets and the $\pi - \pi$ interaction between the adjacent graphene layers are destroyed, and the inter layer distance is expanded. In addition to this, the hydroxyl, carbonyl and the ether groups convert the hydrophobic graphene sheets into hydrophilic ones. As a result of this, the exfoliation of graphite oxide is much easier than the exfoliation of pristine graphite; especially in polar solvents. Once the graphite has been oxidised, it can be exfoliated using sonication or prolonged stirring in water. The graphene oxide produced in this way can be reduced back to graphene by using chemical methods, involving reducing agents such as sodium borohydride $(NaBH_4)$, hydrazine, dimethylhydrazine, or by using heat treatment, UV irradiation or even electrochemically[64].

2.2.2.4. Chemical Vapor Deposition (CVD) of Hydrocarbons on Metals

The fabrication of graphene on metals by chemical vapor deposition (CVD) is one of the most popular routes for graphene synthesis. CVD shows promise for fabrication scale up and the technique is already well established in the industry. CVD of graphene can be established for large areas and is very important for solar cell fabrication as a continuous covering is required. It provides better results as compared to the exfoliation method where graphene flakes are scattered randomly over a substrate.

The CVD of sp^2 carbon involves passing of a hydrocarbon feedstock gas over a catalyst (i.e. a transition metal) at elevated temperatures. The catalyst then decomposes the feedstock catalytically to provide carbon radicals which deposit on the substrate. Graphene has been grown on a number of transition metals, such as Pt, Ru, Ir, Ni, Cu, Co and Re[64,65]. The catalytic character of the transition metals is very well established and is believed to arise from their partially filled d-orbitals, or by the formation of intermediate compounds that can absorb and activate the reacting medium. Hence, the transition metals provide a low energy pathway for reactions by changing oxidation states or by the formation of intermediate compounds. Once the hydrocarbon feedstock has decomposed to provide a source of carbon, it then can be absorbed by the metal and later precipitated to form graphene. In spite of the basic experimental procedure being very simple, the actual understanding of the dynamics of carbon deposition and domain growth is limited. The graphene outcome is affected by the cooling rate, carbon exposure time and the concentration, flow rate and source of carbon feedstock[64].

2.2.3. Photo-Thermal Chemical Vapor Deposition (PTCVD) of Graphene on Steel

2.2.3.1. Apparatus

Carbon nanomaterial thin films are produced using the Surrey Nanosystems NT-1000 CVD system (Figure 2.15) based at the Advanced

Technology Institute, University of Surrey[74]. The system allows for DC (direct current) and AC RF (alternating current, radio frequency) plasma production of graphene or diamond-like carbon respectively on up to $10\ cm$ diameter samples. The system is typically used for process development and is designed for fast turn-around, giving the ability to promptly develop processes.

Figure 2.15: Surrey University Nanosystems NT-1000 CVD system[74]

The Surrey Nanosystems apparatus has the ability to deposit carbon materials, including many forms of diamond like carbon (DLC) and graphitic-carbon (nanotubes and graphene) nanomaterials. Integrated system options (Figure 2.16) include optical (infra-red) heating, which allows for rapid heating as light couples well into absorbing (black) carbon materials; stage cooling, for low temperature DC growth of graphene; and AC RF plasma production, for room temperature growth of DLC. Finally, a variety of process gasses is available to allow for chemical functionalisation (fluorination, nitrogenation, doping etc.).

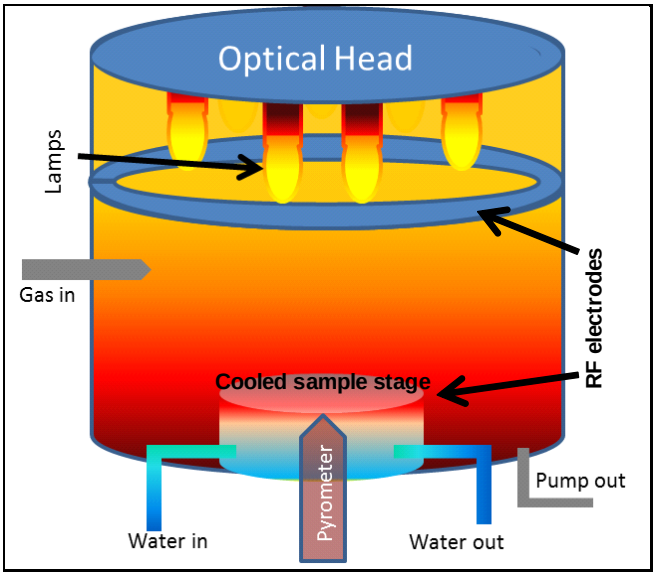

Figure 2.16: Schematic of Surrey Nanosystems NT-1000 CVD system, showing the optical head, RF electrodes and stage cooling system[74]

Two further CVD systems are available at Surrey based on the same apparatus design, but with larger vacuum chambers. The second system (SNS Nanocat) also allows substrates with dimensions up to $10\,cm$ in diameter to be coated with graphene or DLC; the third (a microwave CVD system) allows substrates with dimensions of up to $70 \times 15\,cm^2$ to be coated with DLC.

2.2.3.2. Process

Photo-thermal CVD deposition of graphene has been undertaken in two ways: via a catalyst layer deposited on the steel substrate surface, and by direct graphene growth directly onto the steel surface. Using either method, the as-received substrates are cleaned a with a methanol soaked wipe to remove any dust and grease.

Where used, catalyst deposition proceeds by deposition of a thin catalyst layer $(< 100\,nm)$ of Iron or Nickel using a DC sputtering method. The two sides of the steel substrate are coated sequentially, after which the coated substrate is transferred to the CVD chamber for graphene growth.

The CVD deposition proceeds via white light assisted PTCVD growth of graphene, at elevated temperature, on both sides of the steel substrates simultaneously.

To allow the production of a homogeneous graphene coating on both sides of the steel samples in a single deposition step, the steel substrates were positioned above the cooling stage surface on small pieces of silicon on a silicon wafer (Figure 2.17). This allows the process gasses and the incident light (reflected off the lower silicon wafer) to interact with both sides of the substrate.

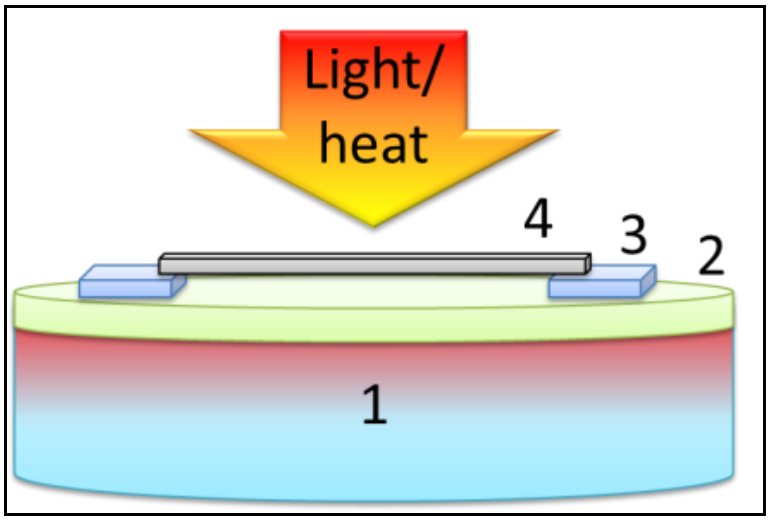

Figure 2.17: Positioning of the steel substrates on the cooling stage in the CVD chamber: (1) cooled sample stage, (2) silicon wafer, (3) silicon support pieces, (4) steel substrate

Example graphene process

The graphene deposition process involves three steps: heating, growth and cooling. The Table 2.6 shows the typical parameters used in a CVD process. The substrates are first heated for $10\,min$ under hydrogen atmosphere to a temperature up to 400 °C. After the heating period, the growth gas (for example: acetylene) is introduced into the chamber, with a consequent small increase in temperature. After the required growth time, the lamps are turned off and the acetylene valve closed. The substrates are then allowed to cool for $10\,min$ under hydrogen atmosphere, before the chamber is purged with nitrogen gas to remove any excess unbound hydrocarbon. The chamber is then vented and opened, to allow the removal of the substrates.

Table 2.6: Typical CVD Process Parameters

Process pressure	$9.6 \times 10^{-7} Torr$		
Carrier gas	H_2	Pressure	$100\ (std.cm^3)$
Process gas	C_2H_2	Pressure	$10\ (std.cm^3)$
Lamp power	$60\%\ (4.8\ kW)$		
Heating time	$10\ min$		
Growth time	$5\ min$		
Approx. cooling time	$10\ min$		

2.2.4. Electrophoretic Deposition (EPD)

Electrophoretic Deposition (EPD) is a two-step process in which charged particles in a stable colloidal suspension move towards an electrode of opposite charge under the influence of a DC electric field and then deposit to form a compact film on the electrode[75]. EPD is usually carried in a two-electrode cell as shown in Figure 2.18.

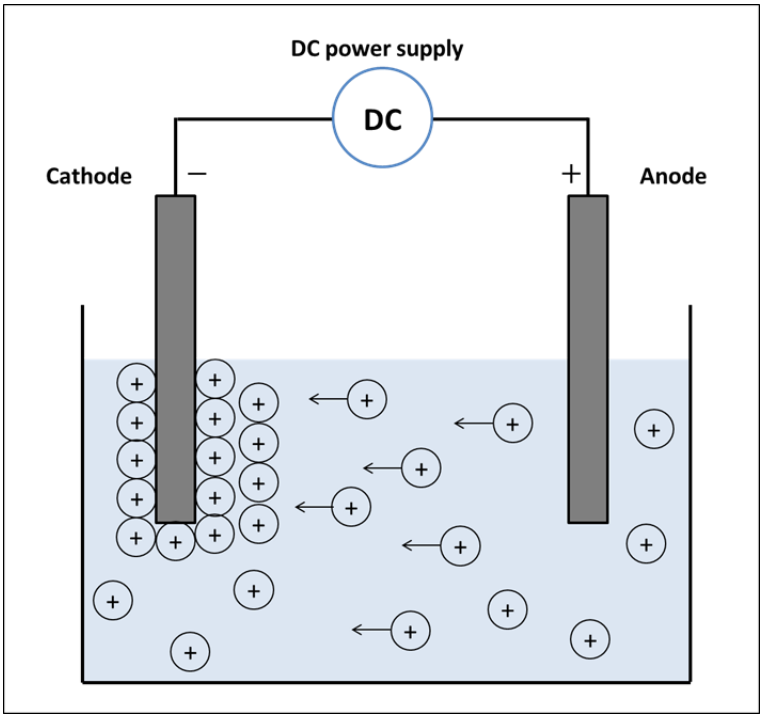

Figure 2.18: Schematic diagram of the two-electrode cell for electrophoretic deposition showing positively charged particles in suspension migrating towards the negative electrode (adapted from[75])

The mechanism of EPD can identified into two different steps; in the first step an electric field is applied between the two electrodes and causes the charged particles, suspended in the suitable liquid to move towards the oppositely charged electrode. This process is termed as electrophoresis (the movement of charged particles in the influence of an external electric field[13]). In the second step, the particles accumulate at the deposition electrode and create a relatively compact and homogeneous film. This is the deposition step. The key parameters that affect the deposition method are the requirement of a stable suspension containing charged particles that are free to move when an external electric field is applied and the particles in suspension will move only in response to the electric field if they carry a charge[75–77].

EPD can be applied to any solid that is available as a fine powder with roughly $< 30\ \mu m$ particle size or as a colloidal suspension. These can include metals, polymers, ceramics and glasses. Usually a heat treatment step is needed after the deposition to further densify the deposits and to eliminate porosity[76,77]. A suitable medium for the stable dispersion of the particles is required for EPD. Organic solvents; alcohols and ketones for example, are commonly used owing to their relatively high density, chemical stability, and low conductivity. However, these have a disadvantage as they are toxic, more costly and they are highly flammable[78]. Aqueous media provide economic and environmental advantages over the organic solvents; however, the main disadvantage is the tendency to electrolyse water at low voltages. This disadvantage can be addressed reducing the ionic conductivity of water or using AC EPD[78].

2.2.4.1. Electrophoretic Deposition of Graphene

EPD has been used as a method to produce porous pure graphene electrodes[78]. A variety of different variants of EPD have been used to form graphene deposits suitable for electrodes. These include graphene oxides (GO) deposition and later conversion to graphene sheets, direct deposition of graphene sheets, graphene sheets with different microstructures by tuning the pH, exfoliated GO reduced before deposition, GO platelets reduced by EPD conditions as well as GO layers with transition metals oxide interfaces[78].

Liu *et al.*[79] deposited graphene on indium tin oxide (ITO) electrodes for applications in supercapacitors. The authors developed a two-step process; EPD of GO and its subsequent reduction to graphene by *in situ* electrochemical reduction. A well dispersed aqueous suspensions of GO were prepared with GO acquiring a negative charge. This was then deposited on ITO electrodes using a constant voltage of $150\,V$ and a deposition time of $45\,s$. The so prepared films were electrochemically reduced to obtain graphene by using potentiostatic reduction in $0.1\,M\,KCl$ solution.

Chen *et al.*[80] deposited graphene nanosheets directly on nickel foam to form an electrode structure using EPD. The two step included preparation of graphene colloids using p-phenylene diamine in ethanol and then EPD on 3D nickel foam acting as a negative working electrode. EPD was carried out at $50\,V$, followed by annealing step at 400 °C for $3\,h$. In addition to this, Chen and co workers[81] reported a simple approach to preparing graphene with p-phenylene diamine as a reducing reagent without any other treatment. They also presented a comparison of ethanol, glycol, DMF and NMP and reported that ethanol suspensions were found to be most suitable for EPD on ITO-coated glass substrates.

2.2.5. Graphene Coated BPPs for PEMFC

The sp^2 hybrid carbon atom arrangement in graphene results in a hexagonal lattice, with each atom bonded to three other carbon atoms. This arrangement results in a very high inherent strength of $0.142\,N.m$ along the carbon bonds[82]. In a case where the graphene layer has no defects, this makes graphene the strongest material ever discovered[82]. The other remarkable characteristics of graphene include a tensile strength of $130\,GPa$, electron mobility of up to $2.5 \times 10^5\,cm^2.V^{-1}.s^{-1}$, thermal conductivity of more than $3000\,W.m.K^{-1}$, Young's modulus of $1\,TPa$ and the capability of sustaining high current densities[82,83]. In addition to these, a key characteristic of graphene in particular, which is impermeability to all gases and salts makes graphene an excellent coating candidate for anticorrosion applications.

Park and Park[84] used EPD to deposit GO on carbon steel from a GO-water suspension. The authors applied the GO coating as a barrier layer for the corrosion protection of carbon steel. The surface morphology of the EPD graphene layers was studied using SEM and Raman spectroscopy was used to study the electrochemical reduction of GO. The authors used potentiodynamic polarisation technique to evaluate the anti-corrosion performance of the graphene oxide electrophoretic deposition (GO–EPD) layer. The bare mild steel and GO–EPD-coated steel were immersed in a $3.5\%\ NaCl$ solution and then the potential was swept from $-0.5\ V\ vs\ SCE$ to $1.5\ V\ vs\ SCE$ at a scan rate of $5\ mV.s^{-1}$. The authors concluded that GO-EPD layer alone did not provide sufficient protection for the steel due to the lack of sufficient density of GO film. In addition to this, the defects on the surface acted as corrosion initiation sites and the corrosive electrolyte permeated into the GO–EPD layer. The authors used the GO–EPD film as an under-coat for the organic coating for carbon steel.

Pu *et al.*[85] studied the growth of graphene using chemical vapor deposition (CVD) on SS 304 and a nickel catalysed Ni/SS 304 stainless steel. The authors reported that a thin, multilayer graphene film could be continuously grown across the metal grain boundaries of the Ni/SS 304 and resulted in the significant enhancement of its corrosion resistance. The Ni layer was electroplated onto SS 304 samples. A quartz tube was used and Ar gas at $100\ std.cm^3$ and H_2 gas at $50\ std.cm^3$ were inlet into the tube. The temperature was raised over $30\ min$ from room temperature to the various target temperatures of 700, 800, or 900 °C. On reaching the target, methane was introduced at $25\ std.cm^3$, and on completion of reaction, methane was terminated with Ar/H_2 continued till the tube reached room temperature.

For the ICR tests, the sandwiched carbon papers/stainless steel assembly were placed between two copper plates and the operating load was in the range of $0-196\ N.cm^{-2}$ with data recorded every $9.8\ N.cm^{-2}$. Electrochemical polarisation tests were carried out using an Autolab potentiostat with $Ag/AgCl$ reference electrode and Pt counter electrode. The electrolyte used was a $3.5\ wt\%\ NaCl$ solution at ambient temperature. The authors concluded that nickel increased the rate of reaction between methane and SS 304 and the surface was completely covered by the

graphene film. Ni plating served the two functions; acted as a barrier layer to slow down the diffusion of carbon atoms and reducing the formation of metal carbides and the high catalytic activity and high carbon solubility increased the pyrolysis rate of the carbon source gas. This resulted in the formation of multiple layers of graphene covering the SS substrate completely. The corrosion performances (Figure 2.19) as well as the ICR performance of the nickel catalysed graphene coated SS 304 were enhanced by the nickel catalysed graphene coating on SS 304. The authors used ICP to analyse the metal ion concentrations in the electrolyte solutions. In case of the SS 314, the electrolyte had Fe, Cr and Ni ions at concentrations of $29,6$ and $2\,ppm$ respectively. On the other hand, the Graphene/Ni/SS304-900-4hr electrolyte had no Fe, Cr, or Ni ions using an instrument with a lower limit of detection of $0.1\,ppm$. It was evident that the graphene layer effectively reduced the concentration of dissolved metal ions protecting the membrane form ion poisoning.

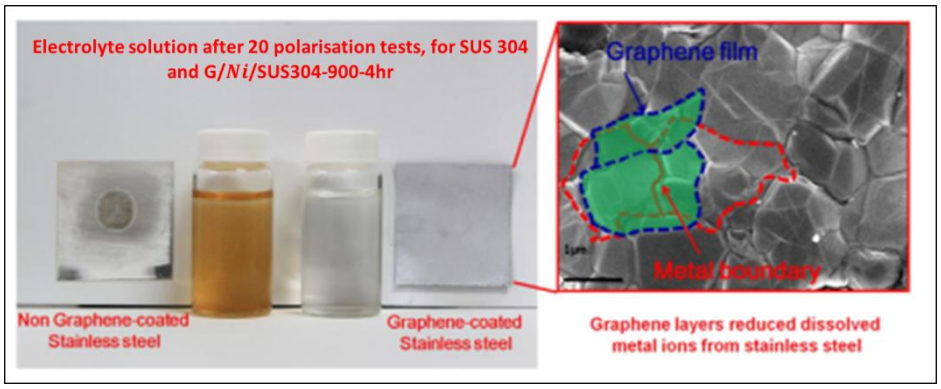

Figure 2.19: Optical images of the samples and the corrosive electrolyte; SS 304 and Graphene/Ni/SS304-900-4hr after 20 polarisation tests; (inset: an SEM image of the Graphene/Ni/SS304-900-4hr sample with the red line outlining the metal grain boundary, the blue line outlining the graphene ripples, and the green area show the metal boundaries covered with a graphene film (adapted from[85])

Taking inspiration from the work of Pu *et al.*[85], Stoot *et al.*[86] conducted a comparative corrosion study of three different samples to be used as bipolar plates in polymer electrolyte fuel cells; SS 304 (SS), Ni seeded SS (Ni/SS) and SS with Ni seed layer coated with a multi-layered graphene thin film (Graphene/Ni/SS) using CVD. Raman spectroscopy revealed minor defects in the graphene film. The authors concluded that there were

no short to medium term advantages in corrosion test by using the Graphene/Ni/SS as compared to Ni/SS samples. The authors did report the advantage of using graphene coated samples over long term tests by partial immersion in boiling seawater for three weeks. The comparison of the Raman spectra recorded before and after immersion testing (Figure 2.20) shows that the graphene coating was intact after the test in boiling simulated sea water ($3.5\ \%\ NaCl$). The ratio of the peak intensities of the D-peak to the G-peak (I_D/I_G) was 0.19 ± 0.07 before the test and 0.16 ± 0.04 after the tests. The spectra were obtained away from the edges and were averaged from different sample locations. The data plotted in Figure 2.20 shows the averaged data with standard deviation error bars represented by the thickness of the lines.

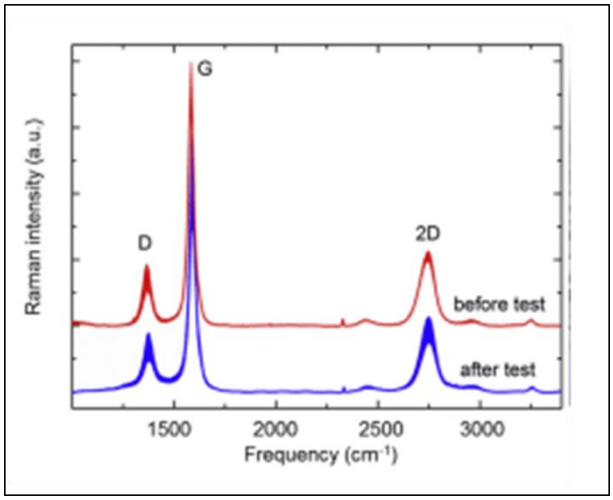

Figure 2.20: Raman spectra of the graphene-coated sample before (red curve) and after (blue curve) testing in the boiling simulated seawater (adapted from[86])

2.3. Conclusions

Fuel cells provide a promising future for cleaner and greener energy. However, there are a number of challenges regarding the initial and the running costs as well as maintaining the durability whilst achieving the highest performance. Bipolar plates are a weight determining and cost defining component of a fuel cell stack and. From the initial stages of fuel cell development, BPPs have been made up of graphite because of the low surface contact resistance and high corrosion resistance provided by

graphite. In spite of these positives, graphite is brittle and is permeable to gases and is not very effective for high volume manufacturability. Additionally, the cost of graphite increases the initial cost of manufacturing fuel cells. The brittleness and porosity of graphite leads to the BPPs being made thicker which then reduce the specific volumetric and gravimetric power density of the fuel cell stack. As the durability and the cost are the two major challenges that hinder the penetration of the fuel cell technology into the energy sector, a significant amount of attention is given to exploring different materials that would have a potential answers to the challenges posted here.

Metal BPPs may address the questions of mechanical strength, durability to shocks and vibrations, gas permeation and manufacturability and cost effectiveness, in comparison to carbon based materials, however the biggest drawback of any metal is the tendency to corrode as all metals are prone to corrosion and they are unable to provide corrosion resistance in the acidic fuel cell environment without forming a passivation layer. Metal dissolution and ion leaching result in the poisoning of the MEA and decrease the overall output of the fuel cell. The passivation layer formed will add to the contact resistance of the BPP.

SSs possess high mechanical strength, high chemical stability, low gas permeability, provide a range of alloying options and the feasibility of mass production. These characteristics make SS a popular option for use as BPPs without any coating. From the published literature, it can be concluded that austenitic and ferritic SSs are the only grades that have been employed as a BPP without any coating. SS provide good corrosion protection by the aid of the passivation layer, however, as a consequence, they do suffer with poor contact resistance. Coatings on SS surface have been used in order to overcome this.

A number of coating viabilities have been discussed in the published literature to achieve the maximum output. Titanium nitrides and chromium nitrides, and carbon based coatings are amongst the most utilised metal based coatings for BPP applications. However, as the coating process adds another step to BPP manufacturing, the overall cost increases.

Low carbon steel is low at cost, but has poor chemical properties for application as a BPP. Conventional low carbon steel has been used as base metal for BPP and for a good corrosion resistance, low carbon steel which is surface treated has been applied. However, the studies of low carbon steel or mild steel as a BPP material has been not that widely explored due to the poor corrosion resistance of these materials under fuel cell operation conditions. This provides an excellent opportunity to explore the applications of low-cost, low carbon steel as a BPP material although the corrosion resistance needs significant improvements. Surface treatments, PVD and CVD coatings, electrochemical deposition of chromium are amongst the most practical options of improving the corrosion performance of mild steel. In addition to this, carbon-based (graphene) coatings have been explored as a potential barrier coating for steel. Graphene has been deposited on various grades of stainless steel as well as mild steel using CVD and EPD methods.

Finally, the literature review provides an insight on the analysis techniques used to study the BPP candidate materials. ICR and electrochemical tests including potentiodynamic and potentiostatic corrosion tests are the primary tests conducted on any material to study the feasibility as a BPP candidate for PEMFC. *In situ* fuel cell operation is conducted on the selected BPP materials. The surface morphology of the material has been widely studied using SEM pre and post corrosion experiments and fuel cell operation. In addition to SEM, XPS is also used for surface analysis. Graphene coatings have been characterised using Raman spectroscopy, TEM and AFM.

The review of published literature lays the foundation for the corrosion analysis of different grades of steel undertaken as a part of this project. The candidate BPP materials have been tested for their ICR and corrosion performance. Post corrosion these have been analysed using SEM. For graphene coated samples, in addition to the above tests, Raman spectroscopy and AFM have been used to analyse the graphene coatings deposited on different steel substrates using two different routes; CVD and EPD. Finally, X-ray CT is used to analyse the corrosion performance of SS 316L material.

3. Electrochemistry of Corrosion

The aim of this chapter is to introduce the concept of corrosion and understand the electrochemistry behind corrosion. It is very important to understand why metals corrode and the reactions involved in different types of corrosion in order to prevent or inhibit corrosion in metals. The presence of a sulphonated membrane in the fuel cell assembly, in addition to the operating temperature of around 80 °C, makes corrosion a bigger problem in PEMFC operations. The fundamental electrochemical test methods used to analyse corrosion, including AC and DC electrochemical test methods used in the study of corrosion, are also discussed in this chapter.

3.1. Fundamentals of Corrosion

3.1.1. Introduction to Corrosion

Theoretically, corrosion can be defined as an irreversible thermodynamic reaction of a material (usually metal) with the environment which often (but not always) results in the degradation of the material or its properties[87,88]. This generic definition includes the degradation of a wide variety of materials; for example, degradation of polymers via ultraviolet radiation. Metals exist naturally, in their lowest energy state, in the form of their oxide or sulphide ores. When pure metals are extracted from these ores, the metals move to a higher energy state which consequently increases their entropy. Thermodynamically, it is the tendency of any metal to then revert to a lower energy state, reforming oxides or other complexes with lower entropy. This tendency of metals to revert to a more stable energy state is known as corrosion[88].

A recent survey published by the World Corrosion Organisation has revealed that the worldwide direct cost of corrosion was US $2.2 trillion in 2010, and the annual cost of corrosion worldwide is over 3% of the world's GDP[89]. These figures include only direct costs, i.e., materials, equipment, services, repairs, maintenance, and replacement; they do not include the

environmental damage, waste of resources, loss of production, or personal injury resulting from corrosion. Beyond the costs of corrosion lie the concerns of safety as human lives depend on safe operation of a range of metallic structures. However, corrosion experts have concluded that 20-25% of these net annual costs could be saved by applying current corrosion protection technologies; the application of which would save about US$ 660 billion worldwide[89,90].

3.1.2. Types of Corrosion

3.1.2.1. Dry or Gaseous Corrosion

In the absence of water, metals may react with surrounding oxygen or sulphurous gases to form oxides or sulphides respectively. The generalised equation for such a reaction with oxygen can be stated as follows:

$$\boldsymbol{xM + \frac{y}{2}O_2 \rightarrow M_xO_y} \qquad \textit{Equation 3.1}$$

Where: M = Metal and O = Oxygen

Most metals, on exposure to air, will form a thin oxide film of $< 100\,\text{Å}$ thickness. Further oxidation of the metal would require more energy, in the form of elevated temperature. If this occurs, it will result in the thickening of the oxide film which will typically produce a colour change as the oxide film grows and causes interference effects in light reflected from the surface. This quality can be attributed to the phase differences in the light reflected from the metal/oxide interface and from the top of the oxide film. A thickness of more than $180\,nm$, in case of iron, will result in the formation of an oxide scale, and the interferences do not appear any more[87,88].

For the further development of an oxide film, it is necessary for the oxygen to permeate or diffuse through the existing oxide film, from the atmosphere to the metal substrate, a mechanism that is not energetically favourable without the addition of external energy. This oxide film therefore plays an important role in control of the further oxidation of the metal, as a stable oxide film provides protection from further oxidation of the metal by shielding the metal from the atmosphere. In dry conditions, the nature of the oxide or sulphide film will therefore depend not only on the oxidation

rate of the metal, but also on the oxygen or sulphur content of the surrounding atmosphere and the ambient temperature.

3.1.2.2. Aqueous Corrosion

Aqueous or wet corrosion is generally more widespread and has a far more severe impact on everyday life, and includes the more commonly recognised rusting of iron and tarnishing of silver, copper, brass, and aluminium. The basic principle of wet corrosion is the same as that explained in section 3.1.2.1 where the metal tends to revert to its lower oxidation state, however, aqueous corrosion is electrochemical in nature, and the mechanism involved in the reaction is more complex. Hence, an understanding of fundamental electrochemistry is necessary to understand corrosion in aqueous media. This complex electrochemical corrosion reaction can cause uniform corrosion or lead to localised corrosion with different rates of corrosion occurring in different areas[88,90].

Hibbert[91] defines electrochemistry as the science of the interaction of phases containing electrons and ions. Metals usually corrode in an environment that can be considered as an electrolyte; the phase that conducts ions. The most common electrolyte in nature is water which is a polar molecule which can undergo self-ionisation and readily solubilises other ions. A lump of solid, containing free electrons, can be termed as the electrode; the physical location where electrochemical reactions take place. When an electrode is introduced into the electrolyte solution, this starts to cause problems for the system to reorganise itself and achieve equilibrium state. If the system then starts to swap electrons, it leads to the formation of a cell and a reaction takes place what we term as an electrochemical reaction[91].

Aqueous corrosion therefore arises in a metal (the electrode) in the presence of an electrolyte which can include atmospheric moisture, rain water, sea water, and aqueous solutions used in the industries that come into contact with metal containers and piping, etc. One or more electrolytic cells are produced for aqueous corrosion to take place. There must be a potential difference developed between the two opposing electrodes formed on the surface of the metal (or more than one metals).

A corrosion reaction is made up of an anodic oxidation reaction liberating electrons and a cathodic reduction reaction consuming electrons. An electrical circuit needs to be completed in order to facilitate the electron flow between the anode and the cathode resulting in the corrosion current. In absence of any of these factors, aqueous corrosion will not occur. The current flows through the electrolyte via ion transport. Faraday's law explains the relationship between the current density at the electrode and the flux of the reacting species:

$$\boldsymbol{j = nFJ} \qquad \textit{Equation 3.2}$$

Where J = flux of reacting species $(mol.cm^{-2}.s^{-1})$

Electrochemistry of Aqueous Corrosion

When soluble ionic compounds are immersed in water, the ionic bonds between atoms are broken and the compound is said to be ionised into positive and negative ions. If a metal is immersed in a solution containing its own ions, the metal loses electrons and enters the solution as ions, for example copper dipped in a copper sulphate solution will result in copper entering the solution.

$$\boldsymbol{Cu \rightarrow Cu^{2+} + 2e^{-}} \qquad \textit{Equation 3.3}$$

The reaction in Equation 3.3 can be defined as the oxidation of copper as the oxidation state of copper is increased from zero to positive two. At the same time, the cupric ions take up electrons to deposit copper back on copper electrode surface.

$$\boldsymbol{Cu^{2+} + 2e^{-} \rightarrow Cu} \qquad \textit{Equation 3.4}$$

In the absence of an external driving force, both the reactions are perfectly balanced and equilibrium exists between the two reactions and they are completely reversible. At this equilibrium, the potential difference is representative of the reversible potential for the electrode/electrolyte system. In order to understand this potential difference, it is important to discuss the inner potential or the Galvani potential $(\emptyset)$. The Galvani potential at a point can be defined as the work needed to bring a unit charge from infinity to that given point. This would result in two Galvani

potentials; $\emptyset_{metal}$ which is the Galvani potential for moving the charge from infinity to the metal surface and $\emptyset_{solution}$ for moving the charge from infinity to the electrolyte solution. Thus, the Galvani potential difference ($\Delta\emptyset$) would then be the difference between the two phases as shown in Equation 3.5:

$$\Delta\emptyset = \emptyset_{metal} - \emptyset_{solution} \qquad \textit{Equation 3.5}$$

Neither the Galvani potential, nor the Galvani potential difference of an electrode/electrolyte system can be measured directly. However, the difference of the two electrode/electrolyte can be measured, i.e., the difference between the two $\Delta\emptyset$. This is more generally termed as the potential difference between the two electrode systems. In practice, a fixed potential reference electrode is used to measure this potential. This is why electrode potentials are always reported versus a specific reference electrode.

The metal in the solution acquires an electrode potential arising from the activities of copper ions described in Equation 3.3 and Equation 3.4 (this is usually measured against the hydrogen electrode which is standardised at $0\,V$ at a temperature of 25 ^{o}C). In case of copper, the standard electrode potential vs the standard hydrogen electrode is $0.34\,V$ and for a zinc electrode it is $-0.76\,V$. If copper placed in a copper sulphate solution and zinc in zinc sulphate solution were to be connected electrically, a potential difference would exist between the copper and zinc electrodes. This forms the basis of a Daniel cell, or a simple battery, as shown in Figure 3.1.

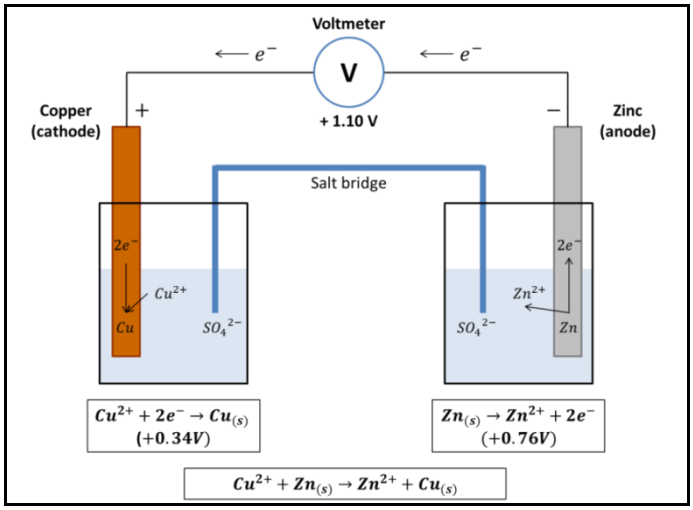

Figure 3.1 :Galvanic / Daniel Cell (adapted from[90])

The potential difference for this cell is calculated as follows:

$$+\mathbf{0.34} - (-\mathbf{0.76}) = \mathbf{1.1}\,\boldsymbol{V} \qquad \textit{Equation 3.6}$$

This difference in the potentials is strong enough to disturb the equilibrium and results in an irreversible reaction that promotes electron flow and produces electricity. Copper attains a more positive potential compared to zinc which is therefore termed noble as compared to copper. The cathodic and anodic reactions can be written as:

$$\boldsymbol{Cu^{+2}} + \mathbf{2}\boldsymbol{e^{-}} \leftrightarrow \boldsymbol{Cu}\,(\boldsymbol{Cathodic} \,/\, \boldsymbol{Reduction\ reaction}) \qquad \textit{Equation 3.7}$$

$$\boldsymbol{Zn} \leftrightarrow \boldsymbol{Zn^{+2}} + \mathbf{2}\boldsymbol{e^{-}}(\boldsymbol{Anodic} \,/\, \boldsymbol{Oxidation\ reaction}) \qquad \textit{Equation 3.8}$$

As the potential difference is high, zinc dissolves, or corrodes, releasing zinc ions. This is termed as galvanic corrosion where the zinc sacrifices itself to protect a more noble metal depending on the electromotive force or the EMF series. A common example of this is corrosion in zinc/copper alloys (i.e. brass) where the zinc corrodes preferentially leaving behind a porous residue of copper and corrosion products. Another example is galvanised steel, where the steel is coated with zinc by dipping in a zinc solution. In this case also, zinc protects the underlying steel.

3.1.2.3. Uniform Corrosion of Single Metal

Uniform (or homogeneous) corrosion is a type of aqueous corrosion that results in an even metal dissolution rate over the entire metal surface exposed to the corrosive environment. If no localised corrosion happens throughout the surface of the metal, the lifetime of the metal can be calculated on the basis of the reaction kinetics. This can be regarded as the most wide-spread form of metallic corrosion and an electrolytic cell containing an anode and a cathode is formed; a potential difference again exists between the electrodes and drives the corrosion reaction. However, as discussed in section 3.1.2.2, if a potential difference does not develop the electrochemical corrosion reaction will not proceed.

To reiterate, most metals, when exposed to air, rapidly form an oxide layer. This oxide layer provides a level of corrosion protection to the metal in an aqueous environment by isolating the metal from the surrounding environment, acting as a barrier to the diffusion of metal ions and the transfer of electrons between the metal and the aqueous electrolyte, hence the rate of corrosion reaction is reduced. Titanium, aluminium and stainless steel form very stable oxide layers which provide a significant amount of corrosion protection as compared to mild steel for example. However any discontinuities or holes in the oxide layer, or differences in the layer thickness, can lead to the exposure of the underlying metal to the environment and subsequently corrosion will occur at those sites.

Corrosion of Iron

A number of non-reversible reactions may take place at the same electrode during homogeneous corrosion, which leads to a uniform reduction in the thickness of the metal; for example iron. This is usually the case when no corrosion products are formed on the metal surface. In acid solutions where hydrogen ions, or protons, are abundantly available, the metal is oxidised and the hydrogen ions in the water are reduced to form hydrogen gas:

$$\boldsymbol{Fe \rightarrow Fe^{+2} + 2e^{-}} \qquad \textit{Equation 3.9}$$

$$\boldsymbol{2H^{+} + 2e^{-} \rightarrow H_2 \uparrow} \qquad \textit{Equation 3.10}$$

Corrosion rates fall as the acidity decreases and the solution achieves neutrality. Alternatively however, the rate of corrosion may rise again in the presence of an alkaline solution due to the formation of metal complexes[88].

Oxygen reduction often plays a key role in the corrosion reaction, especially in neutral and alkaline electrolytes. The electrode reactions depicted in Figure 3.2 explain the dissolution of iron at anodic regions formed within the metal in a neutral or alkaline environment. The formation of the hydroxyl ions as result of the oxygen reduction reaction is the preferred cathodic reaction in these environments and subsequent reactions between the ferrous and hydroxyl ions results in the formation of ferrous hydroxide ($Fe(OH)_2$) that is later converted to ferric hydroxide ($Fe(OH)_3$), more commonly known as ‘rust’, by reacting with oxygen.

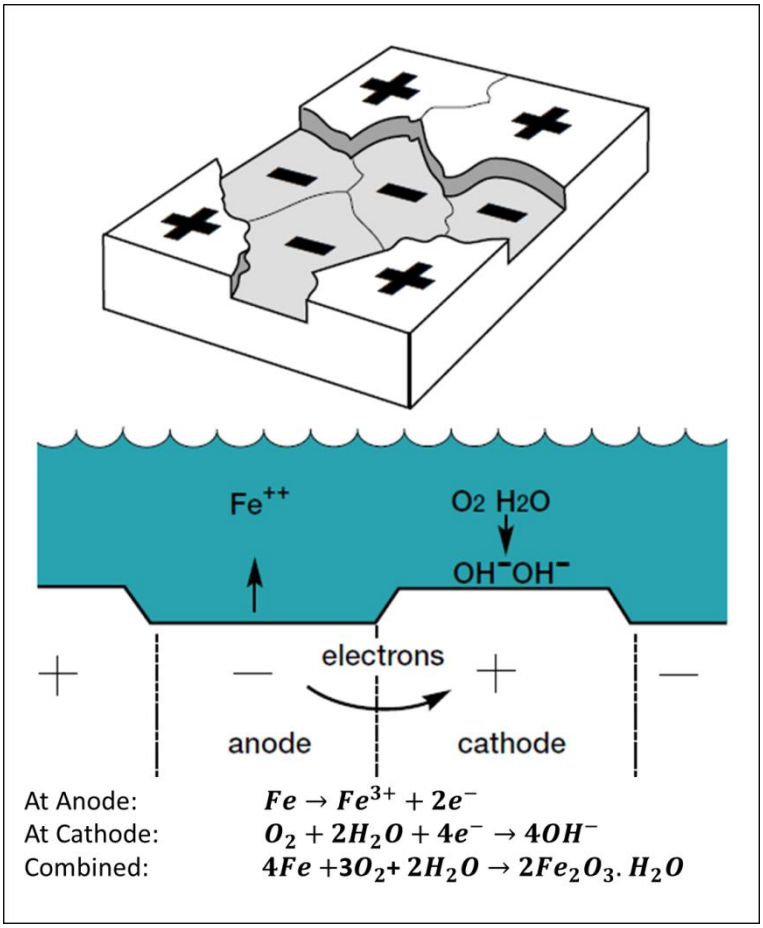

Figure 3.2: Schematic representation of a corrosion reaction (adapted from[88])

In order to understand the electrochemistry behind the corrosion of iron, it is important to understand the phases of iron in a given potential-pH environment. As shown in Figure 3.3, the potential–pH diagram[92] of iron depicts that iron is thermodynamically stable at lower potentials. As the potential rises in alkaline environments, dissolution of iron to Fe^{2+} takes place and at even higher potential, Fe^{3+} can be produced. At higher pH, iron oxides such as F_3O_4 and F_2O_3 are formed. At pH greater than 14, solid iron dissolves to form $HFeO_2^-$.

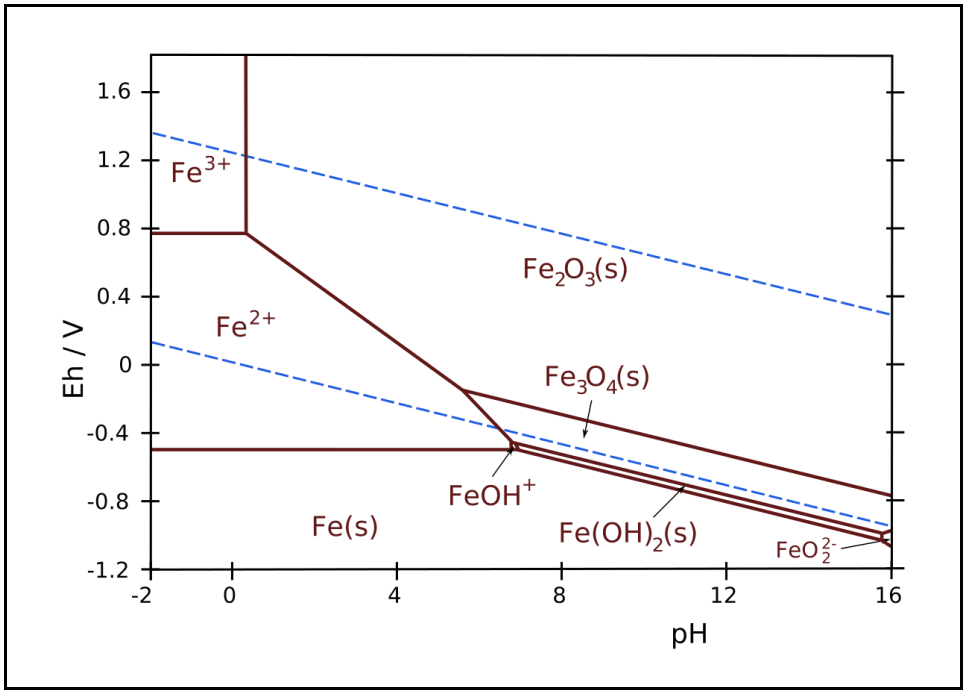

Figure 3.3: Potential-pH diagram of iron (adapted from[92])

Even in acidic solutions OH^- ions are present on the surface of the metal electrode[90] as an adsorbed species according to Equation 3.11:

$$\boldsymbol{H_2O \rightarrow OH^-_{(ad)} + H^+} \qquad \textit{Equation 3.11}$$

Iron then reacts with these adsorbed hydroxyl ions, releases an electron and forms an intermediate species according to Equation 3.12:

$$\boldsymbol{Fe + OH^-_{(ad)} \rightarrow FeOH_{(ad)} + e^-} \qquad \textit{Equation 3.12}$$

These intermediate species then catalyse the charge transfer reaction:

$$\boldsymbol{Fe + OH^-_{(ad)} + FeOH_{(ad)} \rightarrow Fe(OH)^+ + FeOH_{(ad)} + 2e^-} \qquad \textit{Equation 3.13}$$

In acidic media, the $Fe(OH)^+$ ion is unstable and liberates Fe^{2+}ions:

$$\boldsymbol{Fe(OH)^+ + H^+ \rightarrow Fe^{2+} + H_2O} \qquad \textit{Equation 3.14}$$

According to the mechanism described by Bockris *et al.* [93], $FeOH$ is an intermediate product as opposed to an adsorbed species as explained in Equation 3.15 - Equation 3.17:

$$Fe + OH^- \rightarrow FeOH + e^- \qquad \textit{Equation 3.15}$$

$$FeOH \rightarrow FeOH^+ + e^- \qquad \textit{Equation 3.16}$$

$$FeOH^+ \rightarrow Fe^{2+} + OH^- \qquad \textit{Equation 3.17}$$

However, Bockris *et al.* [93] have also suggested the mechanism through OH^- adsorption.

Corrosion of Stainless Steel

Stainless steels can be defined as iron-based alloys with chromium being the main alloying element. For the formation of the characteristic passive layer, at least $10.5\%\, Cr$ is necessary. Different types of stainless steels include ferritic stainless steel, austenitic stainless steel, martensitic stainless steel and duplex stainless steels, which can be distinguished by their crystallographic structures. Ferritic and martensitic stainless steels have less nickel ($< 2\ \%$) and higher carbon content, and can be hardened via heat treatment. Austenitic stainless steels have $18\%\, Cr$ and $8\%\, Ni$, while the duplex stainless steels have the highest chromium content (up to 32%). The corrosion rates for these stainless steels are mainly influenced by the formation of carbides[88,90,94].

The corrosion behaviour of stainless steel in sulphuric acid is dependent on the reducing and oxidising capabilities of the sulphuric acid itself. Sulphuric acid is a reducing agent at concentrations roughly $0 - 65\%$, for all temperatures. At lower temperatures, it is reducing at concentrations up to 85%. At concentrations greater than 85%, it changes to an oxidising agent. Austenitic stainless steel is not very resistant to sulphuric acid and is susceptible to pitting corrosion in presence of chlorides (and the halides in general). The addition of alloying elements can lead to an increase in the corrosion resistance of the steel but it is still a very limited increase. An increase in the nickel content however has shown a beneficial effect and leads to a greater corrosion resistance[90].

3.1.2.4. Non-Uniform or Localised Corrosion

The corrosion reactions discussed in the previous sections have been explained assuming that the corrosion reaction occurs uniformly over the

surface of the metal. This may be applied to the general dissolution of metals in an acid solution, or the everyday example of rusting of iron. However, in practice, this is typically not the case and instead of being uniform, corrosion is concentrated at specific points with the remainder of the metal being unaffected. A number of types of non-uniform corrosion occur which are explained with reference to iron and steel in the following sections.

Differential Aeration Corrosion

As the name implies, differential aeration corrosion[88,90] occurs due to differences in the oxygen available in areas adjacent to the corrosion sites. Electrochemically, the area that is depleted in oxygen is unable to maintain the normal cathodic reaction of hydroxyl formation. As a result of this, it becomes anodic with respect to the area with a sufficient supply of oxygen. This results in the dissolution of the anodic region.

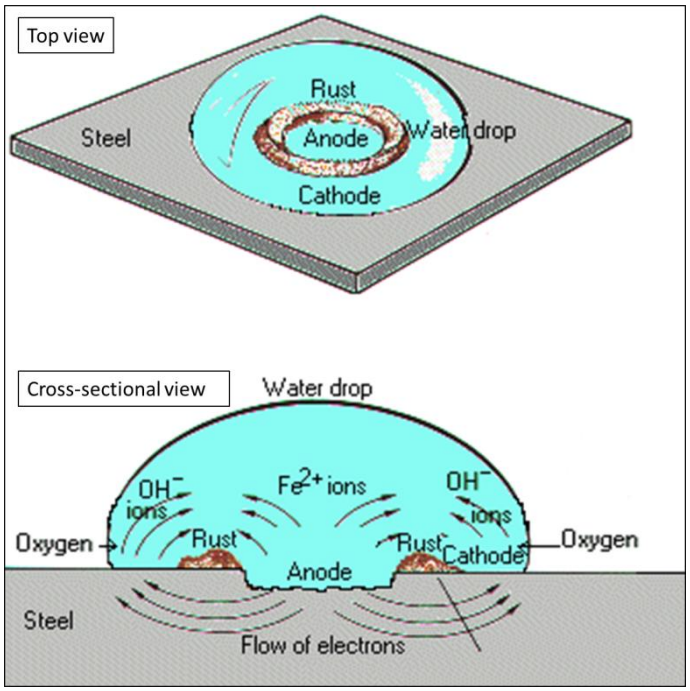

Figure 3.4: Differential aeration corrosion of steel under a droplet of water (adapted from[95])

Figure 3.4 represents the corrosion of iron under a droplet of water. The metal surface has a plentiful supply of oxygen at the edge of the water droplet; the centre of the droplet however is oxygen depleted due to the presence of the water and becomes anodic, leading to corrosion. An

example of differential aeration corrosion would be corrosion resulting from different conditions under soil. Clay, alluvial soil, sand, etc. have different densities and hence the amount of oxygen available in the proximity of these soils is different, resulting in corrosion.

Crevice Corrosion

Crevice corrosion[88,90,94] is essentially a consequence of differential aeration corrosion and is characteristic of metals that form protective passive films such as stainless steel, aluminium, titanium, etc. It arises in deep fissures and is often associated with two different materials in contact with each other such as flanges or washers. The inability of oxygen to diffuse through to the inner recesses of a crevice makes these areas anodic and leads to metal dissolution. Typically, the average separation between the two surfaces within a crevice is between 0.1 and $100\ \mu m$ and, in certain metal-environment combinations, this geometry can lead to accelerated attack on the surface of the metal. A notable point is that crevice corrosion is dependent on the different oxygen concentrations on the inside and outside of the crevice; it cannot be initiated in de-aerated solutions, where oxidising agents are low in concentration, or if electrolyte is excluded from this region completely. There are number of examples of crevice corrosion in everyday life, including flanges on pipes, integrated circuit interconnects, etc. Figure 3.5 shows one such typical example of crevice corrosion under a SS 316L bolt.

Figure 3.5: Crevice corrosion under a Type 316 bolt (adapted from[94])

Pitting Corrosion

Pitting corrosion[88,90,94,96] is characteristic in metals that contain a passive oxide film, which is the case of stainless steel. Pitting corrosion occurs as a result of the localised breakdown of the passive film, often through attack by halide ions (chlorides or fluorides). As the pit develops, the concentration of the chloride ions increases, the localised pH decreases and the environment becomes more corrosive. As a result of this, the tendency of the pit is not to spread over the surface but to penetrate deep in to the metal. This can be very damaging, especially in cases where metal is used for fluid containment. Pitting corrosion will not occur if there is no localised breakdown in the passive film or in a case where the oxide film is completely destroyed. Figure 3.6 shows the breaking of the passive film and the formation of the pit. This is one of the most destructive types of corrosion as it is very difficult to estimate the intensity of corrosion from visual inspection of the surface. The pits penetrate deep within the surface and often lead to complete destruction of the structures without any significant signs of corrosion on the surface of the metal.

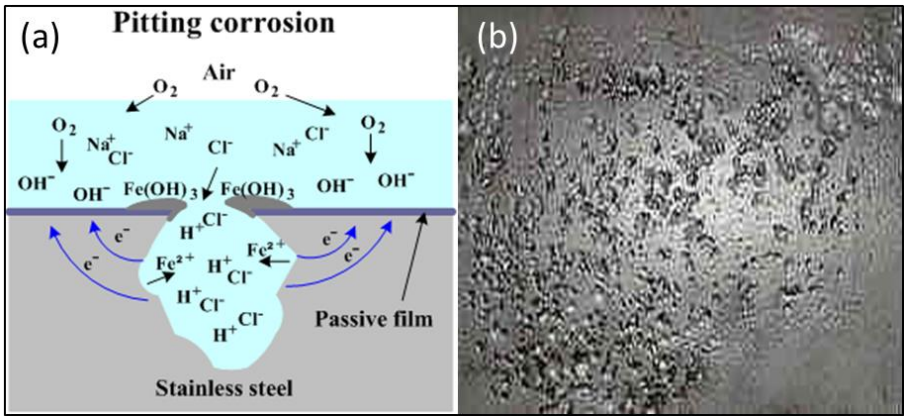

Figure 3.6: (a) Pitting corrosion reaction on breaching the passive layer on a stainless steel sample and (b) an example of pitting corrosion (adapted from[96])

Inter-Granular Corrosion

A characteristic corrosion type for alloys is inter-granular corrosion[88,90]. As the name implies, it occurs in polycrystalline materials at the grain boundaries in metals and alloys. Carbides may be precipitated at the grain boundaries as a result of heat treatment, welding or thermal cycles. In case

of stainless steel, these are principally chromium carbides. This results in the depletion of chromium content in the adjacent areas. These areas become less noble and anodic in nature leading to the development of a potential difference leading to inter-granular corrosion. Modern steel making, however, has minimised this type of corrosion by producing low carbon alloys which subsequently prevent carbide formation.

Stress Corrosion Cracking

Stress corrosion cracking[88] is a conjoint action of stress corrosion and tensile stress, which does not occur in the absence of either condition, and which affects most of the alloys, such as stainless steel, aluminium alloy, brass, etc. The stress corrosion cracking mechanism is initiated by localised corrosion, which then propagates trans-granularly by stress concentration and leads to the formation of the crack. This causes an increase in the local energy that in turn drives the corrosion reaction further. The inherent nature of stress corrosion cracking makes this type of corrosion very dangerous as often very little sign of corrosion is evident but the loss of mechanical strength associated with the network of fine cracks can result in a catastrophic failure.

Atmospheric Corrosion

In clean, dry and pollution free air, the corrosion rate is negligible. However, factors such as moisture, pollutants, air-borne solid particles, temperature, air salinity, etc. affect the rate of corrosion intensely. The rate of corrosion depends on the environment in which the metal is situate, whether it be a rural or urban area, in the vicinity of industrial sites and the nature of those industries. A marine or coastal environment and areas with high humidity and rain can also affect corrosion. High temperature corrosion, molten salt induced corrosion of metals, corrosion in presence of sweet (natural) or sour (hydrogen sulphide rich) gases, stray current corrosion and microbiologically influenced corrosion are some other types of corrosion that are specific to the environment in which the material is exposed to and is often restricted to the presence of key features that are characteristic of these environments[90].

3.1.3. Summary

In this section, the principles involved in the corrosion of metals and the different types of corrosion are discussed. The damage occurring due to corrosion can be severe and have a significant economic impact, however, there are a number of ways to protect the metal from corrosion and reduce adverse effects. The corrosion reaction does not proceed without oxygen and hence corrosion can be controlled by limiting the amount of oxygen available to the metal. This, however, is extremely difficult to achieve given the abundance of oxygen in the atmosphere and hence other methods have been developed, including alloying of the steel during manufacturing, by adding chromium, nickel, molybdenum, manganese, vanadium, etc., and reducing the carbon content. Apart from modifying the chemical composition of steel, the most important method of corrosion protection is by applying coatings on top of the steel substrate. Plating with zinc (galvanising), chromium, and nickel can help by incorporating cathodic and anodic corrosion protection. Phosphates and other inorganic coatings have also been explored, in addition to other organic coatings (such as paints). The most important types of coatings for protecting bipolar plates from corrosion have been discussed in detail in chapter 2.

The corrosion of bipolar plates is a significant concern in terms of the performance of BPPs and hence the overall performance of the fuel cell. As discussed in chapter 2, BPPs contribute significantly towards the weight and cost of a fuel cell. Corrosion of BPPs, or even the formation of a protective oxide film on the surface of the BPP, results in an increase in the interfacial contact resistance of the BPP material and hence a reduction in the overall output of the fuel cell. In order to maximise the fuel cell output and successively improve the performance of BPPs, it is of utmost importance to understand the corrosion phenomenon that occurs at the BPP surface within the fuel cell.

The most important form of corrosion that affects BPPs is the formation of an oxide layer on the surface of the steel. This hinders the conductivity of electrons and hence reduces the overall output of the fuel cell. With long term fuel cell operation, the standby potential of the fuel cell is $0.1\,V$ vs RHE (reversible hydrogen electrode) on the anode and $0.8\,V$ vs RHE on the

cathode. On the anode side, the standby potential falls within the active dissolution potential range for steel and hence results in the corrosion of the BPP on the anode side. Another important point is the presence of fluoride ions in the membrane electrode assembly. The fluoride ions can attack the protective passive layer on the steel and can initiate pitting corrosion. Pitting corrosion is detrimental as, once the oxide film is broken, further corrosion occurs at an accelerated rate.

3.2. AC/DC Electrochemical Test Methods

A basic understanding of the electrochemical phenomena behind the corrosion process provides a foundation for the experimental techniques used in corrosion analysis. Traditional methods of measuring corrosion include examining weight loss or visible appearance at the end of an exposure test in a corrosive electrolyte. However, from an engineering point of view, the time frame for exposure tests is often too long for a timely decision on the design. In contrast to this, electrochemical techniques allow for quick and highly sensitive measurements in a matter of minutes or hours by measuring a very small current using modern electrochemical instruments; the only means of achieving 'real time' corrosion rate measurements. Electrochemical test methods are particularly powerful when combined with other surface test methods such as SEM to study surface degradation as a result of corrosion[90,97]. Electrochemical test methods can be separated into two categories; AC (alternating current) and DC (direct current) electrochemical test methods. These are described independently in sections 3.2.1 and 3.2.2, respectively.

3.2.1. AC Methods: Electrochemical Impedance Spectroscopy (EIS)

The voltage loss occurring as a result of the fuel cell irreversibility was discussed in section 1.3.3. This emphasises the requirement of understanding the irreversibilities and studying them using electrochemical methods. Electrochemical impedance spectroscopy (EIS) can be used to study the electrode surface and the reactions occurring at the surface. For example; a charge double layer forms at the surface of the fuel cell

electrode because of the reactions between the electrons in the electrodes and the ions in the electrolyte and also as a result of the applied voltage. The understanding of the charge double layer would provide an explanation of why activation overvoltage occurs in fuel cell systems. The charge double layer can be characterised using EIS, the use of EIS in fuel cell characterisation will be explained in detail in this section.

When a cell is electrically stimulated, a number of fundamental processes occur at a microscopic level. Collectively these processes lead to what is termed as the overall electrical response of the system. These microscopic processes include: charge transfer or transport of electrons through the electrodes and the electronic conductors within the system; the transfer of electrons at the electrode-electrolyte interface, to and from the charged or uncharged ionic species or atomic species which are originating from the electrodes or the bulk electrolyte (in other words the oxidation or reduction reactions); and the flow of charged species or the agglomerates of those species under the influence of electron deficiency. The movement of these charged particles depends on the Ohmic resistance of the electrodes, the electrolyte and the rate of reaction at the electrode-electrolyte interface. The influence of a local electric field and the surface roughness of the electrodes also affect these rates[98].

The most common method of measuring the impedance of these reactions is by applying a single frequency voltage, or current, to the interface and to measure the responding current, or voltage, respectively. Electrochemical impedance spectroscopy (EIS) is an electrochemical method that studies the current-voltage ratio by applying very small voltage oscillations over a range of frequencies and reading the resultant oscillating current. The resultant sinusoidal current is obtained in response to the applied sinusoidal voltage with a different phase and magnitude, depending on the applied frequency. The impedance can be measured as a function of frequency in the frequency range of $< 1\ mHz$ to $> 1\ MHz$.

The intrinsic properties that influence the conductivity of the electrode and the electrode material system, or an external stimulating factor affecting the conductivity of the system can be studied using EIS. The resultant parameters obtained from the impedance spectrum give information regarding the material itself, such as conductivity, dielectric constant,

mobility of charges, equilibrium concentrations of the charged species, and the bulk generation-recombination rates. Other information that can be derived is related to the electrode interface, such as adsorption reaction rate constants, capacitance of the interface region, and the diffusion coefficient of neutral species in the electrode material itself.

A sinusoidal voltage signal is applied to the cell.

$$\boldsymbol{V(t) = V_m sin(\omega t)} \qquad \textit{Equation 3.18}$$

Where: $V(t)$ = Instantaneous voltage (V) at time t, V_m = Maximum or peak value of voltage (V), $\omega = (2\pi\vartheta)$ = Angular frequency $(radians)$.

The resultant steady state current is measured which can be described as:

$$\boldsymbol{j(t) = j_m \sin(\omega t + \theta)} \qquad \textit{Equation 3.19}$$

Where: $j(t)$ = Instantaneous current response, j_m = Maximum or peak value of current (A), θ = Phase difference.

The phase difference θ between the voltage and the current is zero in the case of purely resistive behavior. The overall relation between the system particle properties and the response thereof to the periodic sinusoidal voltage or current excitation is extremely complex within the time domain. Hence, a solution of a system of differential equations is needed to understand the complex response. The responses of the capacitive and the inductive elements are given as:

$$\boldsymbol{j(t) = [(dV(t)) \,/\, dt]\ C} \qquad \textit{Equation 3.20}$$

$$\boldsymbol{V(t) = [(dj(t)) \,/\, dt]\ L} \qquad \textit{Equation 3.21}$$

Where: C = capacitance (the ability of a component to store electrical charge) and L = Inductance (the ability of a component to induce an electromotive force as a result of a current passing through it).

The combination of these and other factors result in a complex problem. The complex mathematical treatment of this system is significantly simplified by the use of Fourier transformation. In the frequency domain,

the voltage/current relation can be rearranged similar to that of the Ohm's law for DC current:

$$\boldsymbol{j(i\omega) = V(i\omega)/Z(i\omega)} \qquad \textit{Equation 3.22}$$

The complex quantity $Z(i\omega)$ is defined as the 'impedance function' and its value at a specific frequency is then the impedance of the electric circuit at that frequency. For simplicity, $Z(i\omega)$ is written as $Z(\omega)$ and the capacitance complex of $Z(\omega)$ is defined as $1/C.\omega.i.$ and the inductance complex is defined as $L.\omega.i.$

As compared to resistance, impedance is a more generalized concept as it takes into consideration the phase differences. The magnitude and direction of the planar vector (in a right hand orthogonal axes system) can be expressed by the complex number $Z = a + ib$; where i represents the imaginary number of the complex number and the value of $i \equiv \sqrt{-1}$ or $i^2 \equiv -1$. Therefore, the real part of Z, a, is in the direction of the real X- axis and the imaginary part b is along the Y- axis. Hence, impedance is a vector quantity that may be plotted in the plane with rectangular or polar coordinates as depicted in Figure 3.7.

The value of the impedance is:

$$\boldsymbol{Z(\omega) = Z' + iZ''} \qquad \textit{Equation 3.23}$$

and the two rectangular coordinates are:

$$\boldsymbol{Re\ (Z) \equiv Z' = |Z|cos(\theta)} \qquad \textit{Equation 3.24}$$

$$\boldsymbol{Im\ (Z) \equiv Z'' = |Z|sin(\theta)} \qquad \textit{Equation 3.25}$$

The phase angle can be defined as $\theta = tan^{-1}\left({}^{Z''}/_{Z'}\right)$ and the absolute value can be defined as $|Z| = [(Z')^2 + (Z'')^2]^{1/2}$.

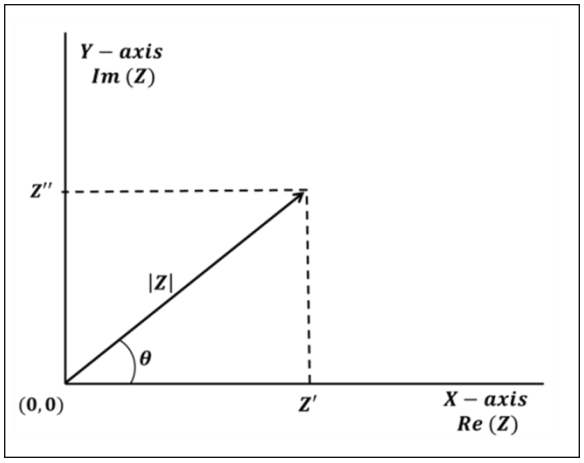

Figure 3.7: The impedance Z plotted as a planar vector using polar coordinates[98]

3.2.1.1. Simple Circuit presentations[98,99]

It is understood that impedance is represented as a complex number. Hence, the data representation in EIS is of utmost importance. As discussed, if the real part is plotted on the X-axis and the imaginary part is plotted on the Y-axis of a chart, the resultant representation is a 'Nyquist Plot'. It is to be noticed that in a Nyquist plot, the Y-axis is negative and that each point on the Nyquist Plot is the impedance at a particular frequency. On the Nyquist Plot the impedance can be represented as a vector of length $|Z|$ and the angle between this vector and the X-axis is the 'phase angle'. A representative circuit is then fitted to the experimental data to obtain the impedance for the respective circuit components. A few simple circuit presentations are described in this section:

Resistance and Capacitor in Series

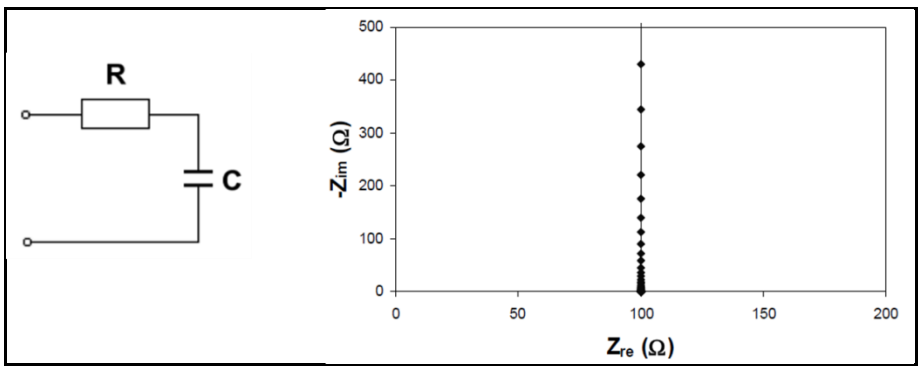

Figure 3.8: A resistor in series with a capacitor (adapted from[98,99]*)*

The impedance plot given for the circuit in Figure 3.8 is produced with a resistance of $100\,\Omega$ in series with capacitor. At high frequencies the capacitor acts as an ideal capacitor with zero resistance, and hence the high frequency intercept represents the circuit resistance alone. As the frequency moves towards lower values, the capacitor introduces resistance on the imaginary axis.

Resistance and Capacitor in Parallel

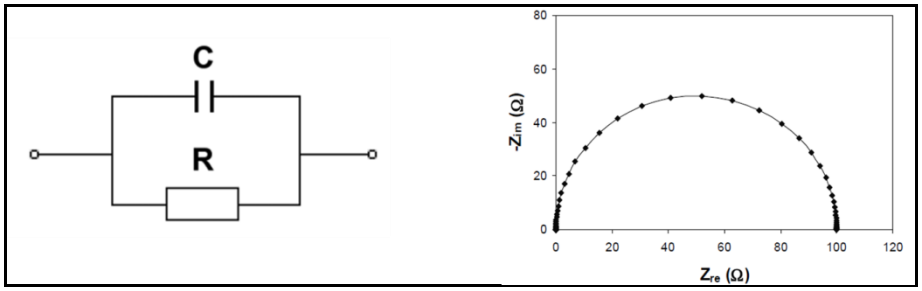

Figure 3.9: A resistor in parallel with a capacitor (adapted from[98,99])

The impedance plot for the circuit in Figure 3.9 is produced using a resistance of $100\,\Omega$ in parallel with capacitor. This results in a perfect semi-circular plot with a diameter which is equivalent to the electrical resistance of the circuit. The characteristic frequency of the process is given by the maximum value of Z'' on the imaginary axis.

Resistance and Constant Phase Element (CPE) in Series

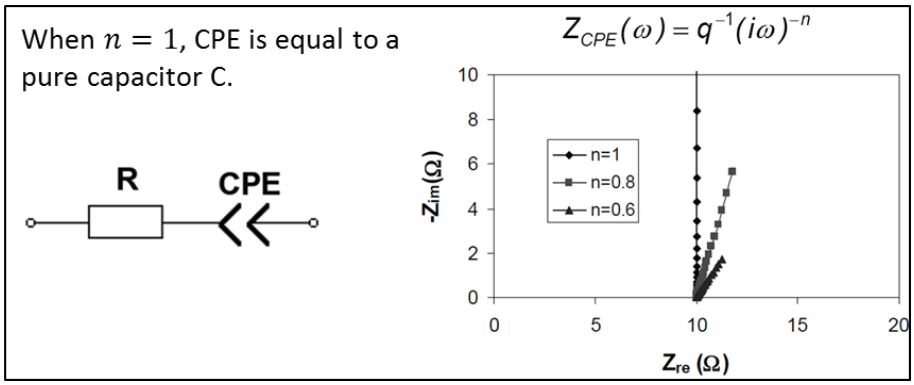

Figure 3.10: A resistor in series with a constant phase element (adapted from[98,99])

A pure capacitor exists only in an ideal situation and can only be represented if the electrode is perfectly smooth. In the real world, the

capacitor is represented by a "constant phase element" (CPE) that takes into consideration the roughness of the electrode. Figure 3.10 shows that, when the ideal situation exists, $n = 1$ and the CPE is represented as a pure capacitor.

Resistance and Constant Phase Element (CPE) in Parallel

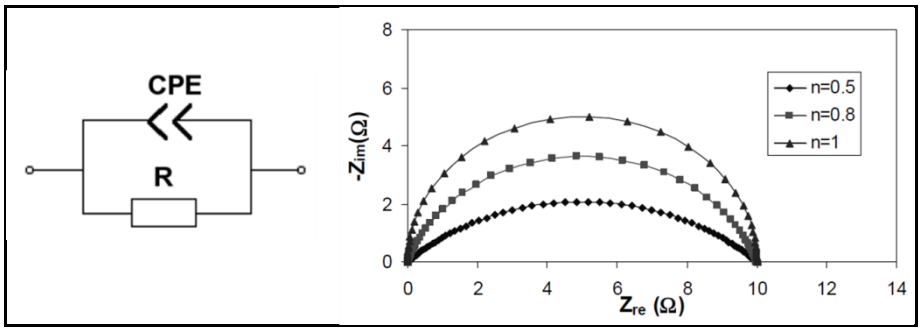

Figure 3.11: A resistor in parallel with a constant phase element (adapted from[98,99])

When a resistor and the CPE are connected parallel to each other, a depressed semi-circle is seen in the impedance plot (Figure 3.11). This can be attributed to the roughness of the electrode and hence to the CPE of the electrode. The lower the value of n, the more depressed the semi-circle.

Resistance along with Warburg Impedance

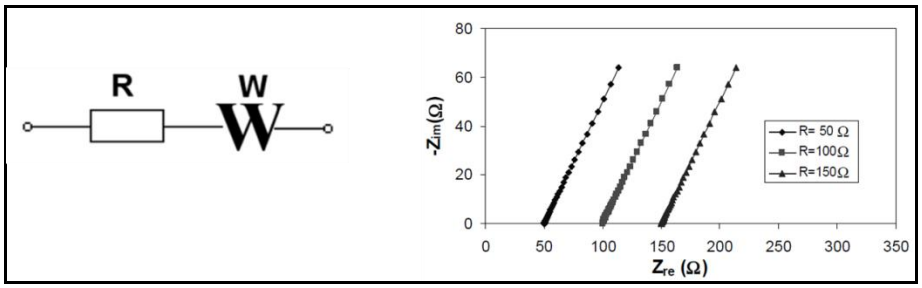

Figure 3.12: A resistor in series with Warburg impedance (adapted from[98,99])

Diffusion within the electrode can create a Warburg element within the circuit (Figure 3.12). A Warburg impedance element can sometimes be difficult to recognize as it is always associated with a charge-transfer resistance and a double layer capacitance. The Warburg diffusion element is a CPE with a constant phase of 45°, which is independent of the

frequency. At higher frequencies the Warburg element is very small as the reactants don't have very far to move to. However, at a low frequency the reactants have to move further and subsequently the Warburg impedance increases.

Resistance and Bounded Warburg Impedance

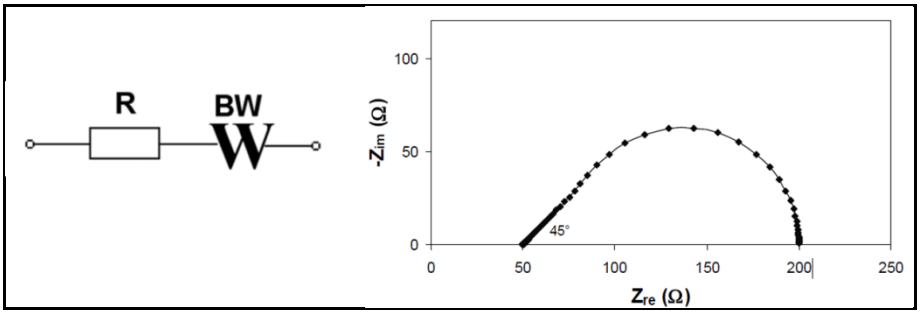

Figure 3.13: A resistor in series with bounded Warburg impedance (adapted from[98,99])

A Warburg impedance concept is only valid when the diffusion layer between the electrode and the electrolyte is assumed to have an infinitely large thickness. In the case where the diffusion layer is bounded, the impedance, at a lower frequency does not obey the simple Warburg element (Figure 3.13). At high frequency the curve shows elements of likes the Warburg impedance and at lower frequencies it looks like a resistor and capacitor (RC) circuit in parallel.

3.2.1.2. Fuel Cell Applications of EIS

The overall performance of a fuel cell depends on the electrolyte, the electrode and the electrolyte/electrode interface, as well as the construction components such as gas supplies and electrical connections. In order to characterise the performance of a fuel cell, the steady state current/potential curve is used, and in this case EIS is a helpful technique in characterising the overall performance of a fuel cell. EIS is used to study the double layer capacitance, reactivity and the structure of the interface, as well as the electrochemical reactions and the mass transport limitations. Importantly, EIS allows remote data collection without any external interference. The cell can be working at the required potential and an AC signal can be used to investigate the system parameters. The limiting

processes can be determined which in turn determines the overall fuel cell performance[100]. In its simplest form for corrosion analysis of steel, the representative circuits are usually defined using a resistor and a capacitor, or a constant phase element as represented here:

A Resistor in Series with A Resistor and Capacitor in Parallel to Each Other $\boldsymbol{R(RC)}$

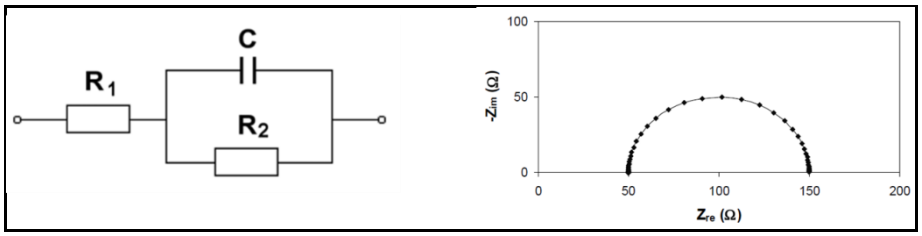

Figure 3.14: A resistor in series with a resistor and capacitor in parallel to each other (adapted from[98,99])

In the case of a resistor in series with a RC circuit (Figure 3.14), the pure resistance, R_1, represents the resistance of the electrolyte and the RC represents the electrode interface.

A Resistor in Series with A Resistor and CPE in Parallel to Each Other $\boldsymbol{R(RCPE)}$

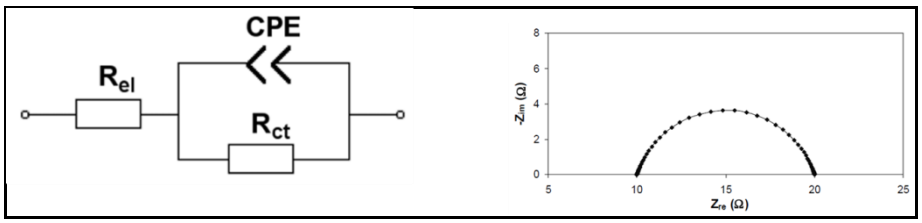

Figure 3.15: A resistor in series with a resistor and constant phase element in parallel to each other (adapted from[98,99])

In the case of a resistor in series with a CPE/resistor circuit in parallel (Figure 3.15), the resistor R_{el} represents the electrode resistance, R_{ct} represents the charge transfer resistance and the CPE represents the double layer capacitance.

3.2.2. DC Methods: Potentiodynamic Polarisation Technique

Corrosion rate measurements using DC methods usually involve applying a small amplitude DC current, or voltage, to the corroding metal and recording the resulting voltage, or current, respectively. From Ohm's law, the change in voltage divided by the change in current yields the resistance, which in this case is more commonly known as the polarisation resistance. This is inversely proportional to the corrosion current and, with a known electrode area, current density can be calculated. Using Faraday's law, the corrosion rate can be calculated in the desired units using appropriate constants[97,101].

To examine the corrosion properties of a material, the first thing to determine is the passivating nature of the material or the presence of uniform corrosion in the given environment. If the metal is undergoing active corrosion, then the rate of corrosion needs to be measured, and a conclusion needs to be reached as to whether the thickness of the material is sufficient to survive the expected lifetime. The rate of corrosion (r), or corrosion rate (CR), is the unit of thickness loss per unit time, and is related to the corrosion current density by Faraday's law:

$$\boldsymbol{r = C\left(\frac{M}{\rho n F}\right) i_{corr}} \qquad \textit{Equation 3.26}$$

where: $(r) =$ rate of corrosion (usually $mm.year^{-1}$), $M =$ Molecular weight of the corroding metal $(g.mol^{-1})$, $\rho =$ Density of metal $(g.cm^{-3})$, $C =$ constant to alter unit of thickness and time to yield results in mm per year, and $i_{corr} =$ Corrosion current density$A.cm^{-2}$.

The rate of corrosion obtained using polarisation electrochemistry is an instantaneous rate. The rate changes as the surface of the samples changes over a period of time. Hence, it can be said that the corrosion rate is a function of time. Long-term exposure tests give an average rate of corrosion over the total exposure time.

The rate of corrosion is calculated assuming that the metal is corroding actively and the corrosion over the total surface of the metal is uniform. If the metal is known to form a passive film in the given environment, it

becomes extremely important to know if the metal is prone to localised corrosion. In terms of predicting the life time of a material, the material loss by uniform passive dissolution is typically small enough to be ignored. However, in the case of a metal-environment system that is susceptible to localised corrosion, the prediction of lifetime of the metal becomes very difficult. Once localised corrosion initiates, the degradation of material thereafter is usually very rapid. Localised corrosion propagation rates typically are not constant with time; rather they tend to change with time.

Potentiodynamic polarisation tests (also known as linear sweep voltammetry - LSV) allow the user to measure the polarisation behaviour of the metal by sweeping the potential while measuring the current response. The potential is usually swept in the positive direction (negative to positive) and it is very important to determine the correct potential sweep rate and the appropriate start and end potentials. If the equilibrium potential of the metal is outside the potential sweep window, then corrosion measurements cannot be undertaken from the data[97].

The American Society for Testing and Materials (ASTM) G5 standard[102] describes a procedure for a potentiodynamic polarisation test on type 430 stainless steel in sulphuric acid, with a scan rate of $0.167\ mV.s^{-1}$ specified in the standard. It is a good practice to select a more negative starting potential of approximately $50\ mV$ compared to the corrosion potential. The initial current response is cathodic which then switches to anodic current at potentials more positive than the corrosion potential. In this way, the corrosion potential can be monitored as the net current at this potential should be zero. This is a result of the equilibrium between the metal and the environment, and both the oxidation and reduction processes occurring at the same rates, resulting in net zero current.

Polarisation behaviour can be of two types, activation polarisation and concentration polarisation, the former being controlled by the free-energy or the potential driving force at the electrode surface and also kinetic limitations. In contrast, concentration polarisation is controlled by the mass transport of the reacting species to the electrode surface or the mass transport of the products away from the electrode surface.

3.2.2.1. Corrosion Rate Measurements by Tafel Extrapolation

The simplest way to determine the rate of corrosion would be to immerse the sample in a corrosive environment for a known period of time and measure the amount of weight lost. This value once normalised to the surface area of the metal, yields the corrosion rate in terms of weight loss per unit area per unit time. The DC polarisation technique yields corrosion current densities which can be converted to corrosion rate using Equation 3.26.

Exchange Current Density and Kinetics at Equilibrium

Considering an electrochemical half reaction of iron at equilibrium:

$$Fe^{2+} + 2e^{-} \leftrightarrow Fe \qquad \textit{Equation 3.27}$$

The reaction at equilibrium is in a dynamic state with both forward and backward reactions occurring at the same speed, as explained in section 3.1.2.2. This equal and opposite rate of reactions at equilibrium can be defined using the exchange current density, j_o. The exchange current density for the hydrogen reaction (Equation 3.10) is very much dependent on the catalytic properties of the metal surface on which the reaction is occurring. As in the case of corrosion in acidic environment, where the primary cathodic reaction is that of hydrogen reduction; the variability in the catalytic properties of the metal and hence the rate of hydrogen reaction can have a significant impact on the overall rate of corrosion of the metal.

Activation Overvoltage and Butler-Volmer Kinetics

In electrochemical terms, overvoltage or overpotential can be defined as the difference between the thermodynamically determined theoretical reversible voltage of a half cell and the experimentally observed voltage for the system: this is the extra potential that is needed to drive a reaction, in addition to the theoretically calculated potential. There are a number of conditions that would result in overvoltage. Assuming that the concentration of the reactants and products at the electrode surface is nearly the same as in the bulk solution, the resultant overvoltage is called activation overvoltage or charge transfer overvoltage. If the concentration at the

surface is below that of the electrolyte, the overall overvoltage is increased and the contribution is termed as mass transport overvoltage. The current is anodic (oxidising and positive) for anodic polarisation that results in a potential change to a value higher than the reversible potential, and the current is cathodic (reducing and always negative) for cathodic polarisation that results in a potential change to a value lower than the reversible potential (Figure 3.16).

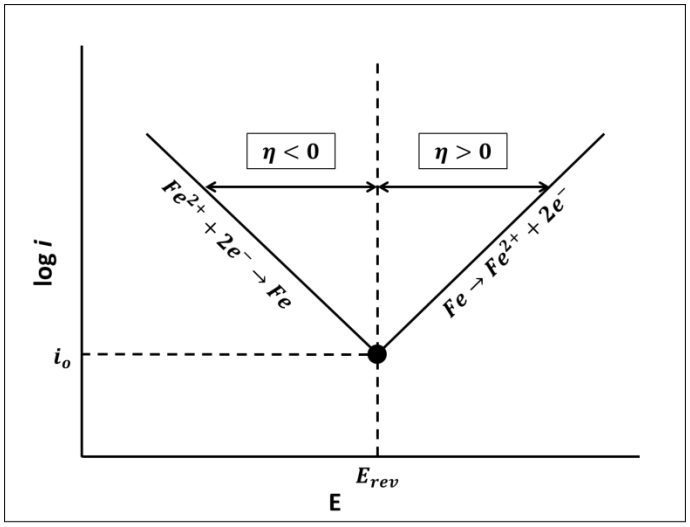

Figure 3.16: Graph of the relationship between current and potential for a simple electrochemical reaction under activation control (adapted from[90])

For an activation overvoltage limited system, the relationship between the rate of reaction or the current density, j, and the driving force for the reaction, i.e. potential, E, is given bythe Butler–Volmer equation.

$$\boldsymbol{j = j_a - j_c} \qquad \textit{Equation 3.28}$$

Where: $j_a \; and \; j_c =$ anodic and cathodic partial current densities respectively in terms of $(A.cm^{-2})$.

It is noteworthy that the cathodic term is negative, as reduction current is always negative, whereas the anodic term is positive as the oxidation current is positive. The net current is positive when the electrode is polarised anodically and negative, in the case of cathodic polarisation. Expanding the individual anodic and cathodic partial current density parameters, the equation can be expressed as:

$$j = j_o exp\left[\frac{(1-\alpha)nF(E-E_{rev})}{RT}\right] - j_o exp\left[\frac{-\alpha nF(E-E_{rev})}{RT}\right] \quad \textit{Equation 3.29}$$

$$j = j_o exp\left[\frac{(1-\alpha)nF(\eta)}{RT}\right] - j_o exp\left[\frac{-\alpha nF(\eta)}{RT}\right] \quad \textit{Equation 3.30}$$

The Butler–Volmer equation describes the kinetics for electrochemical reactions that are controlled by charge transfer across the interface, and the activation energy (overpotential) required to overcome the initial energy barrier for the reaction to happen. The charge transfer coefficient, α, characterises the symmetry of the activation energy barrier and hence is also called the symmetry coefficient. Consequently, α is described to be the fractional length along the reaction coordinate from the metallic state to where the activated state is located. As discussed, when $\alpha = 0.5$, the activated state is exactly midway between the two extremes and hence the reaction is symmetrical. This becomes clear when the Butler–Volmer equation is plotted, as in Figure 3.17 (a) where $\alpha = 0.5$, and (b) where $\alpha \neq 0.5$.

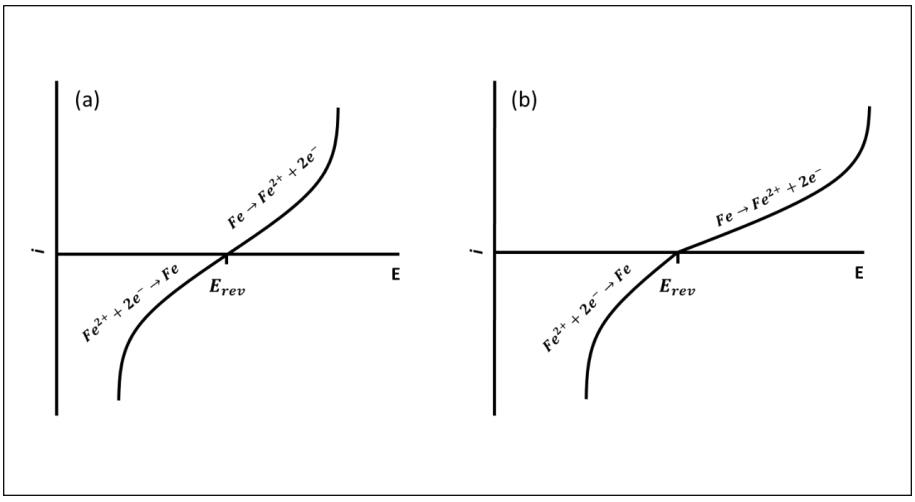

Figure 3.17: Electrode kinetics as expressed by the Butler–Volmer equation: (a) a symmetrical curve when $\alpha = 0.5$ and (b) an asymmetric curve when $\alpha \neq 0.5$ (adapted from[90])

The curve always crosses the X-axis at the reversible potential, and when the curve is plotted as $log\, i$ versus E, the Butler-Volmer equations are straight lines, as plotted in Figure 3.16. However, the Butler–Volmer

equation can be better described by the curve shown in Figure 3.18. The net current at the reversible potential is zero because the forward and reverse current, each equal to the exchange current density, balance each other. The log of the current density approaches negative infinity at the reversible potential where the net current density goes to zero, and the polarisation curve points down towards the reversible potential when the current is plotted on a logarithmic axis.

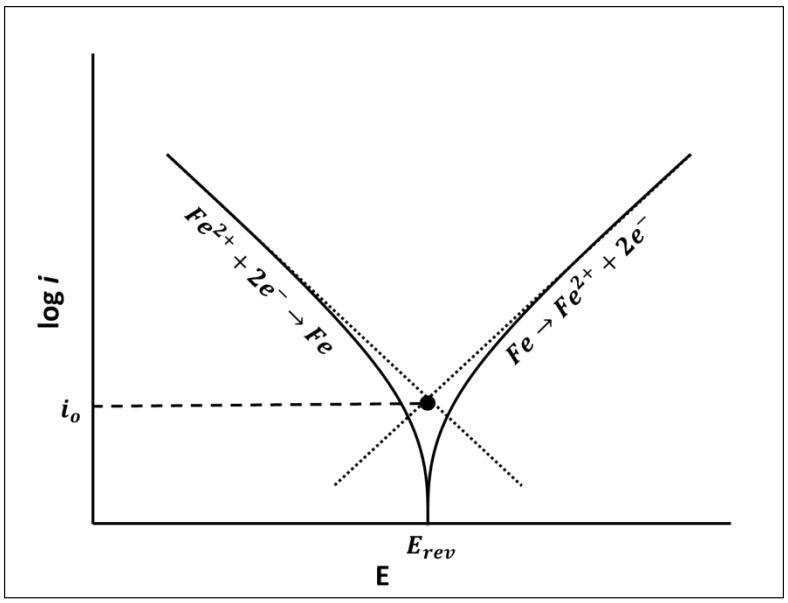

Figure 3.18: Electrode kinetics as expressed by the Butler–Volmer equation, plotted in a logarithmic graph (adapted from[90])

Tafel Equation

For a very low overpotential, the net current flowing would be zero, as the system is very near to the equilibrium potential. However, individual oxidation and reduction currents do flow and cancel each other out. In this ideal scenario, the system can be termed as reversible and will obey the Nernst equation. However, in the case of a sufficiently large value of anodic polarisation away from the reversible potential, i.e. where the overpotential $\eta > \sim 50\, mV$, Equation 3.30 is dominated by the first anodic term; similarly for a large value of cathodic polarisation, the cathodic term dominates the equation. Hence, in the case of a large overpotential, the Butler-Volmer equation simplifies to Equation 3.31 for anodic overpotential and Equation 3.32 for cathodic overpotential;

$$j_{net} = j_o exp\left[\frac{(1-\alpha)nF\eta_a}{RT}\right] \qquad \textit{Equation 3.31}$$

$$j_{net} = -j_o exp\left[\frac{-\alpha nF\eta_c}{RT}\right] \qquad \textit{Equation 3.32}$$

Taking the natural logarithm of both equations, and rearranging them, results in Tafel equations;

$$\eta_a = b_a \, log\left(\frac{j}{j_o}\right) \qquad \textit{Equation 3.33}$$

$$\eta_c = b_c \, log\left(\frac{|j|}{j_o}\right) \qquad \textit{Equation 3.34}$$

Where: $\eta_a =$ Anodic overpotential and $\eta_c =$ Cathodic overpotential, and $b_a = \left\{\frac{2.303RT}{(1-\alpha)nF}\right\} =$ Anodic Tafel slope and $b_c = -\left\{\frac{2.303RT}{\alpha nF}\right\} =$ Cathodic Tafel slope $(Volt\ per\ decade)$.

Typically for metals, corrosion conditions are far away from the reversible potentials, and hence Tafel kinetics is usually an accurate description of the corrosion kinetics. It should be noted that in Tafel kinetics mass transfer is not important.

Mixed Potential Theory

The mixed potential theory is based on the fact that several electrochemical reactions may proceed simultaneously at the same metal-solution interface. In the case of iron in an acid solution, the rest potential (or the corrosion potential) is a mixed potential and lies between the equilibrium of the two participating reactions. The predominant cathodic reaction in this case is hydrogen reduction. Also, as shown in Figure 3.19, the electrode potential is far from the reversible potentials for the two reactions occurring on the surface. Theoretically, four reactions may be possible, i.e. iron dissolution to form Fe^{2+} ions, the reverse reaction, and hydrogen ions forming hydrogen gas, and the reverse reaction. These four reactions are shown in Figure 3.19 which is more commonly known as the Evans diagram that depicts the graphical representation of electrode kinetics data (or current densities) and thermodynamics (or potential) in a corrosive process. The

two thermodynamically possible reactions are represented by the dotted line for the polarisation curve; iron dissolution and hydrogen evolution. The intersection at the extrapolation of the two lines on the polarisation curve results in the corrosion current and the corrosion potential.

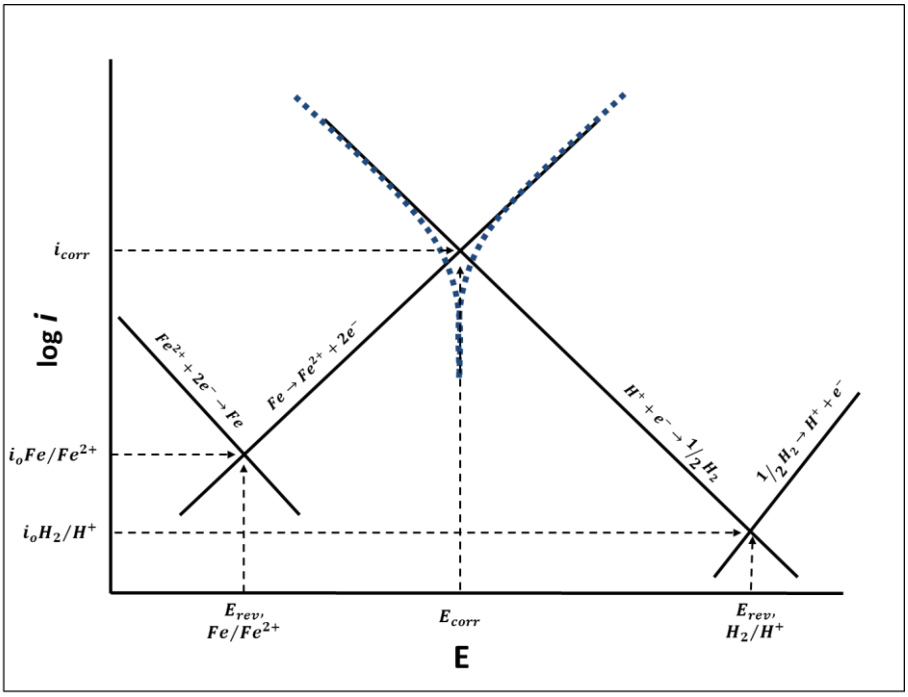

Figure 3.19: Evans diagram for actively corroding iron in an acid solution (adapted from[90])

Corrosion Rate Measurement by Tafel Extrapolation

As discussed in the mixed potential theory, the use of Evans diagrams provides the basis for the determination of corrosion rate by Tafel extrapolation. For a system which is activation controlled, a Tafel behaviour, i.e. a linear relationship between the potential and the log of current density is demonstrated at a potential that is sufficiently far from the open circuit potential or the rest potential of the system ($> 50-70\,mV$). It is to be noted that the current associated with the reaction of the opposite polarity is insignificant at this point of the polarisation curve. Tafel extrapolation starts at a potential of approximately $250\,mV$ negative to the OCP, scanning in a positive direction through the OCP (zero-current potential), and up to about $250\,mV$ positive of the original OCP. The zero-current potential measured during a polarisation experiment might be different to the OCP measured before or after the experiment owing to

reactions that occur during the scan, which may include oxide reduction, dissolution and passivation.

Figure 3.20 demonstrates a potentiodynamic polarisation scan for SS 316L in 1M $H_2SO_4 + 2\ ppm\ F^-$ ions, purged with hydrogen at 80 °C. The potential scan begins at a value $375\ mV$ below the OCP, and continues in a positive direction up to $1.5\ V$ at a scan rate of $1\ mV.s^{-1}$. The potential at which the current switches polarity, the zero-current potential, is where the curve points downwards, i.e. the OCP or E_{corr}. The reducing currents are negative at lower potentials, and the oxidising currents are positive at higher potentials with respect to OCP.

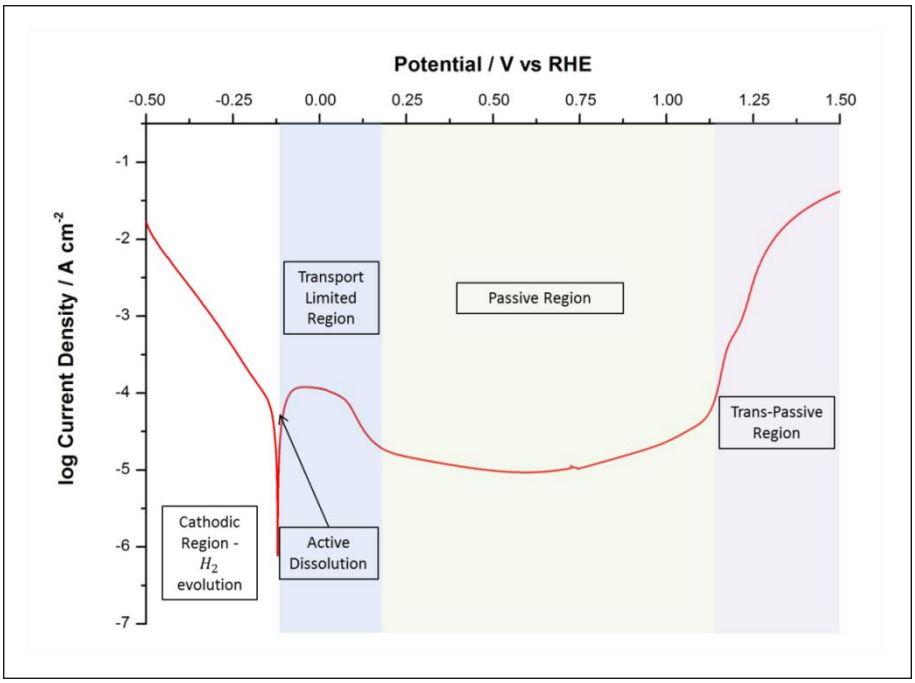

Figure 3.20: Potentiodynamic polarisation curve for SS 316L, in 1M $H_2SO_4 + 2$ ppm F^- ions purged with hydrogen at 80°C, at a scan rate of $1\ mV.s^{-1}$

The cathodic portion of the curve in Figure 3.20 exhibits clear Tafel behaviour over a wide range of potential. It is a simple matter to extrapolate this region to the zero current or corrosion potential to obtain the corrosion current density. However, the anodic portion of the curve does not exhibit clear linear Tafel behaviour. The mechanism for the dissolution of SS 316L in acid solution is quite complex and a line can be drawn in the region just above the corrosion potential, giving a Tafel slope. Such behaviour is not

unknown in corrosion electrochemistry as the anodic portion of the curve is affected by changes on the electrode surface, i.e., surface roughening or film formation. Once the corrosion current is obtained by Tafel extrapolation as discussed here, the corrosion rate of the metal can be calculated using Equation 3.26.

Recalling Equation 3.26 as: $r = C\left(\frac{M}{\rho nF}\right) i_{corr}$, given that all the parameters in the equation are very well defined except for the corrosion current density (i_{corr}); the rate of corrosion is then directly proportional to the corrosion current density. It is of utmost importance to understand the determination of corrosion current density using Tafel analysis of a polarisation curve. As discussed earlier, in order to ensure that the anodic and the cathodic current densities are independent of each other, the linear Tafel region selected should be at least $50 - 70\, mV$ away from the E_{corr}. Secondly, a sufficiently large linear region should be selected for extrapolation to ensure better fitting and a more accurate determination of the corrosion current density (Figure 3.21).

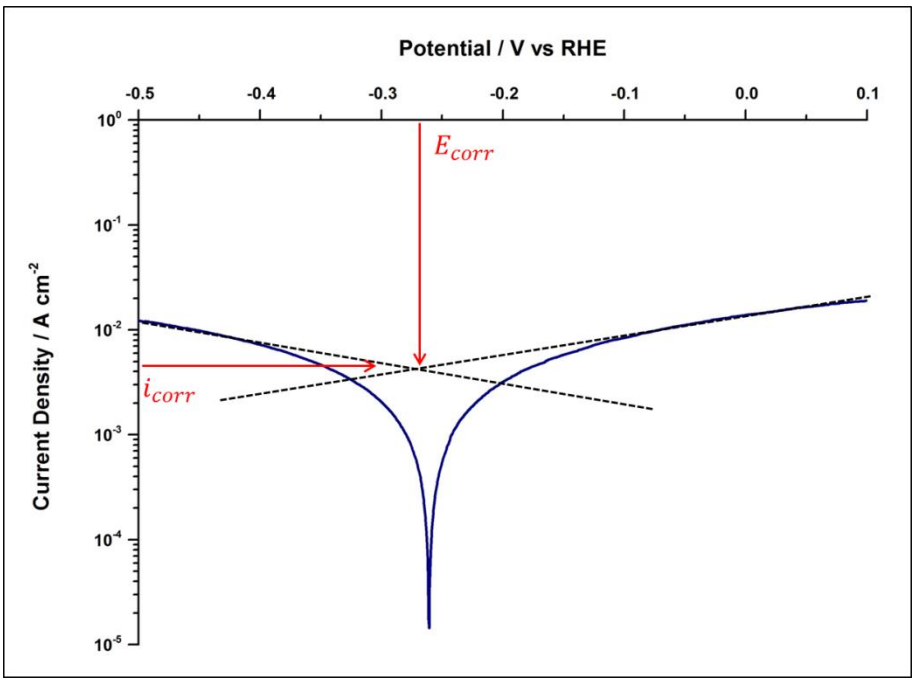

Figure 3.21: Portion of the Potentiodynamic polarisation curve near E_{corr} for mild steel sample, in 0.1M H_2SO_4 + 2 ppm F^- ions purged with air at 80°C, at a scan rate of $1\, mV.s^{-1}$

A step-by-step procedure for determining the corrosion current density and hence the corrosion rate of a steel sample in a given environment using Tafel extrapolation is explained in Figure 3.22 and Figure 3.23 using the screenshots obtained from the general purpose electrochemical system (GPES) interface of the Metrohm Autolab software. As per Equation 3.26, the molecular weight and the density of the corroding metal are provided by the user, along with the number of electrons transferred in the corrosion reaction. The software automatically adjusts for the constant once the corrosion current density is calculated. However, the irreproducible factor in corrosion rate calculations arises from the corrosion current measurements as for the software to calculate the corrosion current, the linear region for Tafel extrapolation is selected manually as explained in Figure 3.22. The anodic and cathodic linear regions are selecting by manually putting two markers each on either side of the corrosion potential or the OCP.

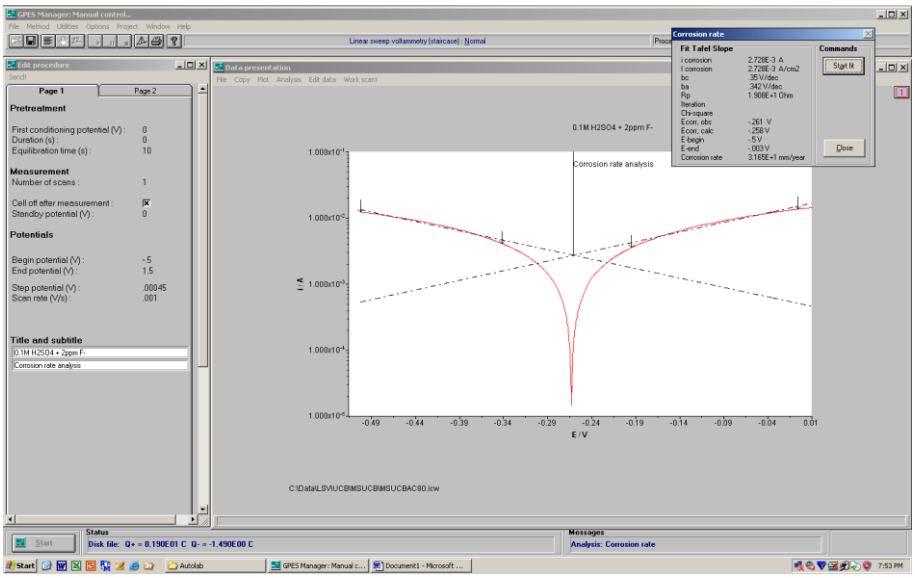

Figure 3.22: A screenshot of GPES software interface - Selection of Tafel region for extrapolation in order to calculate corrosion current density and hence corrosion rate

A rule of thumb to ensure that the best fit has been obtained and the ideal linear regions are selected is to manually inspect the overlay of the fitted curve on top of the actual LSV curve. In order to maintain the reproducibility, it is best practise to ensure that the overlay of the fitted curve fits perfectly on top of the LSV curve. Another point is to ensure that

the observed E_{corr} value and the calculated E_{corr} values are both in close proximity of each other.

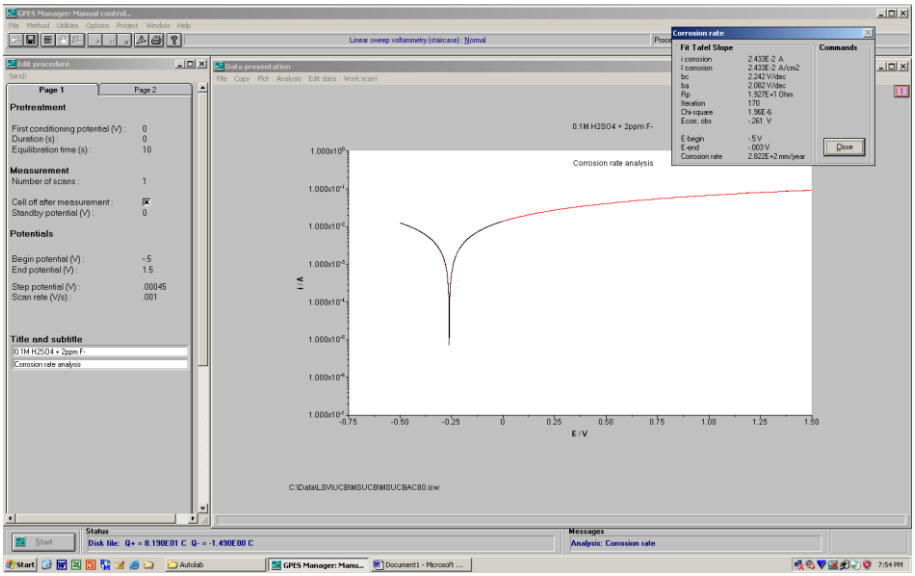

Figure 3.23: A screenshot of GPES software interface – Corrosion rate measurement by Tafel fitting after manual selection of the linear Tafel region

Stern-Geary Equation and Corrosion Rate Measurement by Linear Polarisation

Linear polarisation resistance[90,97,103] (LPR) or simply polarisation resistance (R_p), refers to the linear approximation of the polarisation behaviour at potentials near to the corrosion potential, termed as the Stern-Geary relationship[103]. According to the Stern-Geary approximation, the polarisation current is assumed to change linearly and not logarithmically with a change in potential. This assumption is clearly not valid in general, however, within a few $10 - 20\,mV$ of the corrosion potential it becomes a very good approximation. This is evident in Figure 3.24 when the polarisation curve for SS 316L near the corrosion potential is plotted linearly against current density, as opposed to the log of current density.

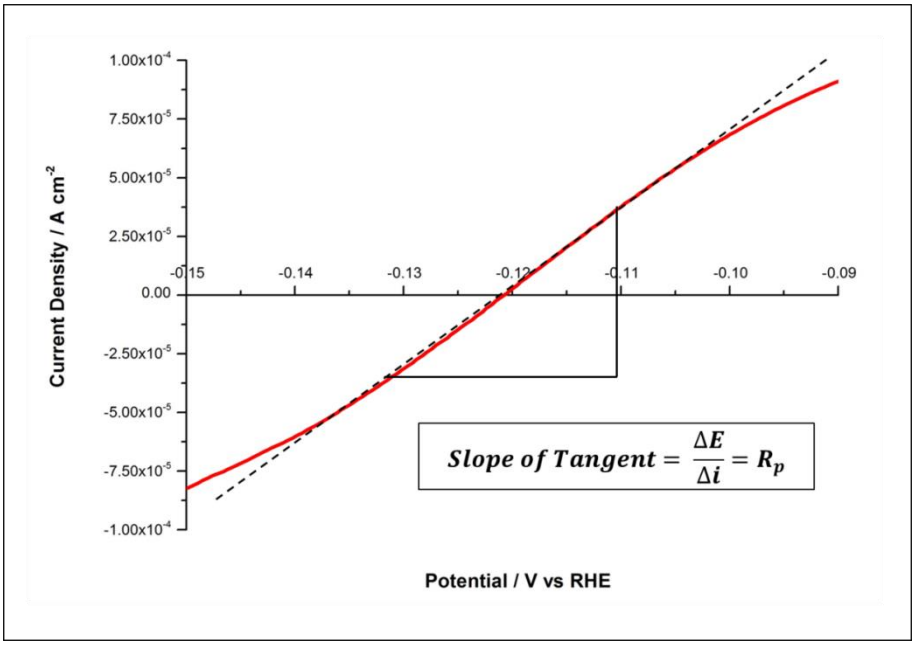

Figure 3.24: Demonstration of the Stern-Geary linear relationship near E_{corr} in the potentiodynamic polarisation curve for SS 316L, in 1M H_2SO_4 + 2 ppm F^- ions purged with hydrogen at 80°C, at a scan rate of $1\ mV.s^{-1}$

The Stern-Geary relationship can be described by;

$$\boldsymbol{R_p = \frac{\Delta E}{\Delta i} = \frac{b_a b_c}{2.303(b_a + b_c) i_{corr}}} \qquad \textit{Equation 3.35}$$

Where: R_p = Polarisation resistance (Ω).

R_p is taken as the slope of the tangent of the curve at the corrosion potential where the net current is zero, i.e., the corrosion potential. The corrosion current can be obtained by rearranging Equation 3.35, and the corrosion rate can be determined.

3.2.3. Summary

AC and DC electrochemical test methods combined together provide the backbone of corrosion test methodologies. AC test methods provide detailed information regarding the sample surface. The use of EIS aids in gathering information on the change is the surface morphology as the sample corrodes. The change in the CPE helps understand the change in the resistance of the sample. However, a key feature of EIS is to define the circuit used for fitting the data generated. A few simple circuit representations have been presented to understand the role of different parameters in circuit fittings and a general circuit for corrosion reactions is also presented that is used in data analysis for the results discussed in chapter 5. DC test methods provide an extremely useful tool in corrosion analysis; the instantaneous corrosion rate measurement using linear sweep voltammetry. LSV curves and Tafel analysis are widely used to measure corrosion rates for different metals in given environment. Both, the theoretical principles and the practical measurement of corrosion rates using Tafel analysis of LSV scans is discussed. The Tafel analysis is used to generate the corrosion rates for bulk of the samples discussed in chapters 5 and 6. In both AC and DC methods, the role of a reference electrode is of utmost important as any voltages reported are reported against a specific reference electrode and hence it is important to ensure that the right reference electrode is used and reported.

3.3. Conclusions

This chapter presents a broad view of the concept of corrosion and corrosion analysis. The main aim is to provide an understanding of what corrosion is and the electrochemical reactions that occur during corrosion. It also provides an insight in to the types of corrosion and the importance of pitting corrosion in the presence of halide ions. PEMFC membrane contains fluoride ions and the use of SS as BPPs provide an ideal combination for pitting corrosion to occur. The motive behind understanding the fundamentals of corrosion is to understand the requirements for coating development for BPP applications. The AC/DC test methods provide an everyday solution to testing corrosion relatively quickly. The majority of work reported in this thesis is based on corrosion analysis using both AC and DC methods. The main aim of this chapter; especially, the test methods section is to understand the interpretation of a linear sweep voltammetry scan and the corrosion rate analysis using LSV curves in a more generic manner. The next chapter provides information on the specific test methods used for corrosion analysis in this project. The detailed information about the electrolyte, reference electrode and other parameters used in each test method are discussed. However, the basic method of corrosion rate analysis using LSV scans remains the same as explained in this chapter.

4. Testing Methodology

The aim of this chapter is to introduce the experimental methods used to characterise the candidate materials in this project, and demonstrate the practical characterisation techniques used to examine aspects of the materials subjected to the AC/DC techniques discussed in the previous chapter. The primary test conducted on the samples is to analyse the interfacial contact resistance (ICR) of the material at different compressions using electrochemical impedance spectroscopy (EIS). The materials are then tested for their *ex situ* corrosion performance using linear sweep voltammetry. Further accelerated corrosion test methods are discussed, which include potentiostatic corrosion tests in simulated fuel cell environment under higher concentrations of acid solutions, and corrosion tests under switched gas environments where the purging gas is periodically switched between hydrogen and air to simulate start-up and shut down effects in *in situ* fuel cell operations.

The later part of the chapter elaborates on the surface characterisation techniques used in the project to complement the electrochemical corrosion analysis. A wide range of characterisation techniques have been used by researchers to study the surface characteristics of BPPs, and these surface characterisation techniques have been used to examine the surfaces of the candidate BPP materials down to the sub-nanometer scale. These techniques have helped the researchers to study the corrosion mechanism, and the effect of surface morphology on the contact resistance of the metals and the coatings. Samples that have been exposed to the corrosion environments have been analysed using scanning electron microscopy (SEM) to study the degradation of the sample and understand the corrosion reaction process.

Raman spectroscopy has been employed to study the characteristics of graphene coatings deposited using chemical vapor deposition, as well as a novel method of depositing graphene using electrophoretic deposition (EPD) technique from a solution of graphene intercalation compounds in an organic solvent. The fundamentals of Raman spectroscopy are discussed

as well the fundamentals of atomic force microscopy (AFM) for the characterisation of graphene layers deposited using EPD. Finally, a novel method of corrosion analysis using 3 dimensional X-ray computerised tomography method is introduced.

4.1. Electrochemical Test Methods

4.1.1. Interfacial Contact Resistance (ICR) Testing Methodology Using Electrochemical Impedance Spectroscopy (EIS)

The majority of the electrical resistance in a metal originates from the resistance offered by the surface of the material; the bulk metal has negligible electrical resistance. This occurs as a result of the oxide layer formed on the surface of the metals through environmental oxidation, as discussed in chapter 3.

ICR measurements have been carried out to determine the surface electrical resistance values of the samples, as characterised between the surface of the material and the GDL that is present in a fuel cell. The ICR values are determined at different compressions using electrochemical impedance spectroscopy (EIS). The test sample is sandwiched between two untreated Toray papers TGP-H-060 (Fuel Cell Store, USA), which are used as GDLs, and compressed between two gold coated copper electrodes (Figure 4.1).

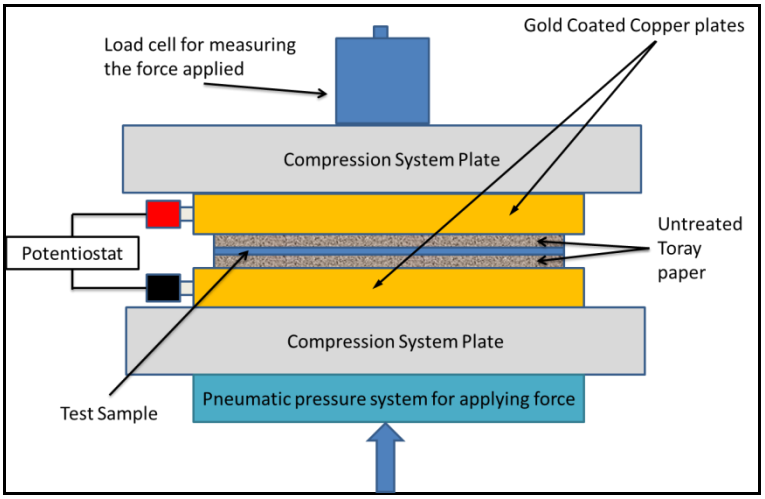

Figure 4.1: A schematic of the ICR testing equipment

Initially, the ICR value of a single untreated Toray paper is measured as a reference before ICR measurements of the sample are taken sandwiched between the GDLs, in a method used by Davies *et al.*[31], Wang *et al.*[26] and Gabreab *et al.*[104]. The ICR of the sample and the Toray paper interface is defined using the following equations:

$$\boldsymbol{R_{total} = 2R_{Gold\ /\ Toray\ interface} + 2R_{Toray\ /Sample\ interface}} \qquad \textit{Equation 4.1}$$

$$\boldsymbol{R_{blank} = 2R_{Gold\ /\ Toray\ interface}} \qquad \textit{Equation 4.2}$$

$$\boldsymbol{R_{sample} = R_{total} - R_{blank}} \qquad \textit{Equation 4.3}$$

The R_{sample} value is divided by two to get the resistance of each interface between the sample and the Toray paper; this is then multiplied by the area of the sample to provide normalised area specific results. The measurements are repeated at different compressions at an interval of $20\ N.cm^{-2}$ between $20\ N.cm^{-2}$ and $200\ N.cm^{-2}$. The compression was applied using a pneumatic air ram (series C95SB50-150, SMC, UK), controlled by a pressure regulator (IR2020 – F02, SMC, UK), and the applied force was measured by a load cell (LC304 – 500, Omega Engineering, UK). The electrical resistance was measured via EIS using potentiostat (Metrohm Autolab, PGSTAT302N) incorporating frequency response analyser (FRA2) software. The frequency range and amplitude used were $100\ kHz - 0.1\ Hz$ and $10\ mV$ applied at the open circuit potential

(OCP), respectively. The circuit was defined as pure resistance and the high frequency intercept for resistance was selected, using the software simulations to define the resistance of the system. The laboratory equipment set-up is depicted in Figure 4.2.

The EIS measurements are obtained using a two-electrode system at varying compression pressures to study the effect of compression on the ICR values of the samples. Theoretically, the resultant output should be a cluster of points on a single value of real impedance on the x-axis as the circuit is defined as pure resistance R (pure resistance is unaffected by frequency of applied potential and hence results in the same impedance at all frequencies). In practice an inductance tail is produced on the imaginary impedance scale axis and, with the aid of the extrapolations using the software; the output is quoted in terms of resistance. The theory of EIS is discussed in detail in section 3.2.1.

The applied force is divided by the sample area $(6.25\ cm^2;\ for\ 2.5 \times 2.5\ cm\ tokens)$ to determine the applied compression pressure per cm^2. It is observed that the ICR values reduce as the compression pressure increases. This occurs as a result of the pressure on the Toray paper and the subsequent increase in the surface area in contact with the test sample. This in turn increases the surface area for electrical conductivity and hence the resistance decreases.

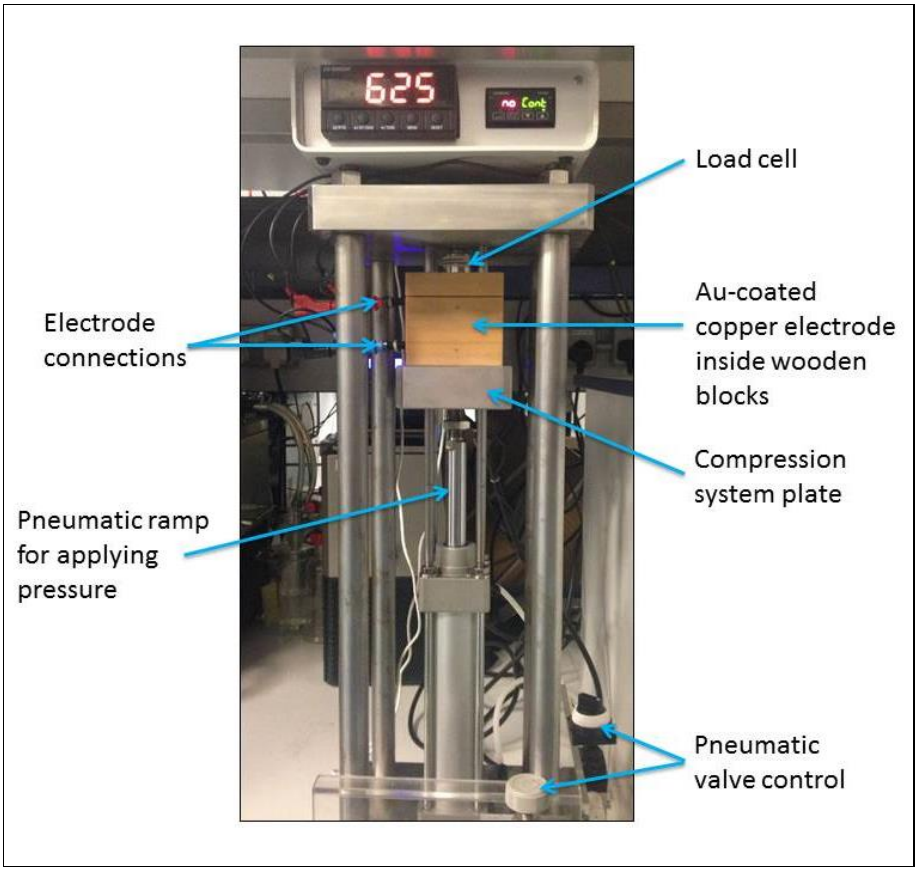

Figure 4.2: ICR test apparatus

4.1.2. Corrosion Reaction Cell (AVESTA Cell)[104]

Electrochemical corrosion tests were carried out using a three-electrode system connected to a potentiostat (Metrohm Autolab, PGSTAT302N). The reference electrode used in the experiments was a Hydroflex® reversible hydrogen electrode (Gaskatel, Germany) and a platinum mesh was used as a counter electrode. The electrolyte solutions were prepared using reagent grade 95% sulphuric acid, reagent plus $> 99\%$ sodium fluoride (Sigma Aldrich, UK) and ultrapure deionised water (18.2 MΩ, Millipore). The corrosion tests were carried out in a reaction cell depicted in Figure 4.3.

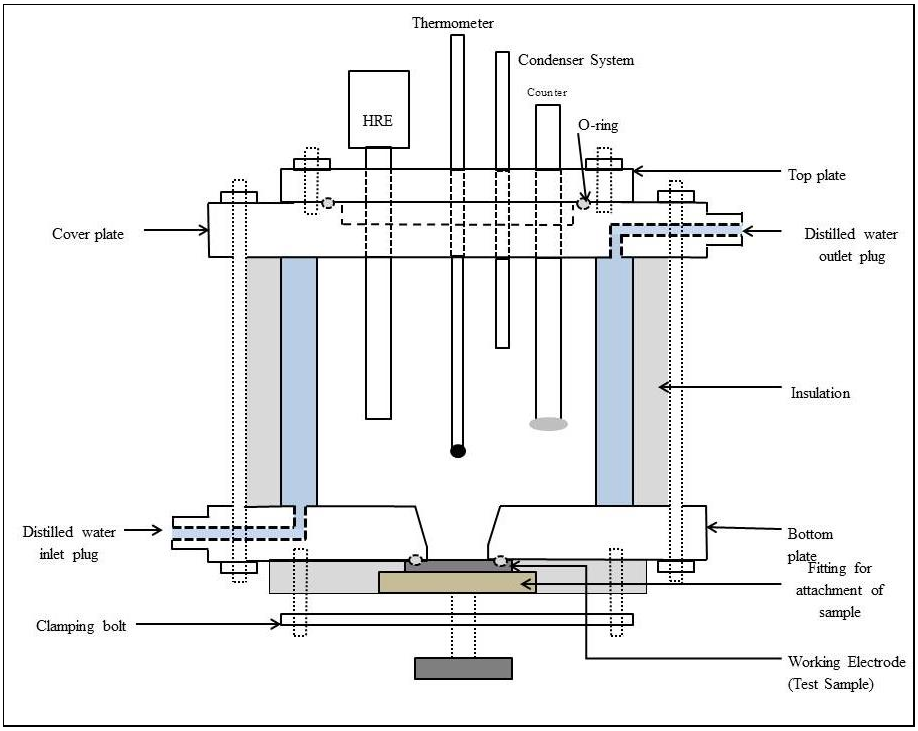

Figure 4.3: Schematic of the corrosion reaction cell (adapted from[104])

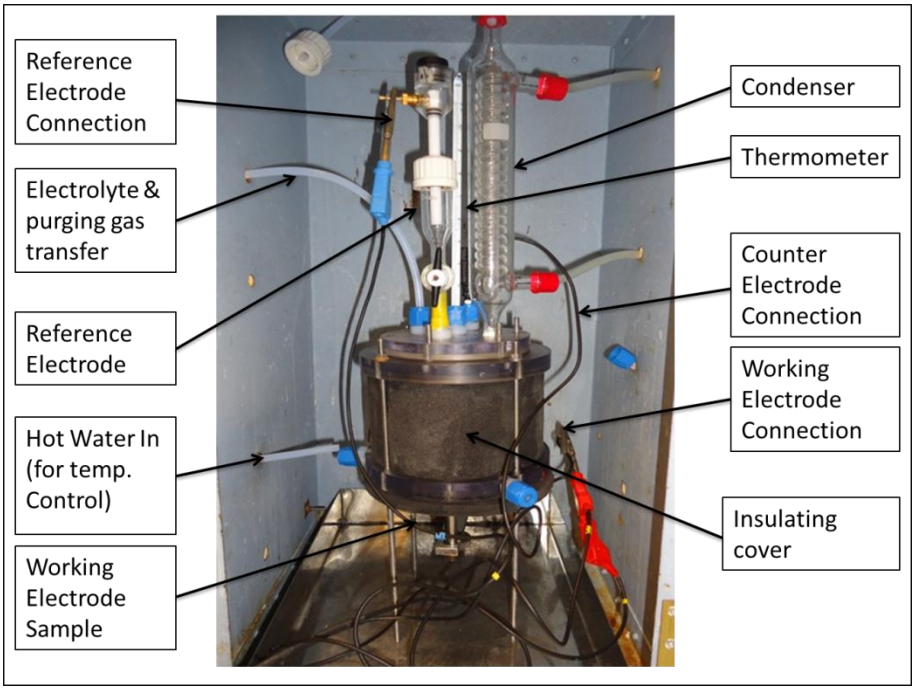

Figure 4.4: Corrosion test apparatus

An image of the corrosion test apparatus is given in Figure 4.4. A constant circulation of water is maintained at a controlled temperature to regulate the temperature of the electrolyte. A condenser system is attached to the reaction vessel, before the gases are transferred to the exhaust system, to

eliminate electrolyte evaporation and maintain the concentration of the electrolyte.

4.1.3. Potentiodynamic Polarisation Tests

The corrosion resistance of the samples was studied using linear sweep voltammetry (LSV) to measure the corrosion rates, as discussed in section 3.2.2. The electrolyte concentration[26,32,42,104,105] for the polarisation tests was $0.1\,M\,H_2SO_4 + 2\,ppm\,F^-$ ions[19]. During the voltammetry scan, the electrolyte was purged with hydrogen, to simulate the anodic fuel cell environment, and with air, to simulate the cathodic fuel cell environment. The LSV scans were repeated at room temperature (25 °C) and an elevated temperature (80 °C) to simulate the fuel cell operating environment. The sample was held at OCP for a period of $100\,s$ to equilibrate with the environment before running the LSV scan. During the LSV scan, the potential was scanned from $-0.5\,V$ to $1.5\,V$ vs RHE at a scan rate of $1\,mV.s^{-1}$. Corrosion rates were determined in mm per year using Tafel analysis discussed in section 3.2.2.1.

4.1.4. Potentiostatic Tests

Potentiostatic experiments have been carried out, in order to study the performance of the candidate samples under a simulated fuel cell environment, by holding the potential of the working electrode to the standby potentials of a fuel cell. Whilst simulating the anodic environment, the standby potential is $0.1\,V$ vs RHE and the electrolyte is purged with hydrogen, whereas at the cathode, the potential is $0.8\,V$ vs RHE and the electrolyte is purged with air[21]. The samples were first allowed to stabilise at OCP for $100\,s$ and then the potential was held at 0.1 and $0.8\,V$ vs RHE respectively for a period of $10\,h$[36] and the current response was measured every $4\,s$. The anode peak current density and the cathode passive current density have been measured. As in the case with potentiodynamic tests, to simulate the operational fuel cell environment, $0.1\,M\,H_2SO_4 + 2\,ppm\,F^-$ ions[56] was used as the electrolyte which was purged with hydrogen and air whilst simulating the anode and the cathode respectively. Again, the experiments were repeated at 25C and at 80 °C.

4.1.5. Accelerated Corrosion Tests

In order to analyse the degradation of the samples, they were exposed to a corrosive environment for an extended period of 48 hours to simulate accelerated corrosion using a $1\,M\,H_2SO_4 + 2\,ppm\,F^-$ electrolyte[19,26,32,42,104,105]. The samples were held at the anode ($0.1\,V$ vs RHE) and cathode potentials ($0.8\,V$ vs RHE) of the fuel cell, and purged with hydrogen and air, and repeated at room temperature and at 80 °C, as for the potentiostatic experiments. The samples were immersed for $48\,h$ and an EIS scan was obtained every $2\,h$. The EIS spectra provide information regarding the change in the resistance of the surface of the sample as a result of the formation of corrosion products on the surface, or the degradation of any coating that may be present on the sample. The EIS spectra were obtained around the OCP by scanning the frequencies over a range of $100\,kHz - 0.1\,Hz$, with a $10\,mV$ amplitude.

4.1.6. *In situ* Fuel Cell Operation

A single cell fuel cell is designed to incorporate flat steel samples as a BPP on the anode side of the cell with a graphite plate as the cathode. The results from this assembly are compared to the results obtained by using graphite as both anode and cathode. This provides an opportuniy to study the performance of SS 316 and other steel BPPs in comparison to graphite. The performance of the fuel cell is tested[106,107] using polarisation tests and constant current tests where the voltage drop is studied with respect to the current density. The fuel cell tests are carried out using 890e Fuel Cell Test System, Scribner Associates Incorporated.

4.1.6.1. Fuel Cell Assembly

The pneumatic ram depicted in Figure 4.5 allows to incorporate a single cell fuel cell within the fuel cell mounting blocks. This assembly allows to control the compression pressure that is applied on the actual fuel cell. The required compression is achieved by controlling the floating piston mechanism that applies the pressure to the fuel cell aseembly using pressure control valves. The two gold coated copper end blocks act as current collectors and provide the necessary electrode connections. In addition to this, these two blocks house the heating cartridges used to heat

the fuel cell assembly to the required temperature (in this project, all fuel cell experiments are carried out at 80 °C).

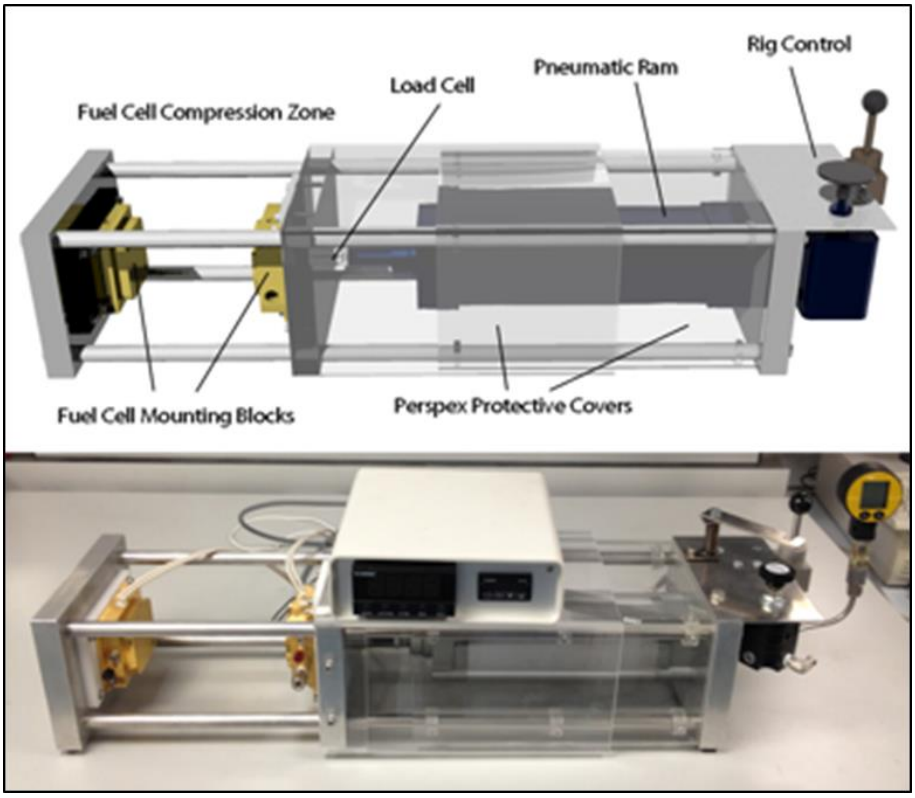

Figure 4.5: A pneumatic ram for housing a single cell fuel cell (adapted from[106,107]*)*

Figure 4.6 shows the schematics for all the components used in the single cell fuel cell. The actual fuel cell assembly is incorporated within an insulating housing. The two gold coated copper plates sit in direct contact with the current collector blocks in the pneumatic ram. These provide necessary connections for current collection as well as heating the fuel cell. The O-rings provide the sealing and prevent any fuel or oxidant leakages. The two graphite plates are shown with flow channels drilled in them. The PTFE plate provides the housing for the MEA and the internal O-rings on the graphite plates seal the actual working area of the fuel cell.

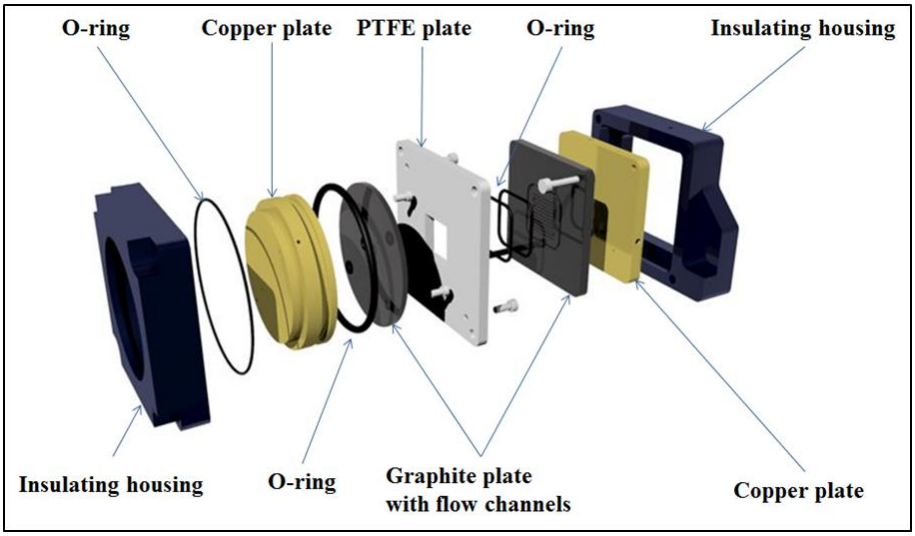

Figure 4.6: A schematic of the components of a single cell fuel cell (adapted from[106,107])

Figure 4.7 shows the graphite plate used as an anode for fuel cell experiments with graphite as anode and cathode. This plate is then modified to incorporate a flat steel token as a BPP during fuel cell operation. The gases (fuel or oxidant) enter from one end of the flow channel and flow through the flow channels and diffuse through the GDL present in the MEA. These gases then react with the catalyst layer and are ionised. On the anode side, hydrogen is ionised to protons and electrons; the protons pass through the MEA and produce water on reacting with oxygen ions on the cathode.

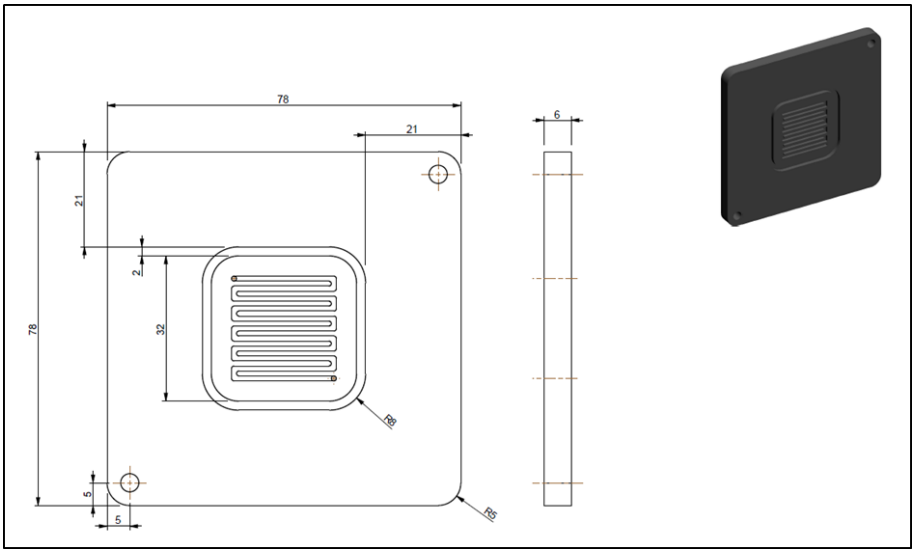

Figure 4.7: A technical drawing for a graphite plate used as anode for fuel cell experiments(all dimensions are in mm) (adapted from[106,107])

4.1.6.2. Methodology for Making MEAs

In the pre-treatment step, the Nafion NR-212 (Ion Power, USA) electrolyte membrane was treated with hydrogen peroxide (VWR, ACS-Reagent Grade) in order to remove any organic contaminants within the membrane. The pre-cut membranes $(60 \times 60\,mm)$ were soaked in a 3% hydrogen peroxide solution for $1\,h$ at 80 °C. After rinsing the pre-treated membranes with de-ionised water, they were soaked in $1M$ sulphuric acid solution (Sigma Aldrich, $95 - 97\%$) for $1\,h$ at 80 °C to pre-activate the membrane. After this, they were again rinsed with de-ionised water and stored in de-ionised water.

The pre-treated and pre-activated electrolyte membranes were then hot pressed in between the two Pt-loaded electrodes with GDL (ELE 0070, Johnson Matthey Fuel Cells) using a hot press (4122CE, Carver, USA) for $3\,min$ at 160 °C at $450\ psi$. The so-formed MEAs are stored completely immersed in de-ionised water and used for fuel cell experiments.

4.2. Surface Analysis

In corrosion science, it is of utmost importance to explain the phenomenon occurring at the surface of the sample material. In addition to the electrochemical techniques, surface analysis tools have been used to build up a comprehensive picture of the corrosion processes, this section describes these techniques in more detail.

4.2.1. Scanning Electron Microscopy (SEM)

The scanning electron microscope (SEM) allows a user to observe and characterise the sample surface at microscopic levels. In order to obtain an SEM image, the surface of the sample is irradiated by a finely focussed electron beam. This beam of electrons is scanned across the sample in a raster pattern by the scan coils. The electron beam is swept linearly across the sample in the x-direction, then returned to its original position whereby it is shifted downwards in the y-direction with a standard increment that defines the resolution of the resulting image. In this project, SEM imaging has been carried out using Zeiss EVO MA10 SEM machine. The working

distance of the sample is maintained around $8.5\,mm$ from the lens and in most cases secondary electrons are used to generate the image.

The types of signals that are produced when the electron beam impinges the surface of the sample include; secondary electrons, backscattered electrons, Auger electrons, X-ray fluorescence photons and photons of various other energies. In order to produce an SEM image, the most important signals are the ones obtained from processing the backscattered and secondary electrons as these vary according to the surface topography of the sample. The secondary electron emission is confined to the volume very near to the beam's impact area which allows the images to be obtained at a relatively high resolution. Modern SEM instruments are equipped with X-ray detectors that allow for quantitative and qualitative chemical analysis of the surface by means of X-ray fluorescence along with the production of the high resolution SEM images.

The final diameter of the electron beam which is referred to as spot size or probe size is the limiting factor in the resolution of the image obtained by the SEM. Similarly, the amount of current that is carried into the final probe spot will decide the intensity of the emitted signals (secondary or backscattered electrons). Theoretically, one would want a spot size with minimum diameter and maximum current intensity. Unfortunately, in practice, the smaller the electron probe, the smaller is the available probe current. Hence, it is up to the operator to adjust the microscope controls to produce a desired image with high resolution and high depth-of-field.

A number of signals are produced as a result of electron beam-specimen interaction, including secondary electrons (SEs) and backscattered electrons (BSEs), both of which are collected by Everhart-Thornley (E-T) electron detectors which consist of a scintillator, a light pipe and a photomultiplier tube. The sample specimen is tilted towards the detector which is located in close proximity to the specimen. The detector assembly is electrically isolated from the rest of instrumentation, and a wire mesh screen is positioned in front of the detector which is held at a positive voltage of approximately $300\,V$. The high positive charge attracts the emitted low energy electrons into the detector system. However, in order to produce a good quality image, the strongest source of SEs should be

located at the point where the beam enters the sample surface, although some fraction of the BSEs from the specimen will also enter the detector.

All the electrons entering the detector system are accelerated by a voltage of $+12\,kV$. The resultant energetic SEs hit the scintillator material to produce light. This light travels down the light pipe to the photomultiplier tube, whereby the light is converted to an amplified electrical signal. The variations that occur in the signal as the beam moves over the sample produces changes in the recorded intensity which result in the production of an image that is visible to the user. The BSEs are most efficiently and selectively removed by an overhead backscatter detector, although a small fraction of the BSEs do enter the E-T detector. A pure BSE signal can be collected with the E-T detector by repelling the SEs with a $-100\,V$ potential on the screen in front of the detector. As mentioned before, the SEs and the BSEs are the most important signal source for producing SEM images, but any signal collected and suitably amplified may be used to produce an SEM image.

4.2.1.1. Application of SEM in Corrosion Studies

SEM is one of the most commonly used surface imaging techniques and finds its application in a wide range of scientific fields. The technique is non-destructive and the images can be obtained relatively very quickly.

Wang and Northwood[108] compared the performances of A36 steel and grade 2 titanium under the simulated cathode and anode conditions of a PEM fuel cell, after which the samples were imaged using SEM. Figure 4.8 and Figure 4.9 depict the SEM images of the A36 steel and grade-2 titanium samples respectively under anode and cathode conditions. The authors have used SEM to depict the difference in the corrosion observed on the two different substrates under the simulated fuel cell conditions. Figure 4.8 shows the SEM images of corroded A36 steel which demonstrates clear signs of corrosion on the substrate sample. However, Figure 4.9 does not show such an extent of corrosion on the titanium samples demonstrating the better corrosion resistance offered by titanium as compared to A 36 steel.

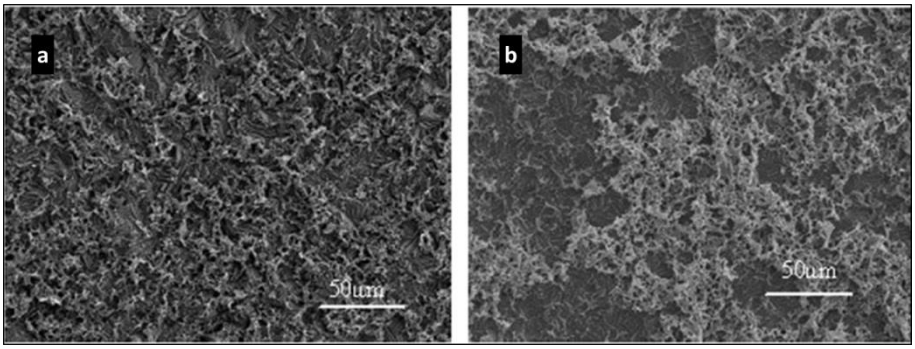

Figure 4.8: SEM micrographs of A36 steel subjected to simulated (a) anode and (b) cathode conditions (bars = 50 μm) (adapted from[108])

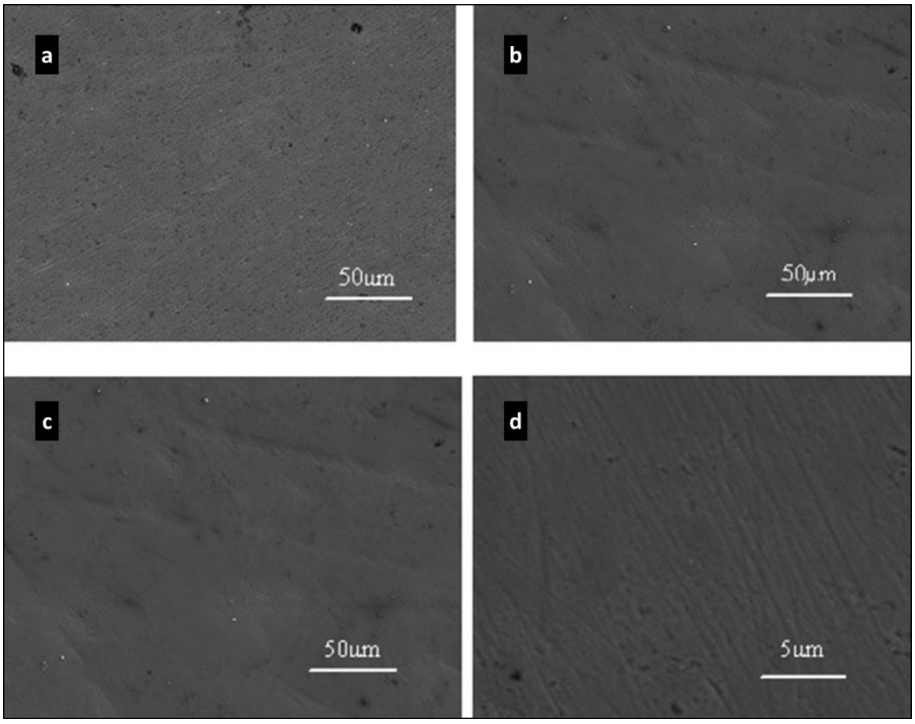

Figure 4.9: SEM micrographs of Ti subjected to simulated (a and b) anode and (c and d) cathode conditions (bars = 50 μm) (adapted from[108])

Wang and Northwood[36] studied the effect of oxygen and hydrogen on the corrosion performance of SS 316L. The substrate was subjected to potentiodynamic and potentiostatic tests under oxygen and hydrogen environments. Figure 4.10 shows the effect of the gases on the corrosion of the SS 316L sample. The authors have used SEM to demonstrate different types of corrosion observed on SS 316L under simulated fuel cell conditions. Figure 4.10 (a) and (b) clearly depict pitting corrosion and inter-granular corrosion. The potential was scanned beyond the passive potential

and in the regions of trans-passive potential resulting in pitting corrosion due to the damage to the passive film of SS 316L. Figure 4.10 (d) shows the corrosion products deposited on the substrate as a result of the corrosion reactions during the potentiostatic tests.

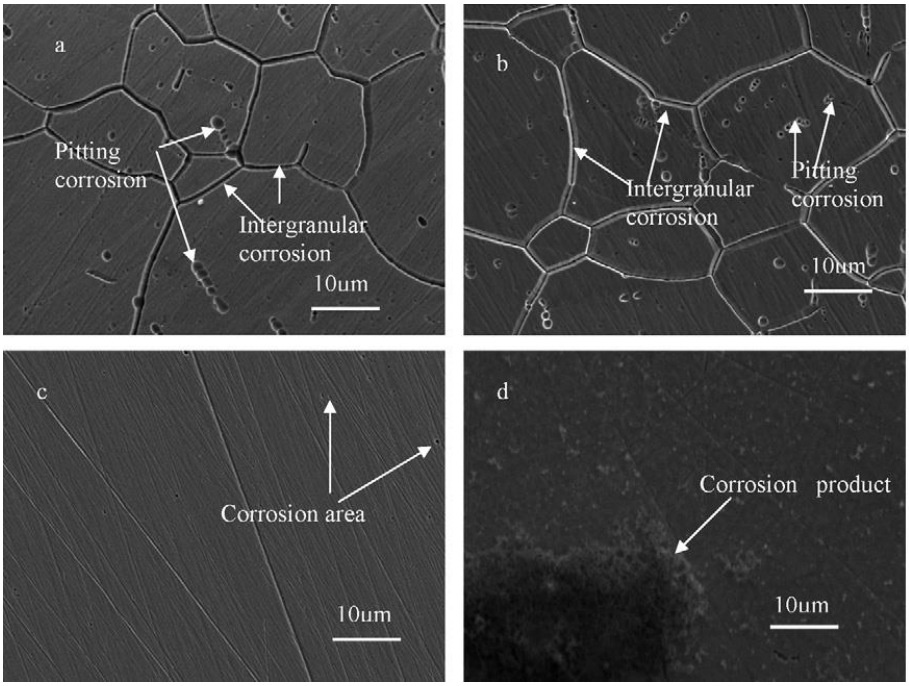

Figure 4.10: SEM images of SS 316L after corrosion: (a) potentiodynamic test with H_2, (b) potentiodynamic test with O_2, (c) potentiostatic test at $-0.1\,V$ vs SCE with H_2, and (d) potentiostatic test at $0.6\,V$ vs SCE with O_2 (bars = $10\ \mu m$) (reprinted from[36])

SEM is a useful analytical technique for studying the corrosion of metals. The SEM images prior and post corrosion of samples reveal useful information on the degradation of the material. The type of corrosion happening can be depicted from the pits and participates that form on the surface of the sample.

4.2.2. Atomic Force Microscopy (AFM)

The atomic force microscope[109–112] (AFM) is one of the most versatile microscopic techniques amongst the family of scanning probe microscopes (SPMs). The SPM generates an image by contacting the specimen rather than just interrogating it with radiation photons, as is the case with optical or electron microscopes. An SPM can reveal atomic level detail from not only

the lateral x and y axes, but also in the z axis, perpendicular to the surface. In this project, AFM analysis has been carried out using BRUKER Dimension icon with ScanAsyst.

The scanning tunnelling microscope[109–111] (STM) was the first of this type of microscope. Binning and Rohrer invented the STM in the early 1980s, and in 1986 they were awarded the Nobel Prize in physics for their work. Soon after this, Binning and colleagues announced the development of the atomic force microscope (1986), and commercial AFMs were available from the early 1990s. The AFM scans the surface in an xy raster pattern with a sharp tip that moves up and down along the z axis as the topography of the surface changes.

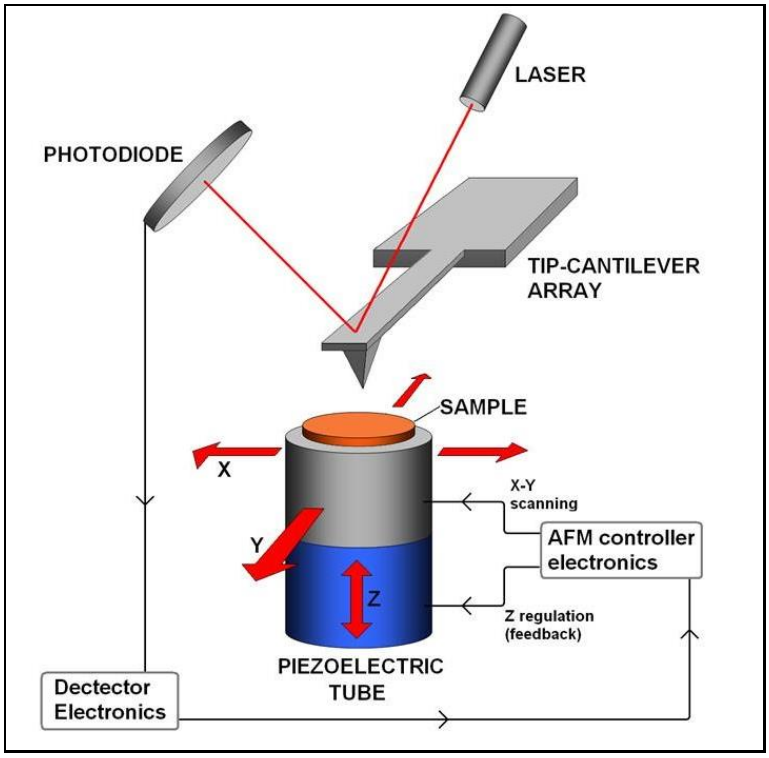

Figure 4.11: Schematic of an AFM (adapted from[113])

An AFM allows the resolution of individual atoms on both conducting and insulating surfaces. A force sensing cantilever stylus is scanned in raster pattern over the surface sample. The force acting between the cantilever and the surface causes minute deflections and these deflections are detected optically as a laser beam is reflected off a spot on the cantilever to a photodiode that in turn detects the motion of the probe. The force on the tip is held constant as the tip is drawn over the surface allowing it to follow

the surface structure; this in turn provides the topographic information. A tubular piezoelectric device moves the sample in all three directions under the tip, while a feedback loop controls the force applied to the tip so as to keep it constant. The positional signal from the laser beam is fed back to the sample piezoelectric transducer which then causes the sample to move up and down maintaining the constant force on the tip.

4.2.2.1. Instrumentation

The Tip and Cantilever

The first and most important part of the AFM is the tip or the stylus which contacts the surface and collects the topographic information. The performance of an AFM depends on the physical characteristics of the tip and the cantilever. The tip is mounted at the end of a small cantilever as depicted in the scanning electron micrograph in Figure 4.12. With the very first AFMs, a very small diamond fragment was manually glued to one end of a gold foil that acted as the cantilever. The cantilever-tip assembly was bonded to a glass chip for easy handling. In the present time, tip-cantilever assemblies are mass manufactured from silicon, silicon oxide or silicon nitride using the same technology which is applied in fabricating integrated circuits. This allows uniform characteristics and excellent reproducibility. The most important parameters for the assembly are sharpness of the tip apex and the aspect ratio of the whole tip. A standard tip is usually a 3 µm high pyramid with a tip radius of approximately 30 nm. The length, width and the thickness of the beam determine the mechanical properties of the cantilever. Cantilevers are usually classified by their spring (or force) constants and their resonance frequencies.

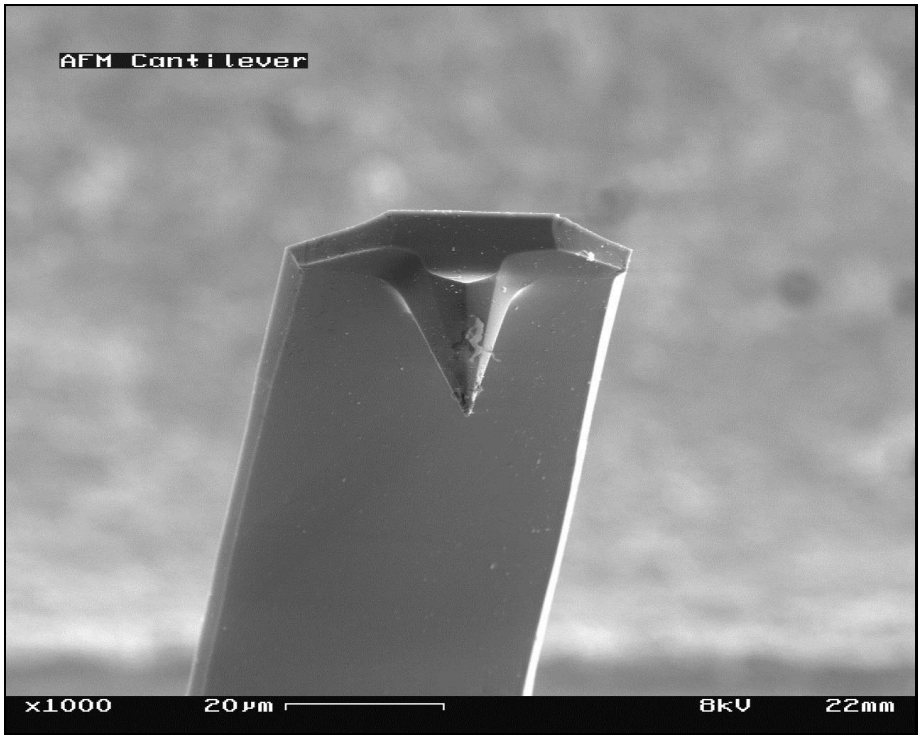

Figure 4.12: Scanning electron micrograph of an AFM tip and cantilever (bar = 20 μm) (adapted from[112])

Deflection Scanners

AFM provides dimensional resolution down to picometres when it comes to measure the vertical deflection of the cantilever. This is achieved by using a laser beam which is reflected from the backside of the cantilever onto a position sensitive photodetector consisting of two side-by-side photodiodes. A minute deflection of the cantilever will result in tilting of the reflected beam that is detected by the photodiode. The difference between the two photodiode signals indicates the position of the laser spot and hence the angular deflection of the cantilever.

4.2.2.2. AFM Modes

The most important modes of AFM imaging are DC Contact Mode and AC Non-Contact or Tapping Mode.

DC Contact Mode

DC contact mode is the most common mode of AFM used in the present time. It is also termed as constant force mode as the tip is in constant

contact with the surface of the sample. The image contrast depends on the applied force and that in turn is dependent on the cantilever force constant or the spring constant of the cantilever. Softer cantilevers are used for soft samples or liquids. As the tip is in constant contact with the sample surface, a significant shear force can be generated damaging the sample, especially in the case of biological samples and living cells. This would also result in the distortion of the image. Further, the samples may trap electrostatic charge which would then contribute to the attraction forces between the tip and the sample surface. This would then lead to frictional forces as the tip moves over the sample, resulting in sample damage and blunting of the tip as well.

AC Non-Contact Mode

All AC modes require the cantilever to be in oscillation using an applied driving signal. This could be achieved by driving the cantilever with a piezoelectric motor, or directly driving by external coil where the probe is coated with a magnetic layer. An oscillating probe is brought into the proximity of the surface of the sample without touching it. As the probe gets closer, it senses the attractive van der Waals forces that would induce a frequency shift in the resonance frequency of the cantilever. In this mode, the tip-sample interactions are minimised and hence excellent vertical resolutions are achieved, but these are accomplished at the cost of lateral resolution. The biggest drawback is that this mode cannot be used for liquid samples, and even on dry samples, if a thick contamination or water layer is present, the tip can become trapped with insufficient energy to detach itself from the sample, owing to the small amplitude of oscillation.

4.2.2.3. Application of AFM

AFM has a wide range of applications in the biomedical field, sufficient even to study living micro-organisms, while in the field of materials research AFM is a useful tool to study the surface profile at a nanometer scales. The technique is commonly applied to study coating deposition on a substrate, and in the field of corrosion science AFM is used to study surface degradation and the formation of pits with sub-nanometer dimensions.

Cho *et al.*[114] used EPD to produce carbon nanotube films. The authors used AFM to characterise the topography of the coatings obtained by EPD. Figure 4.13 depicts a typical CNT coating. The AFM images reveal that the surface is characterised by a network of very long cylindrical-like features which are very small in width and height profile of few hundred nanometres.

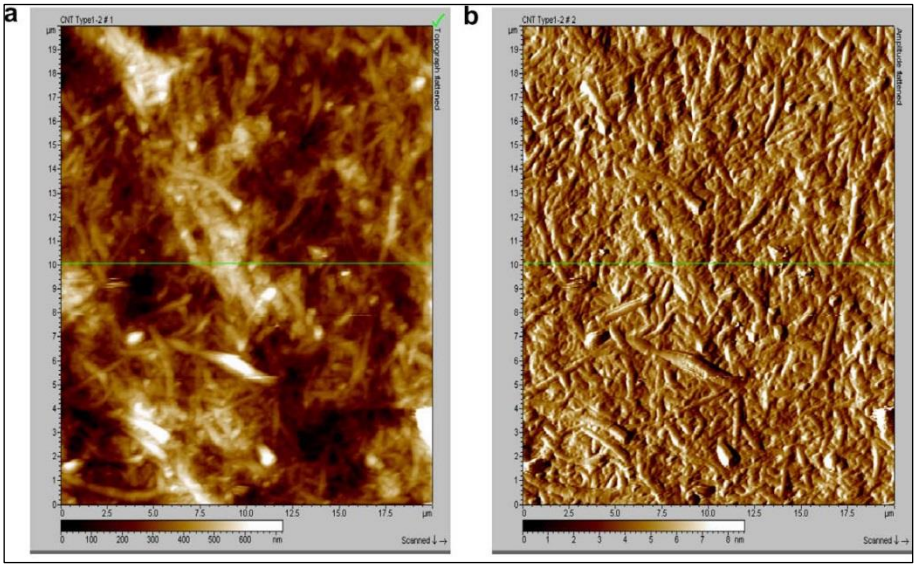

Figure 4.13: An AFM image of the surface of a CNT coating (adapted from[114]*)*

Fukutsuka *et al.*[115] carried out carbon-coating on stainless steel substrates using plasma-assisted CVD from acetylene and argon. The surface morphology of the carbon coating on SS 304 was observed by AFM. Figure 4.14 shows the AFM images that reveal that the carbon coating on the SS 304 substrate was dense. Such morphology would be an aid in preventing the electrolyte from penetrating into the carbon-coating.

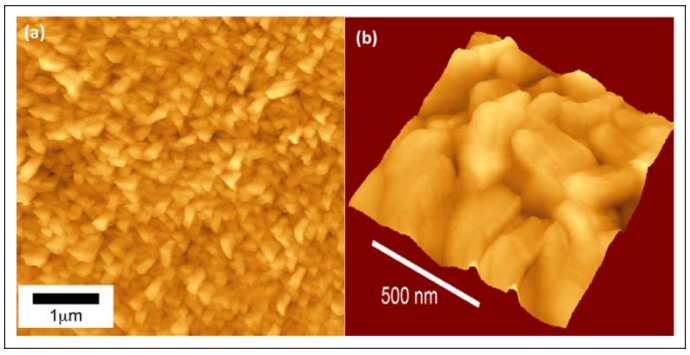

Figure 4.14: AFM images of carbon coated stainless steel (a) $5\ \mu m^2$ *and (b)* $1\ \mu m^2$ *(adapted from*[115]*)*

4.2.3. Raman Spectroscopy for 2D Carbon Compounds

Raman spectroscopy is a spectroscopic technique that uses the inelastic scattering of monochromatic light, usually from a laser source illuminating the sample. In order to obtain a Raman spectrum, a sample is irradiated with a laser source in the visible, near infrared or the ultraviolet regions of the electromagnetic spectrum, and the scattered light is collected using a complex lens system through a spectrophotometer which results in a Raman spectrum. In this project, Raman spectroscopy has been carried out using Thermo Scientific DXR Raman Microscope (USA), with a DXR 532 nm Laser at $8\,mW$ power and a $50\,\mu m$ pinhole, generating a spot size of $0.7\,\mu m$. The objective lenses used for different experiments were 10x, 20x and 50x magnification.

4.2.3.1. The Raman Effect

According to quantum theory, the energy of a photon is given as:

$$\boldsymbol{E_p = h\nu_p = hc\bar{\nu}} \qquad \textit{Equation 4.4}$$

Where: $E_p =$ Energy of photon $(joules)$, $h =$ Planck's constant $(6.6256 \times 10^{-34} joule.sec)$, $\nu_p =$ frequency of photon (Hz), $c =$ velocity of light $(2.998 \times 10^{10} cm.sec^{-1})$ and $\bar{\nu} =$ wavenumber (cm^{-1}).

This photon energy may be absorbed by a molecule, or emitted, and hence the energy of the molecule would change by the amount E_m: the principle of conservation of energy suggests that this change in energy would be equal to the energy of the photon[116]. In the case where the molecule gains energy, E_m is positive and a photon is absorbed, whereas when a molecule loses energy E_m is negative and a photon is emitted[116].

Most of the scattered energy is of the same frequency as the incident light, a process termed elastic scattering or Rayleigh scattering. The signal returned by such scattering is strong due to the high fraction of returned energy. In 1928, C. V. Raman described another type of scattering which is now known as the Raman Effect[117]. This effect had first been predicted theoretically by Adolf Smekal[118] in 1923, before the successful experimental

demonstrations by C.V. Raman and K.S. Krishnan[117] in 1928. In the case of inelastic Raman scattering, two distinct types of scattering can be observed. When the frequency of scattered light is less than that of the incident light it is termed as Stokes scattering, and when the frequency is greater than the incident light is termed as Anti-Stokes scattering[64].

The frequency of the source of monochromatic radiation is usually much higher than the vibrational frequencies of a molecule; but it is lower than the electronic frequencies. The radiation scattered by the sample is analysed in the spectrometer. In case of an elastic collision, the rotational and vibrational energies of a molecule are unchanged, the energy and hence the frequency of the scattered photon is the same as that of the incident photon. In the case of an inelastic Raman collision between the incident photon and the molecule, the vibrational or rotational energy of the molecule is changed by an amount $\Delta E_m = hv_m$. According to the law of conservation of energy, the scattered photon energy, hv_s, must be different to that of the energy of the incident photon, hv_i, and should be equal to ΔE_m.

$$\boldsymbol{hv_i - hv_s = \Delta E_m} \qquad \textit{Equation 4.5}$$

Where: $\Delta E_m =$ Change in the enegy of the molecule $(Joules)$, hv_i and hv_s are the incident and scattered photon frequencies, respectively in terms of (Hz).

If the molecule ends up gaining energy ΔE_m will be positive, while if the molecule loses energy it is negative resulting in the rise of Stokes lines in the Raman spectra.

According to quantum mechanics, the zero point energy is given as $\frac{1}{2}hv_m$. Chemical bonds can act like springs and are capable of displaying simple harmonic motion. The energy of vibration of a molecule can be given as $E_V = \left(V + \frac{1}{2}\right)hv_m$ and in the case of the vibrational energy equation, the only variable is the quantum number V. In the case of a diatomic molecule such as HCl as shown in Figure 4.15, the lines designated $V = 0$ and $V = 1$ represent the vibrational energy levels and the difference between the two is given as $\Delta E_m = hv_m$.

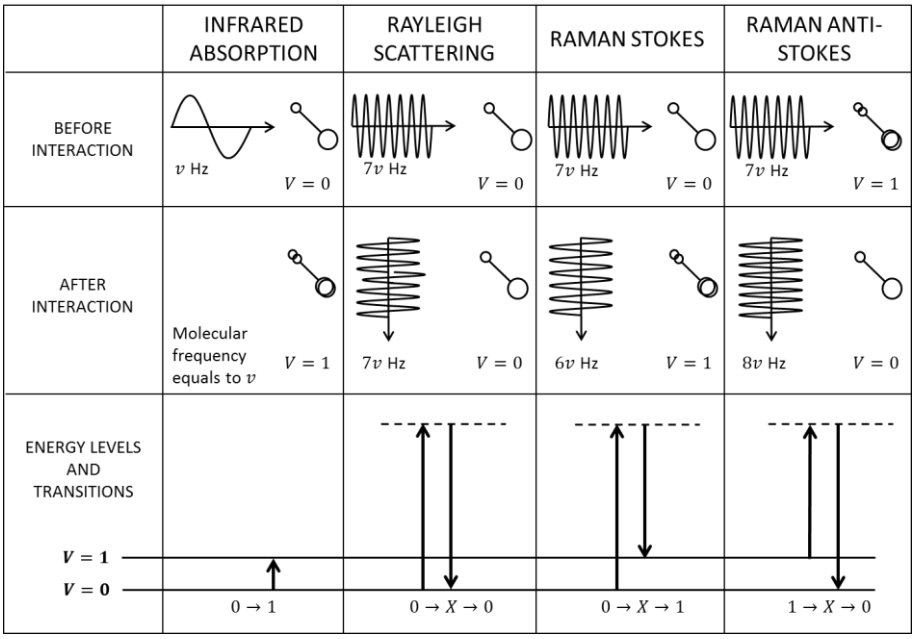

Figure 4.15: Schematic illustration of Raman and Rayleigh scattering and infrared absorption (adapted from[116])

A direct transition between the two levels causes absorption of an infrared photon with a frequency the same as the molecular frequency v_m. In case of Rayleigh and Raman scattering[116], the incident photon frequency is taken as $7v_m$, as shown in Figure 4.15, which is greater than the vibrational frequency. When the incident photon interacts with the molecule in the vibrational ground state $V = 0$, the molecule absorbs photon energy and is momentarily raised to a higher energy level as depicted by the dashed lines in the figure. This is not a stable energy level and hence the molecule immediately loses energy and most probably returns to the original ground vibrational state. Whilst returning to the ground state, it emits a photon whose energy and the frequency are the same as the incident photon. This is Rayleigh scattering.

However, in a very small number of cases, the molecules may fall back to a higher energy level instead of the ground level. The scattered photon will then have less energy than the incident photon, with the difference being given by Equation 4.5. This scattered photon gives rise to Stokes lines in the Raman spectrum. The final possibility is that of a molecule being in an excited state $V = 1$, which absorbs the incident photon and is raised to an unstable high energy level before falling back to the ground state. The energy difference is then made up by the emission of a photon whose

energy is greater than the incident photon by an amount of hv_m giving rise to Anti-Stokes lines in the Raman spectrum. According to quantum mechanics, the allowed changes in the vibrational quantum number of a simple harmonic vibration for Raman transition[116] is $\Delta v = \pm 1$.

4.2.3.2. Raman Spectroscopy of Graphene

Owing to its unique electronic, optical and mechanical properties, graphene has attracted significant interest in the scientific community. Raman spectroscopy is based on an optical microscope and it consequently easy to carry out sample analysis in ambient air with high efficiency and throughput. Raman spectroscopy is one of the most common methods used to analyse the various properties of graphene, such as thickness, stacking geometry, doping, defects, edge chirality and strain[119].

In modern times, Raman spectroscopy has played an important role in the characterisation of graphitic materials[120,121]. Normally, Raman spectroscopy provides an analysis of the lattice vibrational modes as explained in section 4.2.4.1. This makes Raman very sensitive to atomic arrangement and phonon structures and less sensitive to electronic structure. However, in the case of graphene and other carbon based materials, Raman scattering is very sensitive to the analysis of electronic energy levels due to the strong resonance effect[122].

The Raman signal observed for different numbers of graphene layers provides an easy and a non-destructive means to determine single, bilayer and few layer graphene when stacked in a Bernal (AB) configuration[64,123] Normally, graphene layers contain two prominent Raman active peaks[120–124] called the G peak, which sits around $\sim 1580\ cm^{-1}$, and the 2D peak, located at around $\sim 2680\ cm^{-1}$.

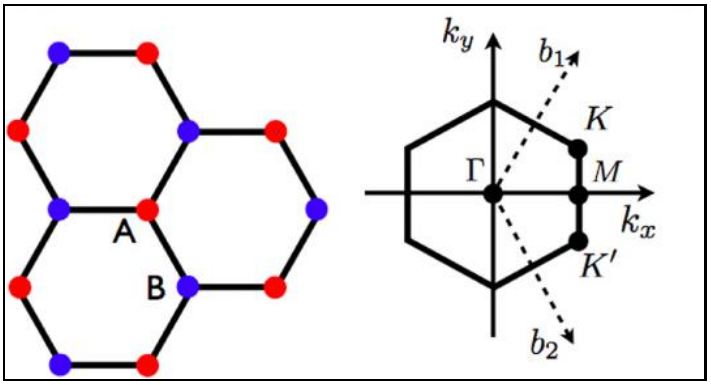

Figure 4.16: Lattice structure of graphene and the first brillouin zone (adapted from[65])

The origin of the G band is from the E_{2g} vibrational symmetry corresponding to the zero momentum phonon at Γ point, the in-plane transverse optical phonon branch. It corresponds to bond stretching of all pairs of atoms in both rings and chains of carbon[64]. The G band comes from the first order Raman scattering process and is linked to a doubly degenerate in-plane zone centre phonon mode. The 2D band on the other hand is a second order, double resonant process of the D band, originating from the breathing mode of an A_{1g} symmetry in sp^2 moieties in rings between non-equivalent K points in the brillouin zone, as shown in Figure 4.16. The first order response of the D band is Raman silent for a perfectly hexagonal sp^2-based carbon structure. The first order D band is only observed in the case of defects or disorders in the layers of graphene where the symmetry is broken and the peak appears around $\sim 1345\ cm^{-1}$. The G, D and 2D bands are depicted in the Raman spectra of pristine graphene and disordered graphene as reported by Ni[125] *et al.* in order to analyse the D peak intensity, the authors have used a standard quantity, I_D/I_G, which is the integrated intensity ratio for the D and G bands. In the case of the reported spectra, the I_D/I_G ratio was ≈ 1.2 and 32% for pristine and defect containing graphene respectively. The authors reported that it was difficult to detect the D peak below a few percent in intensity. In pristine crystals, they have observed I_D/I_G in the range of $0.5 - 1.5\%$[125].

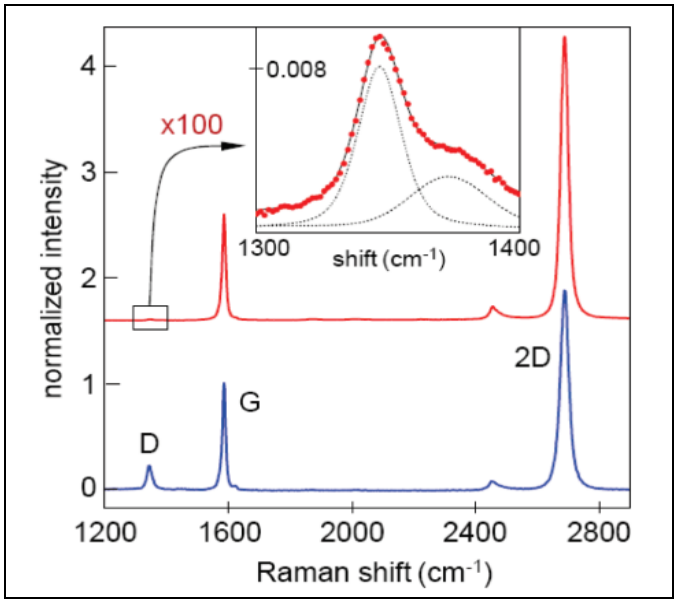

Figure 4.17: Raman spectra of pristine and defect containing graphene (red and blue curves respectively); $\lambda = 514.5\ nm$ *(adapted from*[125]*)*

There is a noticeable difference in the shape and the intensity of the 2D peak of graphene when compared to that of graphite as shown in Figure 4.18. The unique characteristic of the graphene 2D peak is that it is narrower and its intensity is about four times that of the G peak[123,126].

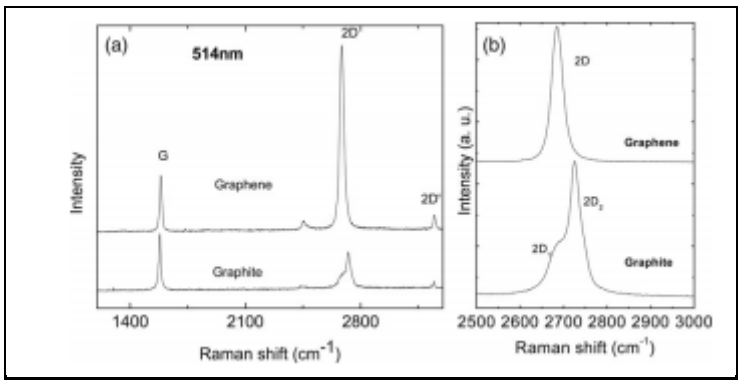

Figure 4.18: (a) Comparison of the Raman spectra of graphene and graphite, measured at $514.5\ nm$*. (b) Comparison of the 2D peaks in graphene and graphite (adapted from*[126]*)*

An even more important aspect of the G and 2D Raman modes is the change in position, shape and relative intensities depending on the number of graphene layers in the sample. Figure 4.19 shows the regions of G and 2D peaks as a function of number of layers in graphene samples measured using a $514\ nm$ and a $633\ nm$ laser source.

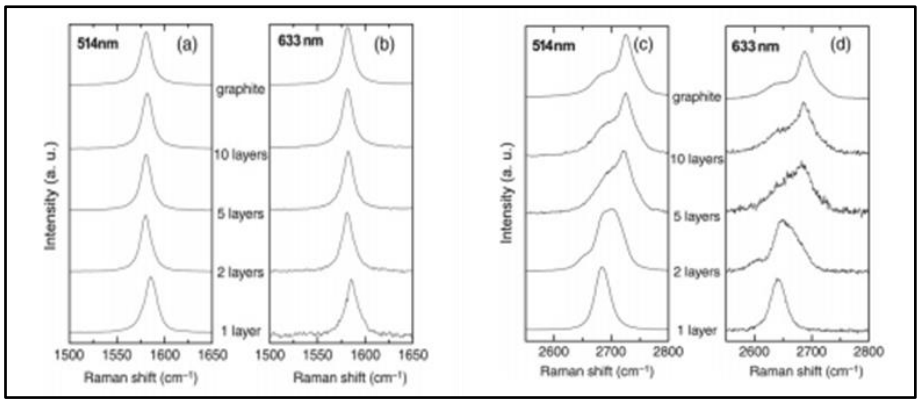

Figure 4.19: (a and b) Evolution of the G peak as a function of the number of layers for 514 *and* $633\ nm$ *excitations, and (c and d) evolution of the 2D peak as a function of the number of layers for* 514 *and* $633\ nm$ *excitations (adapted from*[126]*)*

It can easily be seen that the 2D peak of a bilayer graphene is broader than that of a monolayer in both laser excitations with the position being shifted upwards. The evolution of the 2D peak can be seen as the number of layers evolves up to 10 and after that it matches that from a graphite sample. A large reduction in the relative intensity of the 2D peak is observed as the number of layers increases. Consequently, with five or more layers, it becomes more and more difficult to distinguish the Raman spectra of graphene from that of graphite[126].

4.2.4. 3D X-Ray Microtomography

The surface analysis methods reviewed in the previous sections typically provide a two-dimensional (2D) representation of the sample surface which may include morphology and elemental distribution. AFM does provide a three-dimensional (3D) representation of the surface but is still limited to the analysis of the sample surface. Images of the internal structure of the sample are often obtained using radiation passing through the object and then being detected by a suitable detector. Suitable radiations include the electromagnetic spectrum from microwaves to gamma rays, and particles including protons, neutrons and electrons. 3D X-ray micro computed tomography (CT) is a radiographic technique that can produce 3D images of a material's internal structure at a spatial resolution better than 1 micrometer[127]. The technique is non-destructive, specimen preparation is minimal, and multiple scans can be completed for the same specimen

under different conditions. The principles of X-ray micro-CT are the same as the ones used in computerised axial tomography (CAT) scans in medical imaging for the last 40 years. The lab scale X-ray tomography apparatus used in this project is a Zeiss Xradia Versa XRM-520 (X-Ray Microscope) provided by Carl Zeiss X-Ray Microscopy, USA. The instrument is capable of providing a spatial resolution of $0.7\ \mu m$ and a minimum achievable voxel of $70\ nm$[128].

4.2.4.1. A Brief History of X-Ray Tomography

In X-ray radiography, the X-rays penetrate the sample, and are attenuated due the interactions with the electrons present in the material. An X-ray sensitive detector can be placed behind the sample to detect the 2D image of the sample. The first radiograph was collected by William Röntgen in 1896 who was awarded the first Nobel Prize in physics in 1901[129]. In 2D radiography, the features within the sample behind each other with respect to the direction of the beam are superimposed and cannot be separated. This is overcome by turning the sample and collecting multiples radiographs at different angles.

This technique was further developed and led to invention of medical tomography (CAT scans) by Godfrey Newbold Hounsfield[130] for which the patent was granted in 1976[131]. Hounsfield[129,130] demonstrated that instead of taking a single radiograph at certain angles if the object was rotated by 360° with radiographs being collected at regular angular increments, it was possible to approximately calculate the X-ray attenuation coefficient of any spatial volume inside the object by applying mathematical reconstructions. Hounsfield and Cormack received the Nobel Prize for Medicine for 1979[129].

4.2.4.2. Principles of Operation

The principle of tomography is illustrated in Figure 4.20. The sample to be imaged in placed in the trajectory of the X-ray beam. A proportion of the X-rays are absorbed and the rest are transmitted depending on the composition of the sample. The transmitted X-rays are scintillated to visible light which is focused before detection on a charged couple device detector. The sample is then rotated over 180° or 360° and during the rotation; a number of projections are recorded. These can be in several

hundreds, the higher the number of projections, the better the quality of reconstruction. The set of projections is used to reconstruct the 3D digital image of the sample using back projection mathematics. In case of the reconstructed digital image, each voxel (i.e., the 3D pixel) represents the X-ray absorption at that particular point. In normal lab conditions where the sample is close to the source, the contrast in the image is a result of the different X-ray absorptions by various microstructural features present in the sample. The density of the material, the atomic number and the energy of the X-rays will all affect the absorption coefficient of the sample[132]. Because of this relationship between the X-rays and the sample density, the internal 3D structure of the sample can be inferred from the images. The spatial resolution in the lab based X-ray CT systems is limited by the geometry of the X-ray beam, spot size of the X-ray beam, characteristics of the CCD detectors, optics system and the pixel size of the camera[127,132].

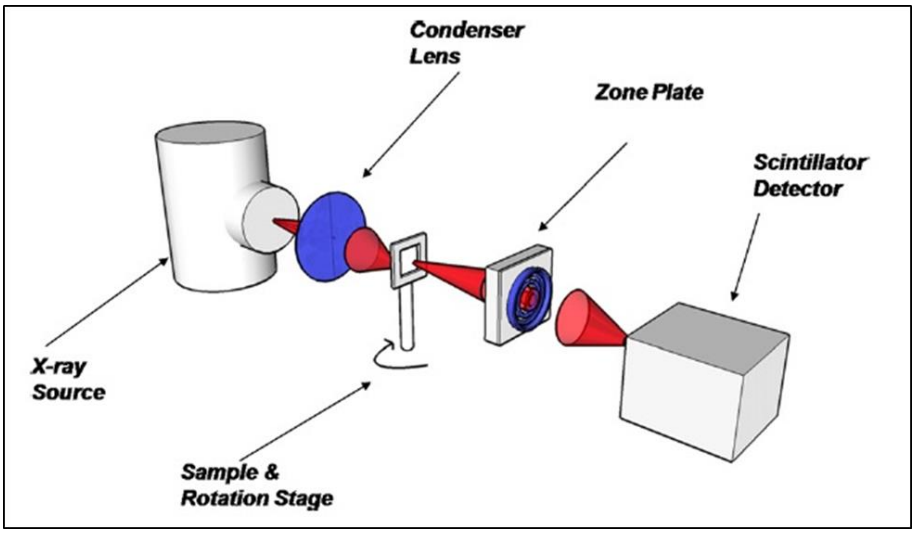

Figure 4.20: Schematic diagram of a lens-based X-ray CT system (reproduced from[133])

4.2.4.3. Lab Scale X-Ray Tomography

In the Versa 520 system used here, the characteristic X-rays are generated by bombarding a tungsten target anode with thermionic electrons. The resulting X-ray beam passes through changeable high energy or low energy source filters resulting in the change in the photon energy impinging the sample. This can be adjusted for particular samples depending on the density of the sample being studied.

The key parameters required for setting up the X-ray CT scan are the source voltage, use of variable low energy or high energy filters, the sample within the field of view, the exposure time, the distance between the source and the sample, the sample and the detector[134]. These parameters determine the resultant photon counts, transmission (the ratio between the transmitted intensity and the initial intensity), the pixel size and the number of projections. In order to achieve a better image quality, the transmission through the most attenuated part of the sample needs to be $20 - 35\ \%$[132,134].

4.2.4.4. Application of X-Ray Tomography in Corrosion

Electrochemical methods, including potential mapping, linear sweep voltammetry, etc. provide information whether the steel is passive or the de-passivation has been initiated. In other words, it can provide information on the surface films and oxide layers. However, this would not provide information on the type of corrosion, the extent or the distribution of corrosion products within the sample or even on the sample surface. X-ray CT can provide an excellent option for analysing, not only the surface of a metal but the extent of corrosion within the structure of the corroding metal. X-ray CT can provide crucial microstructural information, especially in the case of stress corrosion, corrosion cracking and inter-granular corrosion where the corrosion is not necessary restricted to the surface of the metal. Beck[135] *et al.* studied the corrosion of steel reinforcement in concrete that was exposed to 4% chloride by weight of the cement. They studied the corrosion using electrochemical methods as well X-ray CT. The authors pre-damaged the sample by applying static galvanic polarisation within the range of $5 - 25\ \mu A/cm^2$ (1-15 days: $5\ \mu A/cm^2$; 15-25 days: $12.5\ \mu A/cm^2$; 25-40 days: $25\ \mu A/cm^2$). The authors demonstrated that X-ray tomography is a suitable technique to images corrosion pits which were embedded in a mortar with a cover thickness of about $35\ mm$.

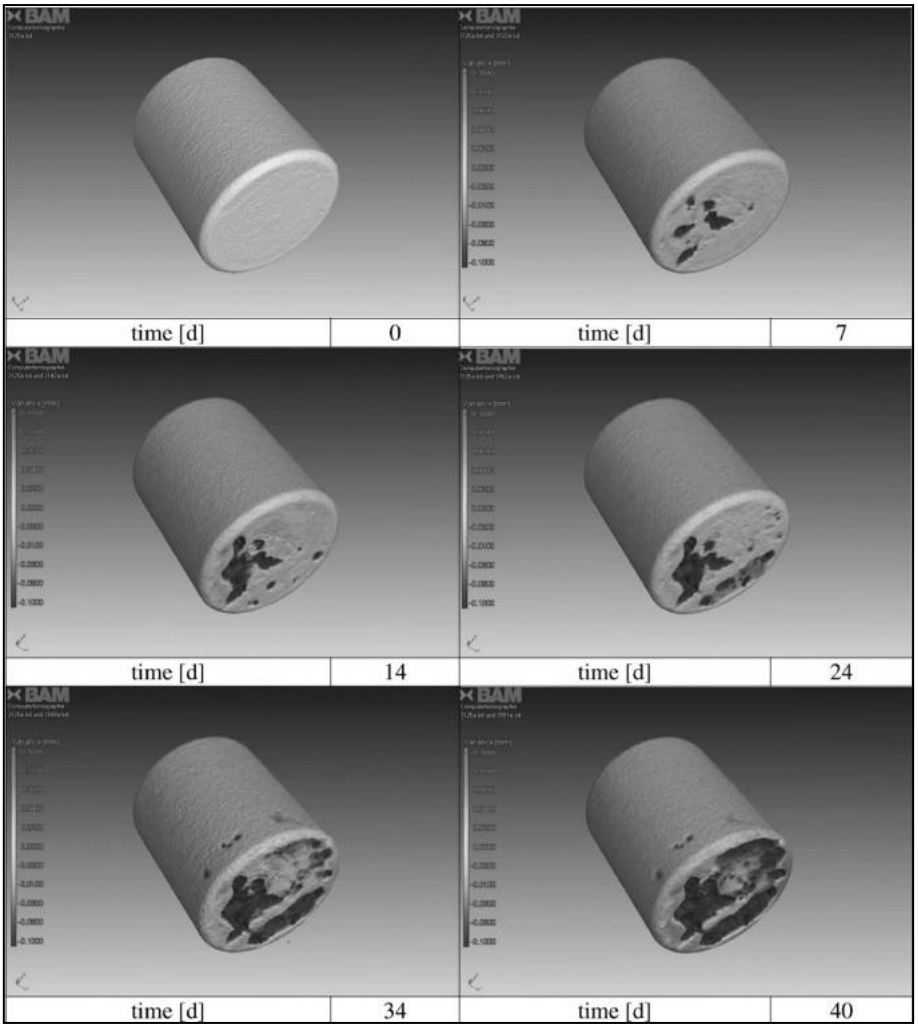

Figure 4.21: Specimen surface of stainless steel reinforced by mortar reconstructed by X-ray tomography (reproduced from[135])

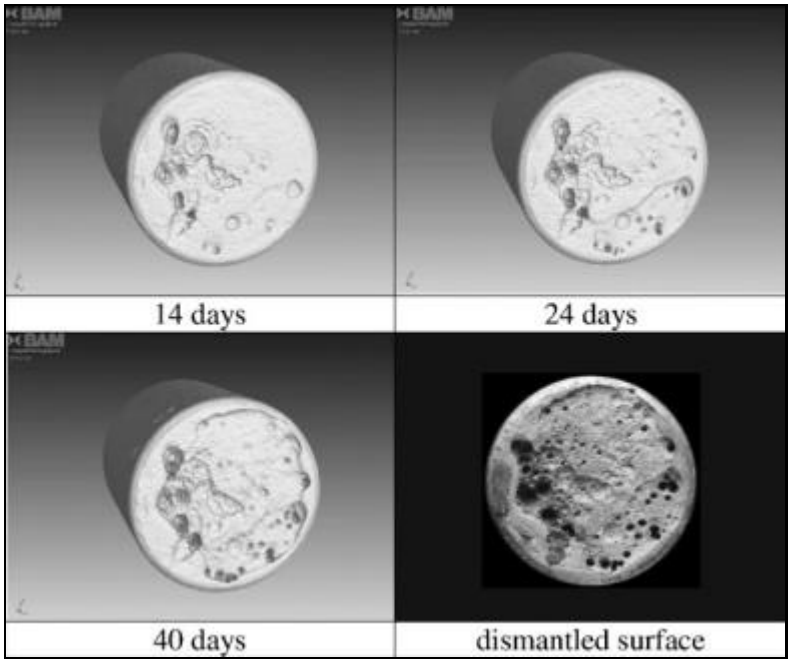

Figure 4.22: Development of pitting corrosion at the bottom of the surface (reproduced from[135])

The authors reported that initially up to the period of 14 days the corrosion was dominated by uniform corrosion attack, as shown in Figure 4.21 and Figure 4.22. Once a higher static current was applied from the 15th day onwards, the appearance of the surface changes significantly and signs of pitting corrosion are visible at the bottom of the sample. X-ray CT provides a suitable method to detect corrosion pits on embedded steel bars. In addition, this method enables the observation of corrosion pits and their growth *in situ* without destroying the specimen.

Similar work was reported by Goebbels[136] *et al.* who studied the self-corrosion of stainless steel cylinders embedded in mortar made up with 4% chlorides. In this work they did not apply static galvanic polarisation as was the case reported by Beck[135] *et al*, rather the authors conducted electrochemical tests and collected tomography images at regular intervals for a period of 14 months. The authors used $225\ kV$ X-ray source with a flat panel detector (Perkin Elmer XRD 1620 AM3 with a CsI scintillator screen, 2048 x 2048 elements). Figure 4.23 shows the surface and the cross section of the sample at the end of the self-corrosion test period of 14 months demonstrating pits on the sample surface.

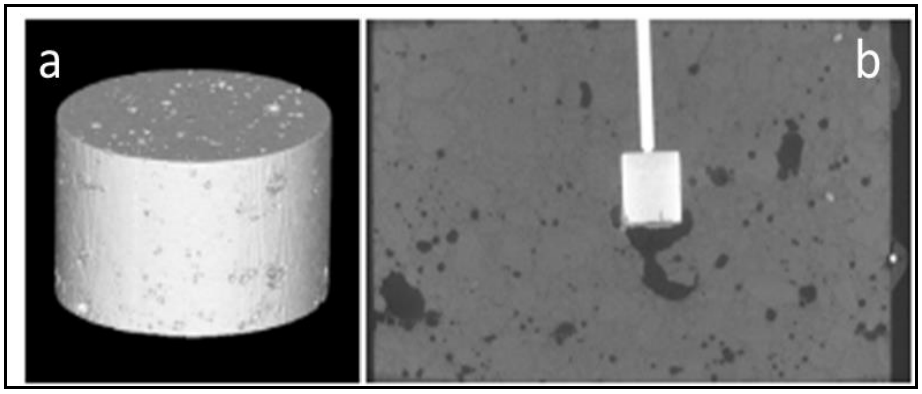

Figure 4.23: (a) X-ray CT image of the surface of the sample and (b) the cross-section of the sample (reproduced from[136]*)*

Cesen[137] *et al.* compared the characterisation of steel in mortar using electrochemical techniques and X-ray micro CT. The authors used 5 mm diameter steel rods for corrosion experiments. These rods were embedded in mortar using four different sample assemblies. The total average corrosion rate was approximately $390\ \mu m$ per year. One specimen was investigated fully by means of X-ray CT. The authors reported some wide pits that were a few tens of µm in width and depth; however, mild general corrosion formed the predominant form of corrosion damage as shown in Figure 4.24.

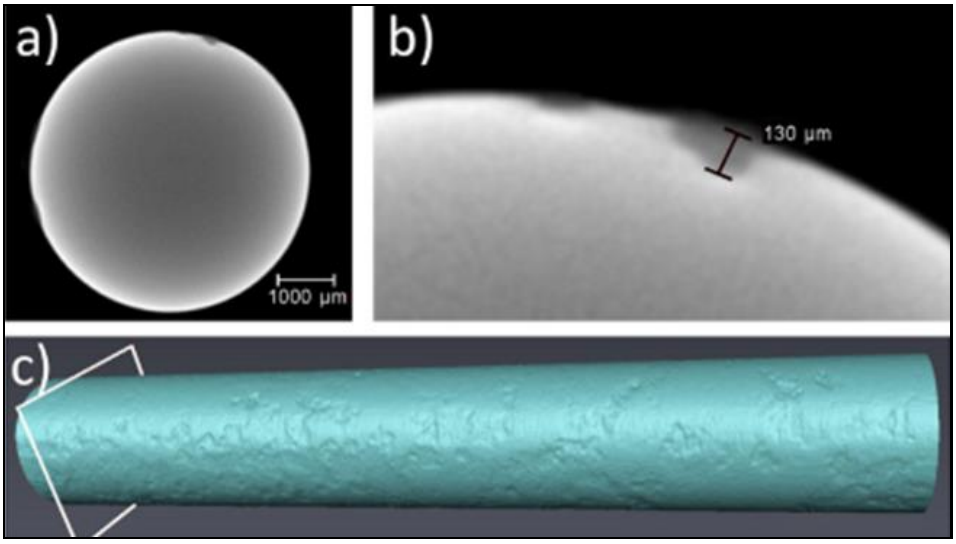

Figure 4.24: X-ray CT image of steel rod (a) cross-sectional view, (b) detail of the cross-section, and (c) longitudinal 3D view (reproduced from[137]*)*

The coupled multi-electrode array was thoroughly investigated by the authors using X-ray CT (Figure 4.25a). The spatial resolution of the X-ray

CT scans was roughly 10 µm. A few electrodes can be seen to have corroded heavily (A4, C2, D2), some showed medium damage (A5, C1, C4, D1, D3, D5), and the other half (A1, A2, A3, B1, B3, B4) remained completely intact. The authors also reported that the X-ray CT observations were in complete agreement with electrochemical data. The scans of 2 electrodes (C2 and D2) seen in Figure 4.25b, show clear pits on the two electrodes were several hundred µm deep.

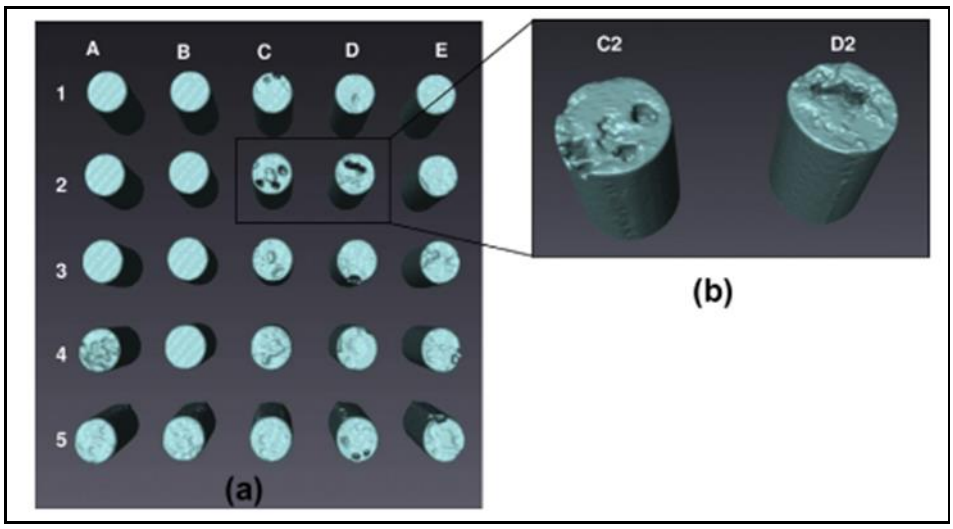

Figure 4.25: X-ray CT scans of the coupled multi-electrode array; (a) the entire array and (b) the selected electrodes (C2 and D2) (reproduced from[137]*)*

In summary, X-ray CT has been employed successfully to study hidden corrosion in case of corrosion in reinforced steel in concrete. X–ray CT has enabled the study of corrosion pits and the calculation of pit parameters in terms of the width and the depth of the corrosion pits. The technique can also provide information on the microstructure of the metal itself. In case of corrosion, it can provide information on the effect of corrosion on the microstructure and any effects on the grain boundaries of the alloys.

5. Electrochemical Corrosion Analysis

The aim of this PhD project is to propose functionally coated mild steel as an alternative to stainless steel for BPP applications in PEMFCs. The chapter presents the results of electrochemical corrosion analysis of commercially purchased AISI (American Iron and Steel Institute) - stainless steel 316L ($300 \times 300 \times 0.5\, mm^3$, Goodfellow, UK, FF210350: $Cr\ 18\%, Ni\ 10\%, Mo\ 3\%$ and Fe to balance with other elements present in $< 1\%$, annealed) material as a benchmark for the present day BPPs used in most of the PEMFCs produced on a commercial scale. The three mild steel materials analysed during the project are; HILAN®; bright nickel-plated mild steel[138], HILUMIN®; ultra-clean nickel-plated mild steel[139], and mild steel black plates (no alloying elements present, $< 0.3\%$ carbon, Fe to balance). All the mild steel substrates are provided by Tata Steel Research & Development, IJmuiden Technology Centre, IJmuiden, Netherlands. In addition to these, a Tata proprietary coated mild steel material has been analysed for its corrosion performance in simulated fuel cell environment.

As discussed in chapter 4, the materials are first analysed for their ICR performance, then their corrosion rates are determined using linear sweep voltammetry. The materials are then analysed for their potentiostatic corrosion performance under simulated fuel cell conditions. The selected samples have been analysed using novel accelerated corrosion tests, simulating start-up and shut down cycles in a fuel cell. SEM images have been recorded to compliment the corrosion data obtained through the electrochemical tests.

This chapter also discusses the *in situ* fuel cell performance of a SS 316L BPP as compared to graphite BPP. The chapter discusses the characteristics of SS 316L when used as a BPP material, and the fuel cell performance shows the effect of the passive layer on the performance of SS 316L. The high cost of SS 316L, along with the decrease in the output due to the oxide film, provides an opportunity to use mild steel as a BPP material. However, due to the lack of alloying elements, the mild steel

materials offer poor corrosion resistance in comparison to stainless steel and coated mild steel would be a viable option for BPP for PEMFC.

5.1. ICR Test Results

The ICR values are measured at different compressions in a range of $20 - 200\,N$ using EIS. The resistance values are plotted against compression for the four bare substrates and the functionally coated mild steel. In all cases, the ICR values decrease with an increase in the compression. The trend in the ICR values for SS 316L has been found to be in agreement with that reported by Silva *et al.*[33], Wang *et al.*[26], Davies *et al.*[31]and Gabreab *et al.*[104]. The absolute ICR values for SS 316L at $140\ N.cm^{-2}$have been found to be higher than that reported by Gabreab *et al.*[104]and Wang *et al.*[26], but similar to those reported by Feng *et al.*[44].

The ICR values for functionally coated mild steel are found to be an order of a magnitude lower than that of SS 316L, corresponding to better conductivity. The ICR values for the bare substrates and that of the functionally coated mild steel at $140\ N.cm^{-2}$ are reported in Table 5.1. The Department of Energy[21] (DOE) 2017 target for contact resistance is $20\ m\Omega.cm^2$ at $140\ N.cm^{-2}$.

Table 5.1: ICR values at 140 N cm^{-2} for bare substrates and functionally coated mild steel

Material	Resistance / $m\Omega.cm^2$ at $140\ N.cm^{-2}$
SS 316L	388
HILAN	61
HILUMIN	116
Bare Mild Steel	276
Functionally Coated Mild Steel	34

The ICR values for bare SS 316L are significantly higher than the DOE target. The high resistance produced by SS 316L can be attributed to the stable oxide film formed on the surface of stainless steels in general including SS 316L. The lower ICR values for the functionally coated mild steel sample, as shown in Figure 5.1, along with the lower cost of the mild

steel base material as compared to SS 316L, provide an alternative option for BPPs in PEM fuel cells. The low contact resistance values offered by the functionally coated mild steel would result in better fuel cell output as result of the reduction in Ohmic losses.

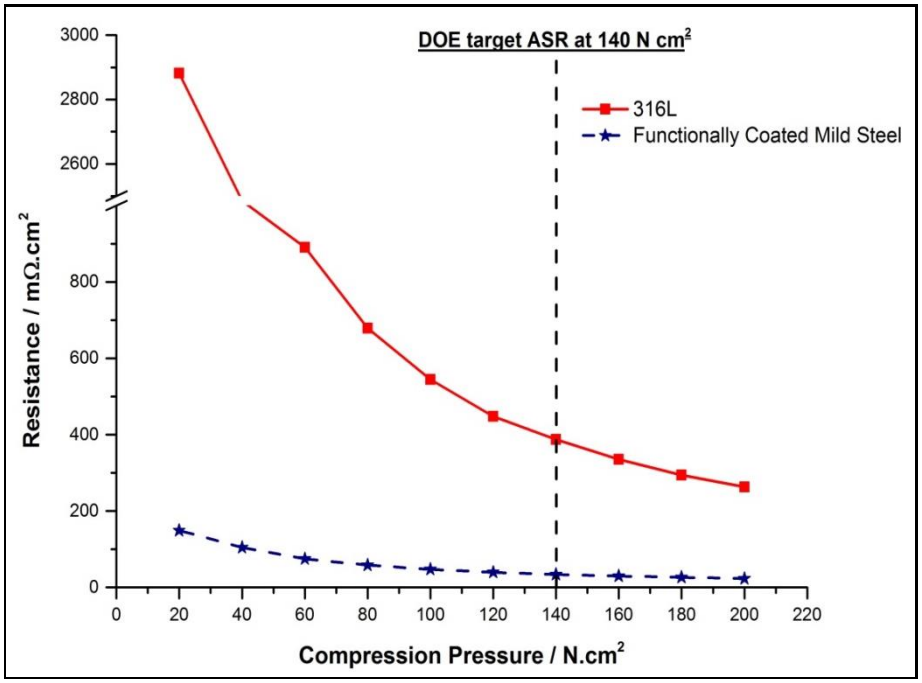

Figure 5.1: Resistance vs compression for SS 316L and functionally coated mild steel

The ICR for the bare mild steel substrate is eight times higher than that of the functionally coated mild steel. The higher values can be attributed to the lack of alloying elements and the formation of iron oxides in the presence of air. HILAN and HILUMIN have ICR values dependent on the final finishing of the nickel coating on the surface. HILAN has a smoother finish compared to HILUMIN resulting in more contact points between the metal surface and the GDL at any given compression pressure. As a result, HILAN has better ICR performance compared to HILUMIN, and in general both these substrates have performed better than the bare mild steel and the SS 316L, as shown in Figure 5.2.

In conclusion, the functionally coated mild steel produces improved conductivity compared to SS 316L, providing an alternative option for BPP applications. The HILAN and HILUMIN steels have shown better ICR performance in comparison to SS 316L. However, the electrical

conductivity of the steels is not the only requirement for BBPs, and the corrosion resistance results will provide a better understanding of the overall performance of the different materials.

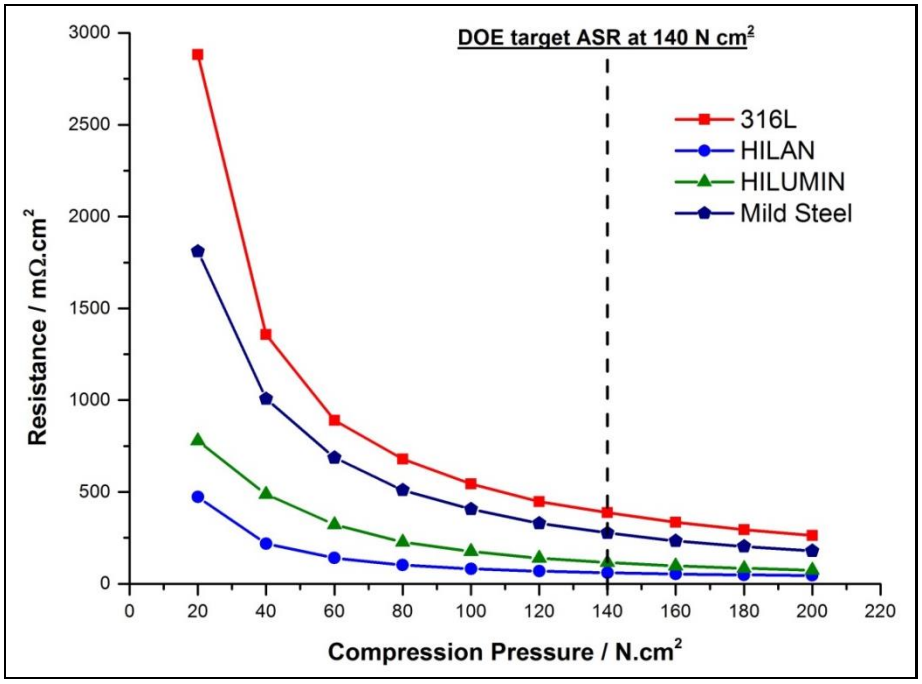

Figure 5.2: Resistance vs compression for the different bare steel substrates

5.2. Potentiodynamic Polarisation Results

Potentiodynamic tests were carried out to investigate the corrosion performance of the bare materials and the coated mild steel. The test solution used was $0.1\ M\ H_2SO_4\ +\ 2\ ppm\ F^-$, purged with air and hydrogen to simulate *in situ* fuel cell cathodic and anodic environments respectively. The tests were repeated at 25 °C (room temperature) and 80 °C (fuel cell operating temperature). The reference electrode used in the experiments was a reversible hydrogen electrode (RHE) and all the potentials reported are against RHE. The potentiodynamic curves for the five materials under different conditions are depicted in Figure 5.3 - Figure 5.6.

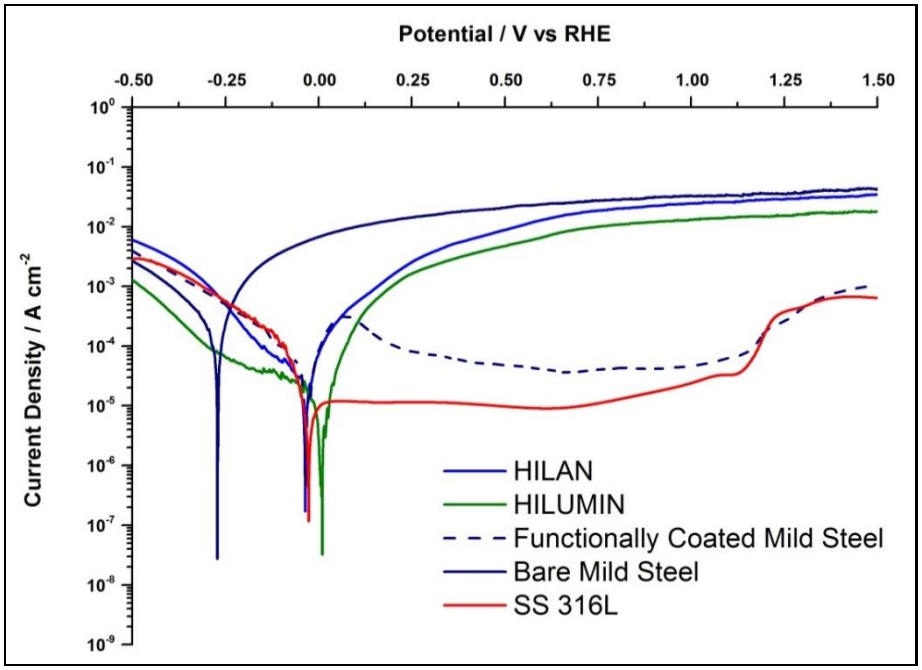

Figure 5.3: Potentiodynamic polarisation curves for the four bare substrates and functionally coated mild steel under air environment at 25 °C

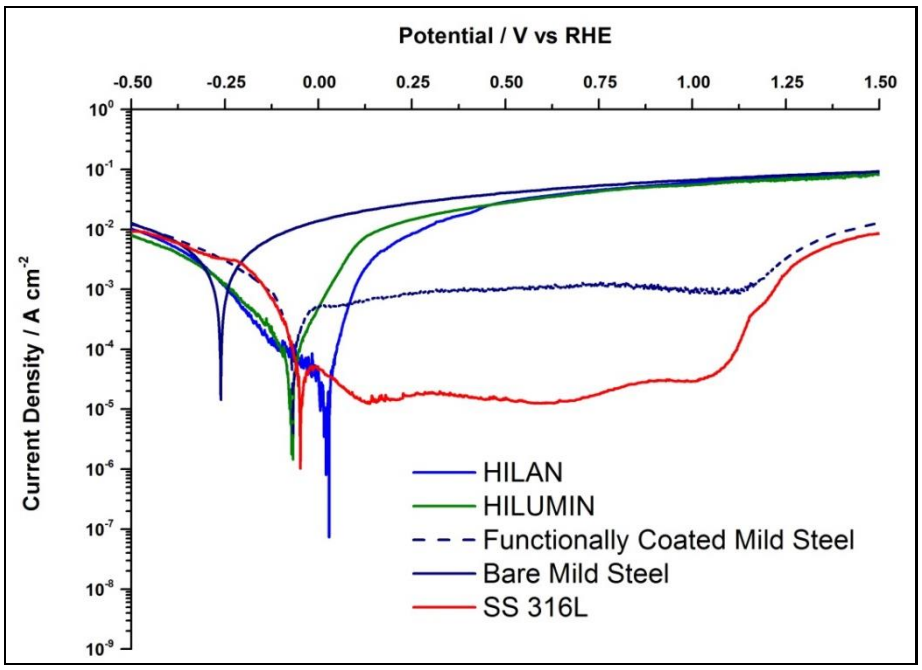

Figure 5.4: Potentiodynamic polarisation curves for the four bare substrates and functionally coated mild steel under air environment at 80 °C

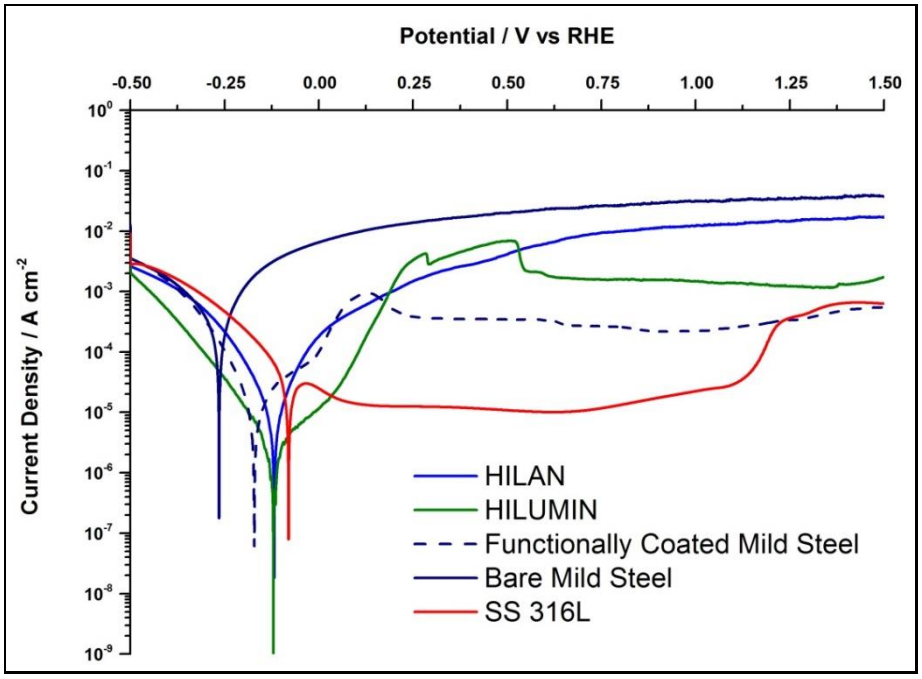

Figure 5.5: Potentiodynamic polarisation curves for the four bare substrates and functionally coated mild steel under hydrogen environment at 25 °C

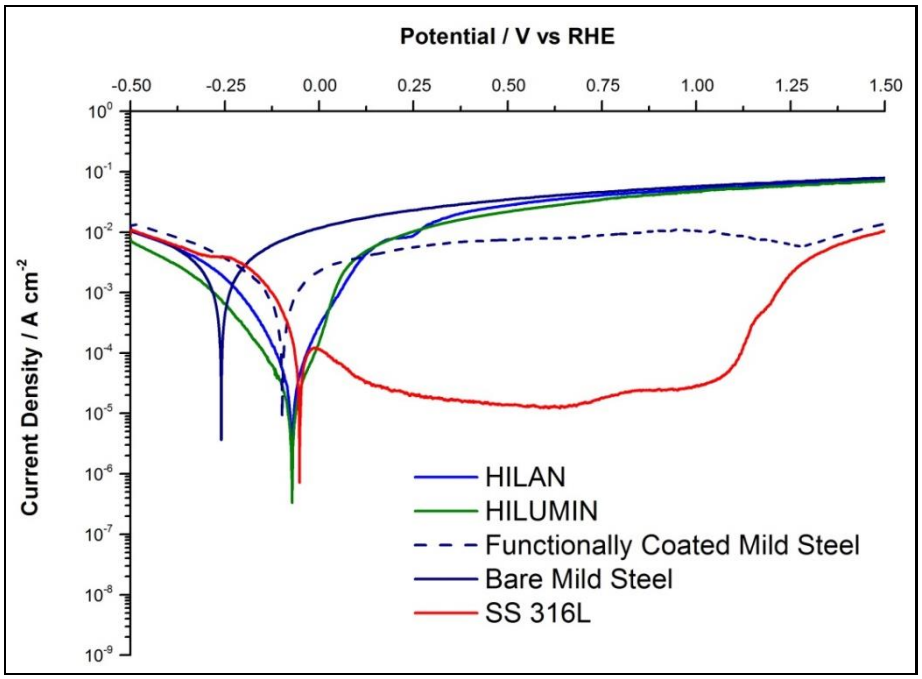

Figure 5.6: Potentiodynamic polarisation curves for the four bare substrates and functionally coated mild steel under hydrogen environment at 80 °C

The key characteristic of SS 316L is the presence of three distinct areas; identified as the active corrosion region, the passive region and the trans-passive region, as discussed in section 3.2.2. Passivation can be defined

as a condition of corrosion resistance occurring due to the formation of a thin surface layer under oxidizing conditions. This oxide layer makes stainless steel highly corrosion resistant under a variety of atmospheres. Chromium forms a very stable surface in oxidising conditions when it is alloyed with Iron, as in the case of SS 316L. The corrosion rate at the anodic current density is almost an order of magnitude higher as compared to the cathodic state, and increases further with the potential in the active state. Once the potential gets above the primary passive potential, the passive film becomes stable and corrosion current density falls to lower values (which is an order of magnitude lower than the active state corrosion current density). The potential beyond $1V$ corresponds to the end of the passive region and the initial point of evolution of oxygen. This may correspond to the potential at which there is a sudden increase in the current density due to the breakdown of the passive film on the metal surface in the anodic region[90]. This inherent passive layer in a SS 316L sample makes it highly corrosion resistant and results in comparatively low passive current density in the fuel cell cathodic region near $0.8\,V$. The presence of a stable oxide film results in the high ICR values reported in section 5.1.

The corrosion current densities and the rate of corrosion calculated using the method discussed in chapter 3.2.2.1 for different substrates under the anodic and cathodic fuel cell conditions are recorded in Table 5.2 and Table 5.3 respectively. The corrosion current densities are measured using the Metrohm Autolab potentiostat with $+/-0.2\,\%$ accuracy and a current resolution of $0.0003\,\%$ of the current range. The current range is selected automatically by the potentiostat. As corrosion rate is directly proportional to the corrosion current, it can be calculated with the same accuracy as of the corrosion current. As a general trend, the corrosion current densities, and therefore the rate of corrosion, increase in all the samples with an increase in the temperature. The corrosion reaction proceeds at higher rates at the operational temperature of the fuel cell as compared to room temperature. Bare mild steel is expected to have a very high corrosion rate under all conditions, compared to the other samples, due to the lack of any alloying elements or passive layer protection. The nickel coated mild steel samples; HILAN and HILUMIN, have demonstrated better corrosion resistance compared to the bare mild steel. However, linear sweep

voltammetry provides the corrosion rates at the corrosion potential or the open circuit potential, whereas a key feature in a fuel cell operation is the corrosion at the cathode operation voltage of $0.8\,V$. In this case, the three mild steel substrates lack any passive layer protection around $0.8\,V$, resulting in high passive currents.

Table 5.2: Corrosion current densities in terms of $\mu A.cm^{-2}$ *under different conditions for the four bare substrates and functionally coated mild steel*

Material	Hydrogen (Anode)		Air (Cathode)	
	25 °C	80 °C	25 °C	80 °C
SS 316L	9.6×10^{1}	4.0×10^{2}	5.4×10^{1}	1.8×10^{2}
HILAN	2.3×10^{1}	8.4×10^{1}	3.4×10^{1}	3.9×10^{1}
HILUMIN	5.6×10^{1}	8.1×10^{1}	2.9×10^{1}	1.6×10^{2}
Mild Steel	5.9×10^{2}	2.2×10^{4}	4.6×10^{2}	2.3×10^{4}
Functionally Coated Mild Steel	2.6×10^{1}	7.7×10^{3}	7.8×10^{1}	5.3×10^{2}

Table 5.3: Rate of corrosion in terms of mm per year under different conditions for the four bare substrates and functionally coated mild steel

Material	Hydrogen (Anode)		Air (Cathode)	
	25 °C	80 °C	25 °C	80 °C
SS 316L	0.7	3.1	0.04	1.4
HILAN	0.2	0.7	0.3	0.3
HILUMIN	0.04	0.6	0.2	1.2
Mild Steel	4.5	173.3	3.6	174.4
Functionally Coated Mild Steel	0.2	59.4	0.6	4.1

To summarise, the functionally coated mild steel material provides some passive protection in comparison to the bare substrates. However, it still produces higher passive currents than SS 316L, which provides the best corrosion protection around the cathode voltage. Compared to bare mild steel, the functionally coated mild steel sample provides improved corrosion protection due to the presence of a passive layer, whilst providing improved conductivity as observed in the ICR results. A further understanding of the

materials' corrosion protection characteristics can be gained using potentiostatic corrosion tests.

5.3. Potentiostatic Tests

Potentiostatic experiments have been carried out by holding the potential of the working electrode at $0.1\,V$ and $0.8\,V$ respectively, to simulate anodic and cathodic PEMFC conditions in $0.1\,M\,H_2SO_4 + 2\,ppm\,F^-$ solution. During the anodic and cathodic experiments the electrolyte solution was purged with hydrogen and air respectively. The low passive current density at the cathode for SS 316L could be attributed to the formation of the SS 316L passive layer at $0.8\,V$ in presence of oxygen. The anodic current response is a result of the active dissolution of steel in the electrolyte at $0.1\,V$. Wang and Northwood[36] measured the potentiostatic current response of SS 316L in a $0.5\,M$ sulphuric acid solution at 70 °C. The anode peak current density for SS 316L, as reported by the authors, was found to be $-0.7\,\mu A.cm^{-2}$, in comparison to $-0.19\,\mu A.cm^{-2}$ as obtained during the experiments reported in this work: for comparison the authors[36] used a $0.5\,M$ sulphuric acid solution as opposed to the $0.1\,M$ solution used in these experiments.

Table 5.4: Anodic and cathodic potentiostatic current response for SS 316L, mild steel and functionally coated mild steel

Material	Temperature °C	Anode peak current density $\mu A.cm^{-2}$	Cathode passive current density $\mu A.cm^{-2}$
SS 316L	25	-2.6 x 10^{-1}	1.0 x 10^{-2}
	80	-1.9 x 10^{-1}	7.3 x 10^{-1}
Mild Steel	25	6.5 x 10^{4}	6.5 x 10^{4}
HILAN	25	1.7 x 10^{2}	8.8 x 10^{2}
HILUMIN	25	9.5 x 10^{1}	6.3 x 10^{2}
Functionally Coated Mild Steel	25	1.6 x 10^{1}	1.4 x 10^{1}
	80	2.0 x 10^{2}	2.9 x 10^{1}

It is evident that SS 316L provides better corrosion protection compared to bare mild steel. The mild steel corrosion current is five orders of magnitude higher than that for SS 316L at room temperature. In the case of mild steel at 80 °C, the 0.5 mm thick samples have dissolved completely in acid, resulting in incomplete current density data for the full experiment duration of $10\ h$. A similar trend is observed for HILAN and HILUMIN as well where higher corrosion current is observed under both anodic and cathodic conditions at 25 °C and the samples have dissolved at the elevated temperature of 80 °C. This emphasises the lack of any corrosion protection offered by the mild steel samples.

The functionally coated mild steel provides improved corrosion protection, with respect to the bare mild steel, however the corrosion current is two orders of magnitude higher than SS 316L, especially in an anodic environment at 80 °C. For comparison, the 2017 DOE[21] standards for current response are defined at less than 1 $\mu A.cm^{-2}$: SS 316L provides the required corrosion protection while the functionally coated mild steel does not meet the standard with respect the current response. For the coated mild steel substrate, the absence of a passive layer has resulted in improved surface conductivity, and hence low ICR, but has resulted in higher corrosion rates when compared to SS 316L. However, the improved performance when compared to bare mild steel provides an option to explore the viability of using the coated mild steel for BPPs.

5.4. Accelerated Corrosion Tests

The EIS response of the samples was determined by the resistive and capacitive properties of the passive film[140]. The measured capacitive response is often imperfect, and hence its spectrum is fitted using a constant phase element (CPE) instead of an ideal capacitive element. The equivalent circuit[46] used for fitting the data from the accelerated corrosion tests is presented in Figure 5.7. As the surface morphology of the working electrode changes, the CPE of the electrode changes, owing to the decrease in the value of the exponential factor n. This results in the formation of a depressed semi-circle. The diameter of this semi-circle provides information on the polarisation resistance of the working electrode

which changes due to corrosion. In an ideal situation, $n = 1$ and the CPE is represented as a pure capacitor; however, in the real world, the capacitor is represented by CPE, which takes into consideration the roughness of the electrode.

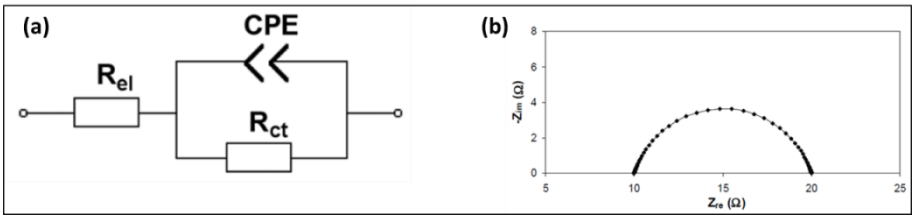

Figure 5.7: (a) Equivalent circuit used to fit the accelerated corrosion test data. R_{el} is the resistance of the electrolyte, R_{ct} is the charge transfer resistance originating from the change in the surface of the working electrode and CPE is the constant phase element for the working electrode. (b) gives an example of a data fit using this equivalent circuit

The parameters CPE and R_{ct} are not only corrosion dependent, but also reflect the overall electrical resistance and dielectric properties of the material. In an environment promoting oxidation, the growth of the oxide layer depends on the transport of the ions, or their vacancies, across the oxide layer. Defects in the oxide layer, such as pores, channels or cracks, allow the electrolyte to penetrate the layer and reduce the electrical resistance. In addition to this, penetration of the passive film results in pitting corrosion, and as a consequence the overall resistance decreases further. A surface oxide layer exhibits a capacitive behaviour owing to the dielectric nature of the oxide and surfaces that exhibit surface roughness or porosity, such as those undergoing corrosive decay, would deviate from this ideal capacitive behaviour[141].

Figure 5.9 presents EIS spectra taken during accelerated corrosion testing of the SS 316L samples, at room temperature under air environment at $0.8\,V$, simulating a cathode fuel cell environment. The SS 316L sample displays high resistance values during the corrosion tests. Over time, the sample starts to form a passive layer in the presence of the oxidative environment and the resistance of the sample increases as the sample is passivated.

Within the time frame for accelerated corrosion tests, monitored using EIS, it was not possible to measure low frequencies at steady state (owing to the ongoing corrosion processed during the EIS scan); therefore the data has been fitted using an extrapolation of the curve. The polarisation resistance values for the SS 316L samples under cathodic conditions at 23 °C are obtained through the EIS data, and fitted using the equivalent circuit represented in Figure 5.7. The polarisation resistance increases with time suggesting the formation of a passive layer that leads to the increase in resistance shown in Figure 5.9.

The two samples held under a cathodic environment, at 23 °C and 80 °C (Figure 5.9 and Figure 5.10), did not show visible surface degradation in terms of physical damage to the surface. However, both the samples held at $0.8\,V$ vs SHE under air environment have developed a thicker passive layer, as indicated by the increase in the polarisation resistance of the material over time.

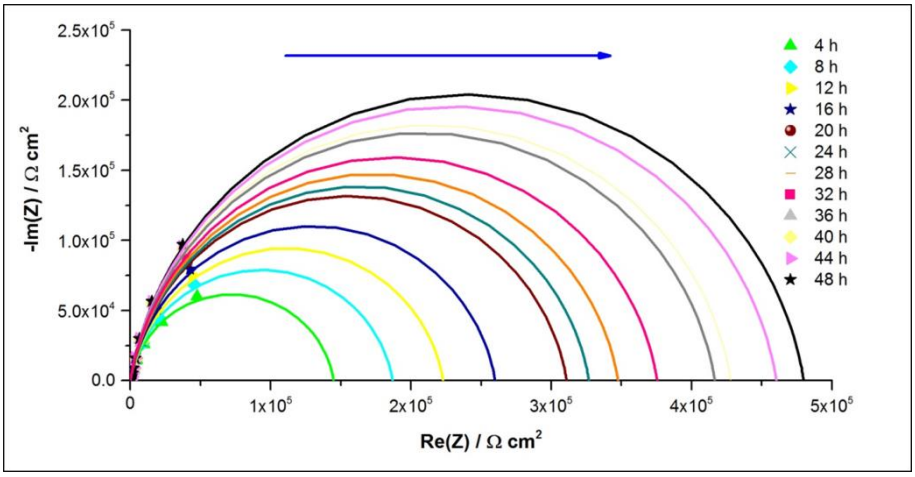

Figure 5.8: Electrochemical Impedance Spectra (symbols: EIS data and lines: fitted data) obtained for SS 316L under cathodic conditions (0.8 V at 23 °C in air)

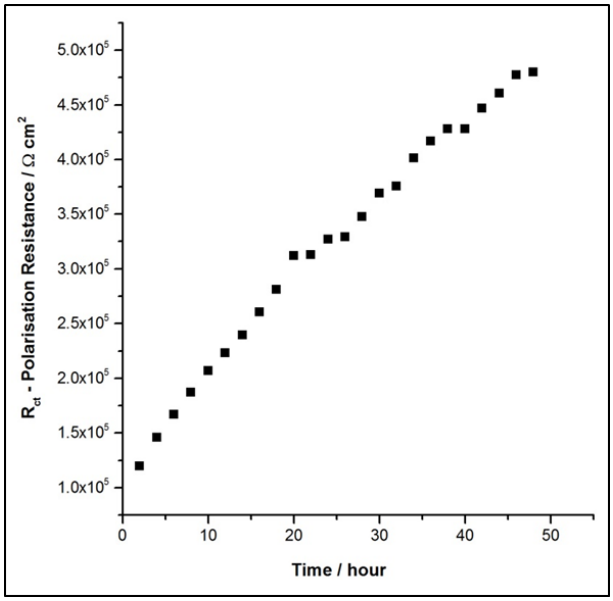

Figure 5.9: Change in polarisation resistance vs time for the fitted data, obtained for SS 316L under cathodic conditions (0.8 V at 23 °C in air)

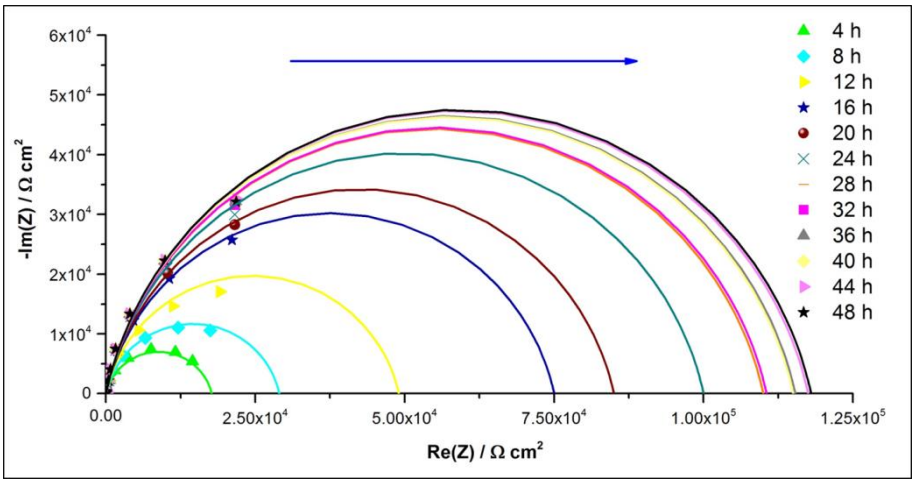

Figure 5.10: Electrochemical Impedance Spectra (symbols: EIS data and lines: fitted data) obtained for SS 316L under cathodic conditions (0.8 V at 80 °C in air)

The sample held at anodic conditions at 23 °C (Figure 5.12) has resulted in the active dissolution of the material. From the potentiodynamic test results in section 5.2, it can be expected that SS 316L will have a comparatively higher corrosion rate under the anodic conditions at $0.1V$. The lack of a passive film at $0.1V$ would result in the higher rate of corrosion, which would result in active dissolution of the material over the duration of the experiment. This is evident in the fitted polarisation resistance values for

SS 316 under anodic conditions, depicted in Figure 5.12. The polarisation resistance decreases with time suggesting that active dissolution of the material occurs.

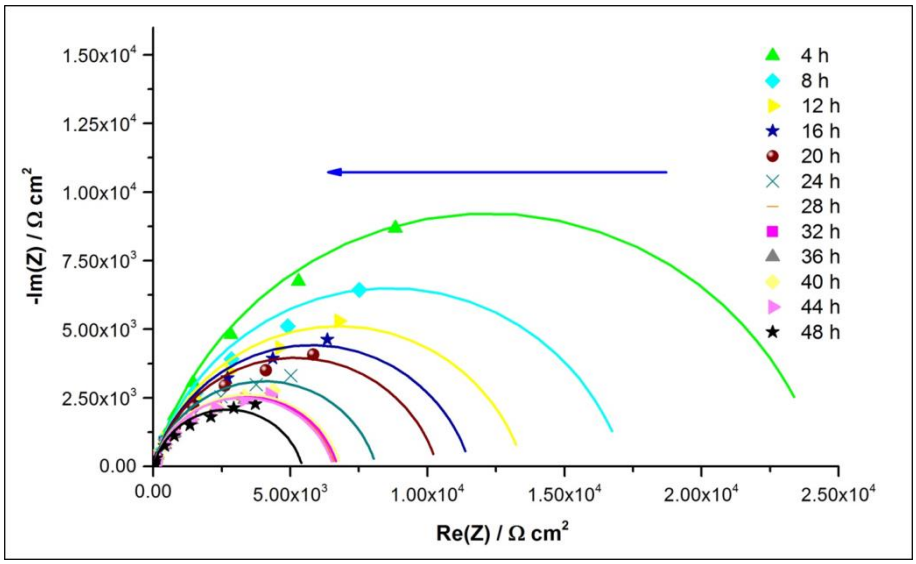

Figure 5.11: Electrochemical Impedance Spectra (symbols: EIS data and lines: fitted data) obtained for SS 316L under anodic conditions (0.1 V at 23 °C in hydrogen)

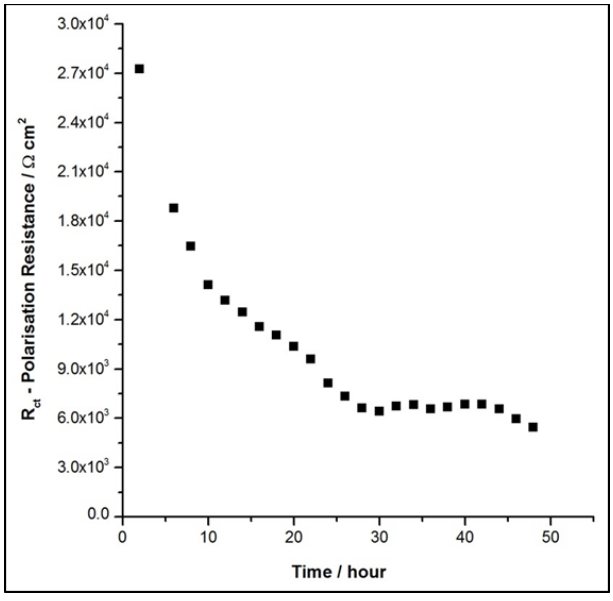

Figure 5.12: Change in polarisation resistance with time for the fitted data, obtained for SS 316L under anodic conditions (0.1 V at 23 °C in hydrogen)

5.4.1. SEM Imaging

SEM images show that the SS 316L corroded at $0.8\,V$ under an air environement resulted in the formation of an oxide layer on the sample surface (Figure 5.13 (b-c)). The oxide layer has subsequently prevented further corrosion of the material, eventually protecting the material from the corrosive electrolyte. The sample held at $0.1\,V$ under a hydrogen environment at 80 $^{\circ}$C has corroded the most (Figure 5.13 (e)) compared to the un-corroded samples. The grain boundaries of the alloy have been damaged, exposing the sample to further corrosion.

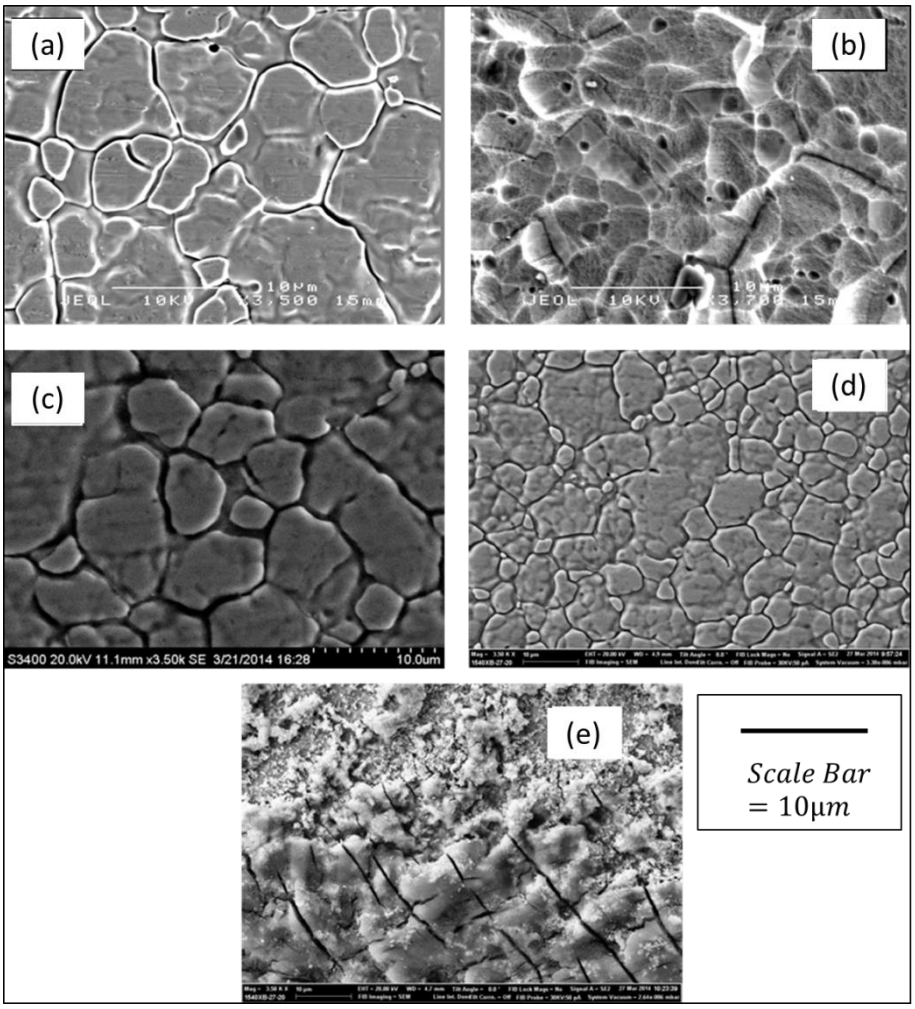

Figure 5.13: SEM images of SS 316L samples: (a) un-corroded, (b) air purged at 23 °C, (c) air purged at 80 °C, (d) hydrogen purged 23 °C, and (e) hydrogen purged 80 °C

The lack of oxygen, which would regenerate the protective oxide layer, in the hydrogen rich anodic environment leads to damage of the passive layer and hence corrosion proceeds at faster rates, aided by the elevated (80 $^{\circ}$C) temperature.

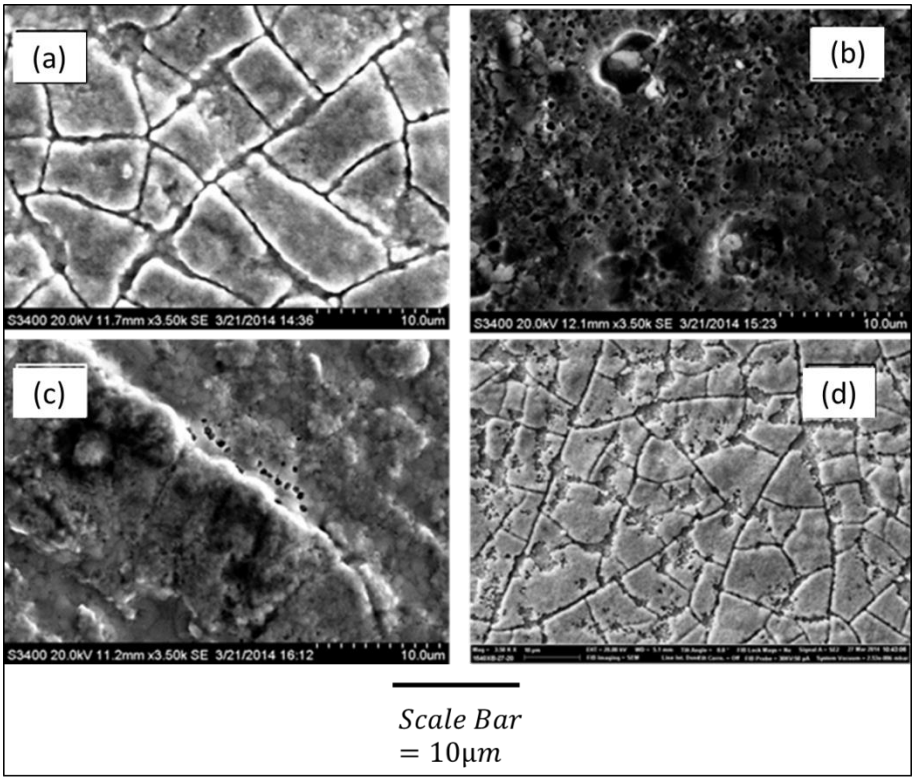

Figure 5.14: SEM images of functionally coated mild steel samples: (a) non-corroded, (b) air purged at 23 °C, (c) air purged at 80 °C, and (d) hydrogen purged 23 °C

The functionally coated mild steel sample has shown a relatively higher rate of corrosion compared to SS 316L under all conditions, as shown in the SEM images in Figure 5.14. The surface of the coated mild steel has also shown signs of pitting corrosion on the surface (Figure 5.15). The disadvantage that any coated mild steel sample has is potential damage of the protective coating layer. If the coating is damaged by any means; either mechanical or as a result of the corrosion reaction, then there is no further corrosion protection available and the mild steel continues to corrode under the protective coating at a rapid rate in the acidic environment.

The rupture of the coating, visible in Figure 5.15, could have been a result of an external coating failure (a scratch or dent), or due to a defect in the coating, formed during application, which exposes the underlying mild steel to the acid solution, leading to corrosion from beneath the protective coating and resulting in the further rupture of the coating from beneath.

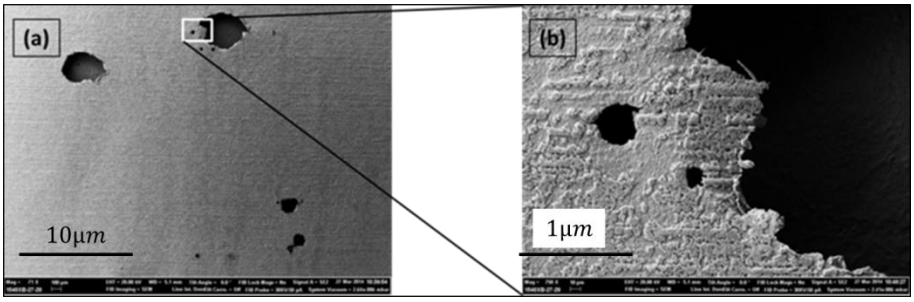

Figure 5.15: (a) SEM image of the functionally coated mild steel sample subjected to the accelerated corrosion test at $0.1\ V$ *vs RHE under a hydrogen environment at 23 °C depicting pitting corrosion and coating failure, and (b) magnified image of the corrosion pit exposing the underlying mild steel*

The SS 316L sample held in an anodic environment at 80 °C undergoes extensive dissolution leading to permanent surface damage. The elevated temperature aids the corrosion reaction and the potential at which the tests have been conducted is within the active dissolution phase range for SS. These conditions combined have an adverse effect on the corrosion performance of the sample. The acidic electrolyte, with 2 ppm fluoride ions added, results in the damage of the passive layer.

Figure 5.16 shows the EIS spectra obtained for the functionally coated mild steel sample in an air environment at 23 °C. The coated mild steel substrates have shown lower electrical resistance, when compared to the SS 316L samples, but have high rates of corrosion. This can be seen in the polarisation resistance of the sample shown in Figure 5.17. The polarisation resistance of functionally coated mild steel is negliible as compared to SS 316L under similar conditions. The lack of any passive protection is evident with the low polarisation resistance values. Moreover, these values do not change over time as was the case in SS 316L, suggesting that the sample is not developing any passive layer in solutions purged with air.

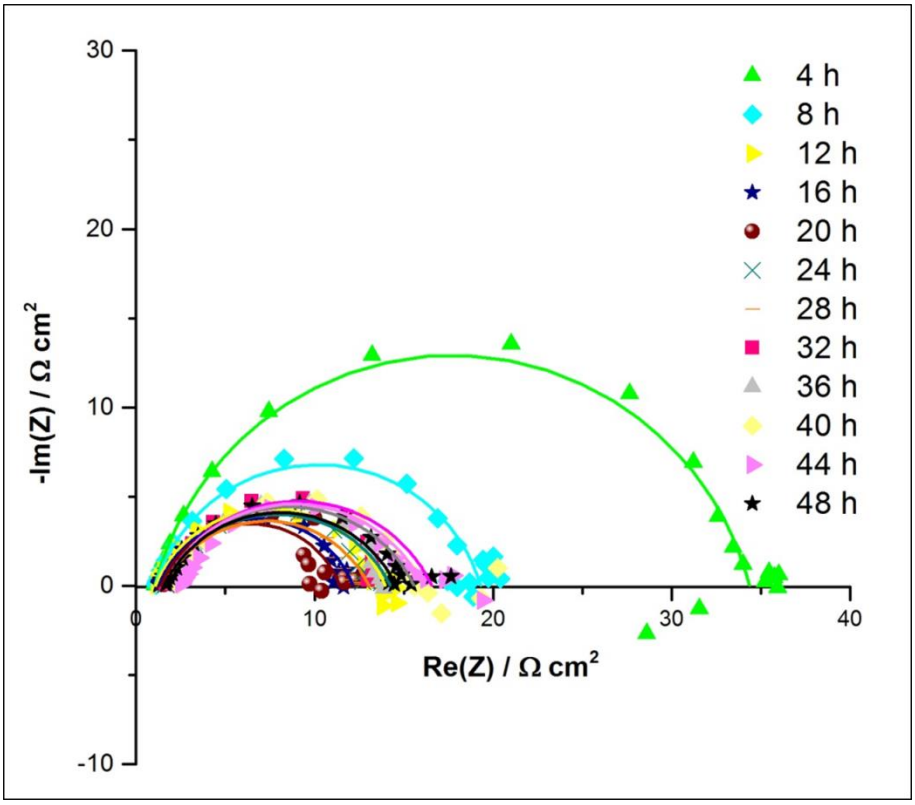

Figure 5.16: Electrochemical Impedance Spectra (symbols: EIS data and lines: fitted data) obtained for functionally coated mild steel under cathodic conditions (0.8 V at 23 °C in air)

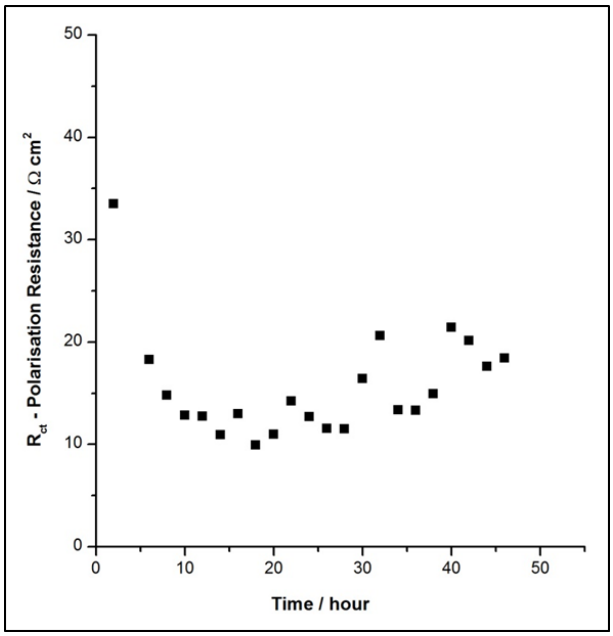

Figure 5.17: Change in polarisation resistance with time for the fitted data, obtained for functionally coated mild steel under cathodic conditions (0.8 V at 23 °C in air)

The improved ICR performance of the coated mild steel sample was attributed to the lack of a passive layer. As a result of this however, the material has not been able to perform as well as the SS 316L samples during the corrosion tests. The low resistance values during the accelerated corrosion tests suggest that the material has been actively corroded, and this is also evident in the potentiostatic current response of the coated mild steel samples. The pitting of the coating results in the exposure of the bare mild steel substrate to the highly corrosive conditions and hence the corrosion reaction progresses at a high rate. It is imperative therefore for the coating to be defect free and remain defect free during the tests, as once the coating is damaged the bare mild steel substrate is exposed. Without any corrosion protection, in the form of a structural alloying content or passive layer, the corrosion then progresses rapidly. A similar trend is observed under air at 80 °C. Comparatively lower polarisation resistance and the lack of development of any passive layer are evident in Figure 5.18.

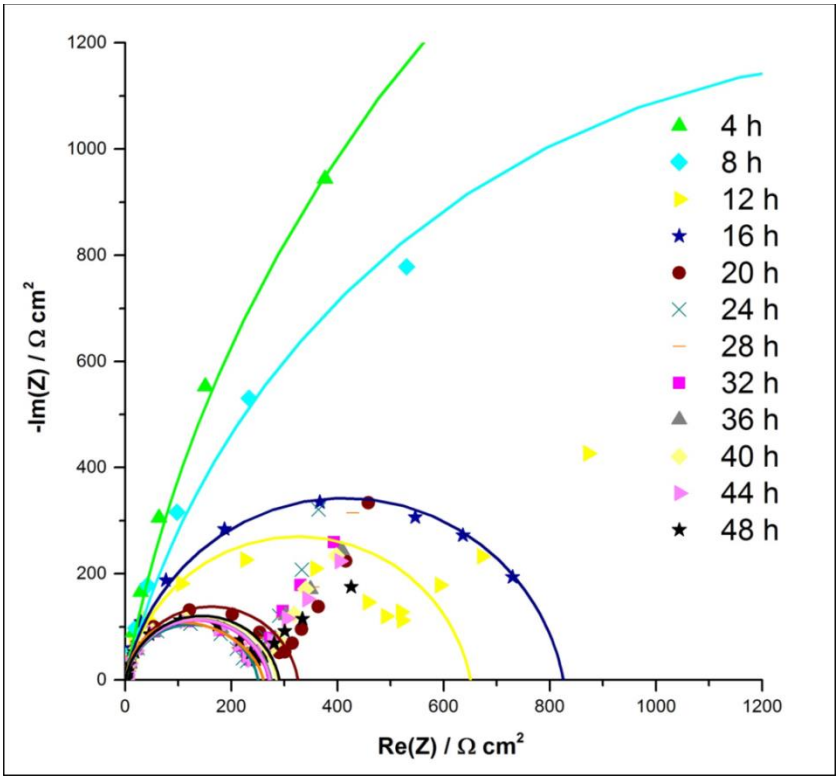

Figure 5.18: Electrochemical Impedance Spectra (symbols: EIS data and lines: fitted data) obtained for functionally coated mild steel under cathodic conditions (0.8 V at 80 °C in air)

5.5. *In situ* Fuel Cell Test Results

In situ fuel cell tests were carried out using the fuel cell test system described in section 4.1.6 with a graphite BPP in the first instance, and then the anode of the fuel cell was replaced with a SS 316L BPP.

The aim is to incorporate a flat stainless steel sample in place of graphite at the anode in order to understand the performance of the steel sample in comparison to the graphite. The key feature for assembling this single cell fuel cell unit is to study the steel samples without machining or hydroforming any flow channels in the sample, thereby allowing for deposition of a range of coatings on a simple BPP geometry. The metallic BPPs used are $25 \times 25\ mm$, with a gas manifold drilled at the two ends ass shown in Figure 5.19. The gas input is provided through these manifolds which would lead the gases to the GDL housed above the sample surface. Owing to the flow of gases and the output manifold being at the other end, it will create a laminar flow of the gases through the GDL on the top of the sample.

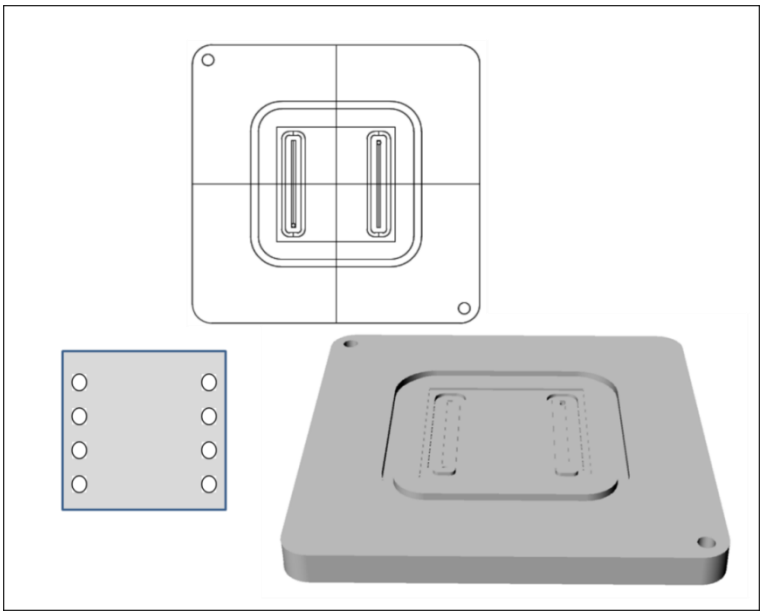

Figure 5.19: A schematic of SS 316L anode used to replace the graphite anode in the fuel cell

The fuel cell is operated using the parameters shown in Table 5.5. The membrane electrode assembly was allowed to equilibrate to the fuel cell

environment for $1\,h$ by running nitrogen through the cell. Once the temperature of the cell and the humidified gases reached the specified value, a polarisation curve was obtained, by scanning the current from $0 - 1000\,mA.cm^{-2}$ and plotting against the voltage, as shown in Figure 5.20.

Table 5.5: Parameters used for fuel cell tests

Parameter	Value
Temperature	80 °C
Flow rate (anode)	100 ml per minute
Flow rate (cathode)	200 ml per minute
Humidified gas temperature	78 °C

The graphite cell was able to produce more current for a given applied voltage and resembles a typical fuel cell polarisation curve, depicting the three losses as discussed in section 1.3.3. The voltage in the fuel cell containing the SS 316L dropped very quickly due to high Ohmic losses, arising due to the high surface resistance produced by the developing passive oxide layer.

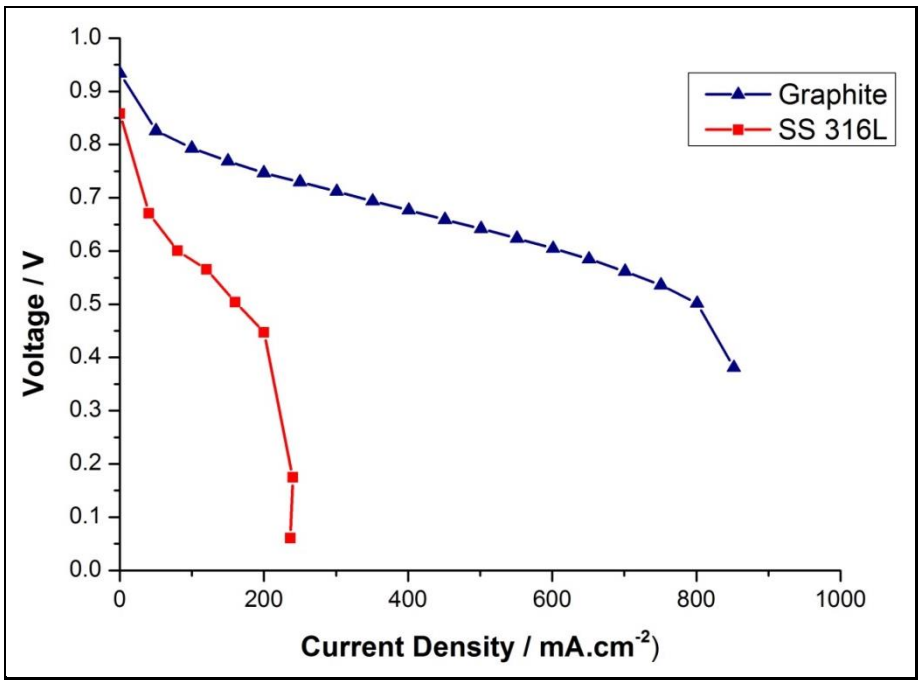

Figure 5.20: Polarisation curves for graphite/graphite and graphite/SS 316L fuel cells obtained at 80 °C

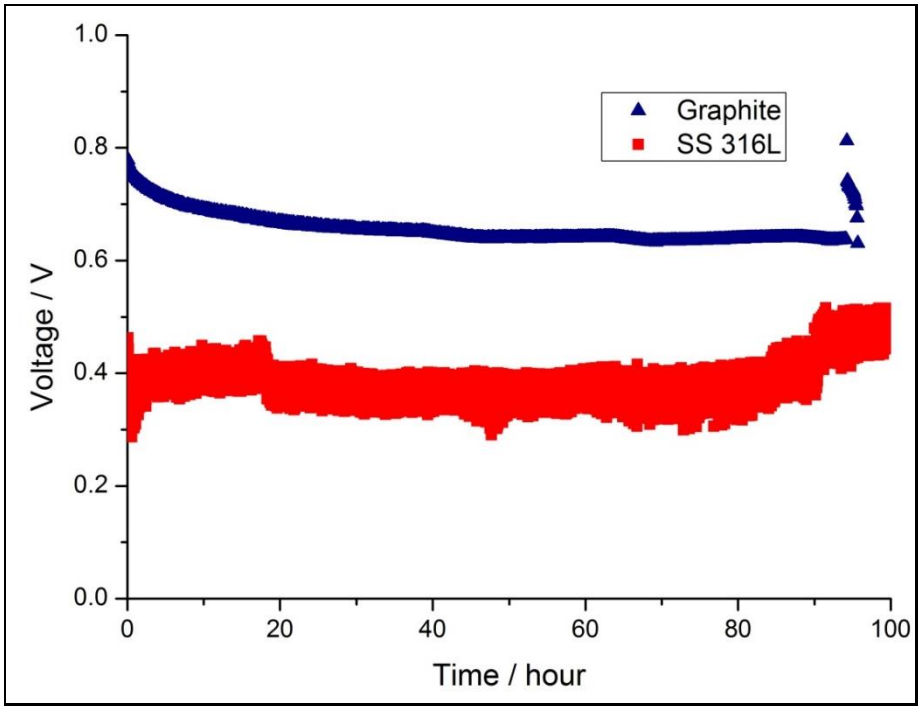

Figure 5.21: $100\ h$ *fuel cell operation for graphite/graphite and graphite/SS 316L fuel cells obtained at 80°C*

After obtaining the polarisation curves (Figure 5.17), the fuel cells were run for 100 hours at a current density of $100\ mA.cm^{-2}$. The graphite/graphite fuel cell recorded a voltage of approx. $0.7\ V$, whereas the graphite/SS 316L fuel cell produced $0.4\ V$. Fuel cell tests were also attempted using the functionally coated mild steel; however, the fuel cell was unable to run as a result of a rapid drop in voltage, due to the poor corrosion performance of the substrate. Figure 5.22 shows optical images of the tokens used as the BPPs during the *in situ* fuel cell tests. The SS 316L showed no sign of corrosion after $100\ h$ of fuel cell operation, however, the functionally coated mild steel tokens have corroded during the conditioning process. The corrosion products and the contamination of the MEA (Figure 5.23) resulted in the inability of running the fuel cell using the functionally coated mild steel. The key feature in the corrosion of the functionally coated mild steel tokens is the appearance of pin-hole defects in the coating that result in further corrosion of the underlying mild steel. An additional feature is that of the coating process. The tokens were pre-drilled to create manifolds for gas flow and the coating process was followed afterwards in an attempt to minimise any bare substrate being exposed to the corrosive environment.

However, the coating seems to have failed from inside of the holes and the cut-edges of the materials, as seen in Figure 5.24.

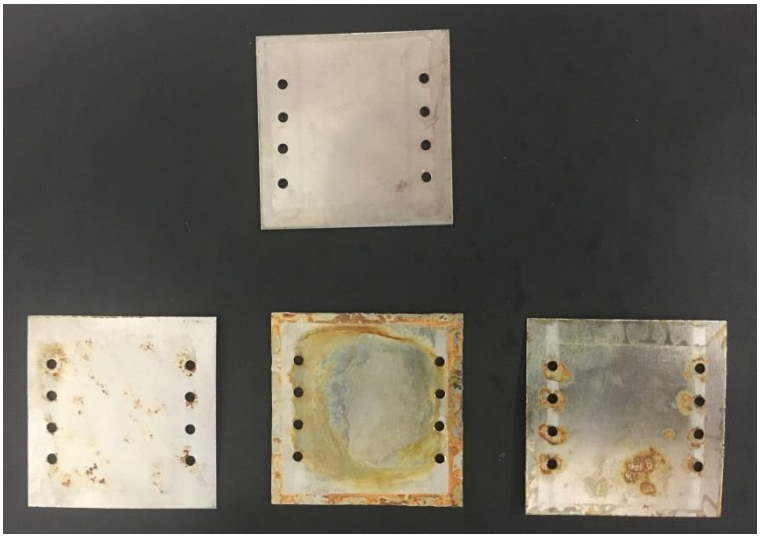

Figure 5.22: Optical images of (top) SS 316L and (bottom) multiple tokens of functionally coated mild steel after fuel cell operation

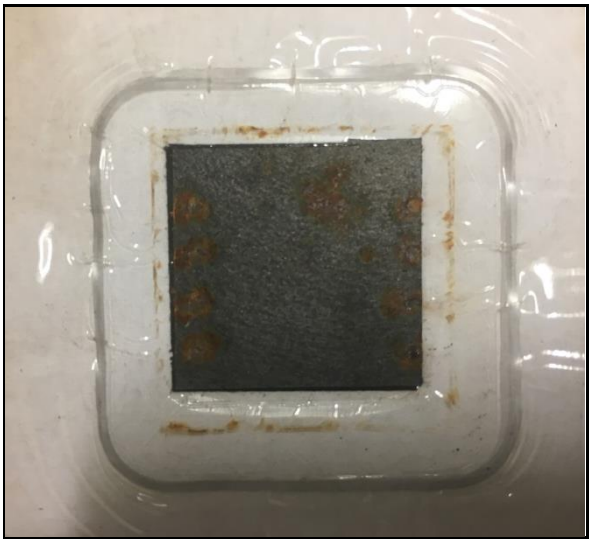

Figure 5.23: Optical image of the contaminated MEA after use of the functionally coated mild steel BPP in in situ fuel cell operation

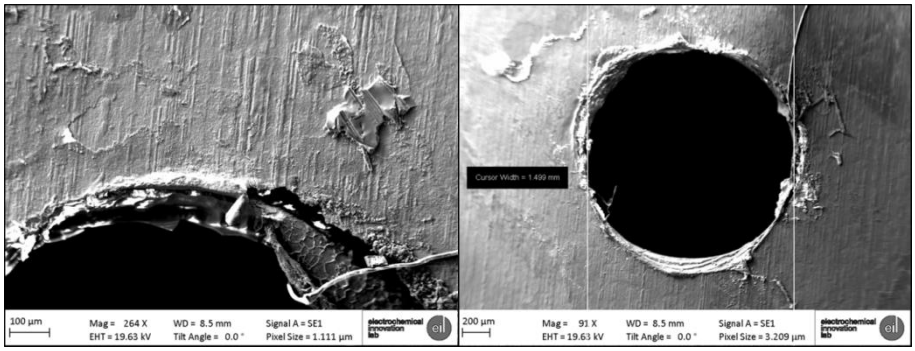

Figure 5.24: SEM image of the corroded holes in the functionally coated mild steel tokens

5.6. Conclusions

SS 316L has been analysed for its *ex situ* ICR and corrosion performance to setup the benchmark results to compare against for the performance of other substrates. A mild steel substrate has been analysed to study the ICR and corrosion performance for the bare substrate and two other nickel coated mild steel substrates to understand the baseline performance without any protective coating. A Tata proprietary coating is then analysed to study the improvements in the ICR and corrosion performances of the functionally coated mild steel with respect to the baseline results and the benchmarked SS 316L results.

Functionally coated mild steel substrate has been reported to have an order of a magnitude better ICR results as compared to bare mild steel and SS 316L substrates. The corrosion rates have been reported to have an improved corrosion performance as compared to the bare mild steel under air environment and under hydrogen at 25 °C. The corrosion performance under hydrogen at 80 °C has been improved by a factor of three, however, under air the improvements are about forty times better as compared to bare mild steel. It provides better ICR performance as compared to SS 316L and bare mild steel both. The corrosion performance is improved as compared to mild steel, however, the corrosion results for SS 316L are still better than the functionally coated mild steel; especially under hydrogen at 80 °C. The potentiostatic results have shown a similar trend in term of the corrosion currents as observed in the potentiodynamic tests.

Accelerated corrosion tests have been carried out using $1\,M$ sulphuric acid electrolyte as compared to the other tests where $0.1\,M$ was used to accelerate the corrosion reactions. The corrosion performance was determined using EIS scans taken at every $2\,h$ during the $48\,h$ accelerated test. The material surface resistance is found to increase under air and decreases under hydrogen with time. This explains the role of oxide layer in providing corrosion protection to SS 316L substrate. The lower resistance value offered by the functionally coated mild steel has resulted in the dissolution of the substrate in the concentrated acidic conditions. The most important thing to notice has been the failure of the coating. The damage to the coating results in the electrolyte reaching the base mild steel material and results in the higher corrosion currents. The key is to develop the coating that is damage free, and robust to withstand the harsh corrosion conditions offered in a fuel cell environment.

The *in situ* fuel cell tests performed using graphite BPP and a SS 316L BPP has shown the effect of the oxide layer on the power output of the cell. Graphite BPP fuel cell has offered above $0.6\,V$ at $100\,mA.cm^{-2}$ as opposed to $0.4\,V$ observed in the SS 316L fuel cell. The *in situ* fuel cell experiments using the functionally coated mild steel BPP did not yield the required power output due to the failure of the coating at the machined sites and it resulted in the poisoning of the MEA. These results once again emphasise the necessity of a robust defect free coating for mild steel substrate if is expected to perform in comparison to SS 316L, as the mild steel does not provide any inherent corrosion protection and as soon as the coating is damaged the whole sample fails to maintain the required potential to run a fuel cell.

6. Graphene Coatings for Steel

This chapter presents the application of graphene as an anti-corrosion coating option for different grades of steel for use as BPPs in PEMFCs. The four grades of steel, used previously for the corrosion analysis in chapter 5, have been coated with graphene using low temperature photo-thermal chemical vapor deposition. The coated samples are then analysed for their *ex situ* ICR and corrosion performance using linear sweep voltammetry, and the performance compared to that of the uncoated substrates. The coating process has been repeated with and without a catalyst layer deposited on the steel substrates, prior to the graphene growth, using the method reviewed in section 2.2.3.

A novel method of deposition of graphene using electrophoretic deposition is also presented in this chapter. Graphene intercalated compounds are used to make a colloidal solution in N-methyl-2-pyrrolidone (NMP), a polar organic solvent. Graphene is subsequently deposited on a SS 316L substrate from the colloidal solution using electrophoretic deposition. Raman spectroscopy and atomic force microscopy (AFM) has been used to analyse the characteristics of the as-deposited graphene layers.

6.1. Photo-Thermal Chemical Vapor Deposition (PTCVD) of Graphene on Steel

Photo-thermal CVD deposition of graphene has been undertaken in two batches: batch 1 via a catalyst layer first deposited on the steel substrate surface and then subsequent growth of graphene on top of the catalyst layer; and batch 2 via direct graphene growth onto the steel surface without any catalyst layer.

In both methods, the as-received substrates were cleaned with a methanol soaked wipe to remove any dust and grease and then air dried. In the case of batch 1, a thin catalyst layer $(< 100\, nm)$ of nickel is deposited using a DC sputtering method. The two sides of the steel substrate are coated

sequentially, after which the coated substrates are transferred to the CVD chamber for graphene growth.

Graphene deposition then proceeds via white light assisted PTCVD growth of graphene on both sides of the steel substrates concurrently. The actual deposition process involves 3 steps: heating, growth and cooling. The substrates are first heated for $10\,min$ under hydrogen atmosphere using halogen lamps. After the heating period, the growth gas (acetylene) is introduced into the chamber for the required growth time $(5\,min)$, after which the lamps are turned off and the substrates allowed to cool for further $10\,min$ under the hydrogen atmosphere. Finally, the chamber is purged with nitrogen gas to remove any excess unbound hydrocarbon molecules.

6.1.1. ICR Test Results (Batch 1 with Catalyst Layer)

The ICR values of all four substrates (HILAN, HILUMIN, Mild Steel and SS 316L) coated with graphene via a catalyst layer were measured using the methods detailed in chapter 5, by collecting EIS scans at different compression pressures within a range of $20\ -\ 200\,N$.

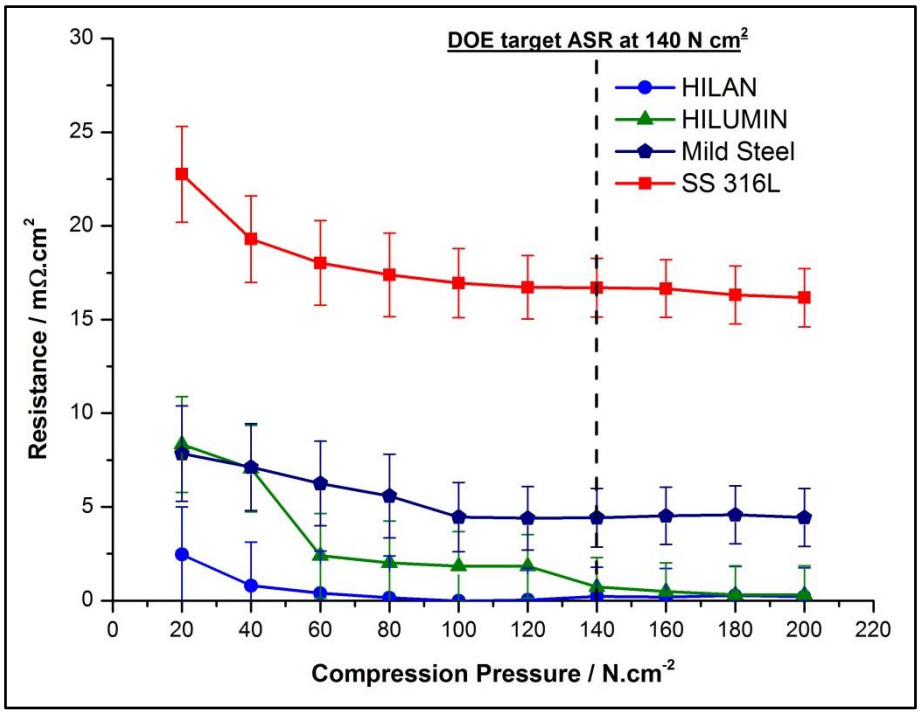

Figure 6.1: Resistance vs compression for different substrates coated with graphene with a Ni catalyst layer

The ICR values for the four different substrates coated with graphene using a catalyst layer are shown in Figure 6.1. A remarkable difference in the ICR values of the catalysed graphene coated substrates is noted as compared to the uncoated substrates. This is evident from the ICR values of all four uncoated and catalysed graphene coated substrates at $140\ N.cm^{-2}$ reported in Table 6.1.

Table 6.1: ICR values at $140\ N.cm^{-2}$ for the four uncoated and graphene with Ni catalyst layer coated samples

Substrate	Resistance / $m\Omega.cm^2$ at $140\ N.cm^{-2}$	
	Uncoated	Graphene Coated
HILAN	56.6	0.2
HILUMIN	114.2	0.7
Mild Steel	274.5	4.4
SS 316L	403.9	16.7

The DOE[21] 2017 target for the ASR for a BPP candidate material is $20\ m\Omega.cm^2$ at a compression pressure of $140\ N.cm^{-2}$. All four substrates coated with catalysed graphene are shown to have ICR values below the DOE 2017 target. The graphene coating therefore provides excellent electrical conductivity to the samples.

The remarkable decrease in the surface resistance of the samples is attributed to a modification of the surface oxide layer as a result of the catalysed graphene coating process. In the first instance, the ion sputtering process which is used to deposit the Ni catalyst layer on the substrates removes any surface oxides from the substrates and deposits a Ni layer. The subsequent graphene growth on the surface then further prevents any oxide growth. Once the oxides are removed, the graphene coating allows for high conductivity through the bulk metal sample.

ICR is a surface characteristic of the samples. A strong passive oxide layer on the steel can hinder the movement of electrons through the surface of the sample. The bulk of the metal sample possesses excellent electrical conductivity and hence, the ICR value is directly dependant on the characteristics of the oxide layer. As the oxides are removed and the

deposition of graphene layer preventing the further formation of oxides, the samples have demonstrated relatively low ICR values.

The ICR values for graphene coated HILUMIN and HILAN are reported to be near zero; i.e., there is no hindrance for electron movement from the Toray paper through to the bulk metal substrate. The ICR values of graphene coated HILAN are below $2.5\ m\Omega.cm^2$ at any given compression pressure. The error bars at each compression pressure in Figure 6.1 represent one standard deviation from the mean values taken for Toray paper only. Taking into consideration the standard deviation, the ICR values for the substrate sample seem to be very low and in case of HILAN and HILUMIN, near zero. The ICR standard deviation for the Toray paper alone is not significant in the case of the bare substrates, where the ICR values are in the hundreds of $m\Omega.cm^2$, but it is significant when considering the low ICR values of the coated substrates.

6.1.2. Potentiodynamic Polarisation Test Results (Batch 1 with Catalyst Layer)

Potentiodynamic tests were carried out to investigate the corrosion performance of the batch 1, catalyst layer assisted graphene coated steels. The test solution used was $0.1\ M\ H_2SO_4\ +\ 2\ ppm\ F^-$, the same as that used for the potentiodynamic polarisation tests of bare substrates in chapter 5. The solution environment, i.e. the purging conditions and the temperature, was replicated to what was used in the corrosion rate analysis of the bare substrates. The reference electrode used in the experiments was a RHE and all the potentials reported are against RHE. The potentiodynamic curves for the four catalyst layer growth assisted graphene coated substrates under air are shown in Figure 6.2 and Figure 6.3.

The corrosion rates for all the four graphene coated substrates are higher than those of the uncoated substrates in air as shown in Table 6.2. In terms of graphene coated HILAN, the corrosion rate is similar to that of uncoated HILAN at 25 °C and is six times higher at 80 °C. In case of HILUMIN, the corrosion rates for coated and uncoated substrates do differ significantly as compared to the other two substrates. Uncoated mild steel had poor corrosion resistance and the graphene coated mild steel has poorer

performance both at 25 °C and 80 °C. SS 316L at 25 °C has the biggest difference in terms of the corrosion rate for the uncoated and graphene coated substrate at 25 °C. The coated sample has performed poorly and the corrosion rate is 25 times higher compared to the uncoated one, the coated material at 80 °C however, has performed slightly better.

Table 6.2: Rate of corrosion in terms of mm per year under air environment for the four uncoated and catalyst assisted graphene coated substrates

Material	25 °C		80 °C	
	Un-coated	Coated	Un-coated	Coated
HILAN	0.3	0.3	0.3	1.7
HILUMIN	0.2	0.4	1.2	1.4
Mild Steel	3.6	21.9	174.4	215.1
SS 316L	0.04	1.0	1.4	1.2

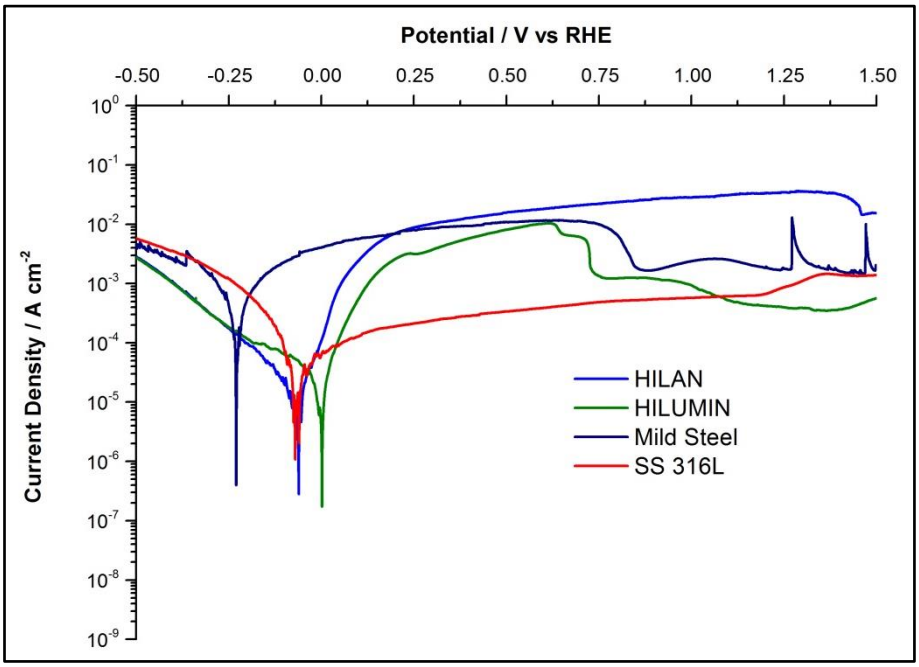

Figure 6.2: Potentiodynamic polarisation curves for the four substrates coated with graphene, using a Ni catalyst layer, under air at 25 °C

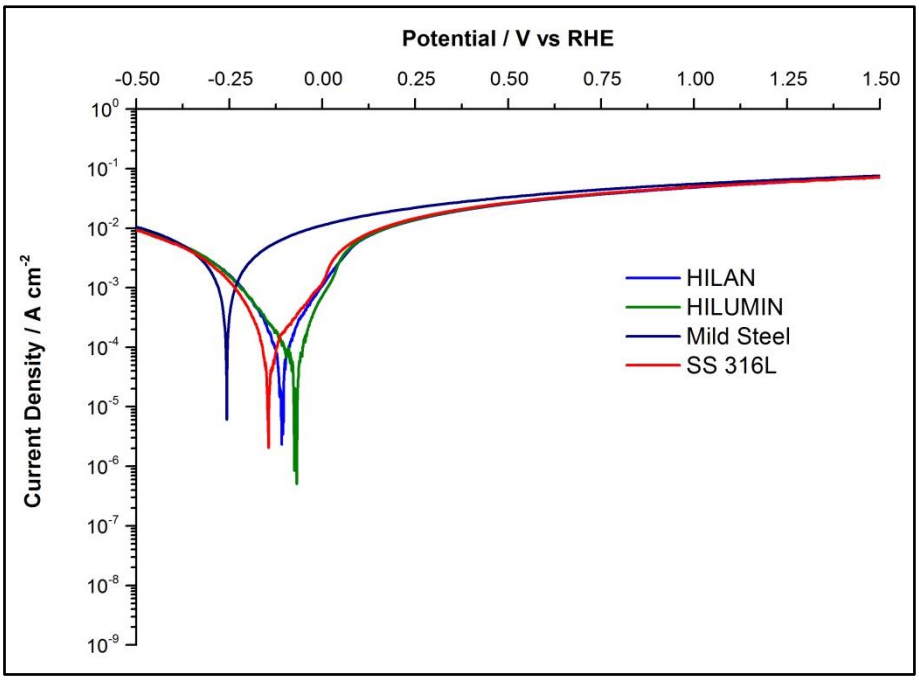

Figure 6.3: Potentiodynamic polarisation curves for the four substrates coated with graphene, using a Ni catalyst layer, under air at 80 °C

As explained in chapter 3, the corrosion rates obtained using linear sweep polarisation provide the corrosion rates for a candidate material within the corrosive environment around the corrosion potential. A remarkable change is observed in the passive current densities for SS 316L. The improvement in the ICR performance of all four coated substrates was attributed to the removal of the oxide layer. The absence of a passive oxide layer has resulted in the high corrosion rates for the substrates. SS 316L has been affected the most as SS possesses a strong oxide layer. In case of graphene coated SS 316L, the removal of the oxide layer has improved ICR performance but has had an adverse effect on the corrosion performance.

SS 316L coated with graphene measured under air at 25 °C has demonstrated some passive behaviour for potentials above the E_{Corr}, however, the passive current density is still higher when compared to the uncoated SS 316L under similar conditions. The SS 316L coated with graphene and measured at 80 °C under air does not exhibit any passive character and the current density is similar to that of other substrates coated with graphene. The current density beyond the E_{Corr} for all four substrates under air at 80 °C is maximised to similar values, which can be

expected to be limited by the surface area of the sample. So in conclusion, the graphene coated substrates do not provide any corrosion protection, especially for measurement in air at 80 °C, and the corrosion current density above the E_{Corr} is consequently limited by the surface area of the sample rather than the passive characteristics of the substrate material. The graphene deposition process removes any surface oxides and hence nullifies the corrosion protection characteristics of different substrates, and all four substrates have exhibited similar passive corrosion current under air at 80 °C.

The potentiodynamic curves for the four catalyst layer growth assisted graphene coated substrates under hydrogen are shown in Figure 6.4 and Figure 6.5, and the corrosion rates are given in Table 6.3.

The graphene coated substrates have shown better corrosion performance compared to the uncoated substrates under a hydrogen environment. However, the key difference still remains that of the passive current densities. The graphene coated SS 316L does not display any of the characteristic low passive current densities, suggesting that the coated substrates lack passive oxide layer protection.

Table 6.3: Rate of corrosion in terms of mm per year under hydrogen environment for the four uncoated and catalyst assisted graphene coated substrates

Material	25 °C		80 °C	
	Un-coated	Coated	Un-coated	Coated
HILAN	0.2	0.01	0.7	0.1
HILUMIN	0.04	0.1	0.6	0.4
Mild Steel	4.5	20.9	173.3	61.4
SS 316L	0.7	0.4	3.1	0.04

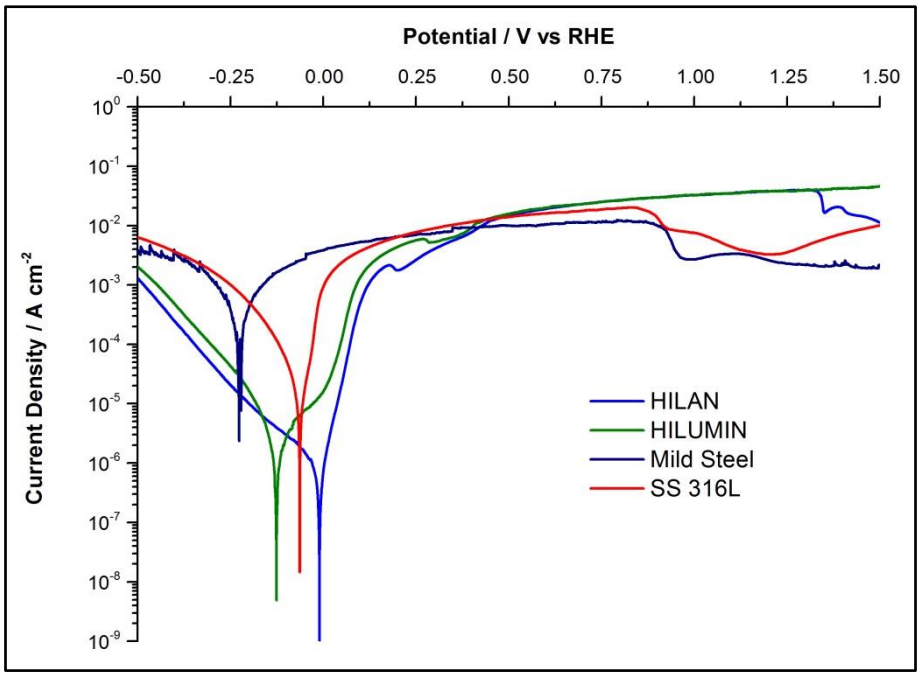

Figure 6.4: Potentiodynamic polarisation curves for the four substrates coated with graphene, using a Ni catalyst layer, under hydrogen at 25 °C

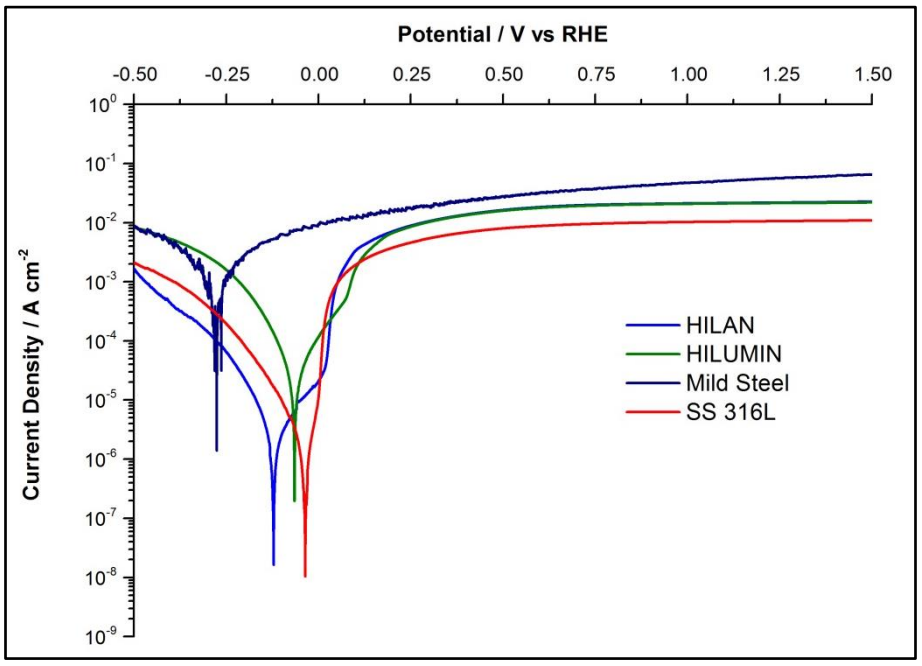

Figure 6.5: Potentiodynamic polarisation curves for the four substrates coated with graphene, using a Ni catalyst layer, under hydrogen at 80 °C

Figure 6.6 shows the potentiodynamic polarisation curves for SS316L under hydrogen at 80 °C with and without a graphene coating. The key difference can be seen in the passive current densities for the graphene

coated substrate, which is almost three decades higher than that of the uncoated SS 316L. This confirms the removal of the oxide layer which results in better ICR performance, but which leads to poor corrosion protection.

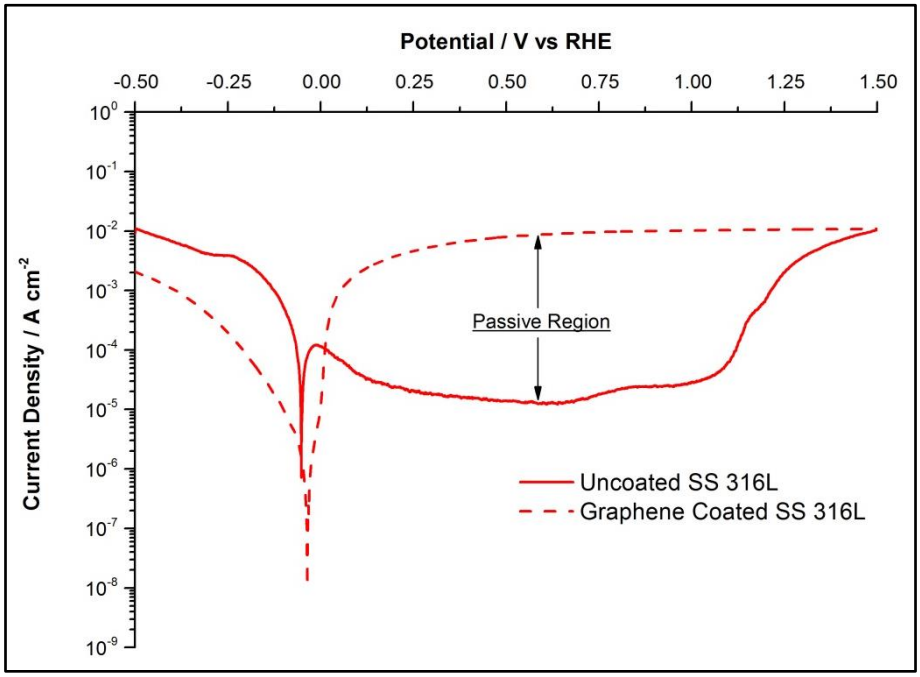

Figure 6.6: Potentiodynamic curves for SS 316L with and without a graphene coating at 80 °C under hydrogen

The graphene coating process includes the deposition of the catalyst layer using sputtering, after which the samples are exposed to highly reducing conditions under a hydrogen environment during graphene deposition. This process removes any surface oxides present on the samples and the graphene deposition then prevents any further surface oxide film being developed on the surface. The lack of a stable oxide film in all the samples is evident in the linear sweep experiments (Figure 6.2 - Figure 6.5) resulting in poor corrosion resistance performance.

On visual inspection via microscopy, the samples have been corroded under the graphene coating, as flakes of coatings are visible with corrosion evident underneath. The visual observations suggest that there is a non-uniform coating on the samples and the electrolyte has penetrated under the graphene coating, resulting in corrosion propagation under the graphene coating.

6.1.3. Raman Analysis of Graphene Coating (Batch 1 with Catalyst Layer)

The as-received graphene coated substrates have been analysed using Raman spectroscopy with $20\times$ magnification using $533\,nm$ laser at $8\,mW$ power. 10 sample spectra were collected for each of the coated substrates and the average data is used to generate the spectrum. If required the spectrum is corrected for background noise and all Raman spectra in this thesis are normalised to the G peak with the G peak intensity of $1000\,a.u.$

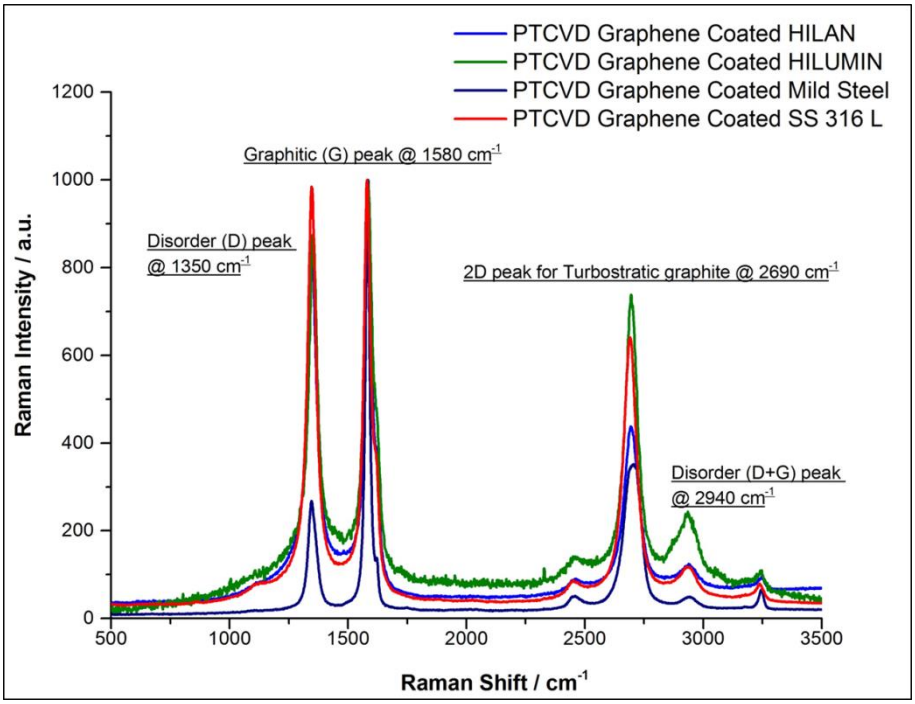

Figure 6.7: Raman spectra of different graphene coated samples

Figure 6.7 shows the Raman spectra for all four graphene coated samples. The spectra display the presence of a 2D graphene peak[142–144] at $2690\ cm^{-1}$ along with the graphitic G peak at $1580\ cm^{-1}$. The presence of a disorder (D) peak at $1350\ cm^{-1}$ suggests that the graphene layers are not continuous and there is defect in the graphene layer. This can originate if the Raman spectra is collected off the edge of a graphene layer. The resulting Raman spectra suggest that the substrates have an uneven graphitic material coverage. Another key characteristic is the broad 2D peak. As discussed in section 4.2.4., the 2D peak gets broader with the increasing number of graphene layers and with the graphene layers

deposited using PTCVD class as turbostratic graphite made up of a few layers of graphene. With PTCVD, the stacking of graphene layers is not controlled, and hence all samples have demonstrated an intense disorder peak. Importantly, the graphene layers have not been damaged after the corrosion scan (Figure 6.8). The presence of a 2D graphene peak in the Raman spectrum post corrosion re-emphasises the corrosion resistant characteristics of the graphene, although the underlying steel has been attacked by the test solution through the gaps in the graphene coating.

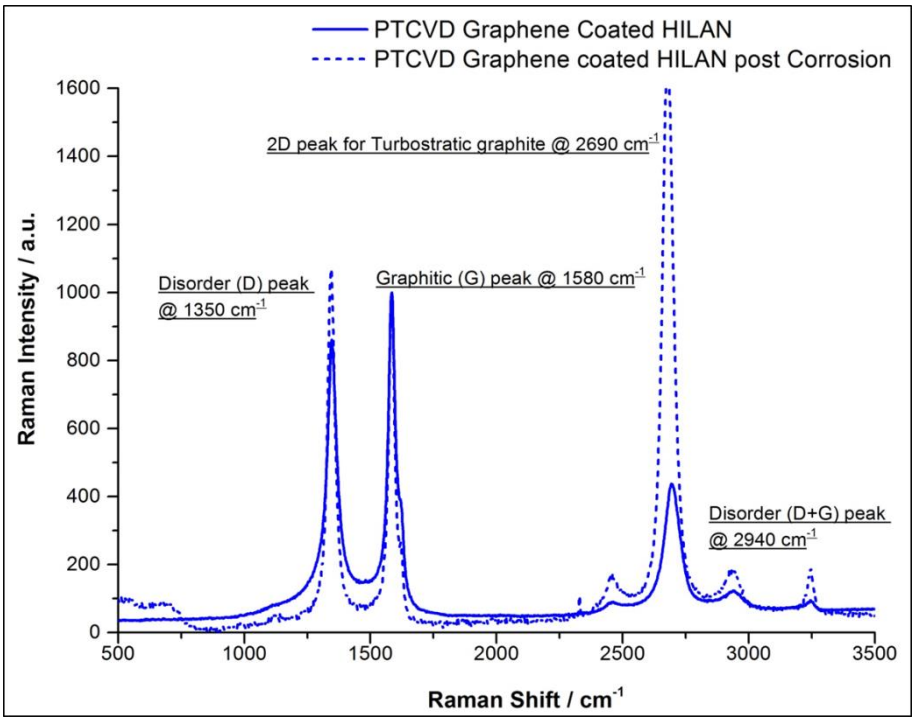

Figure 6.8: Raman spectra of graphene coated HILAN before and after the linear sweep corrosion scan

Subsequently, in theory, if the graphene coating is uniform and has a full coverage of the substrate, the samples should have demonstrated excellent corrosion resistance, in addition to the low ICR values. However, the Raman spectra have been repeated at various positions on the samples, and a number of the measurements have revealed an absence of 2D peaks in some positions. A uniform graphene coating would have resulted in 2D graphene peaks present throughout the sample surface, which confirms the non-uniform nature of the graphene coating.

The high corrosion rates for the samples are therefore a result of a non-uniform graphene layer on the surface that has allowed the electrolyte to

penetrate the sample. The subsequent corrosion has progressed at a high rate under the coating as the steel does not have the protective oxide film. In addition to this, the presence of the iron catalyst interlayer, required for CVD graphene deposition, adds to the corrosion rate as the iron would readily dissolve in the electrolyte used in the experiments. Subsequently, graphene coatings grown without a catalyst layer will be produced for comparison.

6.1.4. Post Corrosion SEM Imaging (Batch 1 with Catalyst Layer)

The graphene coated steel samples have been analysed using SEM to study the surface degradation of the samples as a result of the corrosion analysis., The images display the corrosion occurring as a result of the non-uniform graphene coating coverage, as discussed in the earlier sections, which allows the electrolyte to attack the bulk material under the coating. Figure 6.9 shows the post-corrosion SEM images for the three substrates; HILUMIN, mild steel and SS 316L. In all the three images, the corrosion effect is clearly visible. Indeed in the case of SS 316L, graphene flakes can be seen to have detached from the substrate. This demonstrates the extent of the corrosion that has occurred under the coatings.

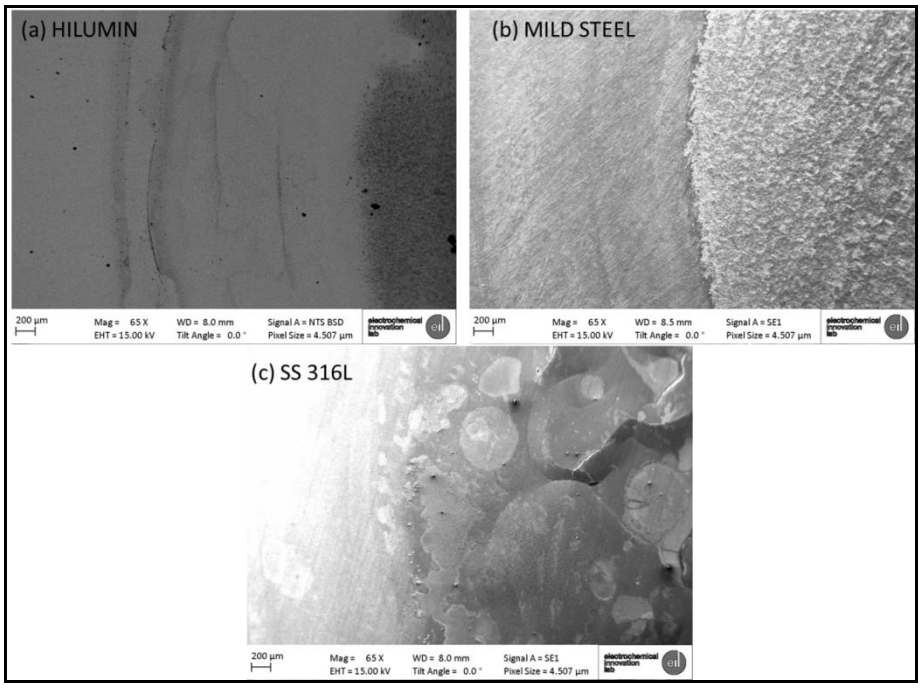

Figure 6.9: SEM Images of graphene coated samples, after the linear sweep corrosion scan, taken at the edge of the corroded area for (a) HILUMIN, (b) mild steel and (c) SS 316L. The left part in each image is the non-corroded graphene coating and the right part is the corroded area (bars = 200 µm)

The coating failure on the SS 316L sample has been further analysed at higher magnification (Figure 6.10). The image clearly depicts the extent of damage to the graphene coating and areas of the bare material exposed to the electrolyte can be clearly seen in the image (marked in red).

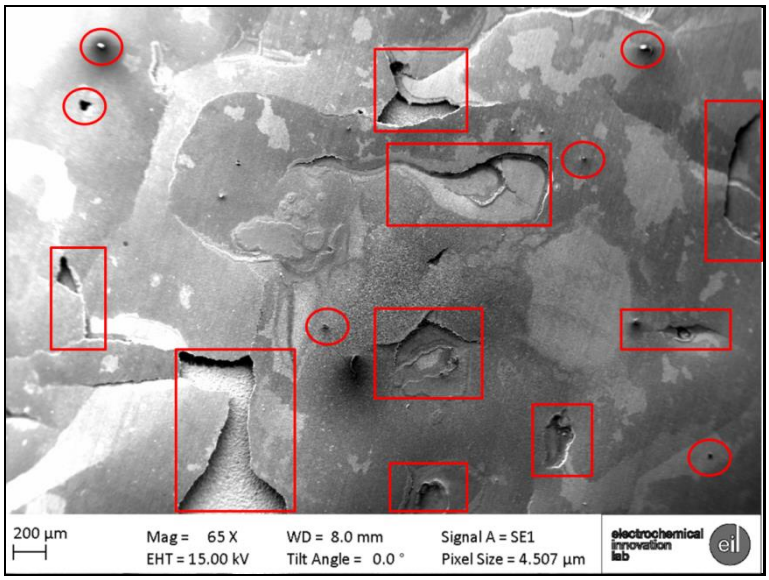

Figure 6.10: SEM image of graphene coated SS 316L sample post corrosion scan, with coating damage and pin holes exposing bare material under the coating highlighted by the red boxes (bar = 200 µm)

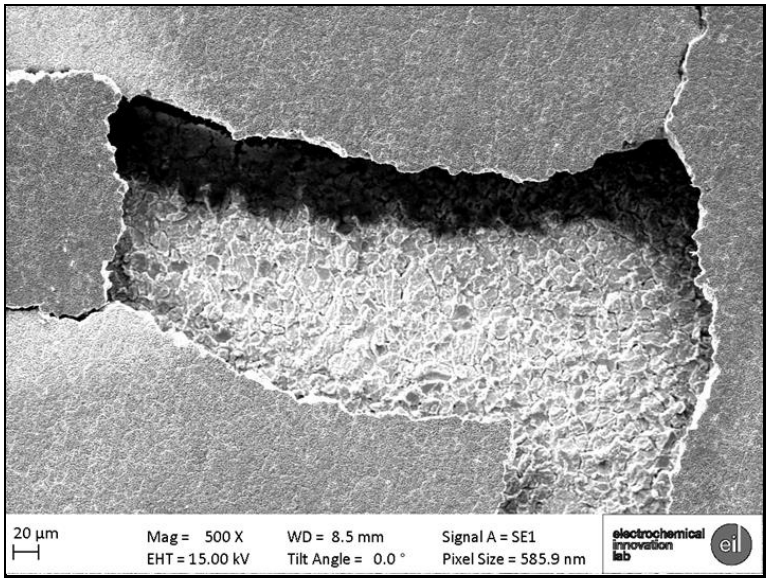

Figure 6.11: A magnified SEM image of a hole in the graphene coating on the SS 316L sample (bar = 20 µm)

It can be seen that the coating itself has not been severely damaged; however, the areas under the coating have come under attack by the acid as a result of the non-uniform coverage of the sample. The coating defects have allowed the electrolyte to seep underneath the coating and the coating has subsequently delaminated as a result of the formation of corrosion products under the coating. Figure 6.11 shows a magnified SEM image of the steel within the hole in the graphene coating.

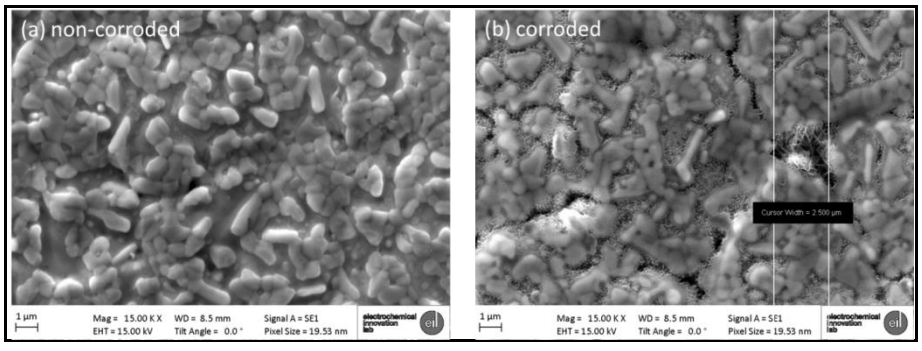

Figure 6.12: SEM image of the graphene coated SS 316L sample; (a) non corroded and (b) corroded areas showing corrosion under the coating as a result of the non-uniform graphene coverage (bar = 1µm)

Figure 6.12 gives a comparison between non-corroded and corroded areas of a SS 316L sample imaged through the pin-holes in the graphene coating, highlighting the corrosion damage that has occurred underneath

the coating. The lack of uniform graphene coverage has resulted in gaps in the coating through which the electrolyte can attack on the bare substrate that does not possess any protective oxide film to counter the acid attack.

6.1.5. Batch 2 Graphene Coating without Catalyst Layer

The graphene coating deposited using the nickel catalysed PTCVD method resulted in improvement in the ICR performance of all the four substrates; however, it resulted in poor corrosion performance. In case of SS 316L, the corrosion performance of the coated sample was marked by a loss in the inherent passive characteristic of the SS 316L samples. The ion sputtering process removed the oxide layer and graphene growth prevented further oxide formation. The second batch of graphene coated samples has been deposited without the catalyst directly onto the steel surface. In correlation with batch 1, the samples have been analysed for their ICR performance and *ex situ* corrosion performance.

6.1.5.1. ICR Test Results (Batch 2 without Catalyst Layer)

The ICR values of all four graphene coated substrates were again measured by collecting EIS scans at different compression pressures within a range of $20 - 200\,N$.

The ICR values for the three different catalyst free graphene coated substrates are shown in Figure 6.13. The graph demonstrates a similar trend observed for the batch 1 substrates with catalyst layer. The ICR values for all four graphene coated substrates with and without catalyst at $140\,N.cm^{-2}$ are compared in Table 6.4.

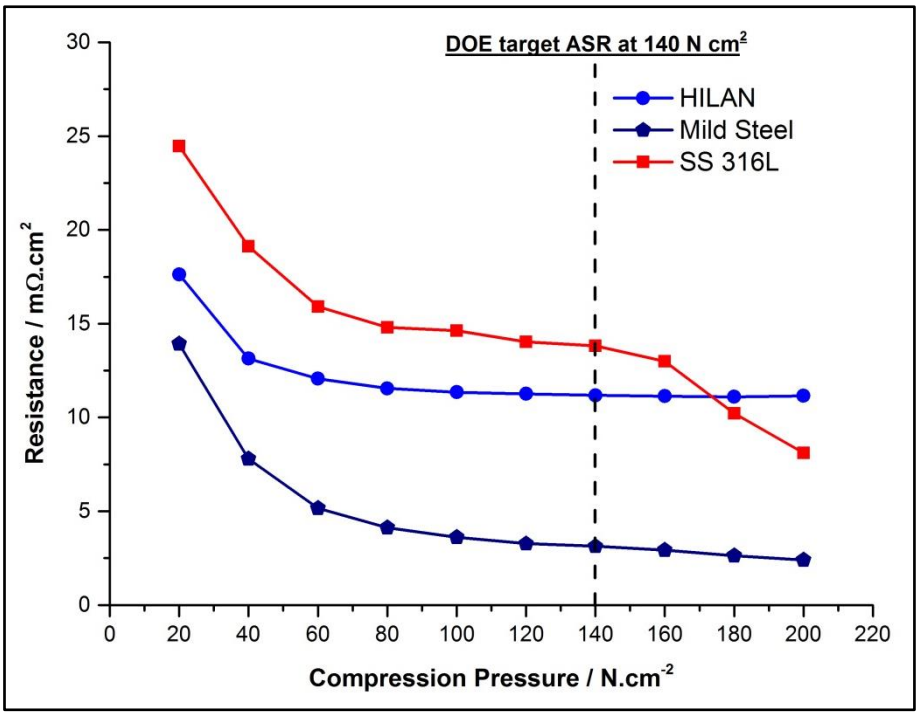

Figure 6.13: Resistance vs compression for different substrates coated with graphene without a catalyst layer

Table 6.4: ICR values at $140\ N.cm^{-2}$ *for the four substrates coated with graphene, with and without the* Ni *catalyst layer*

Substrate	Resistance / $m\Omega.cm^2$ at $140\ N.cm^{-2}$	
	Graphene with catalyst	Graphene without catalyst
HILAN	0.2	11.2
HILUMIN	0.7	Near zero
Mild Steel	4.4	3.1
SS 316L	16.7	13.9

The ICR values for HILUMIN were reported to be negative at all compression pressures except for the first reading at $20\ N.cm^{-2}$, which was $0.84\ m\Omega.cm^2$. It is unlikely that a substrate would have a negative resistance value. As described in section 4.1.1., the ICR values for Toray paper are measured first, and then the ICR for the sample sandwiched between two Toray papers is measured. The Toray paper values are taken away from the sample values, divided by two for resistance of each side and then the value is multiplied by the area to get the areas specific resistance. If the sample has a near zero resistance and if, due to

measurement error or instrumental error, the ICR value for the sample and Toray paper is smaller than the blank Toray paper value, the sample value will be reported as negative; this number then multiplied by the area results in a more negative resistance value. Hence, for any negative ICR value reported, it could be reported that the sample has near zero interfacial contact resistance.

The resistance values for graphene coated mild steel and SS 316L for batches 1 with catalyst layer and batch 2 without catalyst layer are both similar to each other. However, the ICR values for batch 2 graphene coated HILAN are higher than those of batch 1. However, in the case of all four substrates, for catalysed as well as non-catalysed, the ICR values are well below the DOE 2017 target of $20\ m\Omega.cm^2$ at $140\ N.cm^{-2}$.

6.1.5.2. Potentiodynamic Polarisation Test Results (Batch 2 without Catalyst Layer)

The potentiodynamic tests were carried out to investigate the corrosion performance of the batch 2 samples without catalyst layer, using the same test methods as used for batch 1 with catalyst layer. The potentiodynamic curves for the four batch 2 graphene coated substrates under air are shown in Figure 6.14 and Figure 6.15 and the corrosion rates, compared to batch 1, are shown in Table 6.5.

Table 6.5: Rate of corrosion (mm per year) under air for the four graphene coated substrates produced via catalysed and un-catalysed growth routes

Material	25 °C		80 °C	
	Batch 1 (Catalysed)	Batch 2	Batch 1 (Catalysed)	Batch 2
HILAN	0.3	0.4	1.7	1.9
HILUMIN	0.4	0.7	1.4	2.3
Mild Steel	21.9	50.5	215.1	165.3
SS 316L	1.0	1.5	1.2	126.4

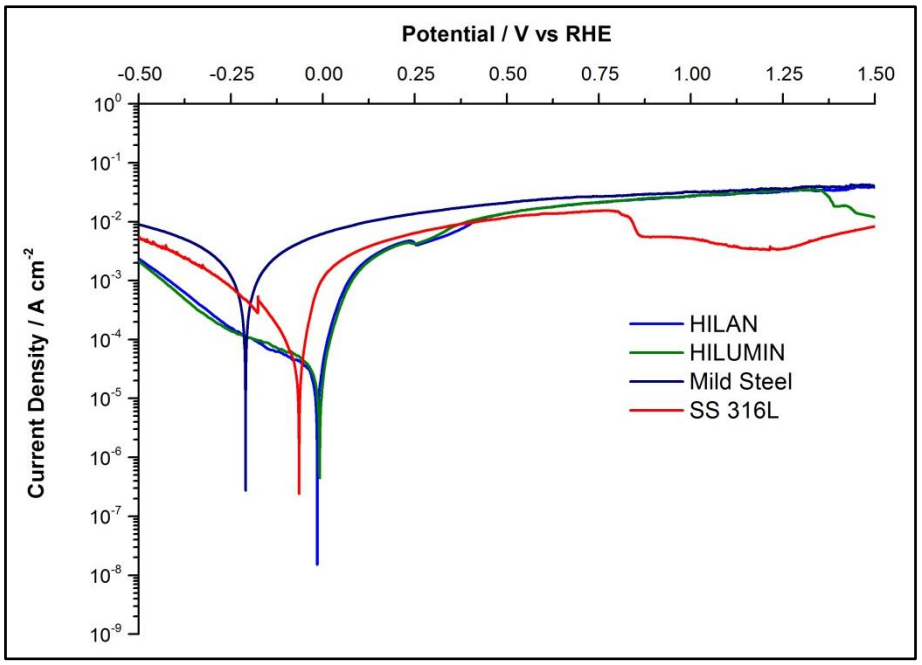

Figure 6.14: Potentiodynamic polarisation curves for the four substrates coated with graphene without a catalyst layer under air at 25 °C

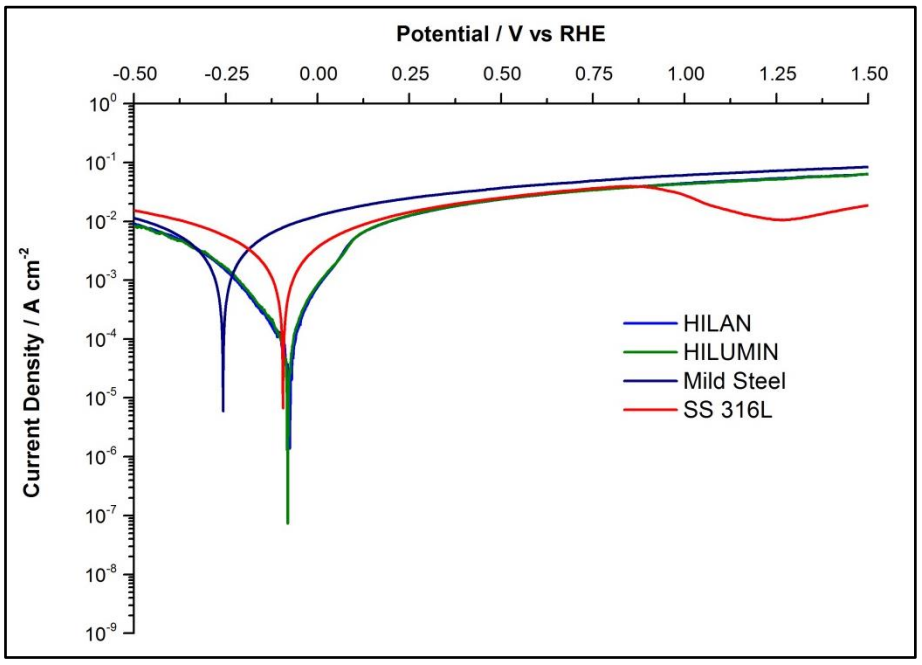

Figure 6.15: Potentiodynamic polarisation curves for the four substrates coated with graphene without a catalyst layer under air at 80 °C

The corrosion rates for the batch 2 graphene coated samples is similar to those observed for the batch 1 samples, with the exception of the SS 316L coated with graphene in hydrogen at 80 °C. The corrosion rate for SS 316L

samples coated with graphene in batch 2 is 100 times higher than that of batch 1. Apart from the SS 316L sample under hydrogen at 80 °C, the other samples have similar corrosion rate. In all cases, the lack of an oxide layer, and hence high passive current densities, are still observed suggesting lack of corrosion protection under cathodic conditions, especially at the elevated temperature of 80 °C.

The potentiodynamic curves for the four catalyst layer assisted growth graphene coated substrates under a hydrogen environment are shown in Figure 6.16 and Figure 6.17, and the corrosion rates are shown in Table 6.6.

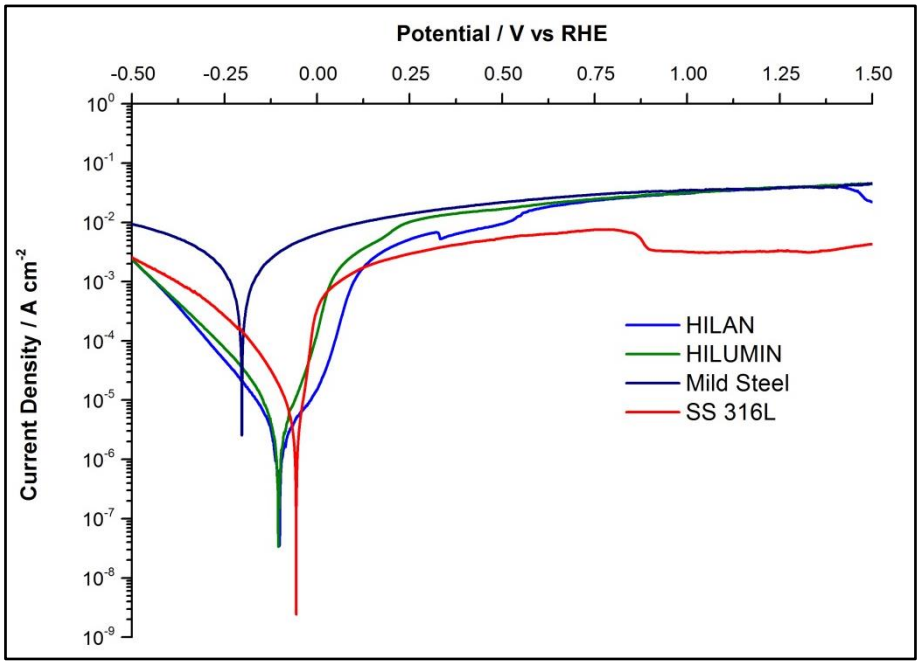

Figure 6.16: Potentiodynamic polarisation curves for the four substrates coated with graphene without a catalyst layer under hydrogen at 25 °C

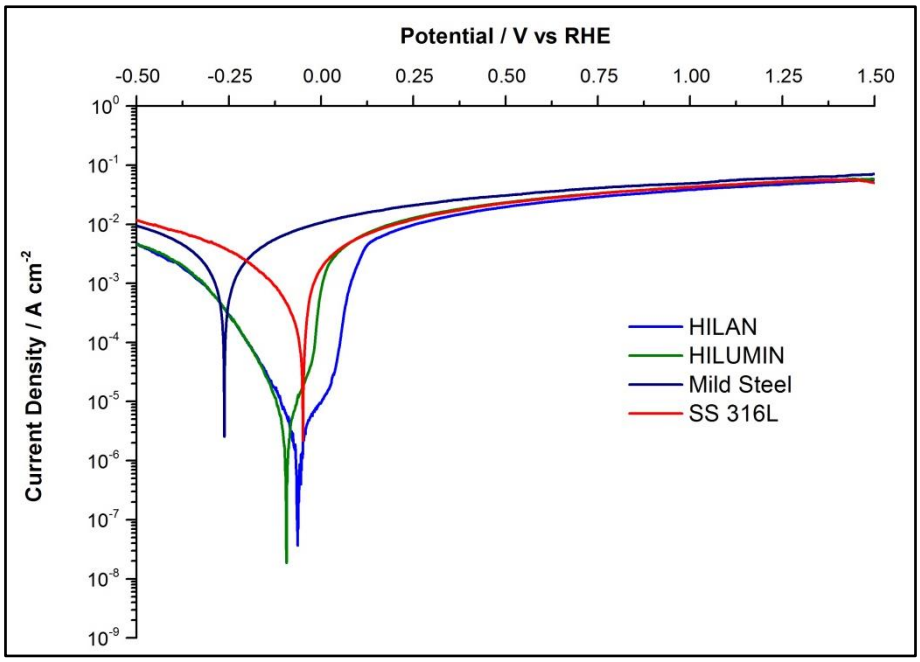

Figure 6.17: Potentiodynamic polarisation curves for the four substrates coated with graphene without a catalyst layer under hydrogen at 80 °C

As observed for the corrosion rates of the four substrates under air, a similar trend is observed under hydrogen. The corrosion rates for HILAN and HILUMIN are similar in both batches, with mild steel offering a lower corrosion rate for batch 2 samples. Similar to the results under air, the batch 2 SS 316L sample displays a large difference in the corrosion rate under hydrogen at 80 °C, compared to batch 1. Batch 2 SS 316L samples have a higher corrosion rate at elevated temperatures in both anodic and cathodic conditions.

Table 6.6: Rate of corrosion (mm per year) under hydrogen for the four graphene coated substrates via catalysed and un-catalysed growth routes

Material	25 °C		80 °C	
	Batch 1 (Catalysed)	Batch 2	Batch 1 (Catalysed)	Batch 2
HILAN	0.01	0.05	0.1	0.03
HILUMIN	0.1	0.1	0.4	0.1
Mild Steel	20.9	10.2	61.4	20.2
SS 316L	0.4	0.03	0.04	14.2

6.1.6. Conclusions

The Graphene coating has proven to be an excellent option for improving the ICR performance of the candidate substrates. HILAN and HILUMIN have demonstrated near zero ICR values at $140\ N.cm^{-2}$, while the other two substrates (MS and SS) have also shown ICR values below the 2017 DOE target of $20\ m\Omega.cm^2$ at $140\ N.cm^{-2}$. This trend is observed across both batches with the exception of HILAN offering slightly higher ICR values for batch 2; although still under $20\ m\Omega.cm^2$ at $140\ N.cm^{-2}$.

The coatings, however, have failed to provide any corrosion protection to the substrates under simulated fuel cell conditions. This does not imply that the graphene coating itself has failed to provide corrosion protection, it is more important to understand the surface coverage of the substrate. It is imperative that a uniform coverage of graphene is achieved on top of the substrate to provide adequate corrosion protection. Any coating defects, pin-holes or discontinuities in the coating will lead to the electrolyte accessing the base material underneath the coating and once the electrolyte gets to the unprotected steel beneath the coating. In the case of mild steel, the corrosion proceeds at higher rates as mild steel does not provide any corrosion protection by itself. In the case of SS 316L, the graphene coating did not provide the required corrosion protection as the coating process had altered the surface chemistry of the SS 316L substrate. The highly reducing hydrogen environment during graphene growth removes any oxides from the surface and the graphene growth itself prevents the reformation of these oxides. Once again, as the electrolyte penetrates to the base material, the substrate corrodes from underneath the coating, resulting in the delamination of the coating.

Raman spectroscopic analysis has confirmed the presence of an inhomogeneous coating of few layer graphene. The non-uniform graphene coverage allows the electrolyte to penetrate the coating and corrode the substrate underneath.

6.2. Electrophoretic Deposition of Graphene

The experiments and the results reported in this section are conducted in collaboration with the Department of Physics and Astronomy, UCL.

This section presents a novel method of graphene deposition using electrophoretic deposition (EPD). Graphene layers are deposited via EPD from a graphene solution prepared using graphite intercalation compounds[145] (GICs) suspended in an organic solvent[146,147]; N-Methyl-2-pyrrolidone (NMP) is used to prepare graphene solution in this project.

6.2.1. EPD Method

A three-step process is used is used to deposit graphene on a SS 316L substrate; formation of GIC, formation of a colloidal solution in NMP and the electrophoretic deposition of graphene from the colloidal solution to the SS 316L substrate using constant DC voltage.

6.2.1.1. Graphite Intercalation Compounds

The formation of graphite intercalation compounds (GICs) can be simply explained as the insertion of atomic or molecular layers of a different chemical species called the intercalant in between the graphene layers in a graphite host as it is a lamellar solid[148]. GICs exhibit unique properties such that graphite being amphoteric in nature; its layers can accept electronic charge from donor species or donate charge to the intercalated species[149]. When an electron donor, for example an alkali metal, is intercalated into graphite, a donor GIC is formed and when an electron acceptor is intercalated, an acceptor GIC is formed[149]. In other words, electrons are either taken away from graphene or donated to graphene resulting in a layered material salt. Another unique characteristic is the staging. Graphite can form GIC with an intercalant for every interlayer space, or for every other interlayer space, or every 3rd interlayer space, or every nth interlayer space to respectively form stage-1, stage-2, stage-3, or stage-n GIC. The first two stages are demonstrated in Figure 6.18.

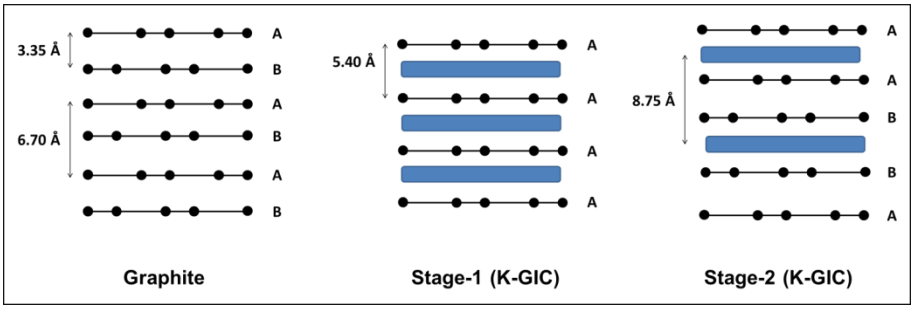

Figure 6.18: Schematic diagram of the staging of graphite intercalates for stages 1 and 2, where the graphene planes are represented by connected open circles and the potassium layers are represented by the blue lines (adapted from[148,149])

A unique characteristic of liquid ammonia is that it possesses the ability to dissolve the alkali metals resulting in the solvation of a large number of electrons in solution. This gives metal-ammonia solutions a very high reduction potential. A free electron in solution can be described as a solvated electron. It is the smallest possible anion and alkali metal atoms serve as electron donors in solvents that mediate outer- sphere electron transfer[150]. Lithium in liquid ammonia gives rise to the most well-known example of the solvated electron. Humphry Davy was the first to describe the blue-coloured solutions of alkali metals in liquid ammonia[150]. This is possible due to the very low dissociation of ammonia and the stability of ammonia with respect to reduction. Ammonia dissociates to H^+ and NH^{2-} in solution at concentrations of only 10^{-10} ppm. Hence, the reaction between the metal ions or electrons with amine is very slow. In other words, the solvated electron solutions are metastable and their decomposition is very slow because of the reduction of the solvent by solvated electrons.

$$\boldsymbol{e^-_{(sol)} + NH_3 \leftrightarrow NH_2^- + \frac{1}{2}H_2} \qquad \textit{Equation 6.1}$$

The main species remaining in the solution are the solvated electrons and the metal ions.

In the formation of the GICs, firstly, ammonia is purified as it may contain some impurities such as oxygen or water molecules. These are removed by the reaction of liquid ammonia with sodium metal in a container.

$$\boldsymbol{Na + H_2O \rightarrow NaOH_{(s)} + \frac{1}{2}H_2} \qquad \textit{Equation 6.2}$$

$$\boldsymbol{Na + O_2 \rightarrow Na_2O_{(s)}} \qquad \textit{Equation 6.3}$$

$$\boldsymbol{Na + NH_3 \rightarrow NaNH_{2(s)} + \frac{1}{2}H_2} \qquad \textit{Equation 6.4}$$

Any excess sodium is removed by the reaction with ammonia. The impurities are removed as solid films on the container walls. As a result pure liquid ammonia is produced which is then transferred to another container in gas phase. The gaseous ammonia is pressurised and introduced as liquid ammonia to a container containing micro graphite (<44 μm) and potassium metal, resulting in a potassium-ammonia GIC. For an example, the $K(NH_3)_xC_{24}$ is produced using $0.267\ g$ (2.225×10^{-2}) moles of micro graphite powder and $0.036\ g$ (9.271×10^{-4}) moles of potassium metal. An excess of potassium metal is used every time to ensure stage-1 intercalation.

6.2.1.2. Colloidal Solution

The potassium-ammonia-GIC is sensitive to air and hence the formation of the colloidal solution is undertaken in an inert environment. In this project all experiments are conducted in argon environment. A $1\ mg/mL$ solution is prepared by dissolving the potassium-ammonia-GIC produced in an NMP solvent. The formation of the GICs results in the increase in the inter-atomic layer distance of the graphene layers. These layers are then exfoliated with the aid of sonication. The as-produced GIC solution in NMP is sonicated for $5\ min$. The energy from the sonication results in the separation of the graphene layers and as discussed in section 2.2.2.2, the organic solvent; NMP in this case, prevents the restacking of these layers. The colloidal solution is then used to conduct the electrophoretic deposition of graphene on to a SS 316L substrate.

6.2.1.3. EPD Set-up

The colloidal solution prepared after sonication is allowed to settle for a period of at least $48\ h$. This is to ensure that any large graphitic chunks are settled at the bottom of the container. After settling, the supernatant is taken to conduct the electrophoretic deposition. EPD of graphene was

carried out using a two-electrode system in an inert environment using the supernatant from the colloidal solution. The schematic diagram of the EPD set-up is shown in Figure 6.19.

As shown in Figure 6.19, SS 316L plates $(25 \times 25 \times 0.5\, mm^3)$ are used as the working as well as the counter electrode. The graphene particles are positively charged due to the presence of potassium and when a constant potential is applied the graphene particles migrate towards the negative electrode under the influence of the applied potential. The key parameters for the deposition of graphene include the concentration of K-ammonia-GIC, the applied voltage and the deposition time. Once the EPD is conducted for a specific amount of time, the electrodes are removed from the suspension and allowed to dry under the inert environment for a period of $24\, h$. After that the electrodes are removed from the inert environment and air stable graphene layer is achieved on SS 316L substrate.

As a novel method of graphene deposition, specific literature on the EPD of charged graphene from colloidal GIC solution was not found in the literature and hence a number of trials were conducted to optimise the deposition parameters to achieve the optimum surface coverage whilst maintaining the few layer characteristics of graphene. The applied voltage and deposition times were varied and in addition to this, $1\, mg/mL$ solution and a $3\, mg/mL$ suspension was also used. In all cases, the suspension was first sonicated for $5\, min$, allowed to settle for $48\, h$ and then the supernatant was used to conduct EPD experiments.

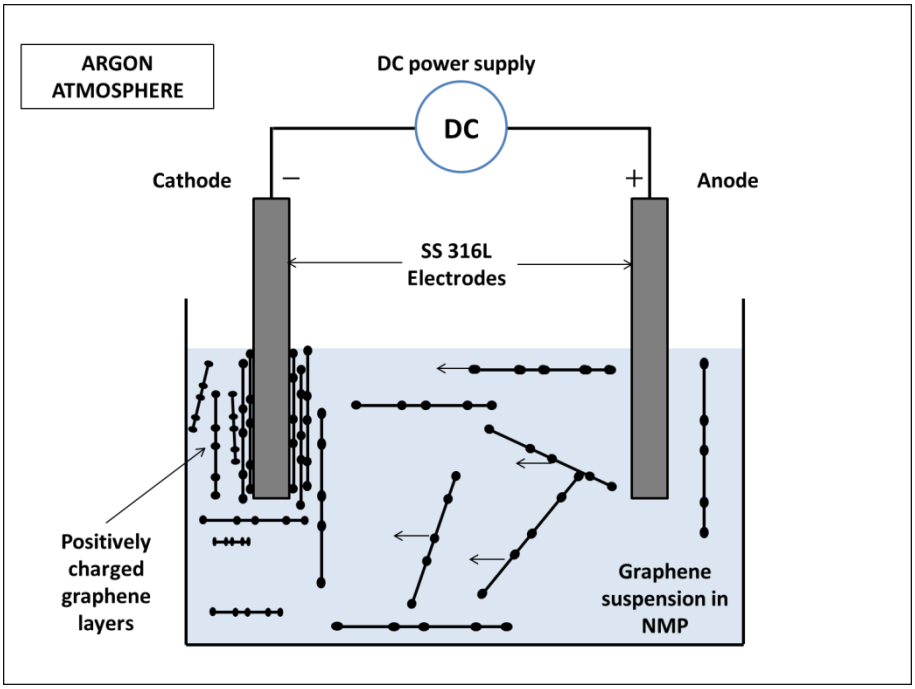

Figure 6.19: Schematic diagram for EPD of graphene from GIC suspension in NMP

6.2.2. EPD Results and Graphene Characterisation

This section presents the results from the EPD of graphene under different conditions. EPD of graphene has been conducted before using aqueous solutions and also graphene oxide has been widely deposited which is then reduced to graphene. At first, a short period of $2\,min$ was used to deposit graphene using a $1\,mg/mL$ solution of graphene in NMP. A potential difference of $2\,V$ was applied between the two electrodes and the electrodes were submerged in the graphene solution for a period of $2\,min$. On Raman analysis of the electrodes, neither graphene nor any graphitic material was detected on either of the electrodes. Subsequently, the time was increased to $5\,min$ and then $10\,min$, without any successful deposition of graphene on the electrodes. At which point, the applied voltage was varied with a constant deposition time of $30\,min$. In our experiments, no graphene particles were detected on the samples after deposition for $30\,min$ using $1, 2, 10$ and $20\,V$. Finally, graphene particles were detected on Raman analysis of the SS 316L substrate after deposition for $30\,min$ at $50\,V$.

6.2.2.1. EPD of Graphene using $50\ V$ for $30\ min$

EPD deposition of graphene was conducted using $50\ V$ for $30\ min$ using a $1\ mg/mL$ solution of GIC in NMP. The coating resulted in a widely distributed uneven coverage of graphene on the SS 316L substrate. On Raman analysis of the substrate, a monolayer graphene was detected on the SS 316L substrate (Figure 6.20) with a 2D peak intensity larger than the G peak intensity, hence resulting in 2D/G peak ratio of larger than 1[64]. The coverage was found to be uneven. In order to achieve maximum coverage, the coating was repeated under the same voltage for a longer period of time and with an increase concentration of GIC to allow the graphene to be deposited uniformly.

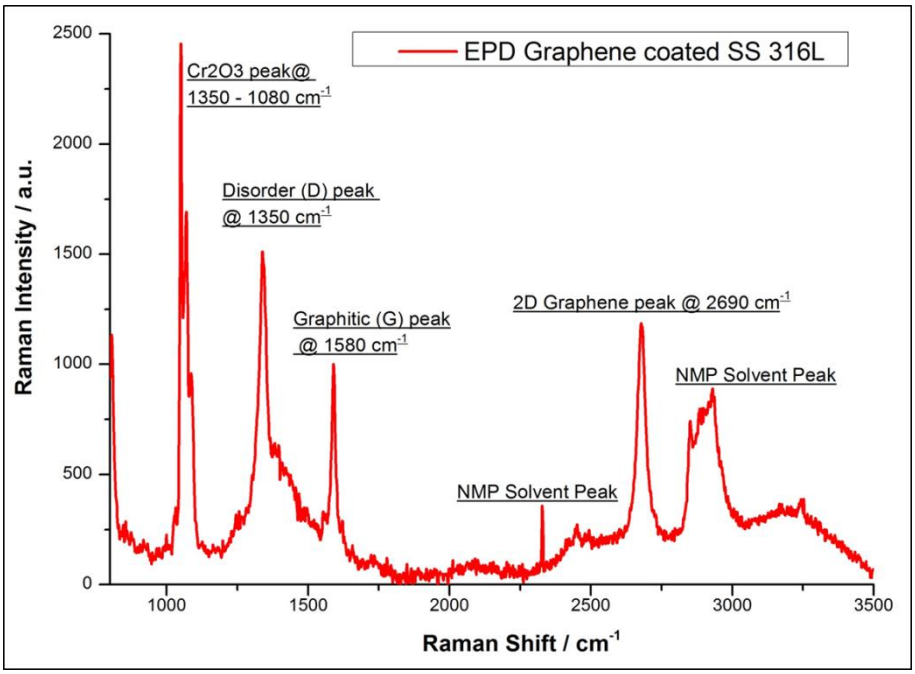

Figure 6.20: Raman spectra of EPD graphene coated SS 316L sample using $50\ V$ for $30\ min$ with a $1\ mg/mL$ solution of GIC in NMP

6.2.2.2. EPD of Graphene using $50\ V$ for $48\ h$

The coating was repeated with at $50\ V$ for a period of $48\ h$ with a $3\ mg/mL$ solution of graphene. The coating run resulted in a better coverage of carbon compounds throughout the sample surface. However, it resulted in the degradation of the solvent and the deposits were found to be that of sooty carbonaceous particles (Figure 6.21). On study of the published

literature[151], the high voltage resulted in the degradation of the solvent molecules.

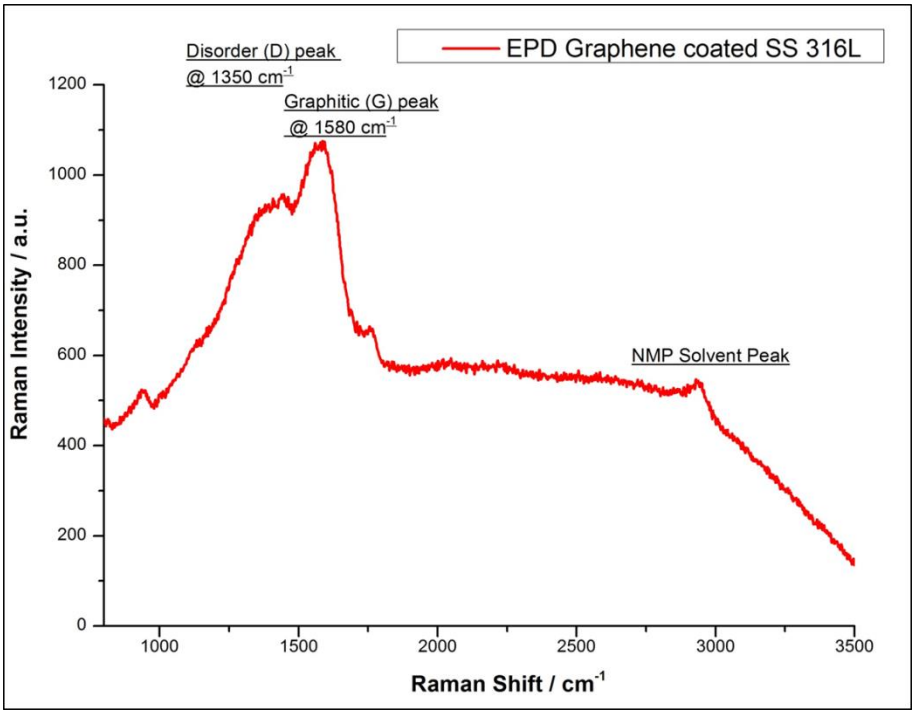

Figure 6.21: Raman spectra of EPD graphene coated SS 316L sample using $50\ V$ *for* $48\ h$ *with a* $3\ mg/mL$ *solution of GIC in NMP*

An optical image of the EPD graphene coated SS 316L substrate is shown in Figure 6.21 The black islands are deposits of sooty carbon. The graphene layers have been burnt due to the high potential difference applied for a long time. The golden coloured particles within the image are a result of the disintegration of the NMP solvent molecules.

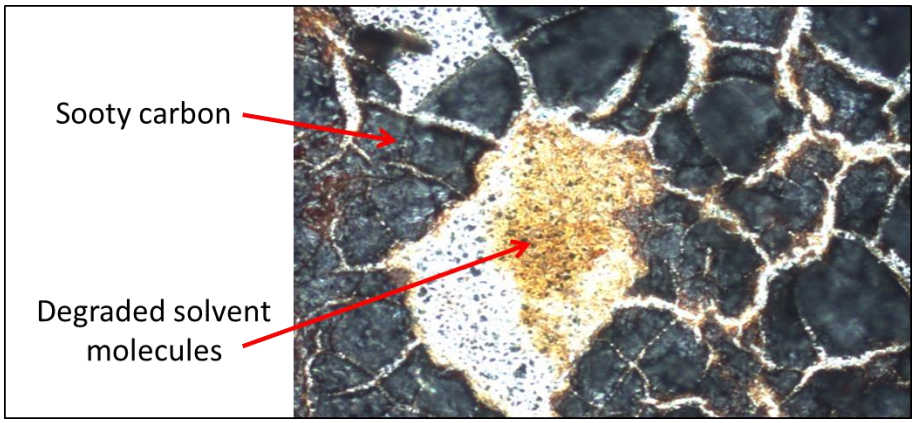

Figure 6.22: Optical image of EPD graphene coated SS 316L sample using $50\ V$ *for* $48\ h$ *with a* $3\ mg/mL$ *solution of GIC in NMP*

6.2.2.3. EPD of Graphene using 1 V for 48 h

From the previous two runs, it was evident that the solvent molecules degraded beyond $50\ V$ and the coating process needed a longer period of time $(48\ h)$ for a successful deposition of graphene. The concentration of the GICs was maintained at $3\ mg/mL$ to achieve better coverage. The coating run resulted in a uniform coverage of graphene through the sample surface and no solvent degradation products were found during Raman inspection (Figure 6.23).

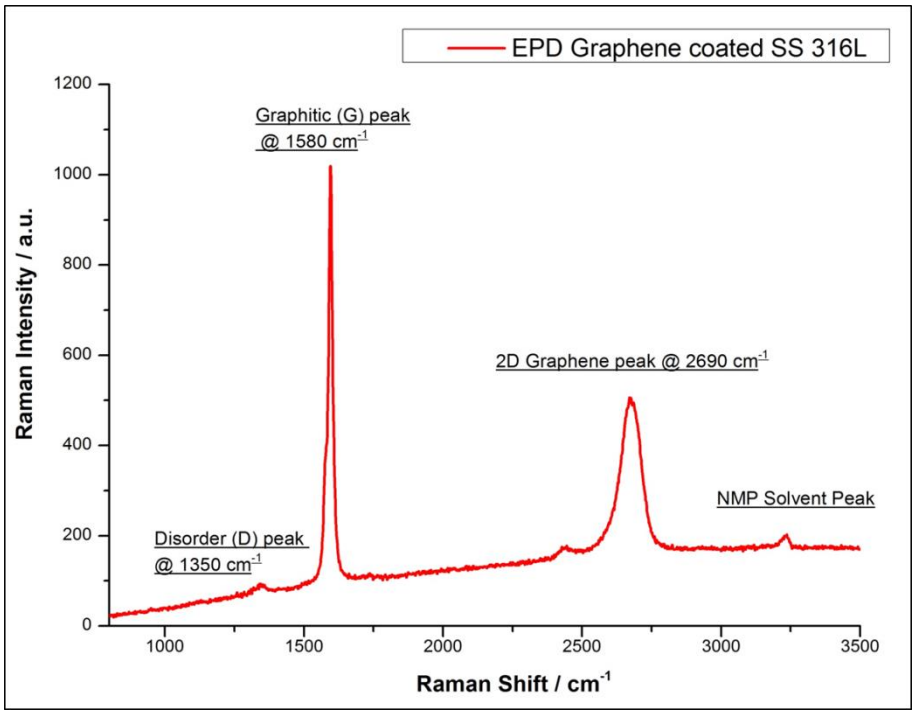

Figure 6.23: Raman spectra of EPD graphene coated SS 316L sample using $1\ V$ *for* $48\ h$ *with a* $3\ mg/mL$ *solution of GIC in NMP*

The uniform coverage of graphene on SS 316L substrate can be complemented by the AFM imaging of the SS 316L substrate coated with EPD graphene with uniform coverage throw-out the substrate. Figure 6.25 shows an AFM image of graphene coated SS 316L substrate with a height profile through the image. The bright yellow spots represent the larger graphene chunks with height profile in terms of hundreds of nanometres.

An optical image of the sample (Figure 6.24) was taken during the Raman spectroscopy scans. Figure 6.24 shoes the grain boundaries of the SS 316L substrate and a graphene deposit on top of the substrate. John *et*

al.[151] have reported that the transmittance of graphene decreases exponentially with the increase in number of layers. The transition from multilayer graphene to graphite occurs at around 80 layers. In other words, the graphitic particles would be opaque. The presence of graphene layers with the grain boundaries being visible through the graphene particle provides evidence to the presence of few layers of graphene that is complementary to the Raman analysis.

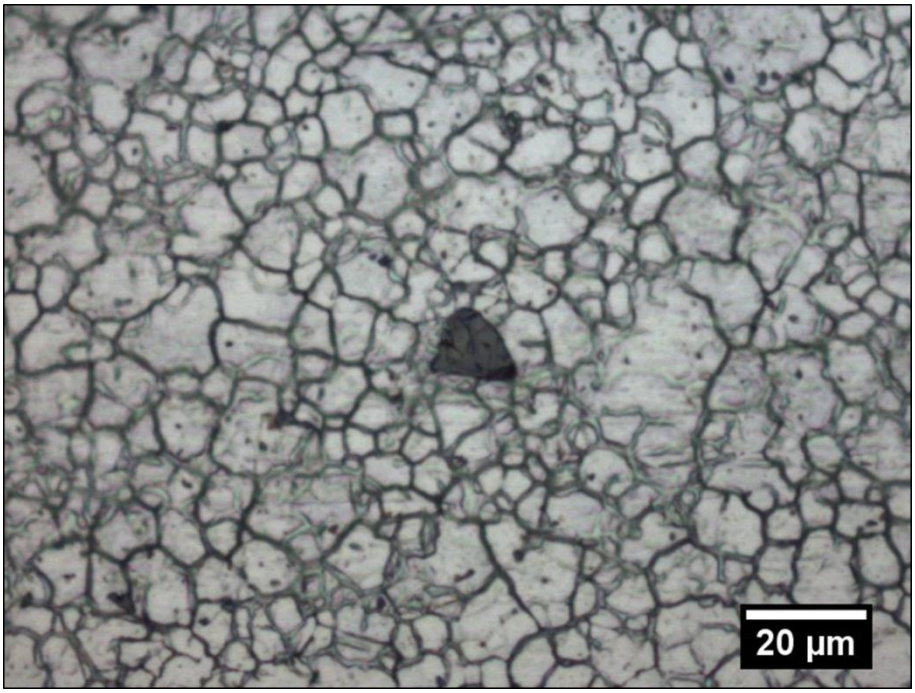

Figure 6.24: Optical image of EPD graphene coated SS 316L sample with a transparent graphene chunk visible on the substrate

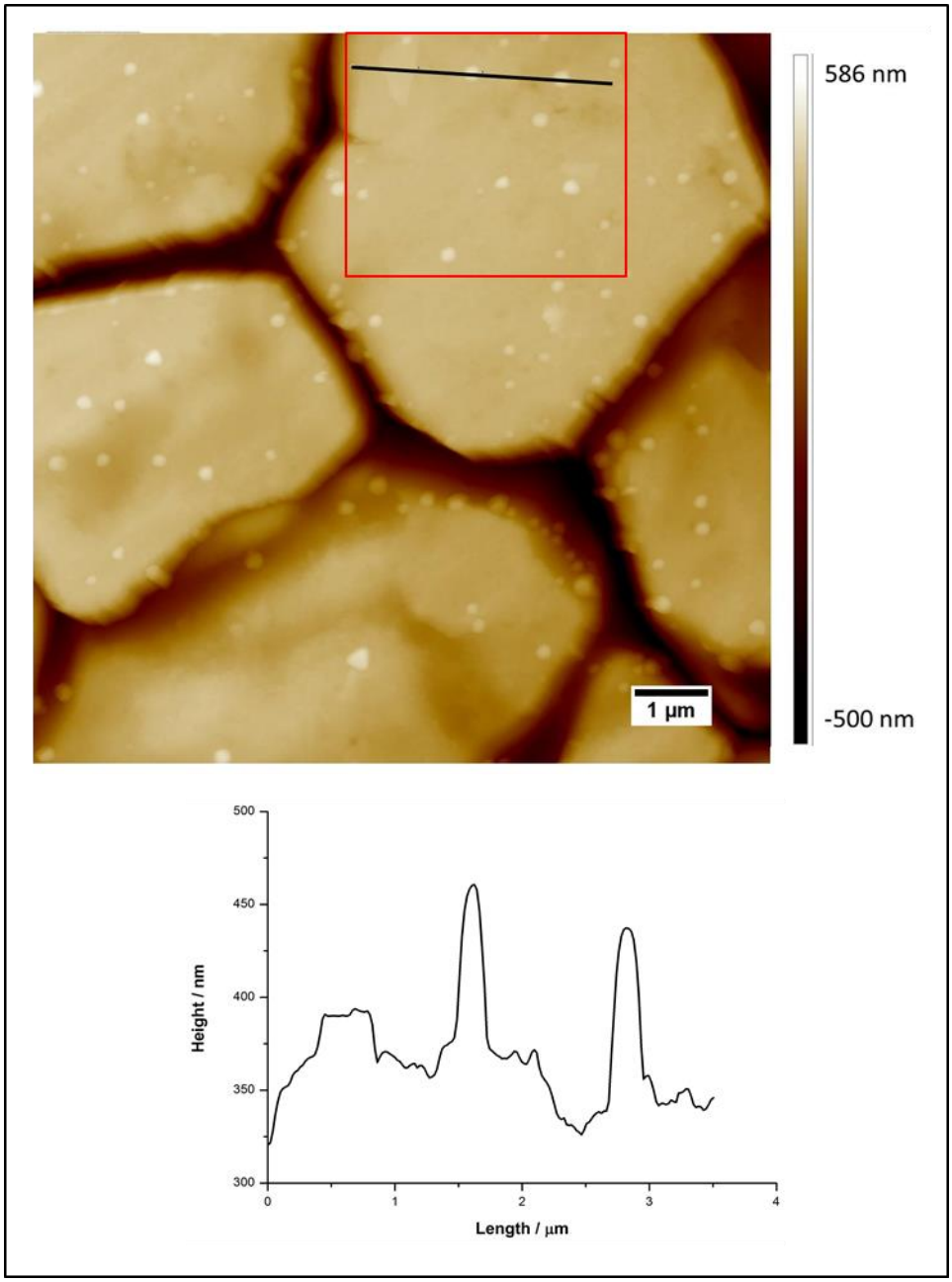

Figure 6.25: AFM image (top) of EPD graphene coated SS 316L with the height profile (bottom) obtained on the black line

Figure 6.26 shows a zoomed in section from Figure 6.25 and another height profile is obtained across the larger and more flat graphene particle with a height profile of around $30\ nm$ and $3\ \mu m$ wide.

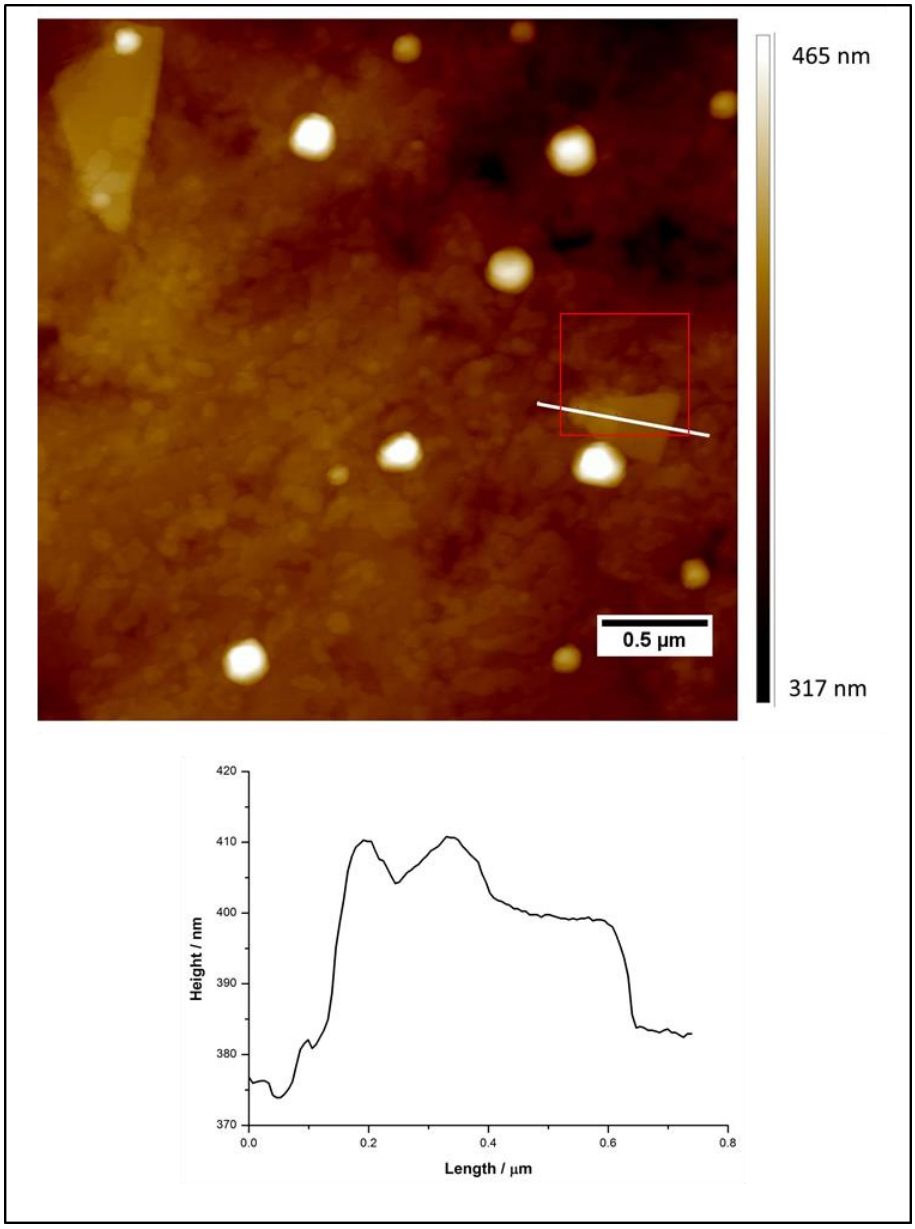

Figure 6.26: AFM image (top) of EPD graphene coated SS 316L zoomed in on the red box in Figure 6.25 with the height profile (bottom) obtained on the white line

Figure 6.27 represents a single graphene particle around $450 \times 100\, nm$ in area and around $10\, nm$ height. This would represent the presence of few layers of graphene.

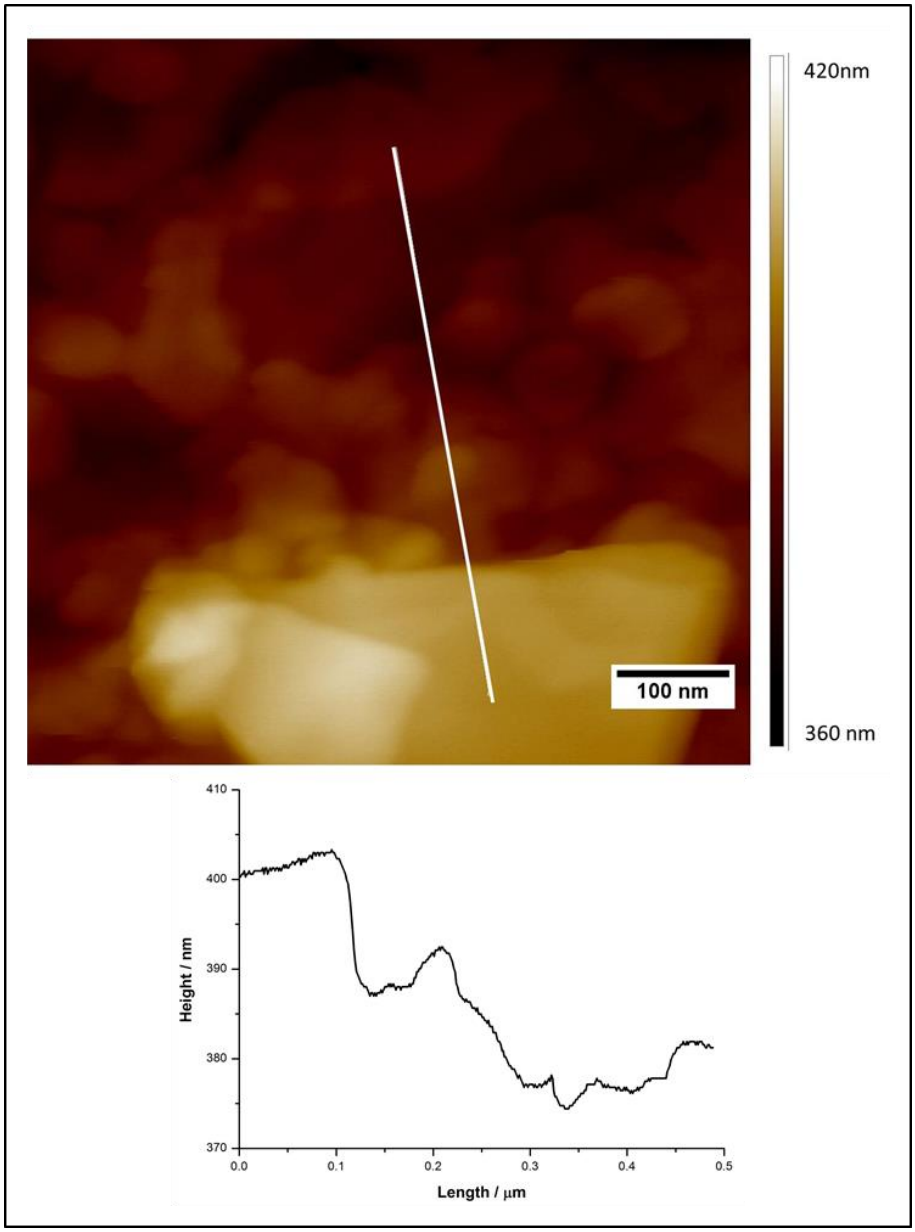

Figure 6.27: AFM image (top) of EPD graphene coated SS 316L zoomed in on the red box in Figure 6.26 with the height profile (bottom) obtained on the white line

6.2.3. ICR Results

The ICR values of EPD graphene coated SS 316L with uniform coverage were measured using the methods detailed in chapter 5, by collecting EIS scans at different compression pressures within a range of $20 - 200\,N$. The ICR values for uncoated and EPD graphene coated SS 316L are shown in Figure 6.1.

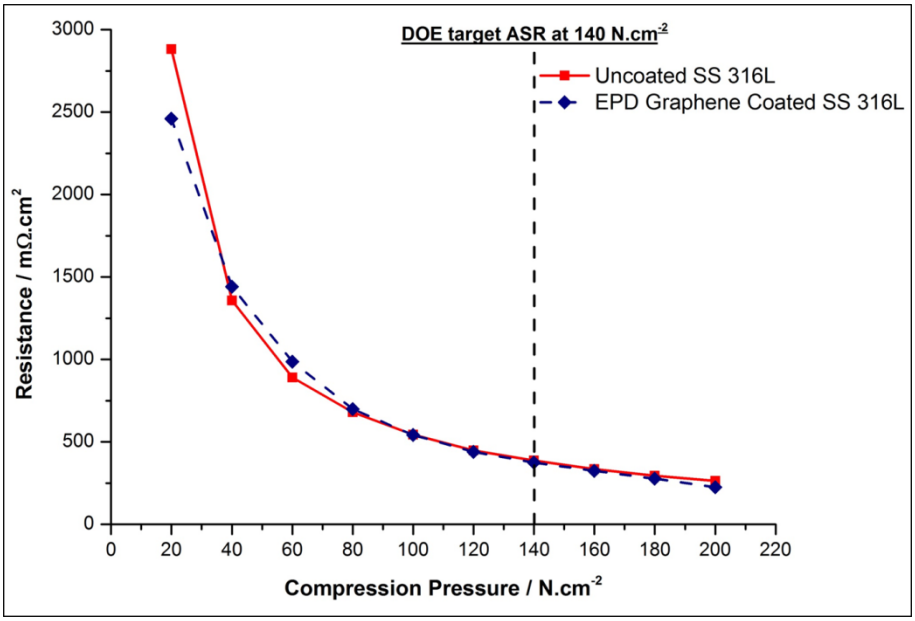

Figure 6.28: Resistance vs compression for uncoated and EPD graphene coated SS 316L substrate

The ICR values for the EPD graphene coated sample follow a similar trend as observed by the uncoated SS 316L substrate. In the case of EPD coating, the coating process is undertaken on the SS 316L sample without any pre-modifications to the substrate. The substrate is cleaned using an acetone wipe to remove any dust or grease and then it is introduced in to the argon environment where the coating process takes place. It can be observed from Figure 6.28 that SS 316L has retained its original oxide layer and hence the ICR results are nearly the same as the uncoated substrate. The ICR values for uncoated and EPD graphene coated SS 316L substrates at $140\ N.cm^{-2}$ were found to be $388\ m\Omega.cm^2$and $374\ m\Omega.cm^2$, respectively.

As described in section 6.1.1, ICR is a surface characteristic of the samples and as the substrate sample was not modified, the graphene layers were deposited on top of the oxide layer of SS 316L. Graphene may provide excellent in-pane electrical conductivity but the electrons would still need to go through the SS 316L oxide layer and then the bulk SS 316L material where the through-plane electrical conductivity is affected by the characteristics of the oxide layer. As the oxide layer is known to hinder the electron movement, both samples have registered similar ICR values at each given compression.

6.2.4. Corrosion Test Results

Potentiodynamic test was carried out to investigate the corrosion performance of the EPD graphene coated SS 316L. The test solution used was the same as used for previous corrosion tests; $0.1\,M\,H_2SO_4 + 2\,ppm\,F^-$. The solution was purged with hydrogen and the temperature was maintained at 80 °C. In order to use the most extreme corrosion conditions for this sample, the solution was purged with hydrogen at 80 °C in comparison to air environment or lower temperatures. This was selected due to the shortage of samples produced using EPD of graphene GICs. If the sample performs well in harsher conditions, it would be expected of the sample to perform better in the other conditions at lower temperature. The potentiodynamic curves for the uncoated SS 316L and the EPD graphene coated SS 316L under hydrogen at 80 °C are shown in Figure 6.29.

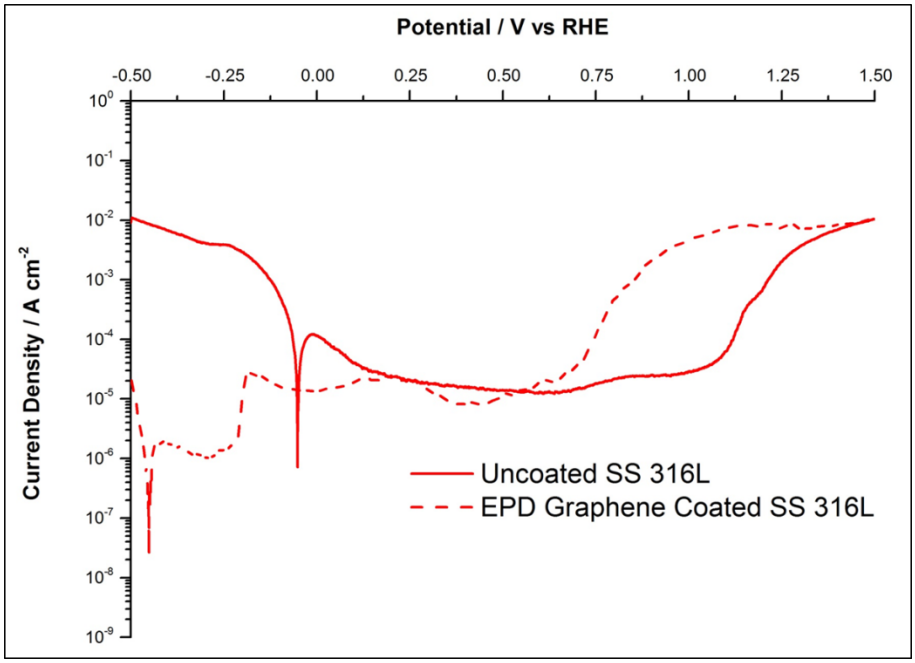

Figure 6.29: Potentiodynamic polarisation curves for uncoated and EPD graphene coated SS 316L substrates under hydrogen at 80 °C

The corrosion rates for EPD graphene coated SS 316L substrates was found to be lower than that of the uncoated substrate in hydrogen as shown in Table 6.2.

Table 6.7: Corrosion current and the rate of corrosion in terms of mm per year under hydrogen at 80 °C for uncoated and EPD graphene coated SS 316L

Material	Corrosion Current $(\mu A.cm^{-2})$	Corrosion Rate $(mm\ per\ year)$
Uncoated SS 316L	4.0×10^{2}	3.1×10^{0}
EPD Graphene Coated SS 316L	5.0×10^{-1}	5.7×10^{-3}

The EPD graphene coated SS 316L has been reported to have the best corrosion performance amongst all the samples studied in the project. The corrosion rate was almost three orders of magnitude lower than that of the uncoated SS 316L. The uniform graphene coating deposited on the SS 316L substrate provides adequate corrosion protection to the substrate. A notable feature in the LSV curve was the shift in the corrosion potential of the EPD graphene coated substrate. The corrosion potential was more negative as compared to the uncoated substrate suggesting the cathodic behaviour of the carbon coating. The passive current densities were reported to be similar for uncoated and EPD graphene coated SS 316L. This would suggest that the SS 316L substrate retains its inherent property of passive corrosion protection and in addition, graphene coating has reduced the corrosion rate of the substrate.

6.2.5. Conclusions

A monolayer graphene confirmed by Raman analysis has been successfully deposited using a novel method of EPD of charged graphene particles from a colloidal solution of GICs in NMP. After a number of trials, uniform graphene coverage has been achieved on a SS 316L substrate with few layers of graphene deposited on the substrate. The graphene has been characterised using Raman spectroscopy and AFM imaging. The graphene has been deposited on SS 316L substrate without any surface modifications and hence it has been reported to have similar ICR performance as was the case with uncoated SS 316L. However, a remarkable improvement is reported in the corrosion performance of the EPD graphene coated SS 316L substrate with three orders of magnitude lower corrosion rates.

7. 3D X-Ray Microtomography for Corrosion Analysis

This chapter presents the 3D X-ray micro tomography analysis of stainless steel. Initially the flat SS 316L token $(25 \times 25 \times 0.5\, mm^3)$ coated with graphene was analysed using X-ray CT. The high aspect ratio of the token geomtry presented a challenge of high attenuation during the sample rotation when the flat token is oriented parallel to the X-ray beam, as opposed to when the token is perpendicular orientation. To overcome this, a stainless steel wire ($0.5\, mm$ diameter, Goodfellow, UK, FF215313: Cr $18\%, Ni$ $10\%, Mo$ 3% and Fe to balance with other elements present in $< 1\%$, annealed) was used for corrosion experiments before X-ray CT analysis. The SS 316L wire used was the same grade as the SS 316L tokens to maintain the uniformity of the corrosion reaction. The diameter of the wire was selected to ensure that the wire was within the field of view for X-ray CT experiments.

Further, the SS 316L wire was then coated with graphene using the CVD method discussed in section 2.2.3. The coated wire was initially CT scanned and then rescanned after the corrosion experiments to study the effect of the corrosion on the steel substrate. 3D X-ray microtomography provides an excellent tool for studying the sub-surface characteristics of corroded samples, especially in case of pitting corrosion where the depth of the corrosion cannot be easily analysed using electrochemistry alone, or even with the aid of other 2D surface analysis techniques.

7.1. Post-Corrosion X-Ray CT of Graphene Coated SS 316L

An X-ray CT was carried out on an SS 316L sample $(25 \times 25 \times 0.5\, mm^3)$ coated with graphene via chemical vapour deposition. The coated token was first analysed for corrosion protection using potentiodynamic polarisation as discussed in chapter 4.1.3. The as-corroded token was then

cut to a smaller token size of $(3 \times 3 \times 0.5\, mm)$ and scanned with Xradia Versa XRM-520. The parameters used for the X-ray CT scan are listed in Table 7.1.

As discussed in section 6.1, the CVD process of depositing graphene on steel substrates; SS 316L in this case, results in the removal of the oxide layer on the sample surface. The corrosion performance of the graphene coated SS 316L was found to be poorer due to the removal of the oxide layer during the graphene deposition process. As a result the coating was de-laminated and the sample underneath was exposed to the corrosive environment, producing corrosion products deposited on the surface amongst the remains of the de-laminated graphene coating. As achieve-ray attenuation in carbon is low, the X-ray image produced shows only the steel substrate and the corrosion products formed on the surface (Figure 7.1).

Table 7.1: List of parameters used for X-Ray CT experiments for a graphene coated SS 316L flat token

Parameter		**Value**
X-Ray Source	Tube Voltage	$80\ kV$
	Current	$88\ \mu A$
	Power	$6.96\ W$
	Source Filter	Low Energy 6
X-Ray Detector	Optical Magnification	$4.0\ x$
	Sensor Binning	2
	Exposure Time	$4\ s$
	Image Size	1013×1013
	Pixel Size	2.8354

Figure 7.1(a) shows the 3D full volume rendering of the graphene coated SS 316L substrate, and Figure 7.1(b) shows the top surface of the sample revealing the surface pits and the deposition of corrosion products formed on the surface. Figure 7.2 shows the cross-section of the XY-plane showing the side view of the sample. The X-Ray CT reconstruction shows the difference in attenuation of the bulk SS 316L substrate and the corrosion products on the top surface.

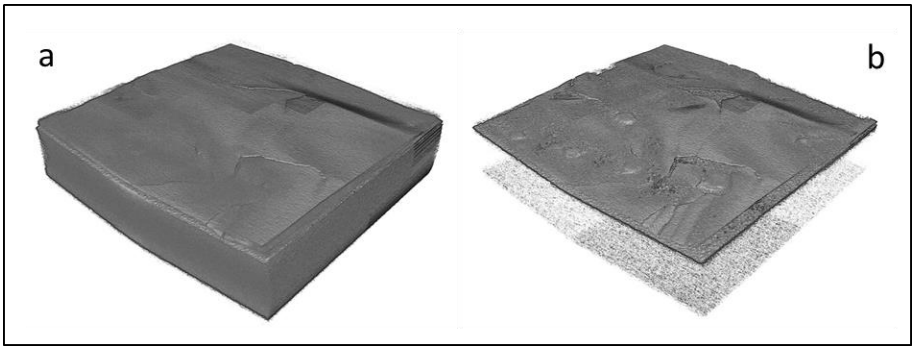

Figure 7.1: X-ray CT image of graphene coated SS 316L token after linear sweep corrosion experiment (a) full volume rendering and (b) showing the corrosion products on the top surface

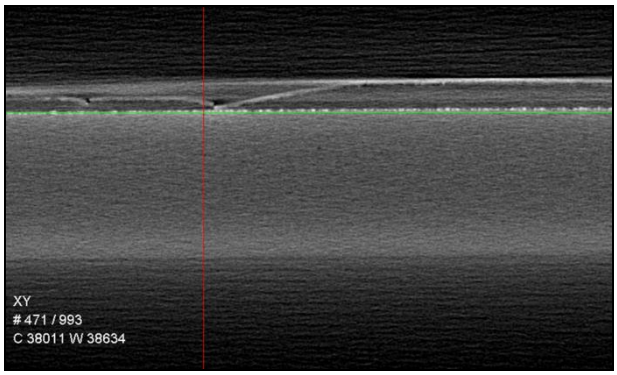

Figure 7.2: An XY-plane image (side view) of a graphene coated SS 316L token after a linear sweep corrosion experiment

Figure 7.3 depicts the top view of the sample which reveals the pits on the surface of the sample and the corrosion products deposited in the form of layers or films. This correlates with the high corrosion current obtained from the linear sweep voltammetry scans during the electrochemical experiments. The electrolyte penetrates beneath the coating and ,with a lack of the protective oxide layer; corrodes the substrate from underneath the coating resulting in corrosion products forming on the surface.

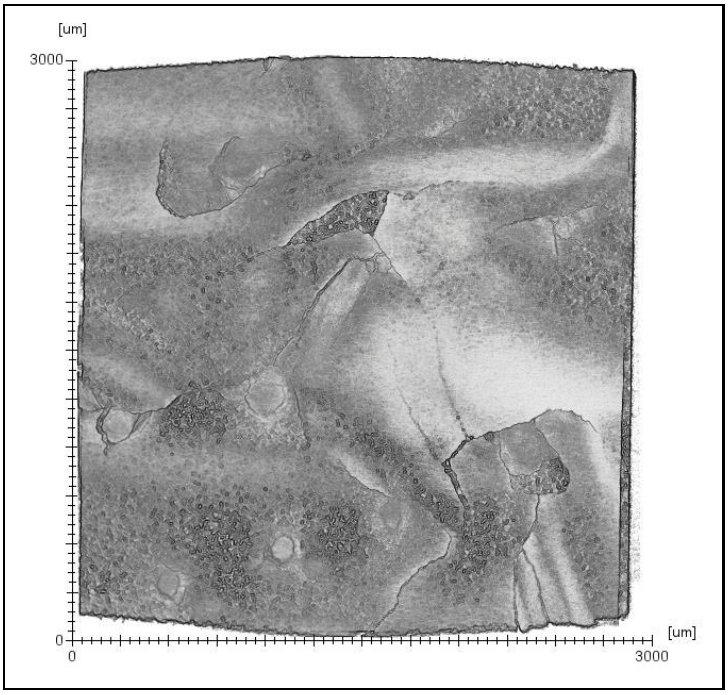

Figure 7.3: An XZ-plane image (top view) of a graphene coated SS 316L token after a linear sweep corrosion experiment showing corrosion products and pits on the surface of the sample

7.2. X-Ray CT of SS 316L Wires

The issue with imaging the flat steel tokens was the high attenuation by the sample when oriented parallel to the plane of the X-ray beam. In order to overcome this, subsequent X-ray CT studies were carried out on $0.5\,mm$ SS 316L wires that can be mounted as a cylinder on the holder allowing uniform attenuation to be obtained through all projections. X-ray CT scans were obtained for a pristine SS 316L wire and for a wire corroded for $48\,h$. The SS 316L wire was corroded under the simulated anodic PEMFC operation conditions. A higher concentration of the electrolyte solution was used, $1\,M\,H_2SO_4 + 2\,ppm\,F^-$ ions, to accelerate the corrosion reaction. The voltage was held at the anode potential $(0.1V)$ whilst the solution was being purged with hydrogen. The reaction temperature was maintained at 80°C to simulate the working of a fuel cell.

The corrosion reaction cell (Avesta Cell) described in chapter 4.1.2 was modified to incorporate the SS 316L wire, instead of the flat token that was clamped at the bottom of the reaction cell. The SS 316L wire was inserted

in the corrosion cell from the top of the cell using sealed Swagelok connections. This arrangement put forth further challenges as, in this case, the corrosion was focussed at the triple phase boundary formed at the surface of the SS 316L wire where the liquid and the gas phases intersected, as shown in Figure 7.4.

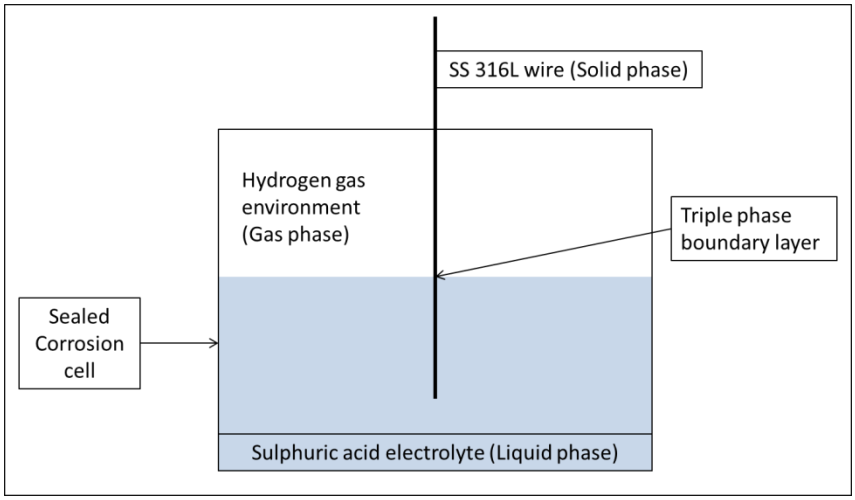

Figure 7.4: Schematic representation of the triple phase boundary where the solid, liquid and gas phase combine to accelerate the corrosion reaction

The corrosion reaction was accelerated at the triple phase boundary point and led to the wire being damaged at this point. Subsequently, the immersed part of the wire would break off from that point and fall into the electrolyte, stopping the electrochemical reaction as a result of production of an incomplete circuit to the reference and counter electrodes. In order to overcome this problem, a new bottom plate was machined for the Avesta cell incorporating a Swagelok connection for assembling the wire from the bottom of the reaction cell and hence eliminating the triple phase boundary as shown in Figure 7.5.

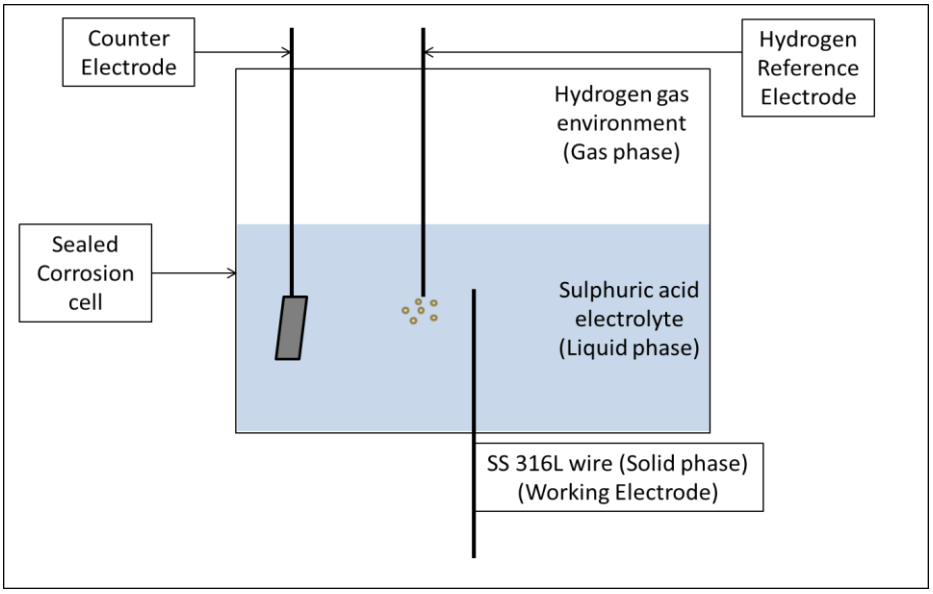

Figure 7.5: Schematic representation of the modified bottom plate in the Avesta Cell, for attaching the wire from the bottom and eliminating the triple phase boundary

7.2.1. Uncoated SS 316L Wire

A pristine SS 316L wire was imaged by X-ray tomography and the resulting 3D image is shown in Figure 7.6. Figure 7.6(a) shows the full volume rendering of the sample and the smooth appearance of the wire surface. Figure 7.6(b) shows the slices through the wire sample in the XZ-plane and Figure 7.6(c) shows the orthogonal slices through the XY-plane. The surface appears to be relatively smooth with no damage or defects. The wire is then exposed to accelerated corrosion conditions under a higher concentration of the electrolyte using potentiostatic experiments in a simulated fuel cell anode environment.

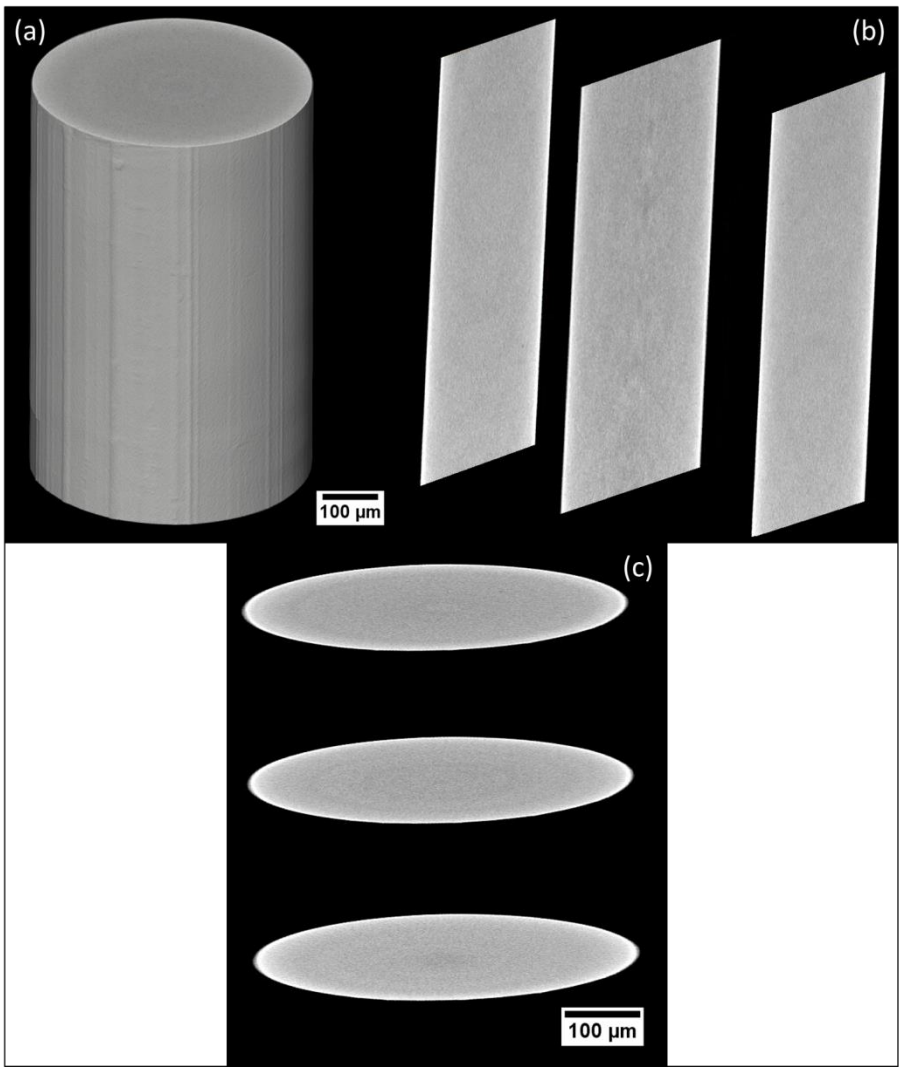

Figure 7.6:X-Ray CT image of a pristine SS 316L wire: (a) full volume rendering, (b) XZ-plane slices and (c) XY-plane ortho-slices

The wire corroded under simulated anode conditions was then imaged using X-ray CT and the resulting 3D volume rendered image is shown in Figure 7.7. The tomogram revealed that the wire is generally corroded, and, in addition to the general corrosion, pits have been formed on the wire surface. The anodic fuel cell conditions would promote uniform metal dissolution under the given corrosive environment, as discussed in chapter 5. However, the presence of $2\ ppm$ fluoride ions added to the sulphuric acid electrolyte aid in the pitting corrosion of the stainless steel. Halides have been known to attack the passive film of the stainless steel materials, and once the passive film is damaged further corrosion is localised within the pits. The surrounding passive film continues to provide some corrosion protection to the base materials and hence corrosion accelerates within the

area of the damaged film resulting in the formation of pits. The pits can be hidden from any surface inspection of the sample. X-ray CT provides an excellent tool to study corrosion hidden underneath the surface or under any external coating if one is applied.

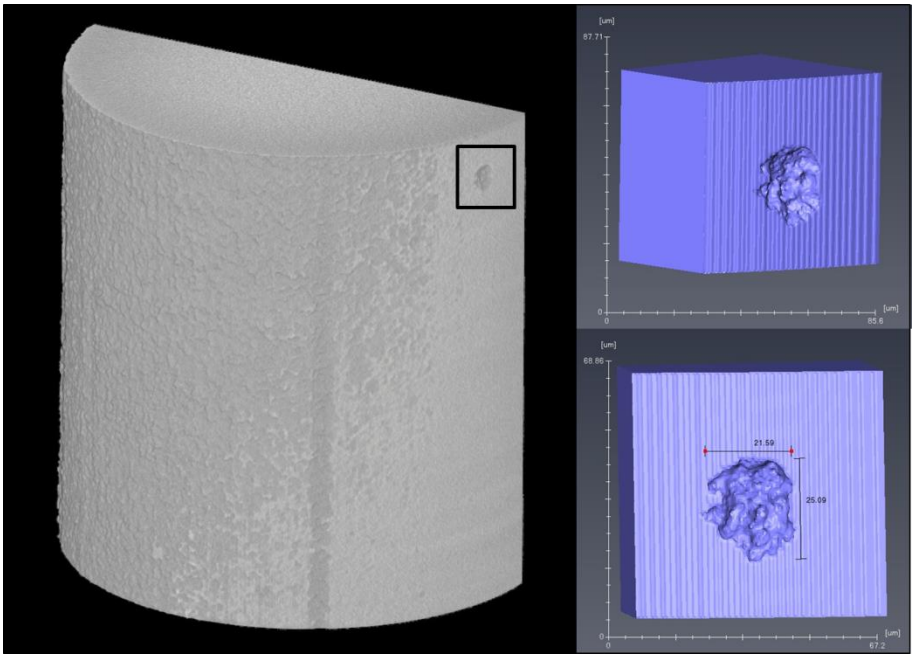

Figure 7.7: 3D volume rendering of a corroded SS 316L wire showing the texture on the surface of the wire as a result of general corrosion (left). A magnified tomograph of the corrosion pit on the surface of the wire (upper right) and the dimensions of the pit (lower right), formed as a result of pitting corrosion, are given.

Figure 7.8 shows the 3D reconstruction of the pit that was recreated from the void in the surface of the sample. The key information that is available using X-ray CT is the volume analysis of the pit, and the comparative imaged volume of the wire. The tomography also gives important information on the upper surface area and depth of the pit. In addition to this, the volume specific surface area (VSSA), obtained as the surface area per unit volume, provides information on how much area the pit is covering inside the surface of the sample. It is difficult to obtain such information using electrochemical data or other 2D surface analysis techniques.

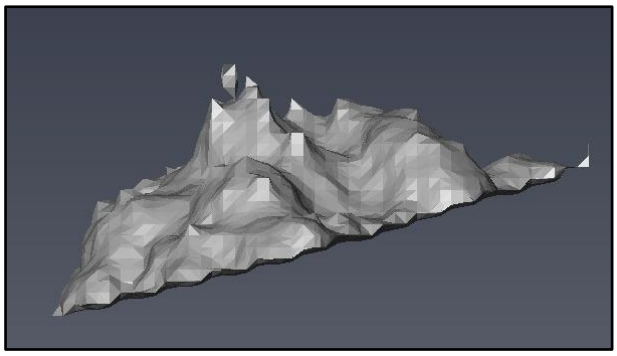

Figure 7.8: 3D reconstruction of the pit by recreating surface from the data of the void.

Table 7.2 lists the area and the volume of the pit shown in Figure 7.8. As VSSA < 1, the pit covers a higher volume with respect to the surface area. The idea of considering the VSSA is to understand the surface of the sample. If the pit was wide and shallow, it would result in a high VSSA as the volume would be lower in comparison to the surface area. If a deep pit is formed with a comparatively smaller surface area, it would result in a low VSSA value. This is very useful in understanding the breaking of the passive layer and the propagation of pitting corrosion due to the presence of halide ions in SSs. It is understood that pitting corrosion results in the localised damage of the passive film and subsequent corrosion propagates deep in to the pit rather than on the surface ass it would be the case with other forms of corrosion such as uniform corrosion. Further, the calculated surface area is based on the surface area of the pit that is exposed after the formation of the pit. An even lower VSSA would be produced if the surface area of the sample is considered that was present originally and has been corroded to form the pit.

Table 7.2: Volume analysis of the major pit formed on the sample surface

Surface Area of Pit (μm^2)	**Volume of pit (μm^3)**	**Volume Specific Surface Area** $\left(\mu m^2 / \mu m^3\right)$
620.8	662.9	0.9

Another SS 316L wire was corroded using the same conditions, the pit distribution is more even throughout the surface of the wire, as shown in Figure 7.9. As previously, the corrosion reaction has proceeded uniformly

throughout the surface of the sample creating surface texture not visible on the pristine wire. In addition to this, multiple pits have formed on the surface as can be seen in the ortho-slices in Figure 7.9. This suggests that pitting corrosion resulted in damage to the oxide film due to the presence of fluoride ions.

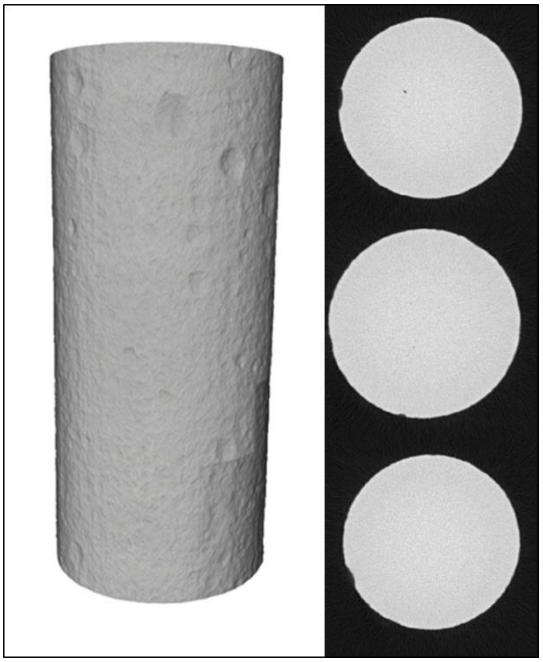

Figure 7.9: 3D volume rendering of a corroded SS 316L wire showing the surface of the wire (left) and the XY-plane ortho-slices (right) depicting multiple pits on the wire surface.

Table 7.3 lists the area, volume and the VSSA for the sample shown Figure 7.9. Tomography data reveals that there were over 500 pits over the surface of the sample covered within the field of view. Table 7.3 lists the volume analysis for the pits that cover more than 1% of total pit volume. The three large pits on the top part of the sample, as seen in Figure 7.10, represent the first three pits listed in Table 7.3. The first two pits have a VSSA of less than one and as the pits become shallower, the VSSA increases as they cover more surface area with respect to their specific volume.

Table 7.3: Volume analysis of the pits with a 1 % of total pit volume

Surface Area of Pit (μm^2)	**Individual Pit Volume (μm^3)**	**% Volume of Total Pit Volume**	**Volume Specific Surface Area (μm)**
2821.2	3536.7	17.3%	0.8
1790.5	2177.0	10.6%	0.8
4268.3	1837.4	9.0%	2.3
2626.2	1296.1	6.3%	2.0
2684.7	1131.8	5.5%	2.4
1588.6	1074.1	5.2%	1.5
1856.7	759.3	3.7%	2.4
958.2	678.2	3.3%	1.4
942.5	601.5	2.9%	1.6
921.6	585.1	2.9%	1.6
799.0	471.5	2.3%	1.7
832.8	465.3	2.3%	1.8
866.0	383.8	1.9%	2.3
865.0	378.4	1.8%	2.3
675.7	302.8	1.5%	2.2
477.2	280.8	1.4%	1.7
536.3	259.3	1.3%	2.1
660.3	236.3	1.2%	2.8

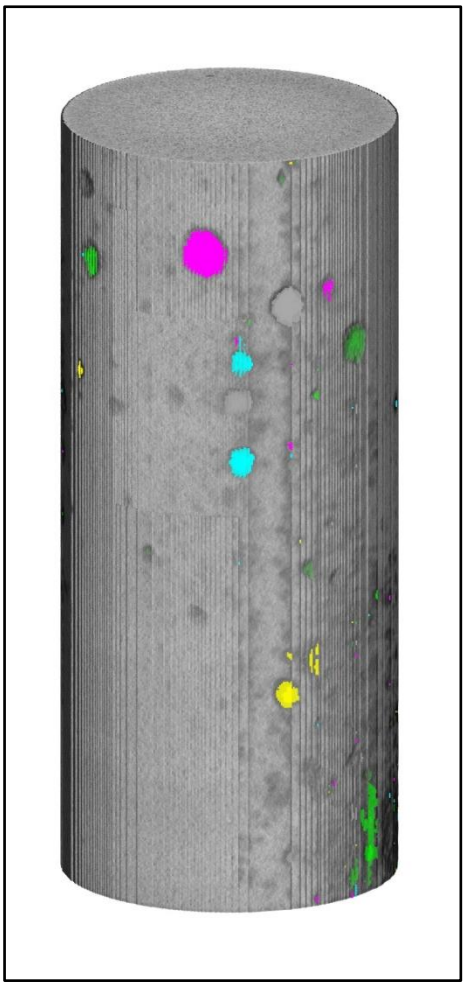

Figure 7.10: 3D volume rendering of a corroded SS 316L wire showing the surface of the wire with multiple pits individually coloured for VSSA analysis

7.2.2. Graphene Coated SS 316L Wire

A $0.5\,mm$ diameter SS 316L wire, used in the previous experiments, was coated with graphene via the CVD method discussed in section 2.2.3. From the results reported, it suggests that the corrosion resistance of the graphene coated SS 316L wires was found to be poor compared to the bare SS 316L wire. The highly reducing environment within the CVD coating chamber removes the oxide layer on the top surface of the SS 316L sample, and the graphene subsequently deposited on the substrate fails to provide adequate corrosion protection as the electrolyte penetrates through the graphene layer. The absence of any protective oxide layer makes the corrosion performance of the coated wire even worse than the bare SS 316L wire. The aim of studying these as-coated, un-corroded and corroded

wires is to understand the application of X-ray CT in the study of corrosion in case of coated materials used for fuel cell applications.

The un-corroded graphene coated wire was analysed using X-ray CT prior to exposure to the corrosion tests (Figure 7.11). The reconstructed surface appears relatively smooth, as was the case with the pristine uncoated SS 316L wire (Figure 7.6).

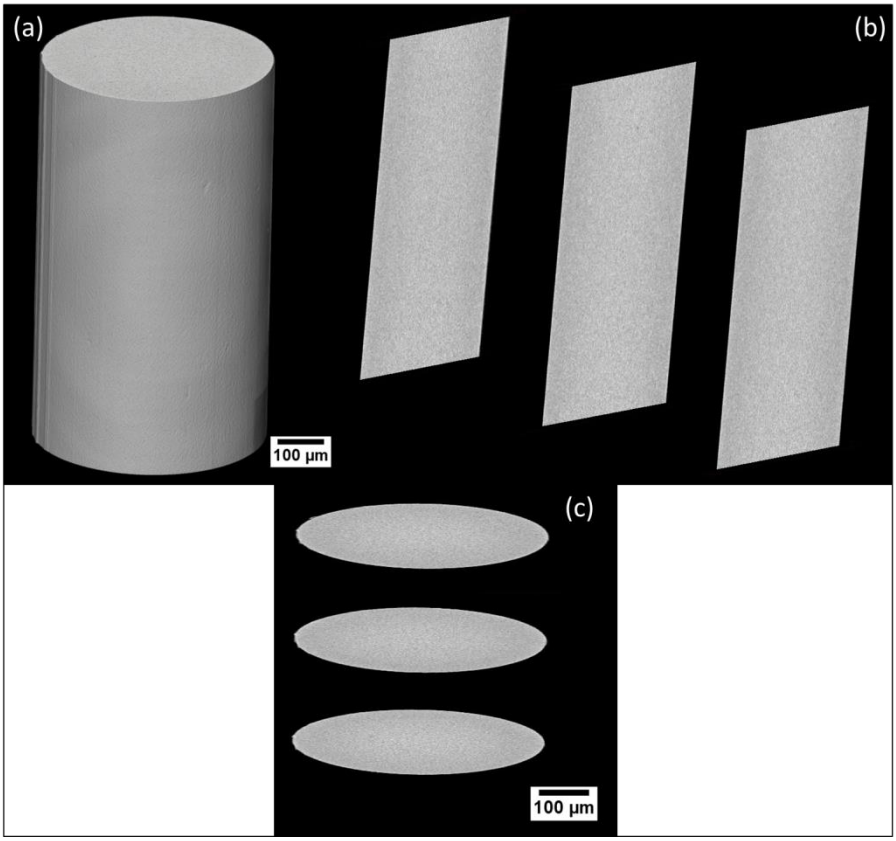

Figure 7.11:X-Ray CT image of an un-corroded graphene coated SS 316L wire: (a) full volume rendering, (b) XZ-plane slices and (c) XY-plane ortho-slices

The same wire was corroded for a maximum period of $2\,h$ only, as it is known that the sample will not provide adequate corrosion protection and may lead to complete dissolution of the wire if it is exposed to the corrosive environment for a relatively long period. The idea was to study the progression of corrosion with time. The coated wire was corroded for $2\,h$, taken out of the corrosion cell and a tomography scan was obtained. The sample was then corroded for further $2\,h$ (total $4\,h$), taken out and scanned

as previously. In the last stage, the sample was corroded for further $8\,h$ (total $12\,h$) and a tomogram was again obtained.

Figure 7.12 demonstrates the 3D volume rendering of the graphene coated SS 316L wire after the potentiostatic corrosion test for $2\,h$. The three images shown in the figure are for the same sample covering the total surface of the wire. The right image displays some smooth surface indicating that the corrosion reaction was not uniform and some areas may have been protected by the coating. However, in comparison to bare SS 316L after $48\,h$, this is still significant corrosion after only $2\,hr$ of exposure. The key features in the corrosion of the graphene coated SS 316L wire are the absence of corrosion pits, and the uniformity of corrosion throughout the unprotected areas exposed to corrosion. This further highlights the fact that the coating process has led to the complete removal of any oxide layers on the SS 316L surface. The subsequent corrosion reaction, therefore, is uniform corrosion, and there is no sign of pitting corrosion visible on the surface. This is emphasised in the case of the tomograms collected after $4\,h$ of corrosion.

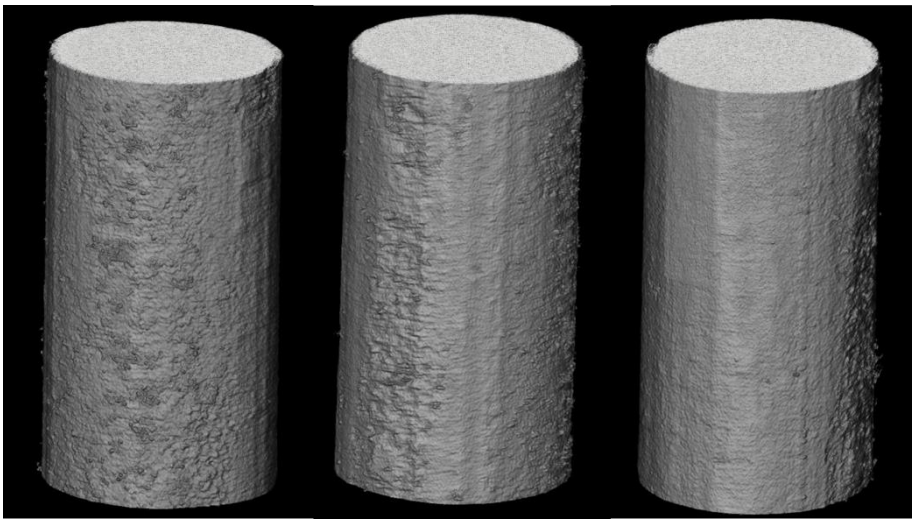

Figure 7.12: Full volume rendering X-Ray CT image of graphene coated SS 316L wire corroded for $2\,h$, showing different surfaces of the full wire

Figure 7.13 shows the tomograms for the graphene coated wire after $4\,h$ of corrosion $(2 + 2\,h)$. As seen in all three images, the total surface of the wire has now started to corrode uniformly. As with the $2\,h$ tomogram, there is no sign of any pits being formed on the surface and the whole surface is

degrading in a uniform manner. However, it is noted that the uniform corrosion itself results in the texture that is visible on the surface, in comparison to the un-corroded graphene coated wire. The corrosion reaction will result in the formation miniature pits uniformly distributed across the surface, which in turn produce the texture that is visible in the images. There is no sign of the deep pits which were produced on the pristine SS 316L wire. Figure 7.14, recorded after $12\ h$ of corrosion, further confirms the corrosion type that is described in cases of 2 and $4\ h$ corrosion. The sample has now started to lose material and the diameter of the wire now reduced.

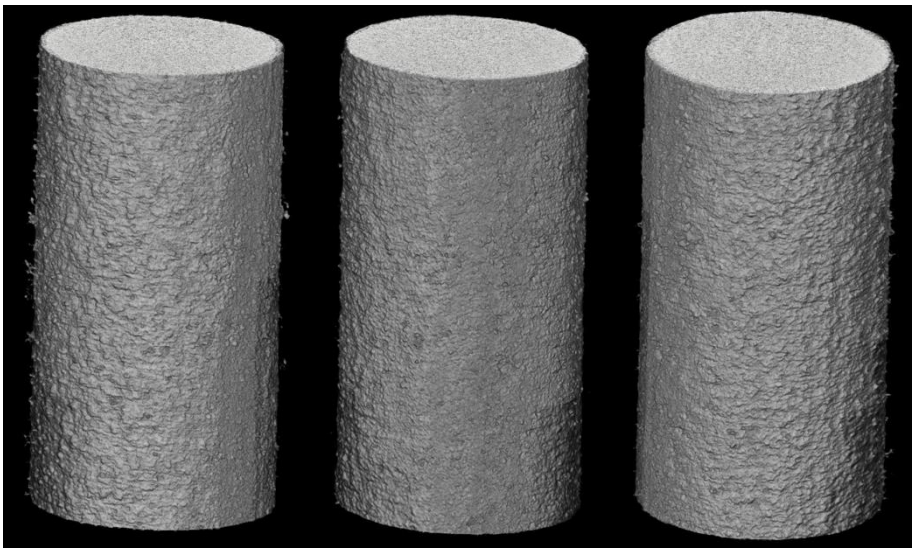

Figure 7.13: Full volume rendering X-Ray CT image of graphene coated SS 316L wire corroded for $4\ h$ showing different surfaces of the full wire

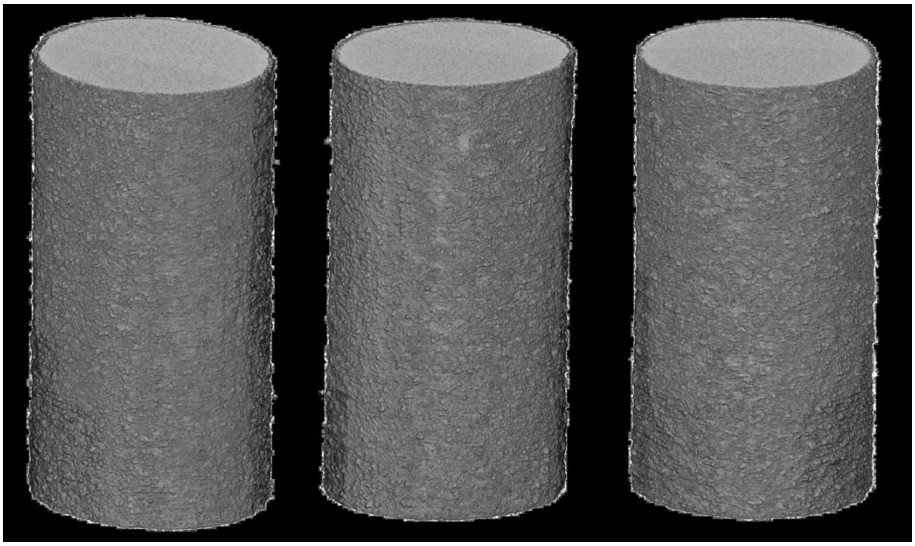

Figure 7.14: Full volume rendering X-Ray CT image of graphene coated SS 316L wire corroded for $12\ h$ *showing different surfaces of the full wire*

Figure 7.15 compares the XY-plane ortho slices obtained from the tomograms of $2, 4$ and 12 h corroded samples. The tomograms show the rough edges apparent on the wire surface, which are more or else uniformly distributed throughout the circumference.

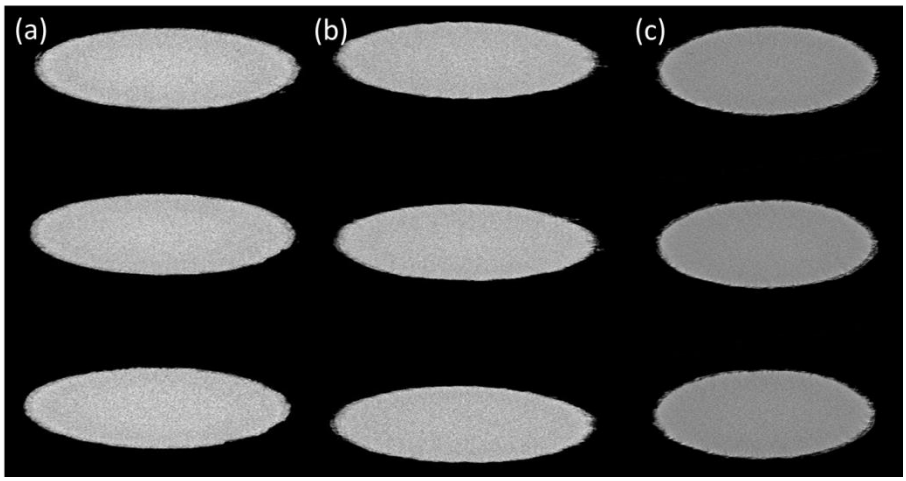

Figure 7.15: Comparison of the XY-plane ortho slices of graphene coated SS 316L wire corroded for (a) $2\ h$*, (b)* $4\ h$ *,and (c)* $12\ h$

7.3. Conclusions

3D X-ray microtomography provides an alternative view to analysing corrosion, beyond the traditional 2D methods. The key feature of using X-ray CT is the ability to view the microstructural features beneath the surface of the sample, so-called hidden features. Volume analysis of surface roughness and pit dimensions provides additional information on the types, and effects, of corrosion on the surface of the sample. Thus X-ray CT data can be correlated to the electrochemical faradaic current measured during the corrosion experiments. The most important application for X-ray CT would be in the case of coated samples. If pitting corrosion occurs, and accelerates, beneath the coating, or if other forms of corrosion are taking place, X-ray CT can provide crucial information about the effects of the corrosion on the substrate. Any cracks or inter-granular damage can be viewed using X-ray CT. Such damage is extremely difficult to predict using electrochemical data alone, or even with the aid of other surface analysis techniques. X-ray CT is also very useful in analysing coating failures, as was the case with graphene coated SS 316L wire.

8. Conclusions and Future Work

The main work undertaken in this thesis was to analyse the feasibilities of using functionally coated mild steel material as a bipolar plate for polymer electrolyte membrane fuel cells. The project has been undertaken in joint collaboration with Tata Steel Europe Ltd. and a Tata proprietary coated mild steel substrate was also analysed for its feasibility as a BPP material in PEMFC. The performances of other coated steel substrates was benchmarked against commercial SS 316L material. Accelerated corrosion tests were conducted on SS 316L substrate and it was applied for *in situ* fuel cell operation to compare against the fuel cell results obtained using traditional graphite.

Graphene possesses excellent chemical and mechanical strength; it is highly durable with excellent corrosion resistance and high electrical conductivity. Graphene deposition was achieved on different grades of steel using photo-thermal chemical vapor deposition and an improved ICR performance was reported. A novel method of graphene deposition was reported using charged graphene solution in NMP using electrophoretic deposition. EPD of GICs was undertaken on a SS 316L substrate and an improved corrosion performance was reported using EPD. Finally, 3D X-ray microtomography was applied as a novel method for corrosion analysis under simulated fuel cell conditions. The following sections present the key conclusions summary on the work pursued in this project and the later sections present the areas that can possibly be expanded further from this thesis.

8.1. Conclusions

The following sections will summarise the main conclusions from electrochemical corrosion analysis of SS 316L, functionally coated mild steel and other grades of steel along with the fuel cell operation of SS 316L (chapter 5), PTCVD of graphene on different grades of steel and EPD of

graphene on SS 316L (chapter 6) and the use of 3D X-ray microtomography for corrosion analysis (chapter 7).

8.1.1. Electrochemical Corrosion Analysis

The impetus behind this thesis was to achieve a functional coating for mild steel substrate that would allow it to be applied as a BPP in PEMFCs. A commercial SS 316L material was analysed to benchmark the results and three different grades of mild steels were used for corrosion analysis and coating development. A functionally coated mild steel was also analysed for its *ex situ* contact resistance and corrosion performance. Nickel coated mild steel was reported to be promising in terms of ICR performance and the presence of nickel coating provide with a temporary corrosion protection in terms of the linear sweep polarisation tests but the inability to form a passive layer results in high passive current densities which make it unsuitable for cathodic environment.

The proprietary coated mild steel material was reported with an improved ICR performance with the values being an order of magnitude lower than SS 316L and the bare mild steel material. The functional coating had also improved the corrosion resistance of the mild steel substrate with improved passive protection. The passive current density was reported to be two orders of magnitude lower than bare mild steel. However, the corrosion performance was still not comparable to SS 316L with the passive current densities being two orders of magnitude higher than SS 316L and almost three orders of magnitude higher in case of anodic conditions at elevated temperatures.

The potentiostatic tests reveal a similar trend, with SS 316L outperforming the functionally coated mild steel by at least two orders of magnitude under all conditions. However, the coating has improved the corrosion performance in comparison to the bare mild steel where the dissolution of the material was only limited by the mass transport due to the area of the sample exposed to the acidic conditions.

SS 316L and functionally coated mild steel were analysed using accelerated corrosion techniques to study the long term corrosion performance of the candidate materials, and SS 316L had performed better

than the coated mild steel. The performance difference was exacerbated under hydrogen at 80 °C. The biggest disadvantage of using a coated material is the damage to the coating as a result of either uneven coating deposition or physical damage of the coating. Once the barrier coating is damaged, the underlying bare mild steel does not provide adequate corrosion protection and results in poor corrosion rates. It is to be noted that in case of coated mild steel, the coating did not provide any sacrificial corrosion protection, it was used as a barrier coating and hence any damage to the coating results in the failure of the substrate in terms of its corrosion performance.

SS 316L has been used for *in situ* fuel cell tests in comparison to traditional graphite BPP to study the effect of the oxide layer on the performance of the fuel cell. The presence of the oxide layer results in the loss of power and reduces the fuel cell output. In a $100\,h$ *in situ* fuel cell test, graphite BPP has maintained a potential of around $0.7\,V$ at $100\,mA.cm^{-2}$ in comparison to around $0.4\,V$ in case of SS 316L BPP.

8.1.2. Graphene Coatings for Steel

Four different grades of steel were coated with graphene using PTCVD method. The graphene coating had resulted in an improved performance in terms of the ICR of all four substrates. The coating was robust and resulted in uniform coverage of the substrate. Graphene was grown on the steel substrates with a bottom-up approach starting with acetylene gas that was disintegrated and graphene was grown from there. As a result of the graphene growth on the substrate itself, the coating adherence to the substrate was found to be very good and the coating did not de-laminate during ICR tests under compression or during cleaning of the substrates with acetone or alcohol wipes. However, the coating did not provide adequate corrosion protection. The corrosion performance of the coating was found to be poorer as compared to the base material itself. A reason behind this would be the permeability of the acid electrolyte through the graphene layers to the base material, where the oxide layer does not exists anymore as a result of the coating process. This leads to the exposure of base metal to an acid electrolyte without the ability to reform the passive layer and hence the corrosion performance was inadequate.

The graphene coating was repeated in two batches; one with a nickel catalyst route and a second without the catalyst. The poor corrosion performance of the first batch was thought be due to the ion sputtering of nickel on the substrate and subsequent removal of the oxide layer. During the second batch, the ion sputtering and nickel catalyst deposition was avoided and graphene was grown directly on steel substrates. Once again, improved ICR was observed with a robust coating adhering to the substrate; however, the corrosion performance was once again not adequate. The ICR was well under the DOE 2017 target with more work needed on the corrosion properties of the coating.

SS 316L was coated with graphene using a novel method of EPD using a charged graphene (GIC) colloidal solution in NMP. GICs have been prepared using micro graphite powder and potassium ammonia complex. The charged GICs are produced with a positive charge as a result of the presence of the potassium ions and successful deposition of graphene has been achieved on the negative electrode during EPD. Monolayer graphene was detected on SS 316L substrate using Raman spectroscopy and subsequently, uniform graphene coating has been achieved by optimising the GIC concentration, voltage, and the deposition time. An improved corrosion performance has been reported with the EPD graphene coated SS 316L where three orders of magnitude lower corrosion rate has been reported. AFM imaging has been used to confirm the presence of various few layer graphene chunks on the SS 316L substrate.

8.1.3. 3D X-Ray Microtomography for Corrosion Analysis

A novel method of corrosion characterisation was discussed in chapter 7 using 3D X-ray microtomography. A SS 316L wire was imaged using X-ray CT before and after corrosion tests under anodic conditions at 80 °C using $1\,M\,H_2SO_4 + 2\,ppm\,F^-$. Further, a CVD graphene coated SS 316L wire has been used to study the corrosion mechanism by conducting X-ray scans before and after corrosion for various times. The aim was to understand the propagation of corrosion with time. A key use of X-ray CT would be studying the pitting corrosion where normal 2D methods such as

SEM or only electrochemical data would not allow the analysis of the effect of pitting corrosion on the substrate.

8.2. Future Work

This section is aimed to present a brief idea of the future work that may be expanded from the work reported here.

8.2.1. Metallic Coatings for Mild Steel

A Tata proprietary coating was analysed and the ICR performance was reported to be within close range of the DOE 2017 target. The corrosion performance has been better than the bare mild steel but it may be developed further to improve the corrosion resistance of the coating up to the levels offered by SS 316L. One of the reasons for the failure of the coating was cracks, pin-holes or other defects in the coating and the delamination of the coating. The electro-plating parameters may be developed further to improve the robustness of the coating and to produce a defect-free coating on the mild steel substrate. This would improve the corrosion resistance of the coating and may provide longevity in terms of the coating performance.

Given the stability of nickel in the alkaline regime, the nickel coated mild steel substrates may be analysed further to be applied as BPP in alkaline fuel cell as opposed to PEMFC. In terms, of the *in situ* fuel cell performance of SS 316L BPP, instead of using flat tokens, flow-fields could be produced on the substrate using hydro-forming or pneumatic pressing. This would still provide a challenge for the coated substrates as the current coated mild steel failed as a result of non-uniform coating under the manifolds. However, a uniform coating could be produced using spray-coating or improved electro-dipping procedure for coating applications.

8.2.2. Graphene Coatings for Steel

Graphene coating was deposited using PTCVD and has resulted in excellent improvements in ICR performance, however, the corrosion performance was not improved. In order to improve the corrosion

performance of the CVD graphene coated samples, the coating parameter could be altered to restrict the damage to the oxide layer before graphene growth. This could be achieved by using argon instead of hydrogen gas during the coating process. Another route would be to utilise the excellent corrosion resistance characteristics of DLC coating. DLC coatings are not very conductive so ICR performance may be hindered. However, DLC can be deposited in a controlled manner. A few layers graphene can then be deposited on top of the DLC coating to provide the required contact resistance. Figure 8.1 depicts the schematic diagram of the two-coating system. The first layer of DLC coating would cover the working are of the fuel cell which would be exposed to the acidic conditions. The DLC coating would provide the required corrosion resistance and an additional layer of graphene would be deposited that would cover the whole substrate surface including the exposed working area. The electrons would pass through graphene and through the substrate sample providing the required electrical conductivity.

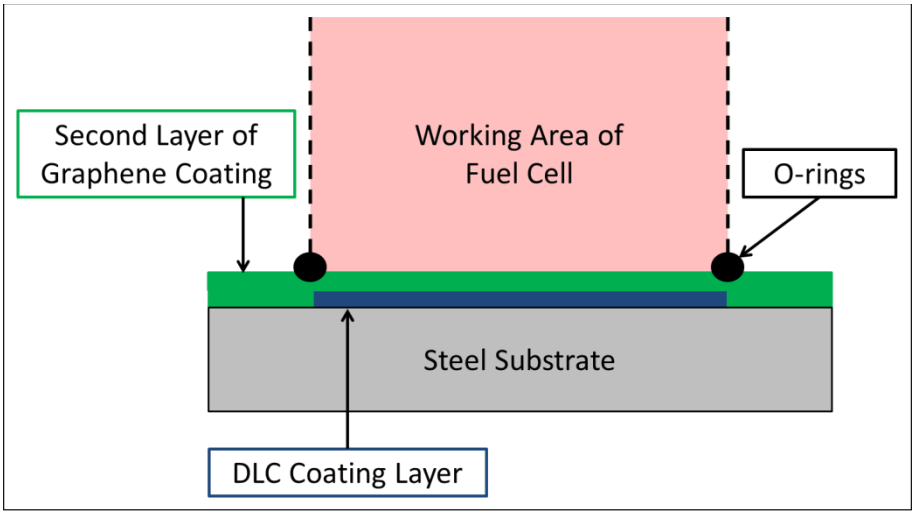

Figure 8.1: A schematic of DLC and graphene coating on steel to improve ICR and corrosion performance of steel

Nickel coated mild steel substrates HILAN and HILUMIN have demonstrated better ICR performance as compared to mild steel or SS 316L. With the successful corrosion prevention provided by the EPD graphene coated SS 316L, the EPD graphene could be applied to the nickel coated substrates to improve their corrosion resistance and to maintain the better ICR performance. Graphene has been successfully

deposited on nickel substrates for various electrochemical applications[80]. The catalysing characteristic of nickel for graphene growth can be maximised for uniform graphene coverage via EPD. EPD graphene could also be applied on pre-machined or hydro-formed SS 316L and other steel substrates to then use them directly for *in situ* fuel cell operation.

8.2.3. 3D X-Ray Tomography of Coated Wire

In future, the application of X-ray CT could be expanded to examine corrosion processes, for example in this setup the sample could be marked with laser etching or other suitable method and then the fresh wire can be scanned using X-ray CT. The sample can then be corroded and re-scanned at the same position as the fresh wire. The fresh wire data can then be directly correlated with the corroded data and exact volume loss can be calculated. This can then be compared to the faradaic current data obtained from the electrochemical corrosion experiments, if the rest of the wire was to be insulated using epoxy resin to expose only the required metal surface that is to be scanned as shown in Figure 8.2. This would allow for direct comparison of material loss obtained from the electrochemical experiments as well as X-ray CT experiments.

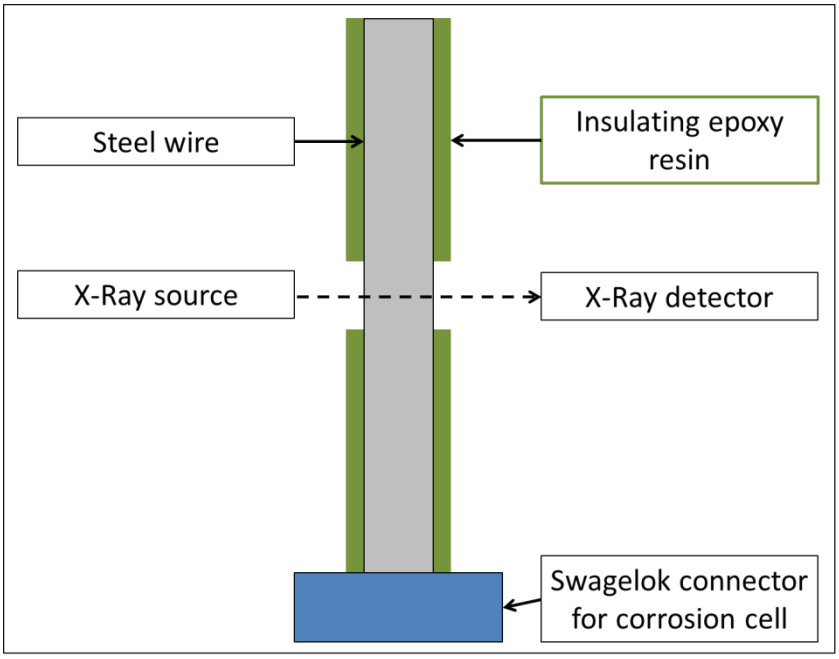

Figure 8.2: A schematic of epoxy resin covered steel wire for X-ray CT scans with the corroded exposed area

Dissemination

Publications

The following is a first-authored peer reviewed publication in which disseminates the work of this thesis.

- Pathan, T.S., Bohm, S., Jansen, M., Mills, C.A., Hajatdoost, S., Brett, D.J.L. and Shearing, P.R. Electrochemical Corrosion Analysis of Functionally Coated Mild Steel in Simulated Fuel Cell Conditions. *Corrosion Engineering, Science and Technology (under review)*

Conference Presentations (Oral)

The following is a list of oral presentations given to disseminate the work of this thesis:

- Pathan, T.S. *et al.* Electrochemical Corrosion Analysis of Functionally Coated Metallic Bipolar Plates in PEM Fuel Cells, *STFC Early Career Researchers Conference 2016*, Abingdon, (Apr 2016)
- Pathan, T.S. *et al.* Electrochemical Corrosion Analysis of Functionally Coated Mild Steel in Simulated Fuel Cell Conditions, *17th Asian Pacific Corrosion Control Conference, Mumbai*, (Jan 2016)
- Pathan, T.S. *et al.* Electrochemical Corrosion Analysis of Functionally Coated Metallic Bipolar Plates in Fuel Cells, *Knowledge Transfer Corrosion Matters Workshop, London,* (Jun 2015)

Conference Presentations (Poster)

The following is a poster presentation given to disseminate the work of this thesis:

- Pathan, T.S. *et al.* Development and Characterisation of Coated Mild Steel as a Bipolar Plate Material for Polymer Electrolyte Membrane Fuel Cells, *Electrochem Conference, Loughborough University,* (Sep 2104)

Industrial Reports

The following is a list of industrial reports submitted to Tata Steel Europe Ltd. to disseminate the work of this thesis:

- A Review of Metal Bipolar Plates for Polymer Electrolyte Membrane Fuel Cells (March 2013).
- *Ex situ* corrosion testing and contact resistance testing of proprietary coated substrates for fuel cell project (August 2013).
- A Review of Surface Analysis Techniques and their Application in The Study of Bipolar Plate Degradation (December 2013).
- An Overview of Electrochemical and Corrosion Characterisation Facilities for Fuel Cell Project (January 2014).
- UCL-TATA Collaborative PhD Project: Progress Report (August 2014).
- Feasibility Study of Graphene Coated Steels as Bipolar Plate Materials in PEM Fuel Cells (November 2015).

References

1. Hook, M., Li, J., Johansson, K. & Snowden, S. Growth Rates of Global Energy Systems and Future Outlooks. *Nat. Resour. Res.* **21,** 23–41 (2012).

2. Hook, M. & Tang, X. Depletion of fossil fuels and anthropogenic climate change - A review. *Energy Policy* **52,** 797–809 (2013).

3. Boden, T. A., Marland, G. & Andres, R. J. Global, Regional, and National Fossil-Fuel CO2 Emissions. (2010). at <http://cdiac.ornl.gov/trends/emis/tre_glob.html>

4. Barbir, F. *PEM Fuel Cells: Theory and Practice*. (Elsevier Academic Press, 2005).

5. EG&G Technical Services, I. *Fuel Cell Handbook*. (U.S. Department of Energy, 2004).

6. Larminie, J. & Dicks, A. *Fuel cell systems explained*. (J. Wiley, 2003).

7. O'Hayre, R., Cha, S.-W., Colella, W. & Prinz, F. B. *Fuel Cell Fundamentals*. *Fuel Cells* **104,** (John Wiley & Sons, 2009).

8. Grove, W. R. On voltaic series and the combination of gases by platinum. *London Edinburgh Philos. Mag. J. Sci. Ser. 3* **14,** 127–130 (1839).

9. Wang, Y., Chen, K. S., Mishler, J., Cho, S. C. & Adroher, X. C. A review of polymer electrolyte membrane fuel cells: Technology, applications, and needs on fundamental research. *Appl. Energy* **88,** 981–1007 (2011).

10. Spiegel, C. *PEM Fuel Cell Modeling and Simulation Using MATLAB*. (Elsevier Inc., 2008).

11. Fuel Cell Today: The Leading Authority on Fuel Cells. Fuel Cell

History. (2014). at <http://www.fuelcelltoday.com/history>

12. U.S.Department of Energy. Types of Fuel Cells. (2011). at <https://www1.eere.energy.gov/hydrogenandfuelcells/fuelcells/fc_types.html>

13. Atkins, P. & de Paula, J. *Atkins' Physical Chemistry*. (Oxford University Press, 2006).

14. Mehta, V. & Cooper, J. S. Review and analysis of PEM fuel cell design and manufacturing. *J. Power Sources* **114,** 32–53 (2003).

15. Zhou, P., Wu, C. W. & Ma, G. J. Influence of clamping force on the performance of PEMFCs. *J. Power Sources* **163,** 874–881 (2007).

16. Brett, D. J. L. & Brandon, N. P. Review of Materials and Characterization Methods for Polymer Electrolyte Fuel Cell Flow-Field Plates. *J. Fuel Cell Sci. Technol.* **4,** 29–44 (2007).

17. Tawfik, H., Hung, Y. & Mahajan, D. Metal bipolar plates for PEM fuel cell—A review. *J. Power Sources* **163,** 755–767 (2007).

18. Antunes, R. A., Oliveira, M. C. L., Ett, G. & Ett, V. Corrosion of metal bipolar plates for PEM fuel cells: A review. *Int. J. Hydrogen Energy* **35,** 3632–3647 (2010).

19. Borup, R. L. & Vanderborgh, N. E. Design and Testing Criteria for Bipolar Plate Materials for Pem Fuel Cell Applications. *MRS Proc.* **393,** 151–155 (1995).

20. Tsuchiya, H. Mass production cost of PEM fuel cell by learning curve. *Int. J. Hydrogen Energy* **29,** 985–990 (2004).

21. U.S. Department of Energy. *Fuel Cell Technologies Program Multi-Year Research, Development and Demonstration Plan*. (2012). at <http://www1.eere.energy.gov/hydrogenandfuelcells/mypp/pdfs/fuel_cells.pdf>

22. Cooper, J. S. Design analysis of PEMFC bipolar plates considering stack manufacturing and environment impact. *J. Power Sources* **129,** 152–169 (2004).

23. Borup, R. L. & Vanderborgh, N. E. Design and Testing Criteria for Bipolar Plate Materials for PEM Fuel Cell Applications. *Proceedings of the Materials Research Society* **393,** 151 (1995).

24. Radhakrishnan, S., Ramanujam, B. T. S., Adhikari, A. & Sivaram, S. High-temperature , polymer – graphite hybrid composites for bipolar plates : Effect of processing conditions on electrical properties. **163,** 702–707 (2007).

25. Kauranen, P., Ganski, A. Von & Hell, B. Injection moulding of graphite composite bipolar plates. **154,** 467–471 (2006).

26. Wang, H., Sweikart, M. A. & Turner, J. A. Stainless steel as bipolar plate material for polymer electrolyte membrane fuel cells. *J. Power Sources* **115,** 243–251 (2003).

27. Costamagna, P. & Srinivasan, S. Quantum jumps in the PEMFC science and technology from the 1960s to the year 2000 Part II . Engineering , technology development and application aspects $. **102,** 253–269 (2001).

28. Hermann, A., Chaudhuri, T. & Spagnol, P. Bipolar plates for PEM fuel cells: A review. *Int. J. Hydrogen Energy* **30,** 1297–1302 (2005).

29. Brett, D. J. L. & Brandon, N. P. Bipolar plates: the lungs of the PEM fuel cell. *Fuel Cell Rev.* **2,** 15–23 (2005).

30. Davies, D. P., Adcock, P. L., Turpin, M. & Rowen, S. J. Bipolar plate materials for solid polymer fuel cells. *J. Appl. Electrochem.* **30,** 101–105 (2000).

31. Davies, D. P., Adcock, P. L., Turpin, M. & Rowen, S. J. Stainless steel as a bipolar plate material for solid polymer fuel cells. *J. Power Sources* **86,** 237–242 (2000).

32. Wang, H. & Turner, J. A. Ferritic stainless steels as bipolar plate material for polymer electrolyte membrane fuel cells. *J. Power Sources* **128,** 193–200 (2004).

33. Silva, R. F. *et al.* Surface conductivity and stability of metallic bipolar

plate materials for polymer electrolyte fuel cells. *Electrochim. Acta* **51,** 3592–3598 (2006).

34. Makkus, R. C., Janssen, A. H. ., de Bruijn, F. A. & Mallant, R. K. A. . Use of stainless steel for cost competitive bipolar plates in the SPFC. *J. Power Sources* **86,** 274–282 (2000).

35. Makkus, R. C., Janssen, A. H. H., de Bruijn, F. A. & Mallant, R. K. A. M. Stainless steel for cost-competitive bipolar plates in PEMFCs. *Fuel Cells Bull.* **3,** 5–9 (2000).

36. Wang, Y. & Northwood, D. O. Effects of O2 and H2 on the corrosion of SS316L metallic bipolar plate materials in simulated anode and cathode environments of PEM fuel cells. *Electrochim. Acta* **52,** 6793–6798 (2007).

37. Wang, H. & Turner, J. A. Reviewing Metallic PEMFC Bipolar Plates. *Fuel Cells* **10,** 510–519 (2010).

38. Ihonen, J., Jaouen, F., Lindbergh, G. & Sundholm, G. A novel polymer electrolyte fuel cell for laboratory investigations and in-situ contact resistance measurements. *Electrochim. Acta* **46,** 2899–2911 (2001).

39. Wind, J., Spah, R., Kaiser, W. & Bohm, G. Metallic bipolar plates for PEM fuel cells. *J. Power Sources* **105,** 256–260 (2002).

40. Hentall, P. L., Lakeman, J. B., Mepsted, G. O., Adcock, P. L. & Moore, J. M. New materials for polymer electrolyte membrane fuel cell current collectors. *J. Power Sources* **80,** 235–241 (1999).

41. Yoon, W., Huang, X., Fazzino, P., Reifsnider, K. L. & Akkaoui, M. A. Evaluation of coated metallic bipolar plates for polymer electrolyte membrane fuel cells. *J. Power Sources* **179,** 265–273 (2008).

42. Pozio, A., Silva, R. F. & Masci, A. Corrosion study of SS430/Nb as bipolar plate materials for PEMFCs. *Int. J. Hydrogen Energy* **33,** 5697–5702 (2008).

43. Weil, K. S., Xia, G., Yang, Z. G. & Kim, J. Y. Development of a

niobium clad PEM fuel cell bipolar plate material. *Int. J. Hydrogen Energy* **32,** 3724–3733 (2007).

44. Feng, K., Shen, Y., Mai, J., Liu, D. & Cai, X. An investigation into nickel implanted 316L stainless steel as a bipolar plate for PEM fuel cell. *J. Power Sources* **182,** 145–152 (2008).

45. Ma, L., Warthesen, S. & Shores, D. A. Evaluation of materials for bipolar plates in PEMFCs. *J. New Mater. Electrochem. Syst.* **3,** 221–228 (2000).

46. Wang, Y. & Northwood, D. An investigation of the electrochemical properties of PVD TiN-coated SS410 in simulated PEM fuel cell environments. *Int. J. Hydrogen Energy* **32,** 895–902 (2007).

47. Li, M. *et al.* Corrosion behavior of TiN coated type 316 stainless steel in simulated PEMFC environments. *Corros. Sci.* **46,** 1369–1380 (2004).

48. Cho, E. a., Jeon, U.-S., Hong, S. -a., Oh, I.-H. & Kang, S.-G. Performance of a 1kW-class PEMFC stack using TiN-coated 316 stainless steel bipolar plates. *J. Power Sources* **142,** 177–183 (2005).

49. Karimi, S., Fraser, N., Roberts, B. & Foulkes, F. R. A Review of Metallic Bipolar Plates for Proton Exchange Membrane Fuel Cells: Materials and Fabrication Methods. *Adv. Mater. Sci. Eng.* **2012,** 1–22 (2012).

50. Taniguchi, A. & Yasuda, K. Highly water-proof coating of gas flow channels by plasma polymerization for PEM fuel cells. *J. Power Sources* **141,** 8–12 (2005).

51. Brady, M. P. *et al.* Assessment of Thermal Nitridation to Protect Metal Bipolar Plates in Polymer Electrolyte Membrane Fuel Cells. *Electrochem. Solid-State Lett.* **5,** A245 (2002).

52. Brady, M. P. *et al.* Preferential thermal nitridation to form pin-hole free Cr-nitrides to protect proton exchange membrane fuel cell metallic bipolar plates. *Scr. Mater.* **50,** 1017–1022 (2004).

53. Wang, H., Brady, M. P., Teeter, G. & Turner, J. A. Thermally nitrided stainless steels for polymer electrolyte membrane fuel cell bipolar plates. *J. Power Sources* **138,** 86–93 (2004).

54. Wang, H., Brady, M. P., More, K. L., Meyer, H. M. & Turner, J. A. Thermally nitrided stainless steels for polymer electrolyte membrane fuel cell bipolar plates. *J. Power Sources* **138,** 79–85 (2004).

55. Lee, S.-H., Kim, J.-H., Lee, Y.-Y. & Wee, D.-M. Effects of low-temperature nitridation on the electrical conductivity and corrosion resistance of 446M stainless steel as bipolar plates for proton exchange membrane fuel cell. *Int. J. Hydrogen Energy* **35,** 725–730 (2010).

56. Hong, W., Han, D.-H., Choi, H., Kim, M.-W. & Lee, J.-J. High-density plasma nitriding of AISI 316L for bipolar plate in proton exchange membrane fuel cell. *Int. J. Hydrogen Energy* **36,** 2207–2212 (2011).

57. Han, D.-H., Hong, W.-H., Choi, H. S. & Lee, J. J. Inductively coupled plasma nitriding of chromium electroplated AISI 316L stainless steel for PEMFC bipolar plate. *Int. J. Hydrogen Energy* **34,** 2387–2395 (2009).

58. Nam, D. G., Choi, C. Y., Jang, J. H., Park, Y. Do & Kang, N. H. PEM Fuel Cell Separator with Thermally Nitrided Low Carbon Steel. *Mater. Sci. Forum* **654-656,** 1823–1825 (2010).

59. Bai, C.-Y., Wen, T.-M., Hou, K.-H. & Ger, M.-D. The bipolar plate of AISI 1045 steel with chromized coatings prepared by low-temperature pack cementation for proton exchange membrane fuel cell. *J. Power Sources* **195,** 779–786 (2010).

60. Bai, C.-Y., Wen, T.-M., Hou, K.-H., Pu, N.-W. & Ger, M.-D. The characteristics and performance of AISI 1045 steel bipolar plates with chromized coatings for proton exchange membrane fuel cells. *Int. J. Hydrogen Energy* **36,** 3975–3983 (2011).

61. Bai, C.-Y., Ger, M.-D. & Wu, M.-S. Corrosion behaviors and contact resistances of the low-carbon steel bipolar plate with a chromized coating containing carbides and nitrides. *Int. J. Hydrogen Energy* **34,**

6778–6789 (2009).

62. Haering, R. R. Band Structure of Rhombohedral Graphite. *Can. J. Phys.* **36,** 352–362 (1958).

63. *Physics and Chemistry of Graphene: Graphene to Nanographene*. (Pan Stanford Publishing, 2013).

64. Warner, J. H., Schaffel, F., Bachmatiuk, A. & Rummeli, M. H. *Graphene: Fundamentals and Emergent Applications*. (Elsevier, 2013).

65. Wu, Y. in *Two-Dimensional Carbon: Fundamental Properties, Synthesis, Characterization, and Applications* (eds. Wu, Y., Shen, Z. & Yu, T.) 1–4 (Pan Stanford Publishing, 2014).

66. Wallace, P. R. The Band Theory of graphite. *Phys. Rev.* **71,** 622–634 (1947).

67. Novoselov, K. S. *et al.* Electric field effect in atomically thin carbon films. *Science* **306,** 666–9 (2004).

68. Geim, A. K. & Novoselov, K. S. The Rise of Graphene. *Nat. Mater.* **6,** 183–191 (2007).

69. Aoki, M. & Amawashi, H. Dependence of band structures on stacking and field in layered graphene. *Solid State Commun.* **142,** 123–127 (2007).

70. Charlier, J. C., Gonze, X. & Michenaud, J. P. First-Principles Study of the Stacking Effect on the Electronic Properties of graphite(s). *Carbon N. Y.* **32,** 289–299 (1994).

71. Hernandez, Y. *et al.* High-yield production of graphene by liquid-phase exfoliation of graphite. *Nat. Nanotechnol.* **3,** 563–8 (2008).

72. Blake, P. *et al.* Graphene-based liquid crystal device. *Nano Lett.* **8,** 1704–8 (2008).

73. Jeong, H.-K. *et al.* X-ray absorption spectroscopy of graphite oxide. *EPL (Europhysics Lett.* **82,** 67004 (2008).

74. Surrey NanoSystems Ltd. Suurey NanoSystems. at <http://www.surreynanosystems.com/>

75. Sarkar, P. & Nicholson, P. S. Electrophoretic Deposition (EPD): Mechanisms, Kinetics and Application to Ceramics. *J. Am. Ceram. Soc.* **79,** 1987–2002 (1996).

76. Van der Biest, O. O. & Vandeperre, L. J. Electrophoretic Deposition of Materials. *Annu. Rev. Mater. Sci.* **29,** 327–352 (1999).

77. Corni, I., Ryan, M. P. & Boccaccini, A. R. Electrophoretic deposition: From traditional ceramics to nanotechnology. *J. Eur. Ceram. Soc.* **28,** 1353–1367 (2008).

78. Chavez-Valdez, A., Shaffer, M. S. P. & Boccaccini, A. R. Applications of Graphene Electrophoretic Deposition . A Review. *J. Phys. Chem. B* **117,** 1502–1515 (2013).

79. Liu, S., Ou, J., Wang, J., Liu, X. & Yang, S. A simple two-step electrochemical synthesis of graphene sheets film on the ITO electrode as supercapacitors. *J. Appl. Electrochem.* **41,** 881–884 (2011).

80. Chen, Y., Zhang, X., Yu, P. & Ma, Y. Electrophoretic deposition of graphene nanosheets on nickel foams for electrochemical capacitors. *J. Power Sources* **195,** 3031–3035 (2010).

81. Chen, Y., Zhang, X., Yu, P. & Ma, Y. Stable dispersions of graphene and highly conducting graphene films: a new approach to creating colloids of graphene monolayers. *Chem. Commun.* 4527–4529 (2009). doi:10.1039/b907723e

82. Böhm, S. Graphene against corrosion. *Nat. Nanotechnol.* **9,** 741–2 (2014).

83. Sarkar, D., Krall, M. & Banerjee, K. Electron-hole duality during band-to-band tunneling process in graphene-nanoribbon tunnel-field-effect-transistors. *Appl. Phys. Lett.* **97,** 263109 (2010).

84. Park, J. H. & Park, J. M. Electrophoretic deposition of graphene

oxide on mild carbon steel for anti-corrosion application. *Surf. Coatings Technol.* **254,** 167–174 (2014).

85. Pu, N.-W. *et al.* Graphene grown on stainless steel as a high-performance and ecofriendly anti-corrosion coating for polymer electrolyte membrane fuel cell bipolar plates. *J. Power Sources* **282,** 248–256 (2015).

86. Stoot, A. C., Camilli, L., Spiegelhauer, S.-A., Yu, F. & Bøggild, P. Multilayer graphene for long-term corrosion protection of stainless steel bipolar plates for polymer electrolyte membrane fuel cell. *J. Power Sources* **293,** 846–851 (2015).

87. Revie, W. R. & Uhlig, Herbert, H. *Corrosion and Corrosion Control*. (John Wiley & Sons, 2008).

88. Fielder, J. W. & Needham, N. G. *The Corrosion of Metals*. (1986).

89. Hays, G. F. Now is the Time. *The World Corrosion Organisation* (2010). at <www.corrosion.org>

90. Bard, A. J., Stratmann, M. & Frankel, G. S. Corrosion and Oxide Films. *Encyclopedia of Electrochemistry* 755 (2007).

91. Hibbert, D. B. *Introduction to Electrochemistry*. (The Macmillan, 1993).

92. Pourbaix, M. *Atlas of Electochemical Equilibria in Aqueous Solutions*. (Pergamon Press, 1966).

93. Bockris, J. O. 'M., Drazic, D. & DesPic, A. . R. The Electrode Kinetics of The Deposition and Dissolution of Iron. *Electrochim. Acta* **4,** 325–361 (1961).

94. The Stainless Steel Information Centre. Corrosion: Pitting and Crevice Corrosion. (2013). at <http://www.ssina.com/corrosion/crevice-pitting.html>

95. Technology, M. Corrosion. (2013). at <http://materialteknologi.hig.no/ml-corrosion.htm>

96. Substances and Technology. Pitting Corrosion. (2012). at <http://www.substech.com/dokuwiki/doku.php?id=pitting_corrosion>

97. Thompson, N. G. & Payer, J. H. *DC Electrochemical Test Methods*. (NACE International, 1998).

98. Macdonald, J. R. & Johnson, W. B. in *Impedance Spectroscopy:Impedance Spectroscopy: Theory, Experiment, and Applications* (eds. Barsoukov, E. & Macdonald, J. R.) 1–20 (Wiley, 2005).

99. Brett, D. J. L. Electrochemical Impedance Spectroscopy for Polymer Electrolyte Fuel Cells. in *Supergen Fuel Cells* 60 (2013).

100. Wagner, N. in *Impedance Spectroscopy: Theory, Experiment, and Applications* (eds. Barsoukov, E. & Macdonald, J. R.) (Wiley, 2005).

101. Cottis, R. & Turgoose, S. *Electrochemical Impedance and Noise*. (NACE International, 1998).

102. G5-94. *Standard reference test method for making potentiostatic and potentiodynamic anodic polarization measurements*. *Annual Book of ASTM Standards* (ASTM International, 2000).

103. Stern, M. & Geary, A. L. Electrochemical Polarization: I. A Theoretical Analysis of the Shape of Polarization Curve. *J. Electrochem. Soc.* **104,** 56–63 (1957).

104. Gabreab, E. M. *et al.* An electrochemical treatment to improve corrosion and contact resistance of stainless steel bipolar plates used in polymer electrolyte fuel cells. *J. Power Sources* **245,** 1014–1026 (2014).

105. Chu, D. & Jiang, R. Comparative studies of polymer electrolyte membrane fuel cell stack and single cell. *J. Power Sources* **80,** 226–234 (1999).

106. Mason, T. J. *et al.* A study of the effect of water management and electrode flooding on the dimensional change of polymer electrolyte fuel cells. *J. Power Sources* **242,** 70–77 (2013).

107. Mason, T. J., Millichamp, J., Shearing, P. R. & Brett, D. J. L. A study of the effect of compression on the performance of polymer electrolyte fuel cells using electrochemical impedance spectroscopy and dimensional change analysis. *Int. J. Hydrogen Energy* **38,** 7414–7422 (2013).

108. Wang, Y. & Northwood, D. O. An Investigation on Metallic Bipolar Plate Corrosion in Simulated Anode and Cathode Environments of PEM Fuel Cells using Potential-pH Diagrams. *Int. J. Electrochem. Sci.* **1,** 447–455 (2006).

109. Skoog, D. A., Holler, F. J. & Crouch, S. R. *Principles of Instrumental Analysis*. (Thomson Brooks/Cole, 2007).

110. Skoog, D. A., Holler, F. J. & Nieman, T. A. *Principles of Instrumental Analysis*. (Thomson Learning, 1998).

111. Morris, V. J., Kirby, A. R. & Gunning, A. P. *Atomic Force Microscopy for biologists*. (Imperial College Press, 2010).

112. Ricci, D. & Braga, P. C. in *Atomic Force Microscopy: Biomedical Methods and Applications* (eds. Braga, P. C. & Ricci, D.) (Humana Press, 2004).

113. University of Virginia. Atomic Force Microscopy. (2011). at <http://pharm.virginia.edu/AFM.html>

114. Cho, J. *et al.* Characterisation of carbon nanotube films deposited by electrophoretic deposition. *Carbon N. Y.* **47,** 58–67 (2009).

115. Fukutsuka, T. *et al.* Carbon-coated stainless steel as PEFC bipolar plate material. *J. Power Sources* **174,** 199–205 (2007).

116. Colthup, N. B., Daly, L. H. & Wiberley, S. E. *Introduction to Infrared and Raman Spectroscopy*. (Academic Press, 1990).

117. Raman, C. V. & Krishnan, K. S. A New Type of Secondary Radiation. *Nature* **121,** 501–502 (1928).

118. Smekal, A. Zur Quantentheorie der Dispersion. *naturwissenschaften* **11,** 873–875 (1923).

119. Zhan, D. & Shen, Z. in *Two-Dimensional Carbon: Fundamental Properties, Synthesis, Characterization, and Applications* (eds. Wu, Y., Shen, Z. & Yu, T.) 153–182 (Pan Stanford Publishing, 2014).

120. Cançado, L. G. *et al.* Anisotropy of the Raman Spectra of Nanographite Ribbons. *Phys. Rev. Lett.* **93,** 047403 (2004).

121. Dresselhaus, M. S., Dresselhaus, G., Saito, R. & Jorio, A. Raman spectroscopy of carbon nanotubes. *Phys. Rep.* **409,** 47 (2005).

122. Cançado, L. G., Reina, A., Kong, J. & Dresselhaus, M. S. Geometrical approach for the study of G′ band in the Raman spectrum of monolayer graphene, bilayer graphene, and bulk graphite. *Phys. Rev. B - Condens. Matter Mater. Phys.* **77,** 245408 (2008).

123. Malard, L. M., Pimenta, M. A., Dresselhaus, G. & Dresselhaus, M. S. Raman spectroscopy in graphene. *Phys. Rep.* **473,** 51–87 (2009).

124. Pimenta, M. A. *et al.* Studying disorder in graphite-based systems by Raman spectroscopy. *Phys. Chem. Chem. Phys.* **9,** 1276–1291 (2007).

125. Ni, Z. H. *et al.* On Resonant Scatterers As a Factor Limiting Carrier Mobility in Graphene. *Nano Lett.* **10,** 3868–3872 (2010).

126. Ferrari, A. C. Raman spectroscopy of graphene and graphite: Disorder, electron-phonon coupling, doping and nonadiabatic effects. *Solid State Commun.* **143,** 47–57 (2007).

127. Landis, E. N. & Keane, D. T. X-ray microtomography. *Mater. Charact.* **61,** 1305–1316 (2010).

128. Zeiss. ZEISS Xradia 520 Versa: Submicron Imaging with New Degrees of Freedom. (2016). at <http://www.zeiss.com/microscopy/en_de/products/x-ray-microscopy/zeiss-xradia-520-versa.html>

129. Banhart, J. in *Advanced Tomographic Methods in Materials Research and Engineering* (ed. Banhart, J.) 3–18 (Oxford University

Press, 2011).

130. Hounsfield, G. N. Computerized transverse axial scanning (tomography): Part I. Description of system. *British Journal of Radiology* **46,** 1016–1022 (1973).

131. Hounsfield, G. N. Apparatus for examining a body by radiation such as X or gamma radiation. (1976).

132. Salvo, L., Su??ry, M., Marmottant, A., Limodin, N. & Bernard, D. 3D imaging in material science: Application of X-ray tomography. *Comptes Rendus Phys.* **11,** 641–649 (2010).

133. Shearing, P. R., Gelb, J. & Brandon, N. P. X-ray nano computerised tomography of SOFC electrodes using a focused ion beam sample-preparation technique. *J. Eur. Ceram. Soc.* **30,** 1809–1814 (2010).

134. Carl ZEISS X-Ray Microscopy. ZEISS Xradia 520 Versa: Scout-and-Scan ™ Control System Quick Reference Guide. (2016).

135. Beck, M., Goebbels, J., Burkert, A., Isecke, B. & Bäßler, R. Monitoring of corrosion processes in chloride contaminated mortar by electrochemical measurements and X-ray tomography. *Mater. Corros.* **61,** 475–479 (2010).

136. Goebbels, J. *et al.* Computed Tomography – A New Tool Studying Hidden Corrosion. in *10th European Conference on Non-Destructive Testing* 1–10 (2010).

137. Česen, A., Kosec, T. & Legat, A. Characterization of steel corrosion in mortar by various electrochemical and physical techniques. *Corros. Sci.* **75,** 47–57 (2013).

138. Tata Steel Europe Limited. HILAN: Bright nickel-plated steel. (2013). at <http://www.tatasteeleurope.com/static_files/Downloads/General Industry Strip/Electro Plated/1462 TATA Hilan.pdf>

139. Tata Steel Europe Limited. HILUMIN: Ultra-clean nickel-plated steel. (2013). at <http://www.tatasteeleurope.com/static_files/Downloads/General

Industry Strip/Electro Plated/1462 TATA Hilumin.pdf>

140. Juttner, K. Electrochemical Impedance Spectroscopy (EIS) of Corrosion Processes on Inhomogeneous Surfaces. *Electrochim. Acta* **35,** 1501–1508 (1990).

141. Iversen, A. K. Stainless steels in bipolar plates—Surface resistive properties of corrosion resistant steel grades during current loads. *Corros. Sci.* **48,** 1036–1058 (2006).

142. Saito, R., Hofmann, M., Dresselhaus, G., Jorio, a. & Dresselhaus, M. S. Raman spectroscopy of graphene and carbon nanotubes. *Adv. Phys.* **60,** 413–550 (2011).

143. Narula, R. & Reich, S. Double resonant Raman spectra in graphene and graphite: A two-dimensional explanation of the Raman amplitude. *Phys. Rev. B* **78,** 165422 (2008).

144. Venezuela, P., Lazzeri, M. & Mauri, F. Theory of double-resonant Raman spectra in graphene: Intensity and line shape of defect-induced and two-phonon bands. *Phys. Rev. B* **84,** 035433 (2011).

145. Eda, G. *et al.* Photoluminescence from Chemically Exfoliated MoS2. *Nano Lett.* **11,** 5111–5116 (2011).

146. Cullen, P. L. *et al.* Ionic solutions of two-dimensional materials. *Nat. Chem.* **9,** 244–249 (2017).

147. Milner, E. M. *et al.* Structure and Morphology of Charged Graphene Platelets in Solution by Small-Angle Neutron Scattering. *J. Am. Chem. Soc.* **134,** 8302–8305 (2012).

148. Dresselhaus, M. S. & Dresselhaus, G. Intercalation compounds of graphite. *Adv. Phys.* **51,** 1–186 (2002).

149. Solin, S. Two-Dimensional Metal-Ammonia-Solutions in Graphite. *J. Phys. IV Colloq.* **01,** C5–311–C5–324 (1991).

150. Chaban, V. V. & Prezhdo, O. V. Electron Solvation in Liquid Ammonia: Lithium, Sodium, Magnesium, and Calcium as Electron Sources. *J. Phys. Chem. B* **120,** 2500–2506 (2016).

151. John, B. M., Mugo, S. W., Timonah, N. S., Ngumbi, P. K. & Ngei, K. Correlation Of Optical Transmittance With Number Of Graphene Layers. *IOSR J. Appl. Phys.* **8,** 42–46 (2016).